DISS. ETH NO. 26470

FOREST STRUCTURE CHARACTERIZATION FROM SAR TOMOGRAPHY

A thesis submitted to attain the degree of

DOCTOR OF SCIENCES of ETH ZURICH

(Dr. sc. ETH Zurich)

presented by
Victor Cazcarra Bes

Telecommunication engineer
University Miguel Hernández of Elche

born on 18.06.1985
citizen of Spain

accepted on the recommendation of

Prof. Dr. Irena Hajnsek, examiner
Prof. Dr. Andreas Huth, co-examiner
Prof. Dr. Stefano Tebaldini, co-examiner
Prof. Dr. Lars M. H. Ulander, co-examiner

2019

Abstract

Forests cover about 30 % of the Earth's land surface. They are an important element of the carbon and water cycle as they can act as both sinks and sources. As a result, they can influence the local and global climate. At the same time, forests are an important economic factor as they provide wood and food, and of high ecological importance as they provide habitat for numerous plants and animals. Due to its importance, the mapping, inventory and assessment of forests and their changes worldwide become a priority for scientists and governments, and is the motivation for this thesis. In particular, the thesis focuses on the study of the three dimensional (3-D) forest structure, as it is a key parameter of the forest ecosystem useful for many applications like biomass estimation, plant biodiversity or forest management and productivity.

Since decades, the most common way to characterize forest structure has been the use of single-tree information collected in situ. However, this type of measurement is typically limited to small and accessible forest areas. Remote sensing techniques overcome these limitations allowing large coverage and the collection of information without physical contact. Across the different remote sensing techniques, synthetic aperture radars (SAR) play an essential role. They provide unique ability to systematically image large areas at high spatial and temporal resolution, while at the same time they allow penetrating into forest volumes (especially at low frequencies) providing information about its 3-D structure.

SAR tomography (TomoSAR) uses multiple SAR acquisitions at slightly different positions to reconstruct the 3-D radar reflectivity, by means of imaging techniques without the need of using scattering models. However, the potential of TomoSAR configurations to extract 3-D structural information with ecological meaning has not been fully assessed yet. In this context, the first goal of this thesis is to establish a link between TomoSAR measurements and 3-D forest structure. In this sense, a framework that allows the qualitative and quantitative characterization of the 3-D forest structure from tomographic SAR profiles has been proposed. From the statistical distribution of the local maxima of the TomoSAR profiles, two indices are proposed to describe the horizontal density and the vertical complexity of a forest. This approach has been evaluated on a TomoSAR L-band data set over a temperate forest in Germany, together with the structure obtained from single-tree ground measurements and Lidar data. The results show a high correlation between the structures derived from the three sources of data, which confirms the ecological significance of the proposed method. Moreover, the same methodology has been used to demonstrate the ability of TomoSAR profiles to detect and characterize structure changes of forest stands.

The second goal of the thesis is to evaluate different TomoSAR algorithms and configurations with a focus on forest structure applications. Fourier beamforming, Capon beamforming and compressive sensing have been analyzed with simulated and real TomoSAR data at L-band. The results indicate that compressive sensing is the most appropriate one for the characterization of forest structure as proposed in this thesis, but it has the drawback of introducing sometimes false local maxima. Furthermore, it has been found that in tandem-like (bistatic) TomoSAR implementations the reconstruction of the profiles is robust to temporal changes of the scattering on a longer time span, in contrast to repeat-pass (monostatic) implementations. Finally, the requirements of TomoSAR acquisitions for distinguishing different structure types have been evaluated in terms of vertical resolution, height of ambiguity and peak side-lobe level of the point spread function. The results show that, for a limited number of images (5 to 7), a non-uniform distribution of the tracks with low vertical resolution (10 to 15 m) is the best compromise to avoid higher values of the peak to sidelobe level that would degrade the quality of the TomoSAR profiles and their interpretation.

The results of the thesis underline the potential of TomoSAR as a 3-D imaging tool for forest structure applications and contribute to better understand the TomoSAR profiles. Moreover, they open the door to further evaluate, investigate and exploit the enormous amount of TomoSAR data that the two upcoming SAR missions (ESA's BIOMASS and DLR's Tandem-L) will provide over all forests of the Earth.

Kurzfassung

Wälder bedecken ungefähr 30 % der Landoberfläche der Erde. Sie sind ein bedeutendes Element des Kohlenstoff- und Wasserkreislaufs da sie sowohl als Senken wie auch als Quellen agieren können. Dadurch beeinflussen sie das lokale und globale Klima. Gleichzeitig sind Wälder ein bedeutender Wirtschaftsfaktor, da sie Holz und Nahrung liefern, und von großer öcologischer Bedeutung, da sie zahlreichen Pflanzen und Tieren Lebensraum bieten. Aufgrund ihrer Bedeutung ist die Kartierung, Inventur und Erfassung des Zustands der Wälder und ihrer Veränderung weltweit für Wissenschaftler und Regierungen zur Priorität geworden. Dies ist daher auch die Motivation für diese Arbeit. Genauer gesagt, beschäftigt sich diese Arbeit mit der Erforschung der dreidimensionalen (3-D) Struktur des Waldes, da dies ein wichtiger Parameter des Waldökosystems ist und daher für viele Anwendungen, wie Biomasseschätzungen, Pflanzenbiodiversität- oder Waldmanagement- und Produktivitätsschätzungen, nützlich ist.

Seit Jahrzehnten ist die gebräuchlichste Methode zur Charakterisierung der Waldstruktur die Verwendung von individuellen Baummessungen, die vor Ort erhoben werden. Allerdings ist diese Art der Messung üblicherweise auf kleine und gut erreichbare Waldbereiche limitiert. Fernerkundungsmethoden überwinden diese Einschränkungen und ermöglichen eine große räumliche Abdeckung und das Erfassen von Informationen ohne physischen Kontakt. Unter den verschiedenen Fernerkundungstechniken spielen synthetische Apertur Radare (SAR) eine essentielle Rolle: Sie ermöglichen auf einzigartige Weise die systematische Abbildung von großen Flächen mit hoher räumlicher und zeitlicher Auflösung. Gleichzeitig können Mikrowellen in das Waldvolumen eindringen (vor allem bei niedrigeren Frequenzen) und dadurch Informationen über die 3-D Struktur erfassen. Das Verfahren der SAR Tomographie (TomoSAR) verwendet mehrere SAR Aufnahmen, um die 3-D Radarrückstreuung zu messen. Dies geschieht durch Abbildungsverfahren die unabhängig von Streumodellen sind. Allerdings ist die Beziehung zwischen tomographischer 3D Information und physikalischer 3-D Waldstruktur bis heute noch nicht etabliert. Das erste Ziel dieser Arbeit ist, in diesem Zusammenhang eine Verbindung zwischen TomoSAR Messungen und der physikalischen 3-D Waldstruktur herzustellen.

Dazu wurde ein Konzept vorgeschlagen, das es erlaubt aus tomographischen SAR Profilen die 3-D Waldstruktur qualitativ und quantitativ zu charakterisieren. Aus der statistischen Verteilung der lokalen Maxima der TomoSAR Profile werden dabei zwei Indizes bestimmt, die die horizontale Dichte und die vertikale Komplexität eines Bestandes beschreiben und ebenso aus der Vermessung der einzelnen Bäume des Bestandes hergeleitet werden können. Das Konzept wurde mit L-band TomoSAR Daten über einem Mischwald in Deutschland, für den auch individuelle Messungen aller Bäume und Lidar Daten vorhanden sind, evaluiert. Die Ergebnisse zeigen eine hohe Korrelation zwischen den drei Datenquellen, wodurch die ökologische Bedeutung der Methode bestätigt wird. Zusätzlich wurde diese Methode genutzt, um die Erfassung und Charakterisierung von Strukturänderungen mit TomoSAR zu demonstrieren.

Das zweite Ziel dieser Arbeit ist die Bewertung verschiedener TomoSAR Algorithmen und Konfigurationen mit Fokus auf Waldstrukturanwendungen. Dazu wurden die Fourier Strahlformung, die Capon Strahlformung und Compressive Sensing mit simulierten und echten TomoSAR Daten untersucht. Die Ergebnisse zeigen, dass Compressive Sensing am besten für die Charakterisierung der Waldstruktur, anhand des in dieser Arbeit vorgestellten Ansatzes, geeignet ist. Allerdings hat es den Nachteil, dass zum Teil falsche lokale Maxima in den L-Band TomoSAR Profilen auftreten. Darüber hinaus wurde gezeigt, dass die Rekonstruktion der Profile bei Tandem-artigen (bistatischen) TomoSAR Konstellationen über einen längeren Zeitraum, robust gegenüber zeitlichen Veränderungen der Streuer ist, wie im Falle von (monostatischen) Repeat-Pass Konstellationen. Abschließend wurden die Anforderungen an TomoSAR Daten zur Unterscheidung verschiedener Strukturtypen in Bezug auf vertikale Auflösung, Mehrdeutigkeitshöhe und dem Haupt- zu Nebenkeulenverhaltnis der Punktverteilungsfunktion untersucht. Dies hat gezeigt, dass für eine begrenzte Anzahl an Aufnahmen (Fünf bis Sieben) in einem realistischen TomoSAR Szenario, eine ungleichmäßige Verteilung der Flugbahnen, mit einer niedrigen vertikalen Auflösung (10 bis 15 m), der beste Kompromiss ist, um höhere Werte des Haupt- zu Nebenkeulenverhaltnis zu vermeiden, die die Qualität der TomoSAR Profile und deren Interpretation verschlechtern würden.

Die Ergebnisse dieser Arbeit zeigen das Potential von 3-D tomographischen SAR Abbildungsverfahren für Waldstrukturanwendungen und tragen zu einem besseren Verständnis des Informationsgehalts von TomoSAR Profilen bei. Desweiteren tragen sie dazu bei, die enorme Menge an TomoSAR Daten zu verwerten, die zukünftige SAR Missionen (BIOMASS der ESA und Tandem-L des DLR) von den Wäldern der Erde liefern werden.

Acknowledgements

This PhD thesis manuscript is just the summary of the technical part of a long journey full of ups and downs that I sincerely think made me better in many aspects. A lot of people helped and encouraged me to start, continue and finish this journey from the professional and personal side.

First of all, many thanks to Andreas Huth, Stefano Tebaldini and Lars M. H. Ulander for accepting being in the committee and reviewing this manuscript.

An important contribution of this PhD is the non-radar point of view perspective that I learnt from all the Biosphere colleagues during the HGF Alliance project. The concept of forest structure used in the thesis is an outcome of many ideas and work done by all colleagues of that project. Special mention and thanks to all colleagues at Helmholtz Centre for Environmental Research (UFZ), Andreas Huth, Edna Rödig, Friedrich Bohn, Rico Fisher and Nikolai Knapp. Michael Heym and Peter Biber from the Technical University of Munich (TUM) and Nesrin Salepci from the university of Jena. Thanks for the discussions about forests, models, lidar and everything related to non-work during the Alliance weeks in Garmisch.

A big part of this PhD would not be possible without the ground data collected in Froschham. Thanks to Ralf Moshammer for organizing the ground measurements and sharing the office during some months, with him I discovered how is possible to measure more than 16000 trees!.

From DLR, I would like to thank Alberto Moreira and Gerhard Krieger for giving me the possibility to work in the Microwave and Radar institute and be always open for any need I had during the PhD. Special gratitude goes to Irena Hajnsek for trusting me, allowing me to be in the enriching project HGF Alliance, as well as to defend the thesis at ETH.

Many thanks to the F-SAR processing team at HR (Ralf, Rolf, Marc, Martin,. . .) for the data acquisition and processing, without them I would not have the data in such a ready-to-use and high-quality level.

I learnt a lot from Kostas, his particular way of seeing life and the scientific questions improved my skills from technical and personal perspectives. Many thanks for trusting and supporting my work in every conference, meeting and paper we did together.

The first steps of this work would not be possible without Marivi. She was my first supervisor, and I learnt many things from her. I really appreciate all the things she did for me and the development of the PhD. Although she could not stay until the end of the PhD, she was always open to help and discuss until the last moment. In the last steps of the PhD, Matteo Pardini, although he helped me since the begging, became my supervisor. Many thanks for all the support you gave me, the discussions about tomography, forest structure, and the detailed comments in the papers and the final manuscript.

Without any doubt, the best thing from DLR is the work atmosphere and the people I met. I would like to thank all of my present and past colleagues from the information retrieval and polinsar groups: Sibylle (thanks for always being willing to help), Astor (my first office-mate that helped me a lot in my first steps in Germany and DLR), Hannah, Thomas B., Thomas J., Sandra, Michelangelo, Maria, Emanuel, Roman, Kristina, Jun Su (many thanks for the polinsar forest height for the introduction!), Alberto (thank you for all technical and what-ever-topic discussions we had (almost) every day), Changhyun (thanks for sharing the office in such a friendly and happy way), Giuseppe (thanks for your support from the previous-PhD perspective and sorry for the champion league final of 2015) and special thanks to Georg for translating to German the abstract and sharing together the last steps of our PhDs, with long discussions and always a positive mood. I would not have enough space to say thank you to all the DLR colleagues from other groups. Special mention to all the *coffee-Italians* as a group (Paola, Michele, Mariantonietta, Matteo, ...), Jose Luis for the happiness of the small talks we have every morning door-to-door and Nestor for all the rundes we had speaking about any topic and trying to solve all the problems in World.

Outside DLR, I first have to say thanks to Juanma and David from the University of Alicante. I could say that they are the starting point of this PhD. They taught me since my first year at the

university, they gave me the opportunity to do my bachelor and master thesis, introduced me to the world of SAR, and encouraged me to start a PhD. I will always remember the period in the lab of the University of Alicante. Mention also here to my university colleagues Fernando Vicente, *Vactor*, Ignacio and Esteban.

I really want to thank my Spanish-Munich friends: Jose, Tamara, Lari, David and Hilario. Maybe they do not know, but they helped me a lot during this hard period of being abroad. I would also like to say thanks to my Alicante friends: Yeray, Miguel, Pedro, Nacho, Joaquin, Alberto and Paco. Thank you so much for all moments we had together since I arrived to Alicante.

A big gratitude is for my family, my parents, Pilar and Jesus, and my sister, Sandra, for supporting and trusting me in every step and decision I took, not only in this PhD, but also in my whole life. Thank you for all the things you always do for me. I want to dedicate the thesis to my grandmother, Andrea. She did not have the luck and the opportunity that I had to study. Thanks for taking care of me since I was a child.

The biggest gratitude of this thesis is for my beloved girlfriend, Maria, whose love, patient and support encouraged me to continue and finish this PhD. Thanks for being always by my side.

And finally, thanks to you, the reader, for spending a bit of time of your life reading this PhD thesis.

Contents

List of Abbreviations

2-D	**Two** **D**imensional
3-D	**Three** **D**imensional
AGB	**A**bove **G**round **B**iomass
CB	**C**apon **B**eamforming
COMET	**CO**variance **M**atching **E**s**T**imator
CS	**C**ompressive **S**ensing
DBH	**D**iameter at **B**reast **H**eight
DEM	**D**igital **E**levation **M**odel
DFT	**D**iscrete **F**ourier **T**ransform
DLR	**D**eutsches **Z**entrum für Luft- und **R**aumfahrt (German Aerospace Center)
E-SAR	**E**xperimental **SAR** (Airborne SAR system of DLR)
ESA	**E**uropean **S**pace **A**gency
ForestGEO	**Forest** **G**lobal **E**arth **O**bservatory network
F-SAR	Successor of the E-SAR airborne SAR system
FB	**F**ourier **B**eamforming
FORMIND	**FOR**est gap **M**odel **IND**ividual-based (formind.org)
GEDI	**G**lobal **E**cosystem **D**ynamics **I**nvestigation NASA mission
HH	**H**orizontal polarization received - **H**orizontal polarization transmitted
HS	**H**orizontal **S**tructure
HV	**H**orizontal polarization received - **V**ertical polarization transmitted
InSAR	**Int**erferometric **S**ynthetic **A**perture **R**adar
Lidar	**L**ight **i**maging **d**etection **a**nd **r**anging
NASA	**N**ational **A**eronautics and **S**pace **A**dministration
MUSIC	**MU**ltiple **SI**gnal **C**lassification
PSL	**P**eak **S**idelobe **L**evel
Pol-InSAR	**Pol**arimtric **In**terometric **S**ynthetic **A**perture **R**adar
Pol-SAR	**Pol**arimtric **S**ynthetic **A**perture **R**adar
PSF	**P**oint **S**pread **F**unction
Radar	**Ra**dio **d**etection **a**nd **r**anging
RGB	Additive color model wit three channels: **R**ed, **G**reen and **B**lue
RH	**R**elative **H**eight
RIP	**R**estricted **I**sometry **P**roperty
SAR	**S**ynthetic **A**perture **R**adar
SDP	**S**emi **D**efinite **P**ositiveness
SLC	**S**ingle **L**ook **C**omplex
Tandem-L	Future radar earth observation satellite at L-band (from DLR)
TomoSAR	**Tomo**graphic **S**ynthetic **A**perture **R**adar
UTM	**U**niversal **T**ransverse **M**ercator
VH	**V**ertical polarization received - **H**orizontal polarization transmitted
VS	**V**ertical **S**tructure
VV	**V**ertical polarization received - **V**ertical polarization transmitted
WSF	**W**eighted **S**ubspace **F**itting

Chapter 1

Introduction

This section acts as a starting point of the thesis manuscript. First, in Section 1.1, a general motivation for this work with an emphasis on the importance of forests and more specifically of forest structure and its changes is presented. Then, Section 1.2 provides an overview of the state-of-the-art techniques for forest structure estimation from ground measurements and remote sensing systems (optical, Lidar and Synthetic Aperture Radar (SAR)). Since of particular of interest of this thesis, Section 1.2.4 describes with more detail the current SAR and especially SAR tomographic techniques with a focus on their ability to extract forest structure information. Section 1.3 reports the research questions and open challenges addressed by the thesis, and finally, Section 1.4 explains the organization of the different parts of the present manuscript.

1.1 Motivation

Forests cover around 30 % of the total land surface of the Earth, and they are one of the most important ecosystems. They are the habitat of a significant amount of vegetation and animal species, they provide key primary resources like wood and food, and they act as a storage of carbon and water. They have a big impact on the local and global climate and protect the erosion of the ground [1]. Climate change is tightly related to forests and their role in the carbon cycle through the biomass. The biomass is the total quantity or weight of organisms in a given area of the forest, is a measure of the forest productivity (for example wood production) and it is related with the amount of carbon that the forest is able to store. Therefore, the degradation and deforestation of forests have a direct connection with the amount of carbon in the atmosphere and as a consequence on the global warming of the Earth [2]. With this, the understanding and monitoring of forest state and dynamics have critical importance for the scientific community [3]–[7].

Among all possible forest information that can be obtained to characterize and understand the forest ecosystem, their structure is a key element [8]. In forestry, it is commonly understood that the forest structure should express and describe the arrangement of trees and vegetation elements in a three-dimensional (3-D) space [9]. Forest structure is an indicator of forest successional stage and development as well as sustainability and habitability, and is therefore an important parameter for assessing more accurately the estimation of forest aboveground biomass (AGB) [10], forest productivity [11], carbon fluxes [12] and biodiversity [13]. Structure changes can be even more important than absolute structure measurements when it comes to forest dynamics and seasonal processes. For example, logging and degradation of forests due to natural or human disturbances can be detected from forest structure before the forest height is affected.

Since decades, the 3-D forest structure has been characterized at local scales by means of ground measurements composed by individual tree parameters [14]–[16]. These types of measurements allow a very detailed description of the 3-D structure of the forest; however, they are limited in terms of spatial coverage and frequency of new measurements over the same area. Therefore, remote sensing systems and techniques are increasingly playing a crucial role in forest observations. By using passive or active system mounted on a space borne platform orbiting around the Earth, forest information at global scale can be obtained with high spatial and temporal resolution. However, in contrast to the individual tree ground measurements, actual space borne configurations are not able, in terms of spatial resolution, to distinguish single trees. Not only, but the specific sensor sensitivity and measurements lead to different sources of information. For instance, optic sensors [17] provide high-resolution two dimensional (2-D) images by collecting the solar radiation from the forest surface, Light Imaging Detection and Ranging (Lidar) sensors [18] provide information about the height and position of the physical elements and SAR [19], [20] gives information not only about the physical structure of the elements, but also about the dielectric properties.

Among all of them, SAR systems can acquire data independently of the day and night cycle, as well as of the presence of clouds. Taking into account that the cloud coverage in some essential forest areas, such as the tropics, is more than 80 % of the time [21], the cloud penetration capability is a powerful (and unique) tool of SAR systems for forest applications. More importantly, the ability of electromagnetic waves to penetrate (especially at low frequencies) into forest volumes, together with advanced radar techniques like SAR tomography (TomoSAR) [22]–[26] enables 3-D imaging capabilities that can potentially be used to extract 3-D forest structure. The increasing interest in using TomoSAR for forest application is reflected in the acquisition configurations and the related forest products of the ESA BIOMASS [27], [28] (at P-band) and the DLR Tandem-L [29] (at L-band) missions.

However, the 3-D image is a 3-D reflectivity, i.e. distribution of backscattering power. The interpretation of such electromagnetic quantity in terms of bio-physical parameters, like forest structure, is not established yet. The lack of this transition from TomoSAR to forest structure information motivates this thesis work. In this context, the thesis is conceptually divided into two main parts. The first part attempts to build up a link between the 3-D TomoSAR reflectivity and 3-D forest structure and its changes through qualitative and quantitative measurements. In the second part, TomoSAR algorithms and configurations are compared in order to obtain reflectivity estimates appropriate for forest structure applications.

1.2 Forest Structure Characterization

A proper quantification of 3-D forest structure is not a straightforward operation. Even for ground measurements, with single-tree information, there is not a unique way to quantify forest structure, and many parameters (or indices) have been proposed. For remote sensing techniques, where in general single-tree information is not available anymore, the specific sensor measurements, resolutions and acquisition configuration make the transition from remote sensing data to (conventional) physical structure measurements and indices very difficult. In the next Sections 1.2.1, 1.2.2, 1.2.3 and 1.2.4, a brief overview of the state-of-the-art for the estimation of forest structure and forest parameters from different sources of data is given.

1.2.1 Ground Measurements

Since the beginning of forestry studies, the only way to study and analyse the distribution of the trees in a forest was through measurements collected in situ [30]. Ground measurements have been collected since decades, and they are still today a primary and excellent source of forest information due to the level of detail, as well as the potential availability of long-term data. Individual tree parameters such as the position, species, diameter at breast height (DBH) (diameter of the trunk at 1.3 m above the ground) and (top) height of trees are measured and collected into the so-called forest inventories [14]–[16]. More recently, ground remote sensing techniques like terrestrial laser scanning have been used to help and improve the acquisition of individual tree parameters in the surroundings of the measurement location [31]–[35].

Despite a detailed individual tree information is available, the quantitative description of forest structure is not straightforward [36]. Indeed, there is not yet an overall and unequivocal measure or descriptor able to express and quantify forest structure in terms of forestry and ecology appropriate for a variety of applications, scales and forest types [37]–[39]. However, there is a common understanding in forestry that more than one index need to be considered to unambiguously characterize the structural heterogeneity, in the horizontal and vertical dimensions, of the forest.

In the framework of this thesis, the quantification of 3-D forest structure is performed by means of horizontal and vertical structure indices. Figure 1.1 shows a representation of such a concept, where two indices describe the horizontal and vertical variability of the trees in the corresponding directions.

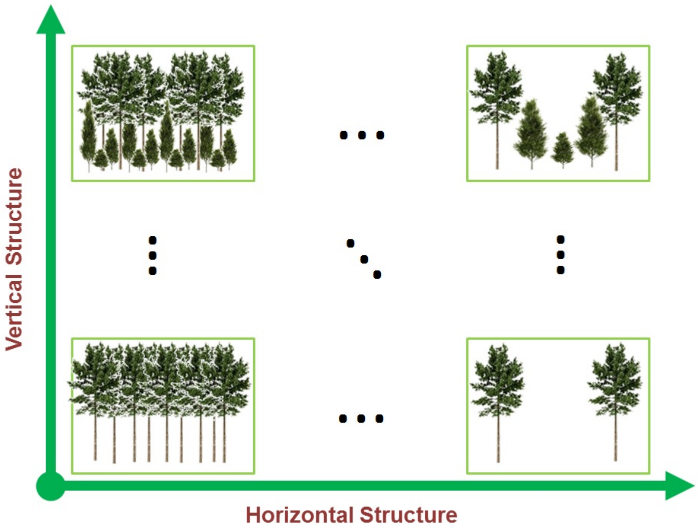

FIGURE 1.1: The horizontal and vertical structure plane proposed and used in Chapters 2, 3 for the classification of 3-D forest structure and its changes.

In the absence of a general defintion of forest structure, different approaches have been followed to derive such horizaontal and vertical structure indices [11]. One way to express the horizontal structure is the stand density index [40], based on the DBH of the trees and the number of tree stems per area unit. Regarding the vertical structure, the variability of the tree size (calculated again in terms of DBH) is accepted as an adequate measurement. It is important to keep in mind that the coverage and the spatial and temporal continuity of ground measurements (for the estimation of the mentioned indices) play a crucial role for a proper forest structure characterization.

Figure 1.2 shows an example of a forest inventory plot covering an area of 25 hectares in Traunstein in the south-eastern part of Germany [41], where species, position and DBH of each tree have been recorded. Figure 1.2(a) shows an optical image of the site and Figure 1.2(b) the positions of each tree with a DBH greater than 5 cm represented with black dots. In the yellow area, all trees with a DBH greater than 1 cm have been also measured, which gives a total amount of more than 16000 trees. Such continuous and extended ground measurements allow a detailed characterization of forest structure, in terms of horizontal and vertical indices (see Chapter 2).

However, the characterization of forest structure employing ground measurements present spatial and temporal limitations. Continuous measurement of all trees can not be achieved in large areas due to cost, in terms of money as well as human effort. One way to extend the coverage is to establish a network of sparse field inventory plots at local scales (< 1 hectare). However, the ability of these measurements to represent the surrounding landscape depends on the possibility to extrapolate any structural metric in-between the sparse field inventories. Another limitation is the difficulty to access forest stands in remote (or dangerous) areas. Finally, the cost of such measurements limits also the possibility to establish a temporal continuity of inventories. As a consequence, the monitoring of forest changes with ground measurements is limited to large temporal scales and/or small areas.

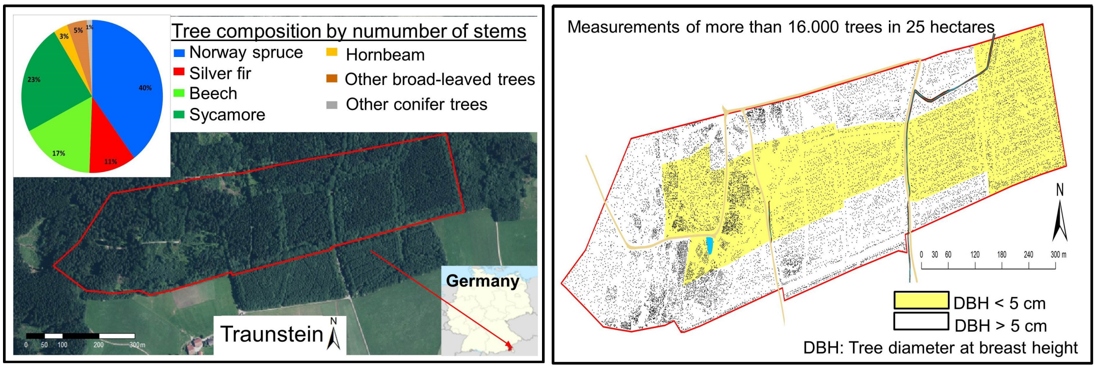

(a) (b)

FIGURE 1.2: Individual tree measurements over the area of Traunstein (Germany) highlighted by a red rectangle in Figure 1.3. (a) Optical image of the area and tree species composition by the number of stems. (b) Positions of each tree with a DBH > 5 cm represented by black dots, in the yellow area also the trees with a DBH > 1 cm have been measured. These data have been used in Chapter 2.

1.2.2 Optical Remote Sensing

Optical imaging sensors collect the reflected solar radiation on the Earth (i.e. passive sensors) in a number of spectral bands in the nano-meters range, from the near-ultraviolet until the far-infrared, depending on the specific sensor used [17]. Optical sensors have been predominant in forest remote sensing since decades due to their relative ease processing, interpretation and continuity of observations since the 1970s [42]. Many forest applications have been developed from optical sensors such as forest/non-forest mapping, forest disturbances monitoring, classification, estimation of biomass, forest phenology or estimation of forest indices like the leaf area index or the normalised difference vegetation index [43], [44]. Aerial photographs are maybe the most commonly used remote sensing product in forestry at a local scales. The high spatial resolution (in the order of a few cms) allows the extraction of information even at single-tree level. Space borne optical sensors increase the coverage at the cost of a reduction of resolution. An additional problem for space borne optical sensors is the cloud coverage, which limits the availability of the data for vast Earth regions and/or long time periods. This is a critical aspect for forest global mapping. For instance, forest regions located in the tropics have an annual cloud coverage of around 80 % of the time [21].

Figure 1.3 shows a crop of an image acquired by the ESA Sentinel-2 satellite (total swath width of 290 km), over the area of Traunstein in the south-eastern part of Germany that contains the two forest test sites (highlighted by red and blue rectangles respectively) used along the thesis. The site in the red rectangle corresponds to the ground measurement in Figure 1.2. Figure 1.4 shows a high-resolution image from an airborne system over the area in the blue rectangle in Figure 1.3. The reduced coverage in Figure 1.4 goes in favour of an increase in resolution, that allows even to recognize individual trees and different types of forests. This difference in resolution is apparent in Figures 1.4 (b) and (c), where a zoom over a small area is compared.

A single optical image gives no access to the vertical dimension, therefore optical sensors are very limited in the extraction of 3-D information. With reference to Figure 1.1, the analysis of top canopy texture can be used to determine the horizontal structure [45], [46]. The vertical structure is much more difficult to be determined as the forest below the top canopy cover is not reachable. More recently, photogrammetric techniques have been applied to stereoscopic acquisitions in an attempt to extract digital surface models [47] and 3-D point clouds [48], that can be used to characterize the 3-D structure. The applicability of these advanced techniques is limited to very high resolution images from airborne systems that only can cover small regions and in forests where gaps between the trees are expected.

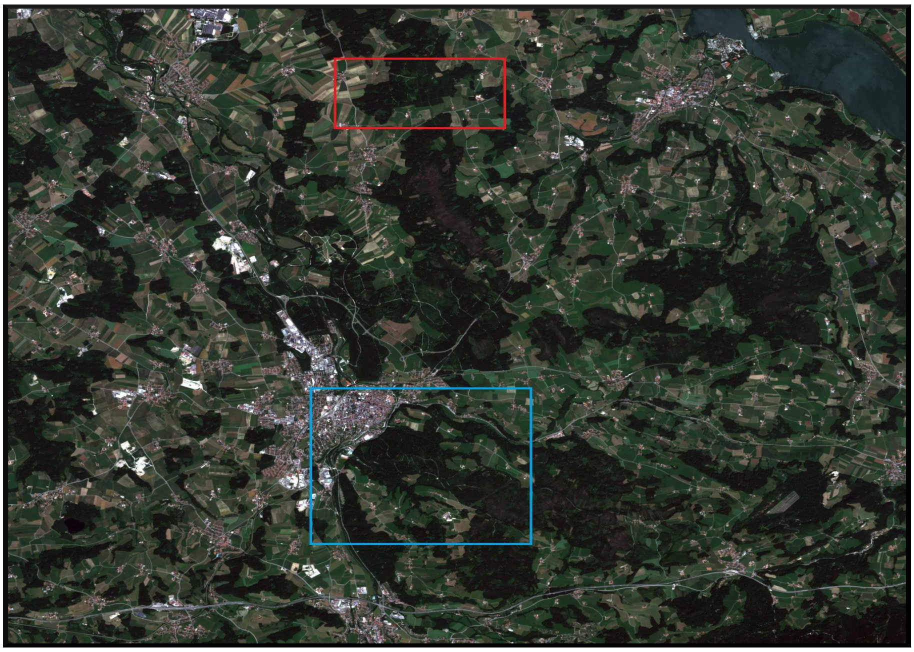

FIGURE 1.3: ESA Sentinel-2 RGB (R=Band 4, G=Band 3, B=Band 2) composite image over the area of Traunstein, Germany (47°52′N 12°38′E) on 28th June 2019. The image covers an area of around 15 by 18 kilometres with a resolution of 10 by 10 meters. The red rectangle highlights the forest area of Figure 1.2, as well as the area used in Chapters 2 and 5. The blue rectangle highlights the forest area used in Chapters 3 and 4.

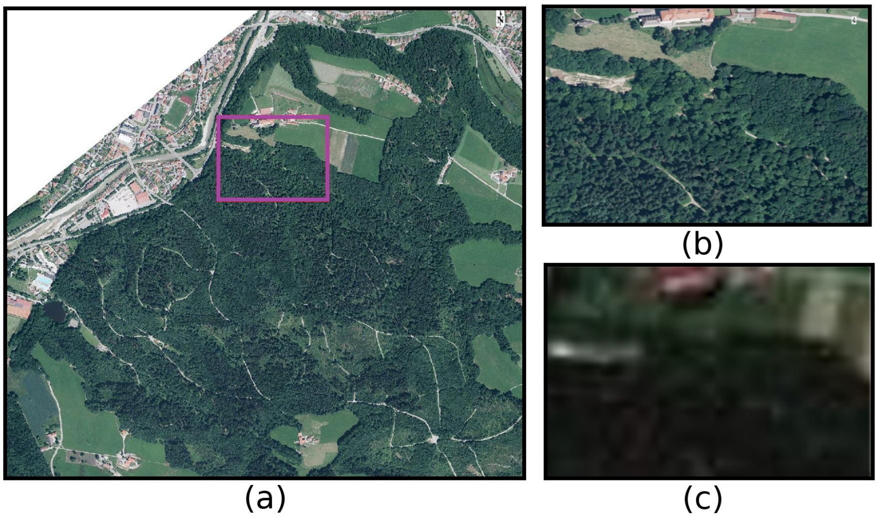

(a) (b) (c)

FIGURE 1.4: (a) High-resolution (20 by 20 centimetres) optical image acquired in 2015 with an airborne system over the area highlighted by a blue rectangle in Figure 1.3. (b) and (c) show a zoom over the purple rectangle for the aerial and the Sentinel-2 image, respectively.

1.2.3 Lidar Remote Sensing

Light Detection and Ranging (Lidar) sensors are active configurations that send a laser pulse in the μm range of the electromagnetic spectrum in nadir-looking geometry [18], [49], [50]. The pulse is reflected by the vegetation elements back to the sensor, which records their amplitude as a function of the time. The time a pulse takes after being transmitted to return to the sensor depends on the range and the scattering properties of intercepted objects within the illuminated part of the scene (i.e., the footprint), and the actual atmospheric conditions. Lidar instruments used in forestry are categorized based on how the vertical distribution of the light energy (i.e. the waveform) is received and recorded. There are two types of Lidar systems:

1. *Discrete return* Lidar systems record only individual (discrete) peaks (time-stamped ranges triggered real-time) of the waveform. They identify peaks and record a point at each peak location in the energy curve. A discrete system may record 1 to 4 returns from each laser pulse [51].
2. *Full-waveform* Lidar systems record the distribution of transmitted and returned light energy. Accordingly, (full) waveform Lidar data contain more information compared to discrete return Lidar systems [52].

Discrete return Lidar operates with small footprints (from 0.1 to 2 m) for fine topographic mapping and forest structure characterization through the position of each of the returns, that correspond to the different physical elements (leaves, branches, trunks, ground) of the forest. However, they achieve low coverage from airborne or drone systems [53]. Large footprint waveform Lidars have several advantages over small footprint ones for vegetation mapping. First, a footprint on ground of 10-25 m has a higher probability to contain ground and trees at the same time. Second, larger footprints can cover wider areas at a lower cost. These two features are of crucial importance for space borne Lidar configurations. Examples of current Lidar waveform systems from space are the IceSAT-2 [54] (not optimized for forest applications) and the NASA's Global Ecosystem Dynamics Investigation (GEDI) mission [55], [56] with the primary goal of study the forests. In the GEDI mission, a full waveform large footprint (25 m) is deployed in the international space station to obtain a near-global measurement of the Earth. However, the footprints are separated by 60 m along-track and 500 m across-track [57], i.e. it produces a spatially sparse set of measurements. This sparsity limits also the capabilities of Lidar sensors for monitoring changes in time, due to the low probability that a footprint samples the same area on ground more than once. Moreover, as well as in the optical sensors, the cloud coverage is a limitation for the Lidar systems for global Earth forest mapping.

Lidar (both from discrete return and full-waveform) is nowadays a remote sensing system widely used in the forestry community to extract 3-D forest structure and canopy heights. This is due to the direct availability of the waveform (or its discrete returns) as a proxy to the vertical distribution of the vegetation elements intercepted by the laser pulse within the footprint [58]–[60]. The projected area of canopy/background materials is often expressed as the canopy gap probability, which is a parameter that is fundamental to link Lidar measurements, vertical and horizontal canopy structure, and the radiation regime of a plant canopy [61], [62]. Moreover, from the full-waveform Lidar, parameters such as ground topography and relative height (RH) metrics can be extracted. The RH metrics express the height interval in which a certain percentage of energy is received above the noise level and with respect to the ground height. RH metrics have been largely used to estimate biomass and to describe the canopy vertical structure [63]. Potentials and challenges of the different Lidar configurations, metrics and Lidar-based parameters for mapping 3-D forest structure are nowadays well established and widely understood [59], [60], [64]–[67].

Figure 1.5 shows examples of point clouds acquired from an airborne discrete return Lidar over a forest area in Traunstein, Germany (red rectangle in Figure 1.3). Each point in Figure 1.5

corresponds to a return from a physical element on the scene. Figure 1.6 shows a map of the top canopy height extracted from the Lidar point clouds, where the black polygon represents the ground measurements area from Figure 1.2.

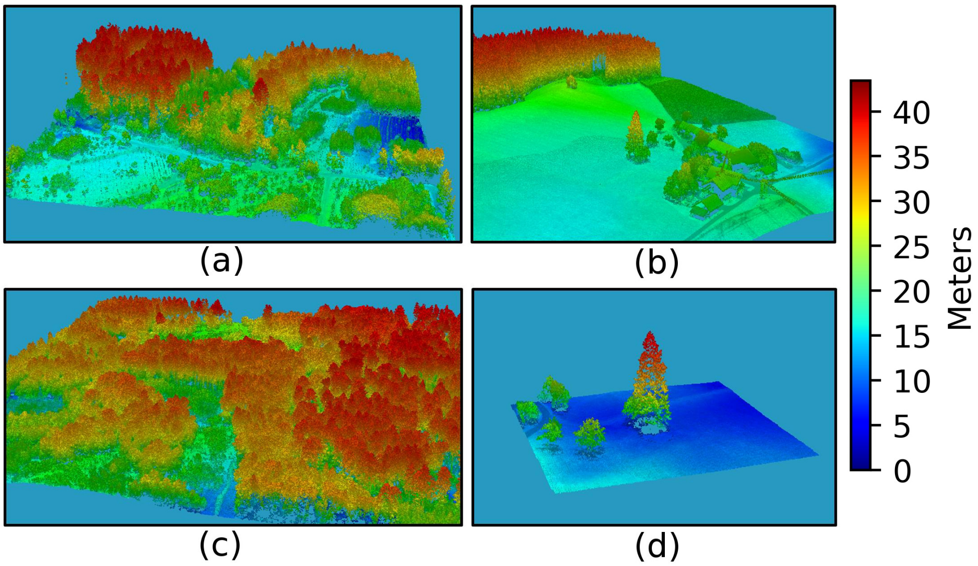

FIGURE 1.5: Lidar point clouds from an airborne discrete return Lidar over the red rectangle in Figure 1.3.

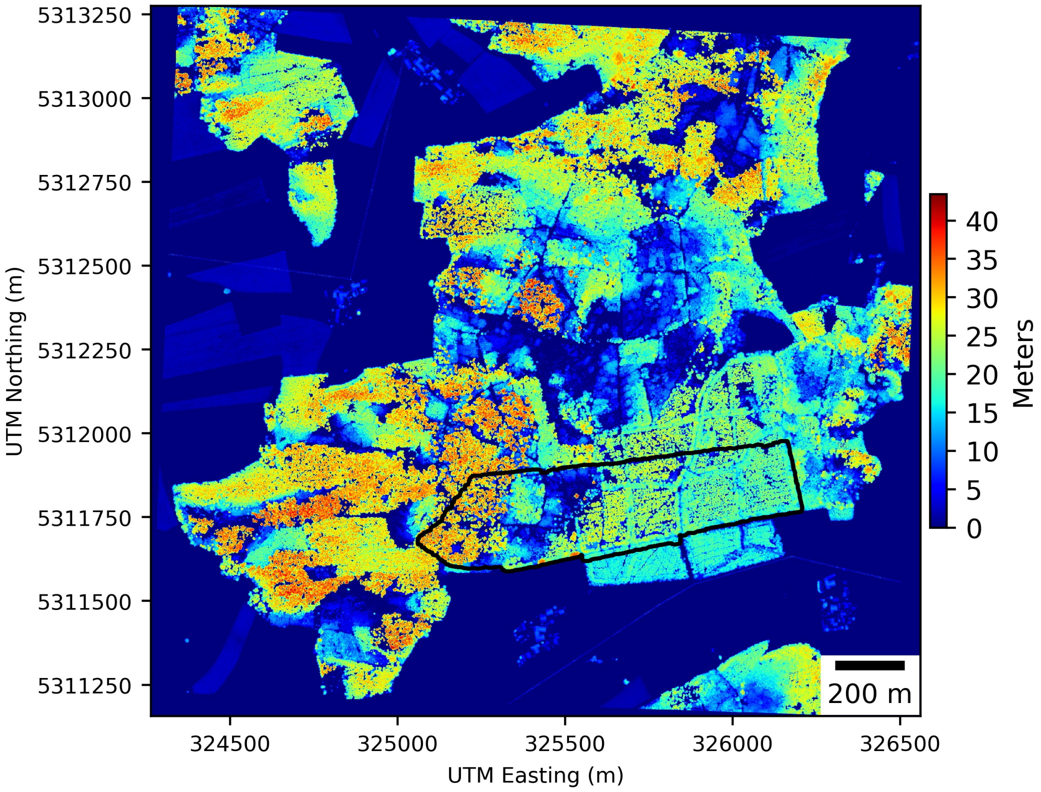

FIGURE 1.6: Forest height extracted from the Lidar point clouds over the red rectangle in Figure 1.3. The black polygon corresponds to the area of ground measurements from Figure 1.2.

1.2.4 SAR Remote Sensing

Synthetic Aperture Radars (SAR) are active remote sensing configurations operating in the microwave regions of the electromagnetic spectrum [19]. A SAR acquisition is based on the use of a radar [68] on a moving platform [20], [69], [70]. Each radar pulse is transmitted in side-looking geometry, interacts with the Earth surface and afterwards, it is scattered back to the sensor and collected on a different position due to the movement of the radar. Taking into account the Doppler effects, the received signals (raw data) are coherently combined to build a virtual antenna, which is much longer than the physical one. This allows the generation of two dimensional (2-D) high-resolution single look complex (SLC) images in range (parallel to the line of sight) and azimuth (parallel to the moving platform direction) of the radar reflectivity of the scene. For the range direction, the resolution depends on the bandwidth of the transmitted signal, while for the azimuth direction depends only on the physical size of the antenna for a SAR with a fixed antenna pointing (stripmap mode).

The radar reflectivity measured in each pixel of the SLC image is a complex number in which the amplitude and the phase depend on the dielectric properties of the scatterers as well as their 3-D geometric distribution within the antenna footprint. Moreover, the side-looking geometry of the SAR system introduces a distortion on the spatial scaling of the scene in ground from near to far range, as well as effects such as foreshortening, layover and shadowing that have to be considered in the interpretation of the images. An example of the magnitude of a SLC SAR image over a forest area is given in Figure 1.7. Lighter values indicate higher levels of backscattered energy, dark values indicate that most of the energy is scattered away from the radar.

SAR signals can penetrate through the clouds or rain, and they are independent of the day/night cycle. These properties, open the door even to potential near-real-time applications with availability of data for continuous global Earth monitoring without cloud coverage problems. Moreover, SAR systems can acquire high-resolution images (between 1 to 10 m on ground) from space with wide swaths (30 to 500 km), continuous collection of data (in contrast to Lidar from space), and revisit times typically between one and two weeks. Radar waves can penetrate even in dense forests depending on the frequency used. While higher frequencies, like K or X-band, are backscattered by the upper part of the forest, lower frequencies such as L or P-band penetrate and interact with the canopy elements and the ground before coming back to the sensor.

The use of SAR for forest application at a global scale is not as wide and established as for optical or Lidar systems, mainly due to the lack of systematic acquisition plans of past and present space borne SAR platforms for continuous forest mapping [42].

However, due to its unique characteristics plus the use of additional techniques such as SAR polarimetry [71] (see Section 1.2.4.1), SAR interferometry [72] (see Section 1.2.4.2) and SAR tomography [22] (see Section 1.2.4.3), the interest of using radar for forest applications is rapidly increasing. Some examples of forest applications are the forest-non-forest mapping [73], forest classification [74] and the estimation of forest-related products as stem volume [75], Biomass [76], canopy density [77] or forest height [78].

Although the complex reflectivity of a SAR image depends on the interaction between the 3-D distribution of scatterers and the transmitted wave, a single SAR image (Figure 1.7) does not allow the direct estimation of 3-D forest structure. This is a direct consequence of the side-looking observation geometry, that projects the 3-D scattering distribution onto the 2-D range-azimuth plane.

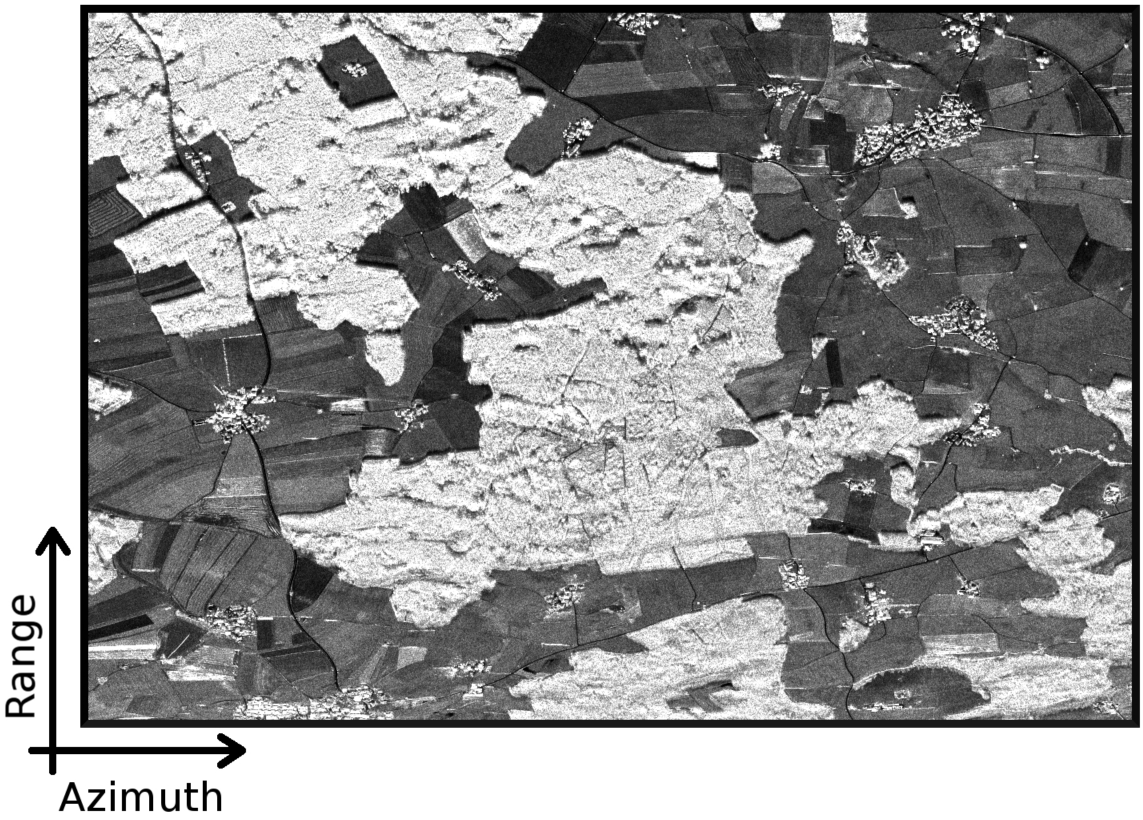

FIGURE 1.7: Amplitude of a SLC SAR image (HH channel) in range-azimuth coordinates over the red rectangle in Figure 1.3 acquired at L-band in May 2017 with the DLR's F-SAR airborne system. The image size is 900 pixels in range (3 m pixel spacing) and 1300 pixels in azimuth (3.2 m pixel spacing). The resolution is 12 m in range and 9.6 m in azimuth (after a spatial averaging of 2 looks in range and 2 looks in azimuth).

1.2.4.1 SAR Polarimetry

A way to increase the observation space within one SAR acquisition and to get more information about the scene is to use polarimetry, which exploits the vector properties of the transmitted electromagnetic wave. The main idea of SAR Polarimetry (Pol-SAR) [71], [79] is to transmit the signal using two orthogonal polarizations of the electromagnetic field (i.e. horizontal and vertical). This allows discriminating between different scattering mechanisms (e.g. dihedral, volume or surface scattering) inside one resolution cell, due to the sensitivity to shape, orientation and dielectric properties of the scattering elements in the scene.

A (full) polarimetric SAR system transmits and receives the pulses in two orthogonal polarizations (e.g. horizontal (H) and vertical (V) directions of the electric field). If all possible combinations are measured (Horizontal received - Horizontal transmitted (HH), Horizontal received - Vertical transmitted (HV), Vertical received - Horizontal transmitted (VH) and Vertical received - Vertical transmitted (VV)), any transmit-receive polarization can be synthesized. With this, every pixel in range-azimuth for a Pol-SAR image is composed of four complex values with its amplitude and phase. It means that, instead of having just a 2-D image to represent the scene, there are four images. In the (most usual) case of backscattering and reciprocal target, this number is reduced to three images representing all possible polarizations.

In Figure 1.8 an example of an RGB (R=HH, G=HV+VH, B=VV) composite Pol-SAR image is given. The comparison of this Pol-SAR image with the classical single-channel SAR image in Figure 1.7 shows the potential of Pol-SAR to better distinguish the different areas (forest, field, ground) and to see more features such as the different orientation of the elements in the scene.

SAR polarimetry is used to extract information in many applications like classification [80], urban [81], land [82], snow and ice [83] or soil moisture [84], [85]. In the particular case of the forestry domain, the different interaction with forest volumes of the different channels makes polarimetry a tool to be considered for forest mapping and classification. For example, model-based decompositions can be used to differentiate between different scattering mechanism in the forest [86]. However, scattering model inversions are limited due to the low number of available parameters, that limits the complexity of the model.

Regarding the characterization of the complete 3-D forest structure, more polarizations do not remove the limit of classical SAR images with one polarization, i.e. the sensitivity to the third dimension (vertical). Therefore, the use of Pol-SAR alone is not sufficient to accurately describe the different elements in the 3-D space and more advanced techniques need to be considered.

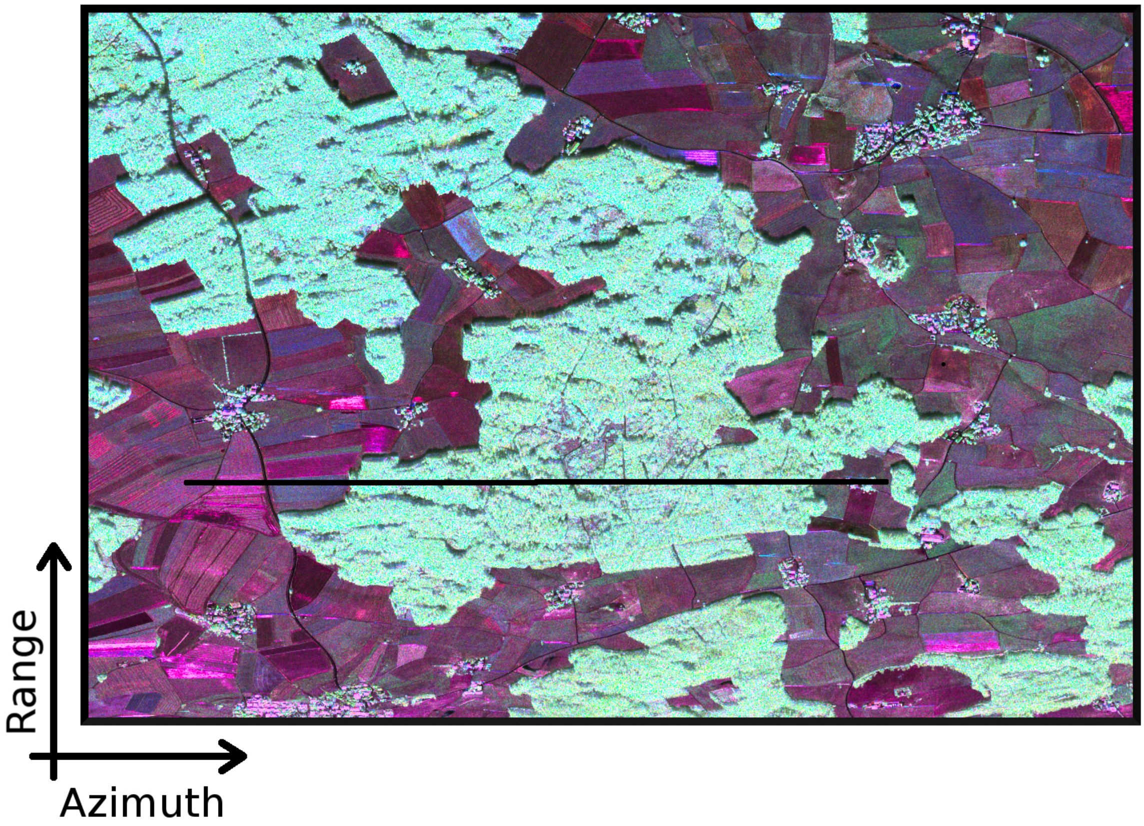

FIGURE 1.8: Polarimetric RGB (R=HH, G=HV+VH, B=VV) composite image in range-azimuth coordinates over the red rectangle in Figure 1.3 acquired at L-band in May 2017 with the DLR's F-SAR airborne system. It covers the same area as in Figure 1.7. The black line corresponds to the area used in Figure 1.10.

1.2.4.2 Polarimetric SAR Interferometry

Synthetic Aperture Radar Interferometry (InSAR) recovers the sensitivity to the vertical dimension by using the phase information of two SAR images from slightly different positions (angular diversity). Indeed, the phase of a SAR image depends on the distance between the sensor and each scatterer on the scene. If the two images are acquired with different view geometries (either with the same sensor at different times or using two sensors simultaneously), they can be used to extract the height of the scatterers on the ground. To do so, first, a co-registration of both images has to be done, in order to align the positions of the samples of both acquisitions. Then, one image is multiplied by the complex conjugate of the other to get the so-called complex interferometric coherence. This value is the main parameter used in InSAR: the coherence phase contains information about the topography, and the coherence magnitude indicates the correlation between the two images [72], [87].

InSAR finds a direct application in the generation of Digital Elevation Models (DEMs) to get the surface topography [88]. In the specific case of forest applications with InSAR, the amplitude of the interferometric coherence can be used for example to identify forest (or non-forest) areas [73] or modelling the deforestation and forest growth [89]. Forest structure-related applications [90]–[93] have been developed starting from the Fourier relationship between InSAR coherences and the vertical radar reflectivity function (see equation 4.2 in Chapter 4), that depends on the frequency, polarization, incidence angle, and the 3-D distribution of the scatterers and their dielectric properties. Thus, the InSAR phase in forest scenarios is related to the height of the center of mass of the vertical reflectivity function. Scattering models can be used to enable the interpretation of the InSAR coherences in terms of structure, like e.g. the interferometric water cloud model. However, the still small InSAR observation space limits the number of parameters defining the model. One way to overcome this limitation is either to include external information or to increase the observation space. In the latter case, one can acquire interferometric pairs in different polarization channels.

Polarimetric SAR interferometry (Pol-InSAR) combines the potential of radar polarimetry to separate different scattering mechanisms together with the vertical capabilities of interferometry [94], [95]. Pol-InSAR is a well-understood technique used in many applications like classification [96], change detection and especially for the estimation of structural parameters of volumes as in vegetation crops [97], [98], snow [99] and forest [78], [100]. In the case of forest application, Pol-InSAR overcomes the uncertainty of the forest height estimates (obtained by the interferometric technique) by using the different penetrations into the forest volume of each polarimetric channel together with data models [101].

The use of Pol-InSAR techniques to estimate forest height has been successfully applied in many sites from airborne [102] as well as space borne data [103]. Moreover, further forest applications, such as Biomass [104] or stem volume estimation [105], have been demonstrated the potential of Pol-InSAR. An example of forest height over the same forest area as Figure 1.6 obtained using Pol-InSAR techniques is given in Figure 1.9. Beyond being an essential forest parameter, forest height alone can be used to characterize the horizontal structure, but it cannot lead to unambiguous estimates of vertical structure, as it represents only the variability of the tree (top) canopy layer.

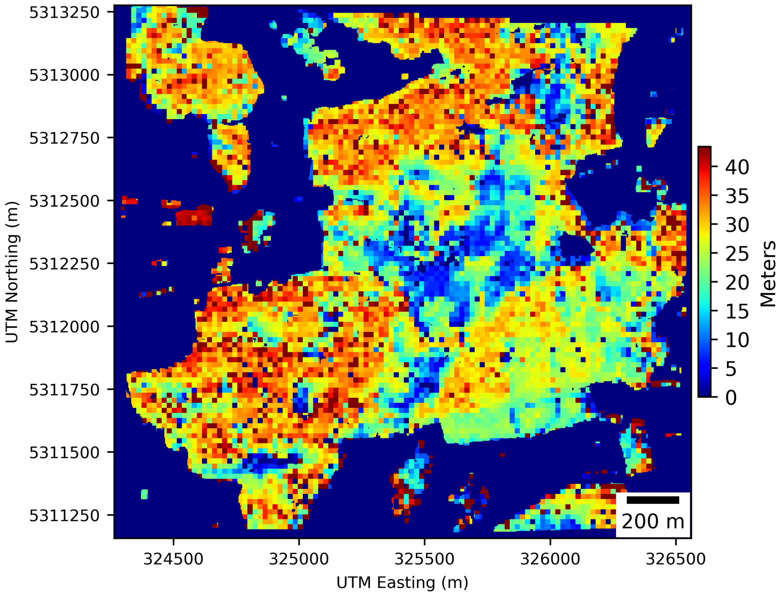

FIGURE 1.9: Estimated forest height using Pol-InSAR techniques at 20 by 20 m resolution over the area within a red rectangle in Figure 1.3 as well as in Figures 1.6, 1.7 and 1.8.

1.2.4.3 SAR Tomography

In order to overcome the limitations of Pol-InSAR techniques and to describe the forest in 3-D, multiple SAR images can be coherently combined to generate a 3-D radar image by inverting the relationship between InSAR coherences and vertical reflectivity profiles. The images have to be acquired from a slightly different track/orbit in order to exploit the concept of synthetic aperture not only on the flight direction, but also in the elevation direction. This concept is known as SAR Tomography [22]–[25] (TomoSAR) and it allows obtaining a 3-D image (range, azimuth and height) of a volumetric media.

SAR tomography is used in urban scenarios for the determination of multiple scatterers in order to resolve layover areas of classical 2-D SAR or to improve the retrieval of deformation velocities due to the denser measurements, better accuracy and more coverage of the result [106]–[108]. For forestry application at low frequency (e.g. L- or P-band), TomoSAR vertical reflectivity profiles are a proxy to the vertical structure of the vegetation volume, which opens the door to a large number of applications than only forest height [100], for example a better (than Pol-InSAR) estimation of volume and ground contributions [109], vegetation structure parameters [110], [111], biomass [112], ground topography [113] or the detection of objects below the forest [114]. Excellent examples of the potential of SAR Tomography (as well as radar in general) for forestry applications are tower-ground based experiments [115], [116], where data is collected continuously to see, not only the structure of the forest, but also its behaviour over different weather and seasonal conditions.

The first important and critical aspect of a TomoSAR inversion is the number of images to be combined. In general, the larger the number of images, the better the reconstruction of the scene that can be achieved. However, the number of images is usually very limited in a TomoSAR data set, due to temporal and/or navigation/orbital constraints. In particular, temporal decorrelation does not allow to use multiple images with significant temporal differences. Not only the number of images is a critical aspect for TomoSAR, but also the choice of an acquisition geometry (i.e. the track displacements) affects the quality of the reconstructed profiles. The achievable resolution in the elevation direction is related to the maximum separation between the different acquisitions, while the minimum separation gives the height at which the radar ambiguities appear.

The limited number of SAR images (in a realistic scenario) makes SAR tomography a highly undetermined problem, which does not have a unique solution. Multiple algorithms, classified as model, non-model or hybrid, can be applied. Fourier [117] and Capon [118] beamforming are considered as non-model or model-free since no assumption (or model) about the data is taken into account. The second group of algorithms simplify the interpretation of the result by using a statistical description of the received signal, scattering mechanisms (point scatters, volumes or double-bounce reflection) or a model that describes the scene [119]–[124]. Between the two mentioned type of algorithms, there are the hybrid ones. Although they do not assume any model, they introduce some constraints such as the sparsity of the data. An example of these algorithms are the approaches based on Compressive Sensing (CS) [106], [125]–[128] and iterative techniques [129], [130] that try to maximize the achieved vertical resolution.

However, although their capabilities have been demonstrated in a number of airborne experiments, the role played by the different algorithms in the interpretation of the data for forest volumes, in terms of forest structure, is still an open issue. TomoSAR profiles have only radar reflectivity information. In other words, the reflectivity profiles need to be further interpreted to extract physical forest information. However, the interpretation of the TomoSAR profiles is challenging due to their additional dependency on the frequency used [131], [132], the dielectric properties of the forest [133], the TomoSAR configuration as well as on the TomoSAR algorithm itself. Some works have been demonstrated the potential of SAR tomography to derive crop parameters [111], forestry-related information such as biomass [10], [134], [135] or forest structure information on the 3-D space [109], [110], [124]. However, these studies are focused on the radar reflectivity instead of the ecological forest structure information. Therefore, the ecological interpretation of TomoSAR profiles is not straightforward, it is still at an earlier stage for forest applications, and there is no an established quantitative link between TomoSAR profiles and a general 3-D forest structure product able to describe the 3-D distribution of trees.

Figure 1.10 shows radar reflectivity profiles, in the azimuth-height plane, over the black line in Figure 1.8 for three different tomographic algorithms, namely Fourier beamforming (a), Capon beamforming (b) and compressive sensing (c). As a visual comparison, in Figure 1.10 (d) a profile over the same area obtained using discrete return Lidar is shown. Figures 1.10 (a), (b) and (c) represent the normalized radar reflectivity of the different scattering elements in the elevation direction for each range-azimuth sample. The results show first, the nice agreement with the Lidar data and second, the different results obtained for each of the algorithms. Fourier and Capon beamforming approaches provide similar results with a smoothing characteristic of the profiles and an increase of the resolution in Capon compared to Fourier. On the contrary, compressive sensing gives sparse profiles with an increase of the resolution respect to Capon, but it introduces false additional local maxima.

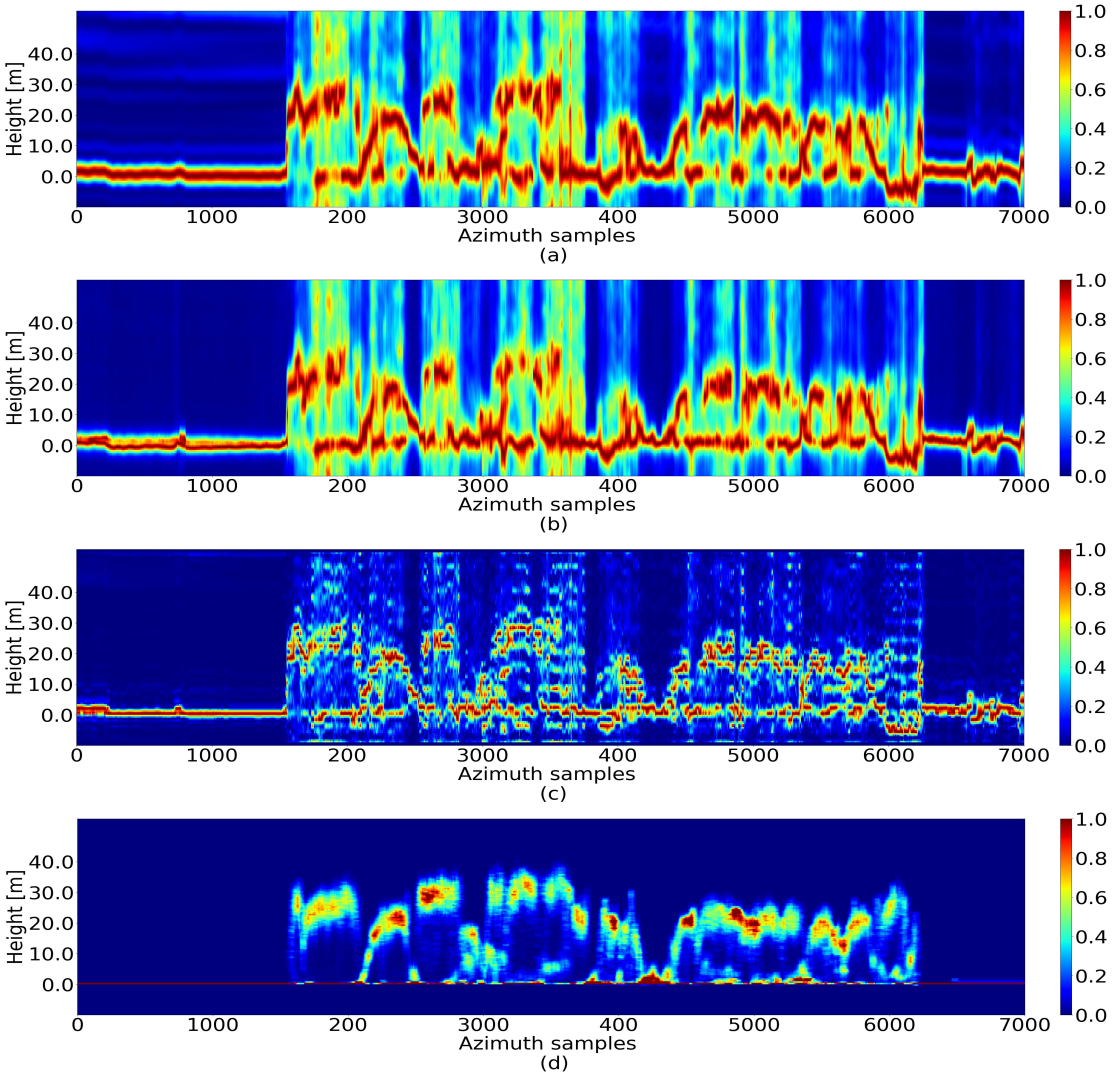

FIGURE 1.10: Radar reflectivity for the HV channel at L-band from (a) Fourier beamforming, (b) Capon beamforming and (c) compressive sensing tomographic algorithms. Each azimuth sample has a pixel spacing of 0.8 m and it is normalised in height by itself, i.e. for each azimuth sample there is a maximum power equal to 1. (d) Lidar point clouds over the same area, red values indicate high density and blue values low density of Lidar returns. The area corresponds to the black line in Figure 1.8.

1.3 Research Goals

After identifying in Section 1.2, the actual state-of-the-art and open challenges in the estimation of 3-D forest structure from ground measurement and SAR remote sensing, two main research questions arise in this context that define the objectives of this thesis:

- Is it possible to characterize physical forest structure and monitor its changes from TomoSAR data?
- Which are the appropriate TomoSAR algorithms and acquisition configurations for forest structure applications?

These two questions divide the whole work conceptually into two parts. In the first part, which includes Chapters 2, 3, the qualitative and quantitative estimation of forest structure and the observation of its changes from ground measurements, Lidar and TomoSAR profiles has been addressed. In the second part, which includes Chapters 4 and 5, tomographic algorithms and system configurations for forest structure applications have been analyzed. The two general research questions have been divided into more specific ones that have been addressed within the thesis:

Specific research questions related to forest structure estimation from TomoSAR profiles:

- In which way 3-D forest structure can be quantified from TomoSAR profiles?
- How does the forest structure derived from inventory data (i.e ground measurements) is related to the structures derived from Lidar and TomoSAR measurements?
- Is it possible to monitor forest structure changes with TomoSAR? Are these changes the same as the ones seen by Lidar, optical images or ground measurements?

Specific research questions related to TomoSAR algorithms and configurations:

- Which are the strengths and weaknesses of the most common tomographic algorithms for imaging forest volumes?
- How do different TomoSAR implementations from space (single-pass such as DLR's Tandem-L mission vs repeat-pass such as ESA BIOMASS mission) affect the TomoSAR profiles?
- How does the configuration (i.e. number and distribution of tracks) of a TomoSAR acquisition affect the 3-D radar reflectivity estimates and the discrimination among different forest structures?

All of the previous research questions have been addressed in the four peer-reviewed publications that are presented in Chapters 2 and 3 mainly for the forest structure part and in Chapters 4 and 5 regarding the TomoSAR part. Additionally, in two more peer-reviewed publications presented in the Appendices A and B, research questions related to the forest structure and the relation of TomoSAR with Lidar data have been also treated.

1.4 Organization of the Thesis

The thesis is organized by chapters that can be read and understood separately. After the abstract and this introduction, the following Chapters 2, 3, 4 and 5 are peer-reviewed journal publications, that are presented without any modification. Only one page as a small introduction at the beginning of each chapter with the key findings/points and the specific contributions of the author and co-authors is included. Therefore, each of these chapters can be understood independently of the others; they contain its own abstract, introduction, methods, results and conclusions that covers the previously mentioned research questions.

In Chapter 2 the horizontal-vertical structure framework for the qualitative and quantitative characterization of forest structure is proposed and applied to single-tree ground measurements, Lidar and TomoSAR L-band data. Chapter 3 shows an application example of this forest structure concept. TomoSAR vertical profiles from both simulated and real data (at L-band), over a temperate forest in Germany, are used to differentiate growth stages and detect and characterize forest structure changes. In Chapter 4 an in-depth comparison of three TomoSAR algorithms (Fourier beamforming, Capon beamforming and compressive sensing) using simulated as well as real (at L-band) data, is carried out. Moreover, the temporal decorrelation effects on two space borne tomographic implementation (repeat-pass and tandem-like) are addressed. Chapter 5 discusses the implications of the number and distribution of tracks in a TomoSAR configuration and the requirements for an adequate characterization of different forest areas. Finally, Chapter 6 concludes the thesis by summarizing the main findings and the possible future works and research directions of the thesis.

Additionally, in Appendices A and B, two more peer-reviewed publications related to the research questions of this work are included. In Appendix A a review of the differences and commonalities between Lidar and TomoSAR profiles for the estimation of forest structure is presented. In Appendix B, the proposed horizontal-vertical forest structure framework is applied on a tropical forest site for ground measurements, full-waveform Lidar and L- and P- band TomoSAR profiles.

References

[1] Y. Pan, R. A. Birdsey, O. L. Phillips, and R. B. Jackson, “The structure, distribution, and biomass of the world’s forests”, *Annual Review of Ecology, Evolution, and Systematics*, vol. 44, pp. 593–622, 2013. DOI: 10.1146/annurev-ecolsys-110512-135914 (cited on page 1).

[2] J. Shukla, C. Nobre, and P. Sellers, “Amazon deforestation and climate change”, *Science*, vol. 247, no. 4948, pp. 1322–1325, 1990. DOI: 10.1126/science.247.4948.1322 (cited on page 1).

[3] A. Agrawal, D. Nepstad, and A. Chhatre, “Reducing emissions from deforestation and forest degradation”, *Annual Review of Environment and Resources*, vol. 36, pp. 373–396, 2011. DOI: 10.1146/annurev-environ-042009-094508 (cited on page 1).

[4] U. Nations, “Non-legally binding instrument on all types of forests”, United Nations, General Assembly, United Nations Forum on Forests, New York, 2007. [Online]. Available: https://digitallibrary.un.org/record/614195 (cited on page 1).

[5] D. Brack, “Controlling illegal logging and the trade in illegally harvested timber: the eu’s forest law enforcement, governance and trade initiative”, *Review of European community & international environmental law*, vol. 14, no. 1, pp. 28–38, 2005. DOI: 10.1111/j.1467-9388.2005.00421.x (cited on page 1).

[6] Food and A. O. of the United Nations, “Global forest resources assessment”, *Main report, FAO Forest paper 163*, 2010. [Online]. Available: http://www.fao.org/3/i1757e/i1757e00.htm (cited on page 1).

[7] M. Finer, S. Novoa, M. J. Weisse, R. Petersen, J. Mascaro, T. Souto, F. Stearns, and R. G. Martinez, “Combating deforestation: from satellite to intervention”, *Science*, vol. 360, no. 6395, pp. 1303–1305, 2018. DOI: 10.1126/science.aat1203 (cited on page 1).

[8] T. A. Spies, “Forest structure: a key to the ecosystem”, *Northwest Science*, vol. 72, no. 2, pp. 34–36, 1998. [Online]. Available: http://andrewsforest.oregonstate.edu/pubs/pdf/pub2564.pdf (cited on page 1).

[9] M. Snyder, “What is forest stand structure and how is it measured?”, *Northen Woodlands*, vol. 64, p. 15, 2010. [Online]. Available: https://northernwoodlands.org/articles/article/what-is-forest-stand-structure-and-how-is-it-measured (cited on page 1).

[10] A. T. Caicoya, M. Pardini, I. Hajnsek, and K. Papathanassiou, “Forest-above ground biomass estimation from vertical reflectivity profiles at L-band”, *IEEE Geoscience and Remote Sensing Letters*, vol. 12, no. 12, pp. 2379–2383, 2015. DOI: 10.1109/LGRS.2015.2477858 (cited on pages 1, 12).

[11] F. J. Bohn and A. Huth, “The importance of forest structure to biodiversity–productivity relationships”, *Royal Society open science*, vol. 4, no. 1, p. 160 521, 2017. DOI: 10.1098/rsos.160521 (cited on pages 1, 3).

[12] E. Rödig, M. Cuntz, A. Rammig, R. Fischer, F. Taubert, and A. Huth, “The importance of forest structure for carbon fluxes of the amazon rainforest”, *Environmental Research Letters*, vol. 13, no. 5, p. 054 013, 2018. DOI: 10.1088/1748-9326/aabc61 (cited on page 1).

[13] K. Bergen, S. Goetz, R. Dubayah, G. Henebry, C. Hunsaker, M. Imhoff, R. Nelson, G. Parker, and V. Radeloff, “Remote sensing of vegetation 3-D structure for biodiversity and habitat: review and implications for lidar and radar spaceborne missions”, *Journal of Geophysical Research: Biogeosciences*, vol. 114, no. G2, 2009. DOI: 10.1029/2008JG000883 (cited on page 1).

[14] H. T. Schreuder, T. G. Gregoire, and G. B. Wood, *Sampling methods for multiresource forest inventory*. John Wiley and Sons, 1993, ISBN: 9780471552451 (cited on pages 1, 3).

[15] B. D. Shiver, B. E. Borders, *et al.*, *Sampling techniques for forest resource inventory*. John Wiley and Sons, 1996, ISBN: 9780471109402 (cited on pages 1, 3).

[16] A. Kangas and M. Maltamo, *Forest inventory: methodology and applications*. Springer Science and Business Media, 2006, vol. 10, ISBN: 9781402043796. DOI: 10.1007/1-4020-4381-3 (cited on pages 1, 3).

[17] S. Prasad, L. M. Bruce, and J. Chanussot, “Optical remote sensing: advances in signal processing and exploitation techniques”, 2011. DOI: 10.1007/978-3-642-14212-3 (cited on pages 2, 4).

[18] P. Dong and Q. Chen, *LiDAR remote sensing and applications*. CRC Press, 2017, ISBN: 9781138747241. DOI: 10.4324/9781351233354 (cited on pages 2, 6).

[19] I. H. Woodhouse, *Introduction to Microwave Remote Sensing*. CRC Press, 2005. DOI: 10.1201/9781315272573 (cited on pages 2, 8).

[20] J. C. Curlander and R. N. McDonough, *Synthetic Aperture Radar: Systems and Signal Processing*. John Wiley and Sons, New York, Nov. 26, 1991, ISBN: 9780471857709 (cited on pages 2, 8).

[21] A. M. Wilson and W. Jetz, “Remotely sensed high-resolution global cloud dynamics for predicting ecosystem and biodiversity distributions”, *PLoS biology*, vol. 14, no. 3, e1002415, 2016. DOI: 10.1371/journal.pbio.1002415 (cited on pages 2, 4).

[22] A. Reigber and A. Moreira, “First demonstration of airborne sar tomography using multibaseline L-band data”, *IEEE Transactions on Geoscience and Remote Sensing*, vol. 38, no. 5, pp. 2142–2152, 2000. DOI: `10.1109/36.868873` (cited on pages 2, 8, 12).

[23] S. Tebaldini, “Multibaseline sar imaging: models and algorithms”, PhD thesis, Politecnico Milano, Milan, Italy, 2010. [Online]. Available: `https://re.public.polimi.it/handle/11311/582330#.XaCG0ajtbmE` (cited on pages 2, 12).

[24] M. Pardini, “Advances and experiments of tomographic sar imaging for the analysis of complex scenarios”, PhD thesis, Università di Pisa, Italy, 2010. [Online]. Available: `https://etd.adm.unipi.it/t/etd-04202010-100622/` (cited on pages 2, 12).

[25] M. Nannini, “Advanced synthetic aperture radar tomography: processing algorithms and constellation design”, PhD thesis, Universität Fridericiana Karlsruhe, Germany, Dec. 2009. [Online]. Available: `https://publikationen.bibliothek.kit.edu/1000016445` (cited on pages 2, 12).

[26] E. Aguilera, “Synthetic aperture radar tomography compressed sensing models and algorithms”, PhD thesis, Technical University of Berlin, 2014. [Online]. Available: `https://elib.dlr.de/85764/` (cited on page 2).

[27] T. Le Toan, S. Quegan, M. Davidson, H. Balzter, P. Paillou, K. Papathanassiou, S. Plummer, F. Rocca, S. Saatchi, H. Shugart, *et al.*, “The biomass mission: mapping global forest biomass to better understand the terrestrial carbon cycle”, *Remote sensing of environment*, vol. 115, no. 11, pp. 2850–2860, 2011. DOI: `10.1016/j.rse.2011.03.020` (cited on page 2).

[28] S. Quegan, T. L. Toan, J. Chave, J. Dall, J.-F. Exbrayat, D. H. T. Minh, M. Lomas, M. M. D’Alessandro, P. Paillou, K. Papathanassiou, F. Rocca, S. Saatchi, K. Scipal, H. Shugart, T. L. Smallman, M. J. Soja, S. Tebaldini, L. Ulander, L. Villard, and M. Williams, “The european space agency biomass mission: measuring forest above-ground biomass from space”, *Remote Sensing of Environment*, vol. 227, pp. 44–60, 2019, ISSN: 0034-4257. DOI: `10.1016/j.rse.2019.03.032` (cited on page 2).

[29] A. Moreira, G. Krieger, I. Hajnsek, K. Papathanassiou, M. Younis, P. Lopez-Dekker, S. Huber, M. Villano, M. Pardini, M. Eineder, *et al.*, “Tandem-l: a highly innovative bistatic sar mission for global observation of dynamic processes on the earth’s surface”, *IEEE Geoscience and Remote Sensing Magazine*, vol. 3, no. 2, pp. 8–23, 2015. DOI: `10.1109/MGRS.2015.2437353` (cited on page 2).

[30] B. Husch, T. W. Beers, and J. A. Kershaw Jr, *Forest mensuration*. John Wiley and Sons, 2002, ISBN: 9780471018506 (cited on page 2).

[31] X. Liang, V. Kankare, J. Hyyppä, Y. Wang, A. Kukko, H. Haggrén, X. Yu, H. Kaartinen, A. Jaakkola, F. Guan, M. Holopainen, and M. Vastaranta, “Terrestrial laser scanning in forest inventories”, *ISPRS Journal of Photogrammetry and Remote Sensing*, vol. 115, pp. 63–77, 2016, Theme issue 'State-of-the-art in photogrammetry, remote sensing and spatial information science'. DOI: `10.1016/j.isprsjprs.2016.01.006` (cited on page 3).

[32] K. Calders, N. Origo, A. Burt, M. Disney, J. Nightingale, P. Raumonen, M. Åkerblom, Y. Malhi, and P. Lewis, “Realistic forest stand reconstruction from terrestrial lidar for radiative transfer modelling”, *Remote Sensing*, vol. 10, no. 6, p. 933, Jun. 2018. DOI: `10.3390/rs10060933` (cited on page 3).

[33] P. J. Watt and D. N. M. Donoghue, “Measuring forest structure with terrestrial laser scanning”, *International Journal of Remote Sensing*, vol. 26, no. 7, pp. 1437–1446, 2005. DOI: `10.1080/01431160512331337961` (cited on page 3).

[34] G. J. Newnham, J. D. Armston, K. Calders, M. I. Disney, J. L. Lovell, C. B. Schaaf, A. H. Strahler, and F. M. Danson, “Terrestrial laser scanning for plot-scale forest measurement”, *Current Forestry Reports*, vol. 1, no. 4, pp. 239–251, Dec. 1, 2015. DOI: `10.1007/s40725-015-0025-5` (cited on page 3).

[35] H. S. Park, H. M. Lee, H. Adeli, and I. Lee, “A new approach for health monitoring of structures: terrestrial laser scanning”, *Computer-Aided Civil and Infrastructure Engineering*, vol. 22, no. 1, pp. 19–30, 2007. DOI: `10.1111/j.1467-8667.2006.00466.x` (cited on page 3).

[36] C. McElhinny, P. Gibbons, C. Brack, and J. Bauhus, “Forest and woodland stand structural complexity: its definition and measurement”, *Forest Ecology and Management*, vol. 218, no. 1, pp. 1–24, 2005. DOI: `10.1016/j.foreco.2005.08.034` (cited on page 3).

[37] M. Del Rio, H. Pretzsch, I. Alberdi, K. Bielak, F. Bravo, A. Brunner, S. Condes, M. J. Ducey, T. Fonseca, N. von Lupke, *et al.*, “Characterization of the structure, dynamics, and productivity of mixed-species stands: review and perspectives”, *European journal of forest research*, vol. 135, no. 1, pp. 23–49, 2016. DOI: `10.1007/s10342-015-0927-6` (cited on page 3).

[38] G. Hui, G. Zhang, Z. Zhao, and A. Yang, “Methods of forest structure research: a review”, *Current Forestry Reports*, Jun. 27, 2019. DOI: `10.1007/s40725-019-00090-7` (cited on page 3).

[39] A. Pommerening, “Approaches to quantifying forest structures”, *Forestry: An International Journal of Forest Research*, vol. 75, no. 3, pp. 305–324, 2002. DOI: `10.1093/forestry/75.3.305` (cited on page 3).

[40] L. H. Reineke, “Perfecting a stand-density index for even-aged forests”, 1933. [Online]. Available: `https://naldc.nal.usda.gov/download/IND43968212/PDF` (cited on page 3).

[41] *The forest global earth observatory (forestgeo)*. [Online]. Available: `https://forestgeo.si.edu/sites/europe/traunstein` (cited on page 3).

[42] J. Reiche, R. Lucas, A. L. Mitchell, J. Verbesselt, D. H. Hoekman, J. Haarpaintner, J. M. Kellndorfer, A. Rosenqvist, E. A. Lehmann, C. E. Woodcock, *et al.*, “Combining satellite data for better tropical forest monitoring”, *Nature Climate Change*, vol. 6, no. 2, p. 120, 2016. DOI: `10.1038/nclimate2919` (cited on pages 4, 8).

[43] H. G. Jones and R. A. Vaughan, *Remote sensing of vegetation: principles, techniques, and applications*. Oxford university press, 2010, ISBN: 9780199207794 (cited on page 4).

[44] P. S. Thenkabail and J. G. Lyon, *Hyperspectral remote sensing of vegetation*. CRC press, 2016, ISBN: 9781138066250 (cited on page 4).

[45] I. Ozdemir and A. Karnieli, “Predicting forest structural parameters using the image texture derived from worldview-2 multispectral imagery in a dryland forest, israel”, *International Journal of Applied Earth Observation and Geoinformation*, vol. 13, no. 5, pp. 701–710, 2011, ISSN: 0303-2434. DOI: `10.1016/j.jag.2011.05.006` (cited on page 5).

[46] D. Pouliot, D. King, F. Bell, and D. Pitt, “Automated tree crown detection and delineation in high-resolution digital camera imagery of coniferous forest regeneration”, *Remote Sensing of Environment*, vol. 82, no. 2, pp. 322–334, 2002, ISSN: 0034-4257. DOI: `10.1016/S0034-4257(02)00050-0` (cited on page 5).

[47] D. R. Miller, C. P. Quine, and W. Hadley, “An investigation of the potential of digital photogrammetry to provide measurements of forest characteristics and abiotic damage”, *Forest Ecology and Management*, vol. 135, no. 1, pp. 279–288, 2000. DOI: `10.1016/S0378-1127(00)00286-3` (cited on page 5).

[48] J. Iglhaut, C. Cabo, S. Puliti, L. Piermattei, J. O’Connor, and J. Rosette, “Structure from motion photogrammetry in forestry: a review”, *Current Forestry Reports*, vol. 5, no. 3, pp. 155–168, Sep. 1, 2019. DOI: `10.1007/s40725-019-00094-3` (cited on page 5).

[49] P. F. McManamon, *LiDAR Technologies and Systems*. Sipe, 2019, ISBN: 9781510625396 (cited on page 6).

[50] P. Axelsson, “Processing of laser scanner data—algorithms and applications”, *ISPRS Journal of Photogrammetry and Remote Sensing*, vol. 54, no. 2, pp. 138–147, 1999. DOI: `10.1016/S0924-2716(99)00008-8` (cited on page 6).

[51] Y. Wang, H. Weinacker, and B. Koch, “A lidar point cloud based procedure for vertical canopy structure analysis and 3d single tree modelling in forest”, *Sensors*, vol. 8, no. 6, pp. 3938–3951, 2008. DOI: `10.3390/s8063938` (cited on page 6).

[52] C. Mallet and F. Bretar, “Full-waveform topographic lidar: state-of-the-art”, *ISPRS Journal of photogrammetry and remote sensing*, vol. 64, no. 1, pp. 1–16, 2009. DOI: `j.isprsjprs.2008.09.007` (cited on page 6).

[53] J. R. Kellner, J. Armston, M. Birrer, K. C. Cushman, L. Duncanson, C. Eck, C. Falleger, B. Imbach, K. Král, M. Krůček, J. Trochta, T. Vrška, and C. Zgraggen, “New opportunities for forest remote sensing through ultra-high-density drone lidar”, *Surveys in Geophysics*, vol. 40, no. 4, pp. 959–977, Jul. 1, 2019. DOI: `10.1007/s10712-019-09529-9` (cited on page 6).

[54] W. Abdalati, H. J. Zwally, R. Bindschadler, B. Csatho, S. L. Farrell, H. A. Fricker, D. Harding, R. Kwok, M. Lefsky, T. Markus, A. Marshak, T. Neumann, S. Palm, B. Schutz, B. Smith, J. Spinhirne, and C. Webb, “The icesat-2 laser altimetry mission”, *Proceedings of the IEEE*, vol. 98, no. 5, pp. 735–751, May 2010. DOI: `10.1109/JPROC.2009.2034765` (cited on page 6).

[55] *Global ecosystem dynamics investigation (gedi) mission. high resolution laser ranging of earth’s forests and topography from the international space station (iss)*. [Online]. Available: `https://gedi.umd.edu/` (cited on page 6).

[56] S. Hancock, J. Armston, M. Hofton, X. Sun, H. Tang, L. I. Duncanson, J. R. Kellner, and R. Dubayah, “The gedi simulator: a large-footprint waveform lidar simulator for calibration and validation of spaceborne missions”, *Earth and Space Science*, vol. 6, no. 2, pp. 294–310, 2019. DOI: `10.1029/2018EA000506` (cited on page 6).

[57] W. Qi and R. O. Dubayah, “Combining tandem-x insar and simulated gedi lidar observations for forest structure mapping”, *Remote Sensing of Environment*, vol. 187, pp. 253–266, 2016. DOI: `10.1016/j.rse.2016.10.018` (cited on page 6).

[58] R. O. Dubayah and J. B. Drake, “Lidar remote sensing for forestry”, *Journal of Forestry*, vol. 98, no. 6, pp. 44–46, 2000. DOI: `10.1093/jof/98.6.44` (cited on page 6).

[59] K. Lim, P. Treitz, M. Wulder, B. St-Onge, and M. Flood, “Lidar remote sensing of forest structure”, *Progress in physical geography*, vol. 27, no. 1, pp. 88–106, 2003. DOI: `10.1191/0309133303pp360ra` (cited on page 6).

[60] A. S. Whitehurst, A. Swatantran, J. B. Blair, M. A. Hofton, and R. Dubayah, “Characterization of canopy layering in forested ecosystems using full waveform lidar”, *Remote Sensing*, vol. 5, no. 4, pp. 2014–2036, 2013. DOI: `10.3390/rs5042014` (cited on page 6).

[61] J. Armston, M. Disney, P. Lewis, P. Scarth, S. Phinn, R. Lucas, P. Bunting, and N. Goodwin, “Direct retrieval of canopy gap probability using airborne waveform lidar”, *Remote Sensing of Environment*, vol. 134, pp. 24–38, 2013, ISSN: 0034-4257. DOI: `https://doi.org/10.1016/j.rse.2013.02.021` (cited on page 6).

[62] W. Ni-Meister, D. L. Jupp, and R. Dubayah, “Modeling lidar waveforms in heterogeneous and discrete canopies”, *IEEE transactions on geoscience and remote sensing*, vol. 39, no. 9, pp. 1943–1958, 2001. DOI: `10.1109/36.951085` (cited on page 6).

[63] J. B. Drake, R. O. Dubayah, D. B. Clark, R. G. Knox, J. B. Blair, M. A. Hofton, R. L. Chazdon, J. F. Weishampel, and S. Prince, “Estimation of tropical forest structural characteristics using large-footprint lidar”, *Remote Sensing of Environment*, vol. 79, no. 2-3, pp. 305–319, 2002. DOI: `10.1016/S0034-4257(01)00281-4` (cited on page 6).

[64] D. A. Zimble, D. L. Evans, G. C. Carlson, R. C. Parker, S. C. Grado, and P. D. Gerard, “Characterizing vertical forest structure using small-footprint airborne lidar”, *Remote sensing of Environment*, vol. 87, no. 2-3, pp. 171–182, 2003. DOI: `10.1016/S0034-4257(03)00139-1` (cited on page 6).

[65] D. Jaskierniak, P. N. Lane, A. Robinson, and A. Lucieer, “Extracting lidar indices to characterise multilayered forest structure using mixture distribution functions”, *Remote Sensing of Environment*, vol. 115, no. 2, pp. 573–585, 2011. DOI: `10.1016/j.rse.2010.10.003` (cited on page 6).

[66] S. Getzin, R. Fischer, N. Knapp, and A. Huth, “Using airborne lidar to assess spatial heterogeneity in forest structure on mount kilimanjaro”, *Landscape Ecology*, vol. 32, no. 9, pp. 1881–1894, Sep. 1, 2017, ISSN: 1572-9761. DOI: `10.1007/s10980-017-0550-7` (cited on page 6).

[67] N. Knapp, R. Fischer, and A. Huth, “Linking lidar and forest modeling to assess biomass estimation across scales and disturbance states”, *Remote Sensing of Environment*, vol. 205, pp. 199–209, 2018, ISSN: 0034-4257. DOI: `https://doi.org/10.1016/j.rse.2017.11.018` (cited on page 6).

[68] M. I. Skolnik, *Radar handbook*. McGraw-Hill, 1970, ISBN: 9780071485470 (cited on page 8).

[69] I. G. Cumming and F. H. Wong, *Digital Signal Processing of Synthetic Aperture Radar Data : Algorithms and Implementation*, 3. Artech house, 2005, vol. 1, ISBN: 9781580530583 (cited on page 8).

[70] G. Franceschetti and R. Lanari, *Synthetic aperture radar processing*. CRC press, 2018. DOI: `10.1201/9780203737484` (cited on page 8).

[71] J.-S. Lee and E. Pottier, *Polarimetric radar imaging: from basics to applications*. CRC press, 2009. DOI: `10.1201/9781420054989` (cited on pages 8, 9).

[72] P. A. Rosen, S. Hensley, I. R. Joughin, F. K. Li, S. N. Madsen, E. Rodriguez, and R. M. Goldstein, “Synthetic aperture radar interferometry”, *Proceedings of the IEEE*, vol. 88, no. 3, pp. 333–382, 2000. DOI: `10.1109/5.838084` (cited on pages 8, 11).

[73] M. Martone, P. Rizzoli, C. Wecklich, C. González, J.-L. Bueso-Bello, P. Valdo, D. Schulze, M. Zink, G. Krieger, and A. Moreira, “The global forest/non-forest map from tandem-x interferometric sar data”, *Remote Sensing of Environment*, vol. 205, pp. 352–373, 2018. DOI: `10.1016/j.rse.2017.12.002` (cited on pages 8, 11).

[74] S. S. Saatchi and E. Rignot, “Classification of boreal forest cover types using sar images”, *Remote Sensing of Environment*, vol. 60, no. 3, pp. 270–281, 1997. DOI: `10.1016/S0034-4257(96)00181-2` (cited on page 8).

[75] L. M. H. Ulander, J. Askne, J. E. S. Fransson, A. Gustavsson, T. Le Toan, T. Manninen, J. Martinez, P. Melon, G. Smith, and F. Walter, “Retrieval of stem volume in coniferous forest from low VHF-band sar”, in *IEEE International Geoscience and Remote Sensing Symposium*, vol. 1, Jul. 2000, 441–443 vol.1. DOI: `10.1109/IGARSS.2000.860558` (cited on page 8).

[76] G. Sandberg, L. Ulander, J. Fransson, J. Holmgren, and T. L. Toan, “L- and P-band backscatter intensity for biomass retrieval in hemiboreal forest”, *Remote Sensing of Environment*, vol. 115, no. 11, pp. 2874–2886, 2011. DOI: `10.1016/j.rse.2010.03.018` (cited on page 8).

[77] M. J. Soja, H. Persson, and L. M. H. Ulander, “Estimation of forest height and canopy density from a single insar correlation coefficient”, *IEEE Geoscience and Remote Sensing Letters*, vol. 12, no. 3, pp. 646–650, Mar. 2015. DOI: `10.1109/LGRS.2014.2354551` (cited on page 8).

[78] F. A. Kugler, “Pol-insar forest height estimation at different frequencies: opportunities and limitations”, PhD thesis, Technische Universität München, 2015. [Online]. Available: `https://mediatum.ub.tum.de/1256389` (cited on pages 8, 11).

[79] S. Cloude, *Polarisation: applications in remote sensing*. Oxford University Press, 2010. DOI: `10.1093/acprof:oso/9780199569731.001.0001` (cited on page 9).

[80] Jong-Sen Lee, M. R. Grunes, E. Pottier, and L. Ferro-Famil, “Unsupervised terrain classification preserving polarimetric scattering characteristics”, *IEEE Transactions on Geoscience and Remote Sensing*, vol. 42, no. 4, pp. 722–731, Apr. 2004. DOI: `10.1109/TGRS.2003.819883` (cited on page 10).

[81] A. Alonso-González, C. López-Martínez, and P. Salembier, "Polsar time series processing with binary partition trees", *IEEE Transactions on Geoscience and Remote Sensing*, vol. 52, no. 6, pp. 3553–3567, Jun. 2014. DOI: `10.1109/TGRS.2013.2273664` (cited on page 10).

[82] S. R. Cloude and E. Pottier, "An entropy based classification scheme for land applications of polarimetric sar", *IEEE Transactions on Geoscience and Remote Sensing*, vol. 35, no. 1, pp. 68–78, Jan. 1997. DOI: `10.1109/36.551935` (cited on page 10).

[83] G. Parrella, I. Hajnsek, and K. P. Papathanassiou, "Polarimetric decomposition of L-band polsar backscattering over the austfonna ice cap", *IEEE Transactions on Geoscience and Remote Sensing*, vol. 54, no. 3, pp. 1267–1281, Mar. 2016. DOI: `10.1109/TGRS.2015.2477168` (cited on page 10).

[84] I. Hajnsek, T. Jagdhuber, H. Schon, and K. P. Papathanassiou, "Potential of estimating soil moisture under vegetation cover by means of polsar", *IEEE Transactions on Geoscience and Remote Sensing*, vol. 47, no. 2, pp. 442–454, 2009. DOI: `10.1109/TGRS.2008.2009642` (cited on page 10).

[85] I. Hajnsek, "Inversion of surface parameters using polarimetric sar", PhD thesis, Friedrich-Schiller-Universität Jena, 2001. [Online]. Available: `https://d-nb.info/963834800/34` (cited on page 10).

[86] A. Freeman, "Fitting a two-component scattering model to polarimetric sar data from forests", *IEEE Transactions on Geoscience and Remote Sensing*, vol. 45, no. 8, pp. 2583–2592, Aug. 2007. DOI: `10.1109/TGRS.2007.897929` (cited on page 10).

[87] R. Bamler and P. Hartl, "Synthetic aperture radar interferometry", *Inverse problems*, vol. 14, no. 4, R1, 1998. DOI: `10.1088/0266-5611/14/4/001` (cited on page 11).

[88] G. Krieger, A. Moreira, H. Fiedler, I. Hajnsek, M. Werner, M. Younis, and M. Zink, "Tandem-x: a satellite formation for high-resolution sar interferometry", *IEEE Transactions on Geoscience and Remote Sensing*, vol. 45, no. 11, pp. 3317–3341, 2007. DOI: `10.1109/TGRS.2007.900693` (cited on page 11).

[89] M. J. Soja, H. J. Persson, and L. M. H. Ulander, "Modeling and detection of deforestation and forest growth in multitemporal tandem-x data", *IEEE Journal of Selected Topics in Applied Earth Observations and Remote Sensing*, vol. 11, no. 10, pp. 3548–3563, Oct. 2018. DOI: `10.1109/JSTARS.2018.2851030` (cited on page 11).

[90] J. O. Hagberg, L. M. H. Ulander, and J. Askne, "Repeat-pass sar interferometry over forested terrain", *IEEE Transactions on Geoscience and Remote Sensing*, vol. 33, no. 2, pp. 331–340, Mar. 1995. DOI: `10.1109/TGRS.1995.8746014` (cited on page 11).

[91] J. I. H. Askne, H. J. Persson, and L. M. H. Ulander, "On the sensitivity of tandem-x-observations to boreal forest structure", *Remote Sensing*, vol. 11, no. 14, 2019, ISSN: 2072-4292. DOI: `10.3390/rs11141644` (cited on page 11).

[92] J. I. H. Askne, H. J. Persson, and L. M. H. Ulander, "Biomass growth from multi-temporal tandem-x interferometric synthetic aperture radar observations of a boreal forest site", *Remote Sensing*, vol. 10, no. 4, 2018, ISSN: 2072-4292. DOI: `10.3390/rs10040603` (cited on page 11).

[93] P. D. C. Bispo, M. Pardini, K. P. Papathanassiou, F. Kugler, H. Balzter, D. Rains, J. R. dos Santos, I. G. Rizaev, K. Tansey, M. N. dos Santos, and L. S. Araujo, "Mapping forest successional stages in the brazilian amazon using forest heights derived from tandem-x sar interferometry", *Remote Sensing of Environment*, vol. 232, p. 111 194, 2019, ISSN: 0034-4257. DOI: `10.1016/j.rse.2019.05.013` (cited on page 11).

[94] K. P. Papathanassiou and S. R. Cloude, "Single-baseline polarimetric sar interferometry", *IEEE Transactions on Geoscience and Remote Sensing*, vol. 39, no. 11, pp. 2352–2363, 2001. DOI: `10.1109/36.964971` (cited on page 11).

[95] S. R. Cloude and K. P. Papathanassiou, "Polarimetric sar interferometry", *IEEE Transactions on geoscience and remote sensing*, vol. 36, no. 5, pp. 1551–1565, 1998. DOI: `10.1109/36.718859` (cited on page 11).

[96] L. Ferro-Famil, E. Pottier, and J.-S. Lee, "Classification and interpretation of polarimetric interferometric sar data", in *IEEE International Geoscience and Remote Sensing Symposium*, IEEE, vol. 1, 2002, pp. 635–637. DOI: `10.1109/IGARSS.2002.1025129` (cited on page 11).

[97] J. Ballester-Berman, "Retrieval of biophysical parameters of agricultural crops using polarimetric sar interferometry", PhD thesis, Universitat D'Alacant, 2007. [Online]. Available: `http://dfists.ua.es/~juanma/docs/thesis_Josep_David_Ballester_Berman.pdf` (cited on page 11).

[98] J. Lopez-Sanchez, "Analysis and estimation of biophysical parameters of vegetation by radar polarimetry", PhD thesis, Universidad Politécnica de Valencia, 1999. [Online]. Available: `http://www.dfists.ua.es/~juanma/docs/tesis.pdf` (cited on page 11).

[99] S. Leinss, "Depth, anisotropy, and water equivalent of snow estimated by radar interferometry and polarimetry", PhD thesis, ETH Zurich, 2015. DOI: `10.3929/ethz-a-010603517` (cited on page 11).

[100] S.-K. Lee, "Forest parameter estimation using polarimetric sar interferometry techniques at low frequencies", PhD thesis, ETH Zurich, 2012. DOI: `10.3929/ethz-a-007615658` (cited on pages 11, 12).

[101] S. Cloude and K. Papathanassiou, "Three-stage inversion process for polarimetric sar interferometry", *IEE Proceedings-Radar, Sonar and Navigation*, vol. 150, no. 3, pp. 125–134, 2003. DOI: `10.1049/ip-rsn:20030449` (cited on page 11).

[102] I. Hajnsek, F. Kugler, S. Lee, and K. P. Papathanassiou, "Tropical-forest-parameter estimation by means of pol-insar: the indrex-ii campaign", *IEEE Transactions on Geoscience and Remote Sensing*, vol. 47, no. 2, pp. 481–493, Feb. 2009. DOI: `10.1109/TGRS.2008.2009437` (cited on page 11).

[103] F. Kugler, D. Schulze, I. Hajnsek, H. Pretzsch, and K. P. Papathanassiou, "Tandem-x pol-insar performance for forest height estimation", *IEEE Transactions on Geoscience and Remote Sensing*, vol. 52, no. 10, pp. 6404–6422, 2014. DOI: `10.1109/TGRS.2013.2296533` (cited on page 11).

[104] T. Mette, "Forest biomass estimation from polarimetric sar interferometry", PhD thesis, Technische Universität München, 2007. [Online]. Available: `http://mediatum.ub.tum.de?id=624618` (cited on page 11).

[105] S. Abdullahi, F. Kugler, and H. Pretzsch, "Prediction of stem volume in complex temperate forest stands using tandem-x sar data", *Remote sensing of environment*, vol. 174, pp. 197–211, 2016. DOI: `10.1016/j.rse.2015.12.012` (cited on page 11).

[106] X. X. Zhu and R. Bamler, "Very high resolution spaceborne sar tomography in urban environment", *IEEE Transactions on Geoscience and Remote Sensing*, vol. 48, no. 12, pp. 4296–4308, Dec. 2010. DOI: `10.1109/TGRS.2010.2050487` (cited on page 12).

[107] G. Fornaro and F. Serafino, "Imaging of single and double scatterers in urban areas via sar tomography", *IEEE Transactions on Geoscience and Remote Sensing*, vol. 44, no. 12, pp. 3497–3505, Dec. 2006. DOI: `10.1109/TGRS.2006.881748` (cited on page 12).

[108] F. Lombardini, F. Cai, and D. Pasculli, "Spaceborne 3-D sar tomography for analyzing garbled urban scenarios: single-look superresolution advances and experiments", *IEEE Journal of Selected Topics in Applied Earth Observations and Remote Sensing*, vol. 6, no. 2, pp. 960–968, Apr. 2013, ISSN: 1939-1404. DOI: `10.1109/JSTARS.2012.2211339` (cited on page 12).

[109] S. Tebaldini and F. Rocca, "Multibaseline polarimetric sar tomography of a boreal forest at P-and L-bands", *IEEE Transactions on Geoscience and Remote Sensing*, vol. 50, no. 1, pp. 232–246, 2012. DOI: `10.1109/TGRS.2011.2159614` (cited on page 12).

[110] M. Neumann, L. Ferro-Famil, and A. Reigber, "Estimation of forest structure, ground, and canopy layer characteristics from multibaseline polarimetric interferometric sar data", *IEEE Transactions on Geoscience and Remote Sensing*, vol. 48, no. 3, pp. 1086–1104, 2010. DOI: `10.1109/TGRS.2009.2031101` (cited on page 12).

[111] H. Joerg, "Multi-frequency polarimetric sar tomography for the 3-D characterization and monitoring of agricultural crops", PhD thesis, ETH Zurich, Zurich, 2018. DOI: `10.3929/ethz-b-000259515` (cited on page 12).

[112] A. T. Caicoya, "Allometric estimation of aboveground forest biomass using forest structure parameters estimated by means of multi-baseline sar measurements", PhD thesis, Technische Universität München, 2016. [Online]. Available: `https://mediatum.ub.tum.de/?id=1284783` (cited on page 12).

[113] M. Mariotti D'Alessandro and S. Tebaldini, "Digital terrain model retrieval in tropical forests through P-band sar tomography", *IEEE Transactions on Geoscience and Remote Sensing*, vol. 57, no. 9, pp. 6774–6781, Sep. 2019. DOI: `10.1109/TGRS.2019.2908517` (cited on page 12).

[114] M. Nannini, R. Scheiber, R. Horn, and A. Moreira, "First 3-D reconstructions of targets hidden beneath foliage by means of polarimetric sar tomography", *IEEE Geoscience and Remote Sensing Letters*, vol. 9, no. 1, pp. 60–64, 2012. DOI: `10.1109/LGRS.2011.2160329` (cited on page 12).

[115] H. T. M. Dinh, S. Tebaldini, F. Rocca, C. Albinet, P. Borderies, T. Koleck, T. Le Toan, and L. Villard, "Tropiscat: multi-temporal multi-polarimetric tomographic imaging of tropical forest", in *2012 IEEE International Geoscience and Remote Sensing Symposium*, Jul. 2012, pp. 7051–7054. DOI: `10.1109/IGARSS.2012.6351947` (cited on page 12).

[116] L. M. H. Ulander, A. R. Monteith, M. J. Soja, and L. E. B. Eriksson, "Multiport vector network analyzer radar for tomographic forest scattering measurements", *IEEE Geoscience and Remote Sensing Letters*, vol. 15, no. 12, pp. 1897–1901, Dec. 2018. DOI: `10.1109/LGRS.2018.2865673` (cited on page 12).

[117] P. Stoica, R. L. Moses, *et al.*, *Spectral analysis of signals*. Pearson Prentice Hall Upper Saddle River, NJ, 2005, ISBN: 9780131139565 (cited on page 12).

[118] J. Capon, "High-resolution frequency-wavenumber spectrum analysis", *Proceedings of the IEEE*, vol. 57, no. 8, pp. 1408–1418, 1969. DOI: `10.1109/PROC.1969.7278` (cited on page 12).

[119] B. Ottersten, P. Stoica, and R. Roy, "Covariance matching estimation techniques for array signal processing applications", *Digital Signal Processing*, vol. 8, no. 3, pp. 185–210, 1998. DOI: `10.1006/dspr.1998.0316` (cited on page 12).

[120] S. R. Cloude, "Polarization coherence tomography", *Radio Science*, vol. 41, no. 04, pp. 1–27, 2006. DOI: `10.1029/2005RS003436` (cited on page 12).

[121] M. Pardini, A. T. Caicoya, F. Kugler, S.-K. Lee, I. Hajnsek, and K. Papathanassiou, "On the estimation of forest vertical structure from multibaseline polarimetric sar data", in *Geoscience and Remote Sensing Symposium (IGARSS), 2012 IEEE International*, IEEE, 2012, pp. 3443–3446. DOI: `10.1109/IGARSS.2012.6350680` (cited on page 12).

[122] R. Schmidt, "Multiple emitter location and signal parameter estimation", *IEEE transactions on antennas and propagation*, vol. 34, no. 3, pp. 276–280, 1986. DOI: `10.1109/TAP.1986.1143830` (cited on page 12).

[123] F. Lombardini, F. Cai, and D. Pasculli, "Spaceborne 3-D sar tomography for analyzing garbled urban scenarios: single-look superresolution advances and experiments", *IEEE Journal of Selected Topics in Applied Earth Observations and Remote Sensing*, vol. 6, no. 2, pp. 960–968, 2013. DOI: `10.1109/JSTARS.2012.2211339` (cited on page 12).

[124] O. Frey and E. Meier, "Analyzing tomographic sar data of a forest with respect to frequency, polarization, and focusing technique", *IEEE Transactions on Geoscience and Remote Sensing*, vol. 49, no. 10, pp. 3648–3659, 2011. DOI: `10.1109/TGRS.2011.2125972` (cited on page 12).

[125] A. Budillon, A. Evangelista, and G. Schirinzi, "Three-dimensional sar focusing from multipass signals using compressive sampling", *IEEE Transactions on Geoscience and Remote Sensing*, vol. 49, no. 1, pp. 488–499, 2011. DOI: `10.1109/TGRS.2010.2054099` (cited on page 12).

[126] X. Li, L. Liang, H. Guo, and Y. Huang, "Compressive sensing for multibaseline polarimetric sar tomography of forested areas", *IEEE Transactions on Geoscience and Remote Sensing*, vol. 54, no. 1, pp. 153–166, 2016. DOI: `10.1109/TGRS.2015.2451992` (cited on page 12).

[127] E. Aguilera, M. Nannini, and A. Reigber, "A data-adaptive compressed sensing approach to polarimetric sar tomography of forested areas", *IEEE Geoscience and Remote Sensing Letters*, vol. 10, no. 3, pp. 543–547, 2013. DOI: `10.1109/LGRS.2012.2212693` (cited on page 12).

[128] X. X. Zhu and R. Bamler, "Tomographic sar inversion by l1-norm regularization-the compressive sensing approach", *IEEE Transactions on Geoscience and Remote Sensing*, vol. 48, no. 10, pp. 3839–3846, 2010. DOI: `10.1109/TGRS.2010.2048117` (cited on page 12).

[129] X. Peng, X. Li, C. Wang, H. Fu, and Y. Du, "A maximum likelihood based nonparametric iterative adaptive method of synthetic aperture radar tomography and its application for estimating underlying topography and forest height", *Sensors*, vol. 18, no. 8, p. 2459, 2018. DOI: `10.3390/s18082459` (cited on page 12).

[130] G. M. del Campo, M. Nannini, and A. Reigber, "Towards feature enhanced sar tomography: a maximum-likelihood inspired approach", *IEEE Geoscience and Remote Sensing Letters*, no. 99, pp. 1–5, 2018. DOI: `10.1109/LGRS.2018.2858571` (cited on page 12).

[131] M. Pardini, M. Tello, V. Cazcarra-Bes, K. P. Papathanassiou, and I. Hajnsek, "L-and P-band 3-D sar reflectivity profiles versus lidar waveforms: the afrisar case", *IEEE Journal of Selected Topics in Applied Earth Observations and Remote Sensing*, no. 99, pp. 1–16, 2018. DOI: `10.1109/JSTARS.2018.2847033` (cited on page 12).

[132] M. Pardini, J. Armston, W. Qi, S. K. Lee, M. Tello, V. Cazcarra Bes, C. Choi, R. O. Papathanassiou Konstantinos P. and Dubayah, and L. E. Fatoyinbo, "Early lessons on combining lidar and multi-baseline sar measurements for forest structure characterization", *Surveys in Geophysics*, vol. 40, no. 4, pp. 803–837, Jul. 1, 2019. DOI: `10.1007/s10712-019-09553-9` (cited on page 12).

[133] M. Pardini, K. P. Papathanassiou, and F. Lombardini, "Impact of dielectric changes on L-band 3-D sar reflectivity profiles of forest volumes", *IEEE Transactions on Geoscience and Remote Sensing*, no. 99, pp. 1–14, 2018. DOI: `10.1109/TGRS.2018.2850357` (cited on page 12).

[134] D. H. T. Minh, T. Le Toan, F. Rocca, S. Tebaldini, M. M. d'Alessandro, and L. Villard, "Relating P-band synthetic aperture radar tomography to tropical forest biomass", *IEEE Transactions on Geoscience and Remote Sensing*, vol. 52, no. 2, pp. 967–979, 2014. DOI: `10.1109/TGRS.2013.2246170` (cited on page 12).

[135] E. Blomberg, L. Ferro-Famil, M. J. Soja, L. M. H. Ulander, and S. Tebaldini, "Forest biomass retrieval from L-band sar using tomographic ground backscatter removal", *IEEE Geoscience and Remote Sensing Letters*, vol. 15, no. 7, pp. 1030–1034, Jul. 2018. DOI: `10.1109/LGRS.2018.2819884` (cited on page 12).

Chapter 2

Forest Structure Characterization From SAR Tomography at L-Band

M. Tello-Alonso, V. Cazcarra-Bes, M. Pardini and K. P. Papathanassiou

IEEE Journal of Selected Topics in Applied Earth Observations and Remote Sensing
Published in October 2018. DOI: 10.1109/JSTARS.2018.2859050

Key findings/points:

- Definition of a framework for qualitative and quantitative estimation of 3-D forest structure.
- Validation using three different sources of data: ground measurements at single-tree level, Lidar and tomographic SAR data.
- Benefits of tomographic SAR data with respect to only height.

The author's contributions:

- M. Tello-Alonso is the main author of the manuscript, contributed with the main ideas, the structure of the paper and the interpretation of the results.

The co-author's contributions:

- V. Cazcarra-Bes contributed to:
  - Writing of many parts of the manuscript.
  - Development and implementation of the tomographic algorithm.
  - Processing of the ground measurements and the Lidar data.
  - Contribution with ideas and interpretation of the results.
- M. Pardini contributed with ideas and helped on the interpretation of the results.
- K. P. Papathanassiou contributed to the main ideas and revised the work.

Forest Structure Characterization From SAR Tomography at L-Band

M. Tello-Alonso[1], V. Cazcarra-Bes[1,2], M. Pardini[1] and K. P. Papathanassiou[1]

[1]Microwaves and Radar Institute, German Aerospace Center (DLR), 82234 Wessling, Germany
[2]Institute of Environmental Engineering, ETH Zürich, 8093 Zürich, Switzerland

Abstract

Synthetic aperture radar (SAR) remote sensing configurations are able to provide continuous measurements on global scales sensitive to the vertical structure of forests with a high spatial and temporal resolution. Furthermore, the development of tomographic SAR techniques allows the reconstruction of the three-dimensional (3-D) radar reflectivity opening the door for 3-D forest monitoring. However, the link between 3-D radar reflectivity and 3-D forest structure is not yet established. In this sense, this paper introduced a framework that allows a qualitative and quantitative interpretation of physical forest structure from tomographic SAR data at L-band. For this, forest structure is parameterized into a set of a horizontal and a vertical structure index. From inventory data, both indices can be derived from the spatial distribution and the dimensions of the trees. Similarly, two structure indices are derived from the 3-D spatial distribution of the local maxima of the reconstructed 3-D radar reflectivity profiles at L-band. The proposed methodology is tested by means of experimental tomographic L-band data acquired over the temperate forest site of Traunstein in Germany. The obtained horizontal and vertical structure indices are validated against the corresponding estimates obtained from inventory measurements and against the same indices derived from the vertical profiles of airborne Lidar data. The high correlation between the forest structure indices obtained from these three different data sources (expressed by correlation coefficients between 0.75 and 0.87) indicates the potential of the proposed framework.

2.1 Introduction

Forest structure is eminently linked to the three-dimensional (3-D) size, location, and arrangement of trees, trunks, and branches in a forest [1], [2] and reflects therefore the forest state and its evolution [3]–[5]. Accordingly, forest structure is an indicator of forest successional stage and development as well as sustainability and habitability and is therefore an important parameter for assessing forest productivity [6], biomass level, and biodiversity [7]–[9]. Forest structure changes reveal dynamic processes as growth, regeneration, decay, and natural or anthropogenic disturbance. Knowledge about such processes is important for modeling the function and the evolution of forest ecosystems and for developing accurate and robust forest biomass estimators [10].

The wide range of applications that require forest structure information imposes a wide range of measurement and observation requirements. For biomass and carbon applications, yearly global scale monitoring at spatial resolutions on the order of 1 ha are sufficient [3]. On the other hand, ecology and biodiversity applications are often addressed at landscape-to-regional level and require forest structure information at spatial and temporal scales associated to the occurring changes, i.e., down to single tree level with monthly to seasonal updates [7].

These requirements cannot be satisfied by the currently available means of forest monitoring. Traditionally, forest structure characterization relies on sampling at local scales by means of field inventory plots or more recently terrestrial laser scanning techniques able to catch the 3-D arrangement of vegetation compartments. However, any extrapolation to larger scales depends on the ability of these measurements to represent their surrounding landscape. At the same time, in many cases, the temporal continuity of such plots measurements is very difficult to be established.

Remote sensing techniques have the potential to overcome — at least some of — these limitations and to make a significant contribution in qualitative and quantitative monitoring of 3-D forest structure [3], [7]–[10]. Today, two remote sensing technologies allow the measurement of 3-D forest information: Lidar and synthetic aperture radar (SAR) tomography. While the capabilities and challenges of the different Lidar configurations for mapping 3-D forest structure are today well established and widely understood, the potential of tomographic SAR configurations is not fully assessed yet. Note here that the horizontal variability alone that can be estimated by conventional remote sensing techniques is often not sufficient to describe unambiguously vegetation structure [10] so that 3-D descriptors and measurements are required for a complete characterization.

SAR tomography relies on a set of SAR images acquired under slightly different incidence angles as for example along slightly displaced tracks or orbits to estimate the 3-D distribution of the backscattered power, also known as the 3-D radar reflectivity. The reconstruction the 3-D radar reflectivity is today established and has been demonstrated in several experiments across different forest ecosystems [11]–[15]. The Appendix 2.5 summarizes the main tomographic reconstruction algorithms.

However, the link between the reconstructed 3-D radar reflectivity and the physical forest structure is not as well understood and far from being established. There are several reasons that make this task challenging. One of them is related to the interpretation of the reconstructed 3-D radar reflectivity in terms of 3-D forest structure attributes. Obviously, the 3-D radar reflectivity depends on the system frequency and polarization employed, on the acquisition geometry (e.g., incidence angle) used, and on the (3-D) spatial resolution achieved. The fact that the scatterers *seen* by the radar change with frequency and polarization makes a generic interpretation of the 3-D reflectivity difficult. In addition, with decreasing frequency, the scattering contribution of the ground under the forest adds to the one of the forest making the interpretation of lower forest components located close to the ground more difficult. This paper focuses on 3-D radar reflectivity at L-band, where in general a significant penetration into and through the forest volume is expected implying scattering contributions from the forest volume and from the underlying ground.

While forest structure is primarily associated to the geometric properties of tree and forest stand elements, the radar reflectivity depends in addition to geometric properties also on the dielectric properties of the scattering elements of the forest. This makes the interpretation of the reconstructed 3-D radar reflectivity —and especially its change— ambiguous. As a consequence, the estimation of forest structure has to be robust enough to reflectivity variations that are not relevant to structure as for example caused by rain or temperature gradients [12], [13] while still remaining sensitive enough to morphological variations.

When attempting to relate the reconstructed 3-D radar reflectivity to physical forest structure descriptors established in forestry and/or ecology, one faces a significant discrepancy. The physical forest structure descriptors are built on individual tree parameters that do not have a direct correspondence in the reconstructed 3-D radar reflectivity due to the insufficient spatial resolution of the SAR configurations that does not allow individualizing scattering contributions of single trees. This paper aims to contribute to the interpretation of L-band 3-D radar reflectivity in terms of physical forest structure. In this sense, a framework that allows the estimation of qualitative and quantitative 3-D forest structure information from 3-D radar reflectivity reconstructed by SAR tomography at L-band is proposed. In Section 2.2, forest structure estimation from field and remote sensing data is discussed and a pair of structure indices that allow the characterization of horizontal and vertical forest structure is introduced. The two indices allow setting up a schema for the systematic characterization and quantification of 3-D forest structure that can be applied on inventory and remote sensing data. In Section 2.3, experimental results obtained from airborne tomographic SAR data acquired at L-band and (airborne) Lidar data over the temperate forest of Traunstein in Germany are presented. The structure indices derived from the tomographic SAR, the Lidar, and the inventory measurements are discussed and compared with each other. The advantage of 3-D forest structure information versus forest height information only is discussed. The effect of the spatial scale on the interpretation of the obtained results is also assessed. Finally, conclusions are drawn in Section 2.4.

2.2 Forest Structure Estimation

2.2.1 Forest Structure Estimation From Field Data

Since both forestry and ecology have been traditionally based on field data, the discussion on forest structure metrics has been essentially carried out on an individual tree basis. On plot level, it is usually approached by estimating different attributes based on individual trees within the plot, such as height, basal area, canopy dimensions, species composition, and/or stand density, which are then used to derive a structure index. Numerous indices have been proposed in the literature, such as the aggregation index [16], the diametric differentiation index, the mingling index, the contagion index, or the complex stand index [17]. However, all of them have limitations in the sense that no one provides a univocal characterization of any possible tree distribution within the stand [18]–[21]. As a consequence, there is not yet an overall measure able to express forest structure in terms of forestry or ecology. Nevertheless, despite the difficulties in defining an index appropriate for a wide span of applications and forest types, there is a common understanding that in order to express forest structure, two complementary aspects of forest structure need to be considered, namely the structural heterogeneity in the horizontal and in the vertical dimension. In this sense, horizontal structure reflects stand density, whereas vertical structure accounts for tree size variability.

Regarding horizontal structure, it is worth noting here that stand density is not exclusively related to the number of trees per unit area, but rather to site occupancy and therefore tree volume per area [5]. One standard metric in forest practice is absolute basal area [22]. But in order to compare stands of different ages, it is preferable to introduce measures linking space utilization to tree size [21]. The most common among them is the stand density index [23], closely related to the basal area. It relates the stand density with the equivalent density of a stand with an actual quadratic mean diameter of 25 cm. In the scope of this paper, this metric is employed for the estimation of horizontal structure from field data:

$$HS_{field} = N\left(\frac{D_g}{25}\right)^{1.605} \tag{2.1}$$

expressed in trees per hectare, where N is the number of stems per hectare and D_g is the quadratic mean diameter at breast height in cm [24], within the structure window. In the following, the area of the structure window, i.e., the size of the polygon enclosing the trees that are accounted when computing the statistical quantities defined in 2.1, 2.2, 2.3 and 2.4 will be referred to as unit scale. Several subsequent refinements of this index have been discussed in the literature [25]. Accounting only for the tallest trees in the stand allows a better characterization of canopy closure, while being more consistent by assuming the same allometric relationship between the size and density for all the trees involved in the estimation. Also, without loss of generality, HS_{field} is normalized to its maximum and then $1 - HS_{field\ norm}$ is employed in order to reflect disorder: 0 indicates low and 1 indicates high structural disorder or complexity.

Vertical structure can be evaluated by the size differentiation, the Gini coefficient, the Shannon index [26], or as the standard deviation of tree heights [6], [27], among others. However, due to the fact that tree height measurements are often not performed, these indices are usually not possible to be estimated directly from inventory data. As an alternative, the standard deviation of tree diameter at breast height (dbh) that reflects as well the tree size variability [5] has been used that can be directly estimated from standard inventory measurements. Furthermore, according to [2] and [4], dbh variability appears to be more sensitive to successional stages than measures of height diversity alone. Therefore, in the scope of this paper, vertical forest structure from field data VS_{field} is estimated as the standard deviation of tree dbh:

$$VS_{field} = std\left(\{dbh\}\right) \tag{2.2}$$

expressed in cm, where $\{dbh\}$ is the ensemble of diameter at breast height of all the trees included in the structure window, given in cm. Without loss of generality, the vertical forest structure descriptor from field data is normalized to its maximum within the image and becomes unitless.

Using now the horizontal HS_{field} and vertical VS_{field} structure indices, it is possible to define a plane, referred to as HV plane in the following, on which forest stands can be projected depending on their structure (see Figure 2.1). The complementary aspect of horizontal and vertical structure can be observed in Figure 2.1. Four stands are projected in the plane defined by their horizontal and vertical structure. The four stands sketched can only be unambiguously discriminated when both the horizontal and the vertical dimensions are accounted for. First, two monolayered stands have been sketched. They have low vertical structure because they are mainly constituted by trees of similar size. The difference between them relies in the horizontal axis, due to their different density. On the other hand, two multilayered stands have been considered as well. They both have similar high vertical structure. The difference between them relies again in the horizontal dimension.

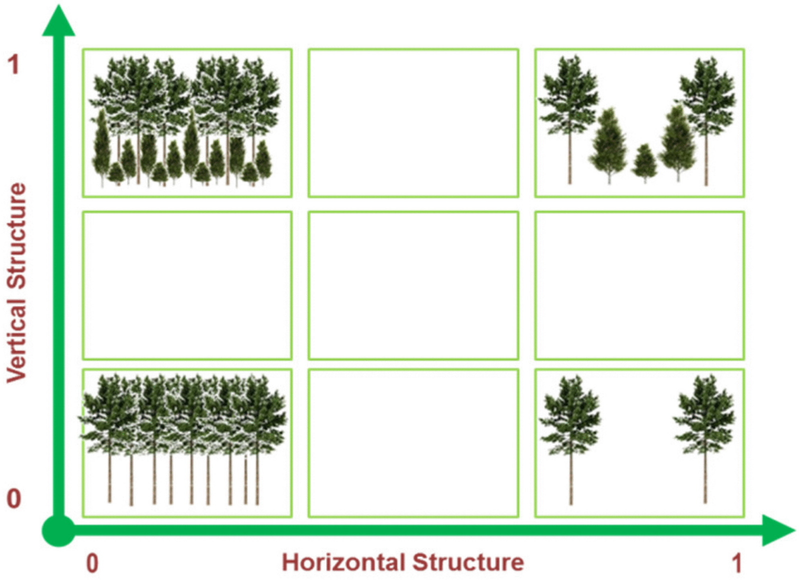

FIGURE 2.1: Horizontal and vertical forest structure measures are complementary and allow the definition of a plane where stands can be projected according to their structure complexity. As an example, the position of four different examples of forest stand is shown here.

2.2.2 Forest Structure Estimation From TomoSAR Data

The objective of this section is to define a framework for the estimation of forest structure from L-band TomoSAR data. For this, the definition of structure indices applicable to TomoSAR data that meet the same notions as the forest structure indices derived from inventory data discussed in the previous section will be attempted. The challenge is to circumvent the fact that individual tree-based measures are usually not possible to be retrieved with TomoSAR data, which hampers a direct translation of the metrics employed in ecology and forestry. The main principles and processing steps in SAR tomography relevant for this paper are summarized in the Appendix 2.5.

2.2.2.1 Physical Interpretation of Reflectivity Profiles

Figure 2.2 shows an example of an (normalized) L-band 3-D reflectivity transect (referred as tomogram in the following) through a managed temperate forest, crossing stands at different growth stages. Four different areas are highlighted and denoted by numbers. For each of these four areas, a representation of the tree distribution as obtained from the field inventory data is given (left column) and the corresponding reflectivity profiles (middle column). Looking at the two representations makes evident that the differences in the 3-D reflectivity profiles reflect the differences in forest structure for each of the areas. As indicated by the schematic tree representations, areas 2 and 3 are monolayered dense stands, whereas areas 1 and 4 are constituted by significantly more diverse tree sizes. Looking at the reflectivity profiles, besides the ground, most of the maxima are concentrated in a 10 m height range going from 20 to 30 m and from 10 to 20 m for areas 2 and 3, respectively, whereas they are distributed along more than 30 m, from 10 to 40 m for both areas 1 and 4. The 3-D distribution of the local reflectivity maxima (i.e., the reflectivity peaks) shown in the right column of Figure 2.2 is distinctive for the four different forest structure types considered in this example.

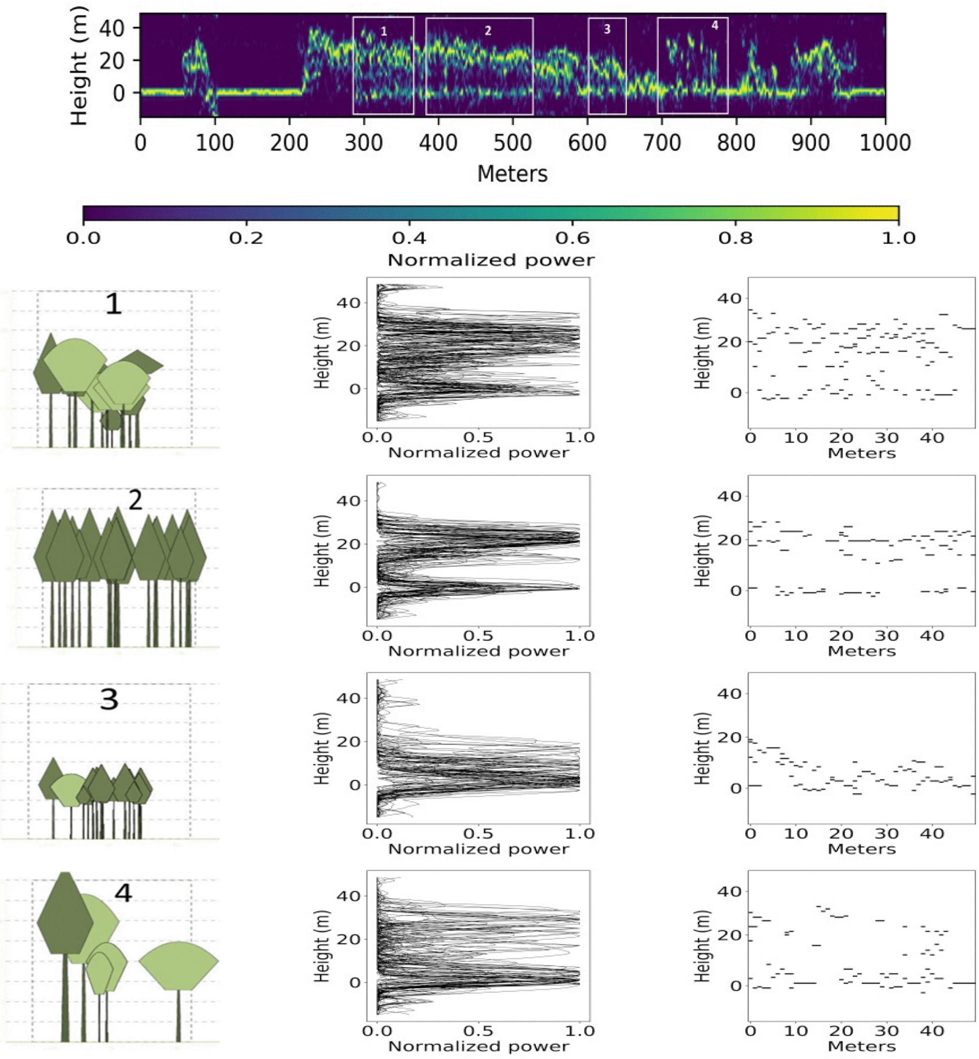

FIGURE 2.2: (Top row) Example of normalized tomogram along a managed highly heterogeneous temperate forest. (Left column) Schematic representation of the trees distributions, (middle column) corresponding reflectivity profiles superimposed, and (right column) peaks of the reflectivity profiles, for the four areas highlighted in the tomogram.

This indicates that the 3-D distribution of reflectivity peaks at L-band reflects the variability in the distribution of trees. Even if the physical significance of reflectivity peaks in terms of forest structure is not established, a number of models and experiments in the literature support this assumption [28]–[30]. From an experimental perspective, the comparison of vertical reflectivity profiles at L-band with the height distribution of trees derived from airborne laser scanning data confirms that reflectivity peaks are produced at the range of heights occupied by the branches [31].

The discussion above triggers the idea to define measures of forest structure based on the (spatial) 3-D distribution of reflectivity peaks ignoring their (absolute) intensity. This choice has several advantages. First, it allows to attenuate the impact of radar reflectivity variations due to nonstructural effects. The location of the reflectivity peaks appears significantly more robust than the relative distribution of energy against changes induced by rain events, temperature gradients, seasonality [13], and/or the choice of the TomoSAR algorithm itself [32]. This allows the use of tomographic super-resolution algorithms that allow to critically improve the vertical resolution beyond the Rayleigh resolution, by taking into account the associated loss of radiometric accuracy and or consistency. Among all TomoSAR algorithms in the literature, compressive sensing (CS) provides the highest super-resolution under the relevant TomoSAR conditions, and for this reason it has been used in the following (see the Appendix 2.5). At the same time, using the distribution of peaks only allows to reduce the dimensionality of the observation space required for the definition of a structure metric.

2.2.2.2 Definition of Horizontal and Vertical Forest Structure Indices From TomoSAR

The objective of this section is to define indices of horizontal and vertical structure from the 3-D spatial distribution of the ensemble of reflectivity peaks. These indices should reflect the same notions of spatial variability of the canopy cover and tree size distribution as the indices defined in 2.1 and 2.2. Following the discussion in Section 2.2.2.1, it can be assumed that the presence of forest layers at different heights within a stand is reflected by a higher variability in the height of the reflectivity peaks. Based on this, it is possible to define one horizontal and one vertical index of structure from the 3-D distribution of the reflectivity peaks.

For the horizontal structure index HS, first the height of the highest peak in the unit scale h_{max} is estimated and a *top layer* is defined as the range of heights between 0.6 h_{max} and h_{max}. The blue layer in Figure 2.3 shows the *top layer* as obtained for the first area shown in Figure 2.2. Once the *top layer* is defined, the horizontal structure descriptor is computed as the number of peaks within the *top layer* divided by the unit area S. Note that the definition of the *top layer* is rather empirical, relying though on a definition suggested in [33].

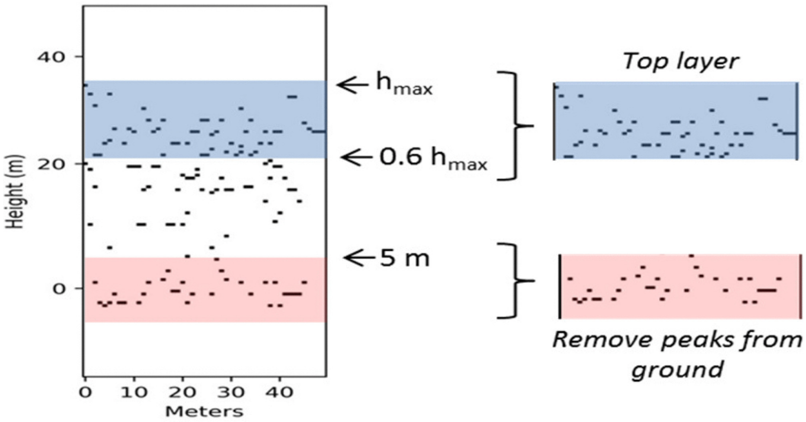

FIGURE 2.3: Definition of top layer for the horizontal structure index and the threshold to remove peaks introduced by the ground scattering contributions.

Let's assume $P = \{p_1, p_2, ..., p_o\}$ the set of O reflectivity peaks in a given unit scale and $H_P = \{h_1, h_2, ..., h_M\}$ the set of M heights at which these peaks are produced. With this, the horizontal structure index is defined as follows:

$$HS = \frac{n\left(P_{top}\right)}{S} \tag{2.3}$$

where $n\left(P_{top}\right)$ is the total number of peaks in the top layer.

Without loss of generality and similar to HS_{field}, HS is normalized to its maximum HS_{norm} within the scene and $1 - HS_{norm}$ is considered in order to reflect disorder: 0 indicates low and 1 indicates high structural disorder or complexity.

The vertical structure index VS is defined as follows:

$$VS = M' var\left(H'_p\right) \tag{2.4}$$

where H'_p is the vector of size M' obtained from H_P after accounting all peaks that appear at the same height only once and ignoring the peaks of the ground. At lower frequencies, the presence of the ground scattering contributions introduces reflectivity peaks that are not directly related to the forest volume. In order to exclude the ground induced peaks, a minimum height is set and peaks below this height are disregarded. In this paper, the height threshold is set to 5 m (see the red area in Figure 2.3), implying that understory (1–3 m) is also ignored. Finally, the descriptor of the vertical forest structure VS is normalized to its maximum VS_{norm} within the scene.

Several considerations should be raised here. First, while the majority of peaks occur at the position of the canopies, this is not always the case. This can be due to sidelobes in the reconstruction of the vertical reflectivity as a result of a suboptimum sampling (i.e., number and/or distribution of acquisitions), the insufficiency of the reconstruction algorithm, or the erroneous detection of reflectivity peaks (see the reflectivity profiles in Figure 2.2). As a consequence, it is of advantage to define forest structure descriptors by means of a statistical measure in order to be robust enough to false peak detections. In this context, no reliable information can be extracted from a single peak and the larger the number of peaks, the more accurate the estimated height frequency distribution becomes, ensuring a sufficient number of peaks impose restrictions on the range of spatial scales that can be employed. The chosen scale should be large enough to comprise a statistically meaningful number of trees and small enough to occupy a homogeneous area in terms of structure. The definition of these bounds is not straightforward, essentially because they depend on the forest heterogeneity. For instance, compared to homogeneous stands, a highly structured stand requires sampling on a larger scale to reflect its heterogeneity.

Furthermore, the structure indices introduced rely on the assumption that a group of trees of similar height causes a reflectivity peak at the height of the common canopy. However, groups of trees of the same height but different species, might produce peaks at different heights as a result of the different crown architecture (i.e., shape) introducing an ambiguity in the vertical structure index.

Finally, it should be noted that the indices suggested in this section are not absolute measures. Different systems at different resolutions might produce a different set of peaks for the same scene. Since the measure of vertical structure reflects a relative distribution of peaks in the vertical dimension, it will not be affected by differences in range and azimuth resolution. The horizontal one may present lower values with poorer resolutions. In order to account for this, before estimating the structure measures, the ensemble of peaks is projected on a geographic grid always at a resolution of 1 x 1 m. This step allows bringing the number of peaks identified by systems at different resolutions to comparable ranges. This framework has already proven its validity in forest structure changes tracking in a temporal series of TomoSAR data acquired by systems with different characteristics essentially in terms of resolution (range, azimuth, and vertical) and viewing geometries [34].

2.3 Experimental Results on a Temperate Forest

2.3.1 Description of the Test Site and Available Dataset

In this section, the method suggested for forest structure estimation from TomoSAR data at L-band is applied on a temperate forest. The test site considered is Traunstein, a managed forest located in South-Eastern Germany, recently included in the ForestGEO network. The location, diameter at breast height and species of around 16000 trees were sampled in 2015 in an area of 25 ha (see the area indicated with a black perimeter in Figure 2.4). In terms of structure, the site is characterized by a spatial structure gradient with different stages of management. The eastern part is mostly covered by monospecific homogeneous stands, while the western part is dominated by multilayered mixed stands.

In May 2017, a tomographic radar dataset at L-band was acquired over the area in a repeat pass interferometric mode by the DLR's F-SAR system [35] (see Figure 2.4 bottom). The different parameters of the dataset are summarized in Table 2.1. In 2016, airborne Lidar measurements were acquired over the same site (see 2.4 top).

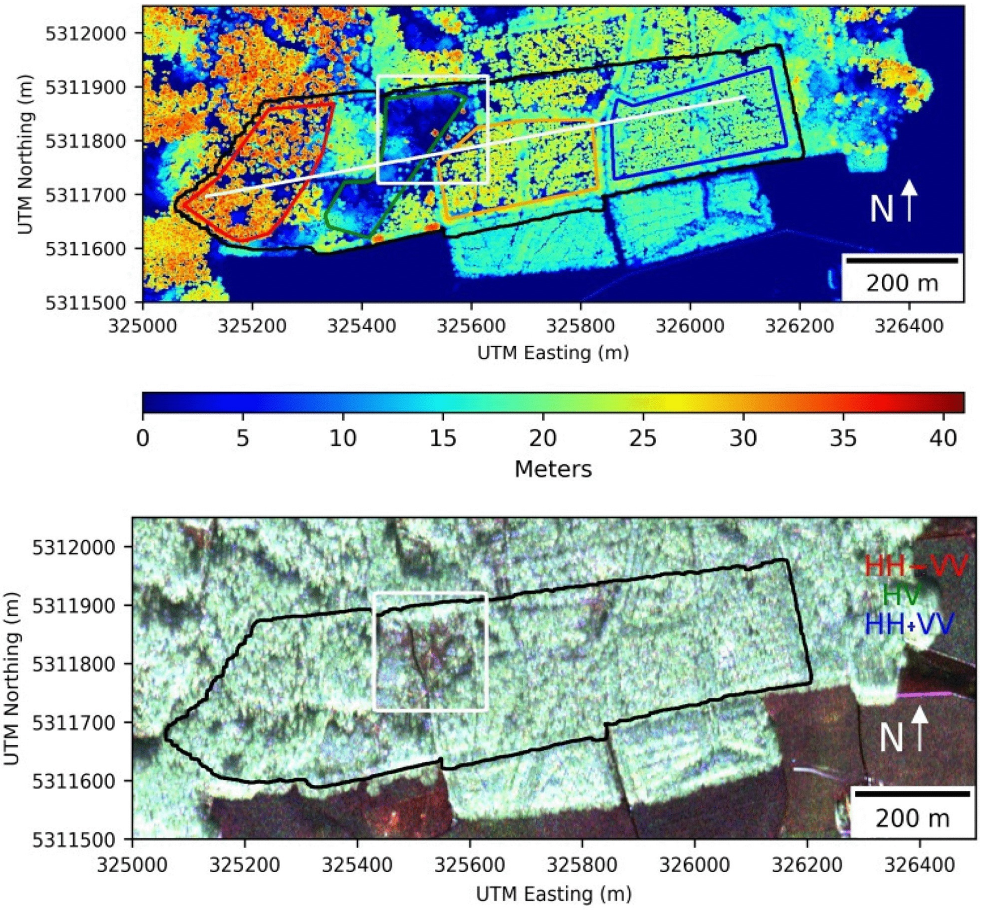

FIGURE 2.4: (Top) Map of Lidar heights over the test site and (bottom) Pauli representation (i.e., using |HH–VV|, |HV| and |HH+VV| as the RGB channels).

As shown in Table 2.1, the SAR single look complex (SLC) images have a resolution of 1.2 m in range and 0.6 m in azimuth. A multilook of 5 x 11 SLC samples in range and azimuth, respectively, is applied in the tomographic processing for the estimation of the covariance matrices, which leads to independent reflectivity profiles every 6 x 6.6 m. The Appendix 2.5 summarizes the main tomographic processing steps employed.

TABLE 2.1: Main parameters of the tomographic SAR dataset.

Tracks	k_z distribution[1]	Height of ambiguity	Resolution		
			Vertical[2]	Slant Range[3]	Azimuth[3]
9	Uniform distributed from 0 to 0.55	91 m	11.4 m	1.2 m	0.6 m

[1] k_z is the vertical wavenumber at the centre of the image; [2] Rayleigh resolution; [3] Before tomographic processing.

Then, the significant peaks from each reflectivity profile are identified. In order to do so, several standard approaches have been tested. Since the local maxima we intend to identify in the reflectivity profiles have significantly higher amplitude than spurious peaks caused by noise (as it can be observed in Figure 2.2), no meaningful differences in terms of performance between the methods have been found in this case. For the results reported in this paper, the profile is first convolved with a Gaussian wavelet at two scales. Within the wavelet coefficients, the ones with amplitude higher than the mean plus three times the standard deviation are accepted as actual peaks. As already mentioned, the identified peaks are projected on a geographical 1 x 1 m grid before the estimation of the structure indices.

After choosing a scale, the forest structure indices are then computed at this scale by applying 2.3 and 2.4 from Section 2.2.2.2. This is implemented by means of a sliding window, whose dimensions correspond to the chosen scale sliding through the samples in the geographical 1 x 1 m grid. Note that, throughout the paper, the scale is set to 50 x 50 m (except of Section 2.3.4, where a multiscale analysis is performed).

A similar analysis has been carried out as well with Lidar data in the same test site. For the Lidar data, a return is recorded every 0.5 x 0.5 m. First, the 100 returns in 5 x 5 m are combined to obtain an aggregated vertical profile. Then, each of these profiles is treated in the same way than the radar ones: The peaks are identified and the structures are estimated following 2.3 and 2.4 with a sliding window.

Figure 2.5 shows a 1 km long transect along the site (indicated by the white line in Figure 2.4 (top)), as seen by both the Lidar (a) and the TomoSAR (b) systems. At each position of the transect, the projection of the Lidar returns as well as the TomoSAR peaks across 20 m are represented. Higher values (yellowish colors) reflect the co-occurrence of numerous peaks at a given height, whereas lower values (bluish colors) imply that no peaks are detected there. It is worth clarifying here that Figures 2.2 and 2.5, besides covering different sites, are showing different variables: Figure 2.2 shows the normalized reflectivity, whereas Figure 2.5 shows the aggregation of reflectivity peaks. Four areas are highlighted in this plot, numbered from 1 to 4, from East to West. For instance, Area 1 corresponds to a homogeneous monolayer stand of spruces. For this young stand, most of the peaks are concentrated in a limited range of heights and only a few ones appear beneath this dominant layer. In Area 2, the dispersion in the vertical distribution of peaks is slightly increasing, reflecting the transition to a multilayered stand. Area 3 is essentially constituted by very low vegetation, irregularly scattered in space. Finally, at the western part of the plot, Area 4 comprises an older stand, with a significantly higher structure complexity that is consistently reflected in a wider distribution of peaks. By comparing the distribution of the Lidar returns with one of the tomographic peaks along the transect, the differences between the different areas in this example appear clearer in the TomoSAR transect. The Lidar returns appear mostly concentrated at the top of the canopy, in a similar way all along the transect. For example, the main difference between Areas 4 and 1 is that the returns in Area 4 are a few meters higher, but they are not significantly more scattered in the vertical dimension than the ones in Area 1. This is reflected in the values of the horizontal and vertical forest structure indices in this transect (see Figures 2.5(c) and (d)).

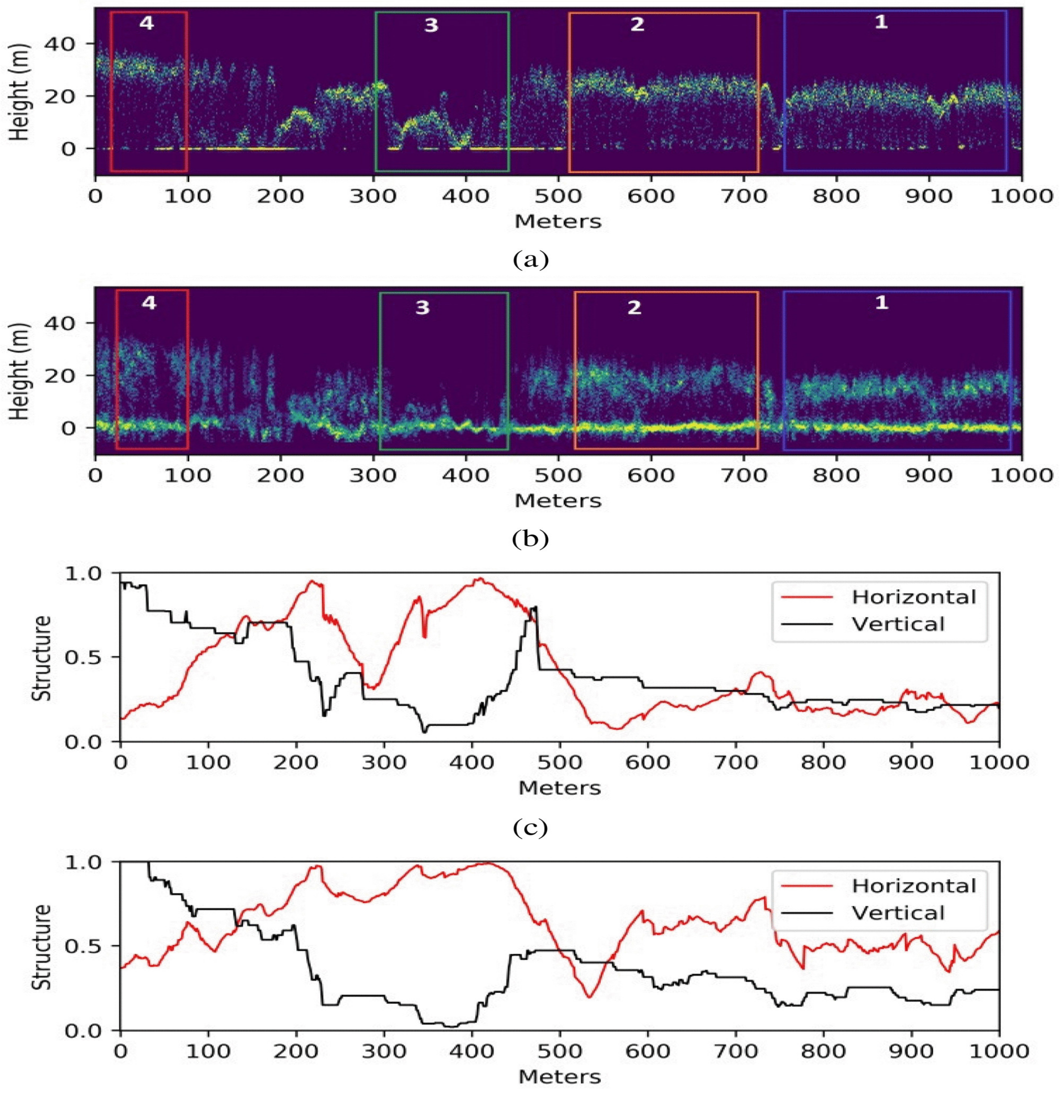

(a)

(b)

(c)

(d)

FIGURE 2.5: Transect across the test site as observed through (a) the Lidar returns and (b) the peaks of the TomoSAR reflectivity profiles. Corresponding forest structure indices as estimated from (c) Lidar and (d) TomoSAR, following 2.3 and 2.4 (aggregated Lidar vertical profiles are treated as TomoSAR reflectivity profiles).

2.3.2 Results

The maps of horizontal and vertical structure are estimated in the site for the three different sources of data available at a structure scale of 50 x 50 m. First, the horizontal and vertical structures from the field data are computed following 2.1 and 2.2, respectively. Then, the horizontal and vertical structures for the two sources of remote sensing data are estimated according to 2.3 and 2.4. The resulting maps of horizontal and vertical forest structure are shown in Figures 2.6 and 2.7. Despite several local dissimilarities, the general spatial patterns for the three maps are similar. In terms of horizontal structure, the test site is quite homogeneous, apart from the central area with low and scattered vegetation. In terms of vertical structure, a gradient of increasing complexity from East to West is distinctly noticeable.

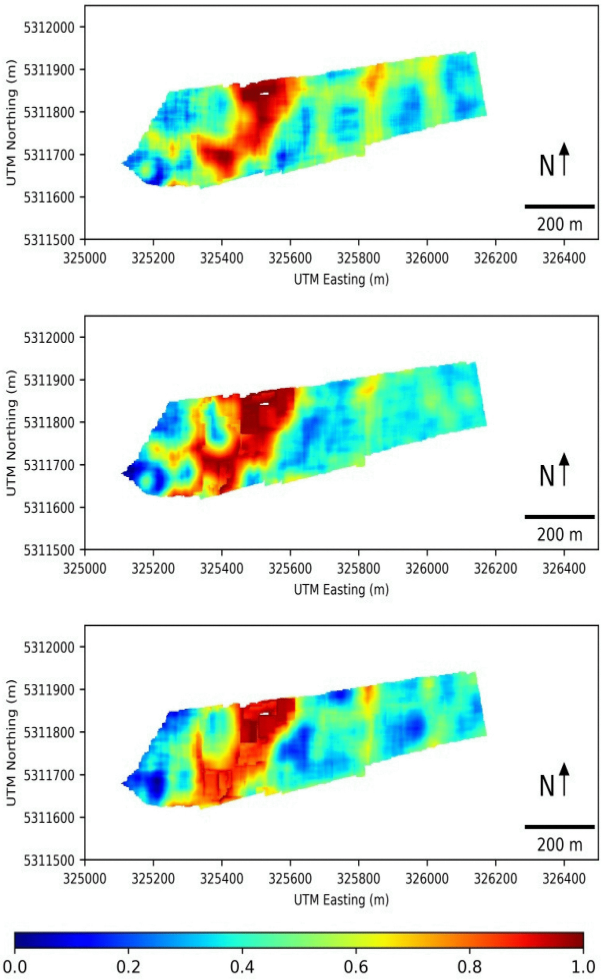

FIGURE 2.6: Maps of horizontal forest structure, as estimated from (top) field, (middle) Lidar and (bottom) TomoSAR data.

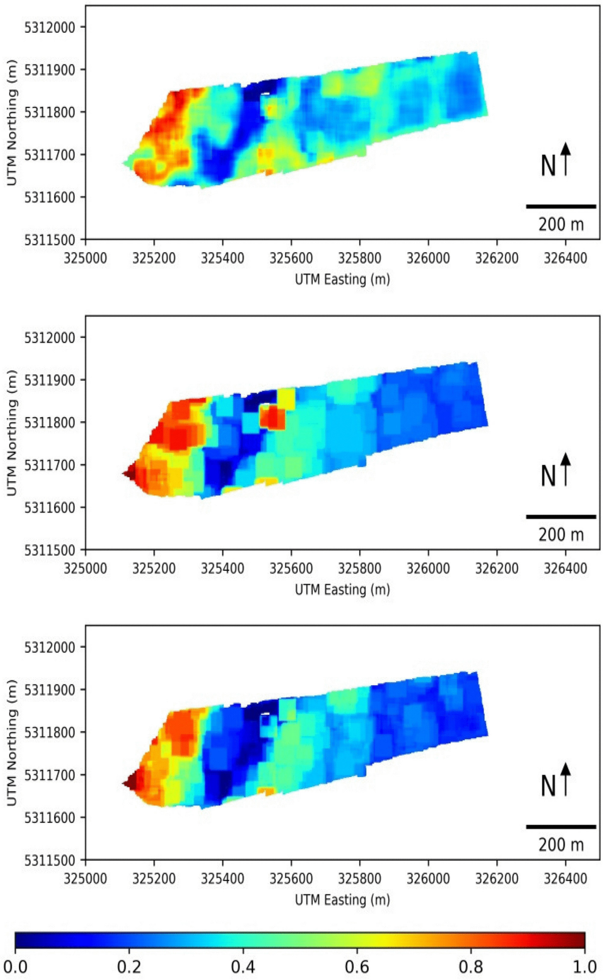

FIGURE 2.7: Maps of vertical forest structure, as estimated from (top) field, (middle) Lidar, and (bottom) TomoSAR data.

The discrepancies between the different maps are mainly due to differences in resolution and viewing geometries affecting in particular stand borders. Such an example is shown in Figure 2.8, which shows the area within the square indicated in Figure 2.4. When the vertical structure is estimated from field data, a local maximum can be observed in the map. When estimated from Lidar, this maximum is spread over a much larger area and when estimated from TomoSAR, no vertical structure maxima are retrieved in this point. According to field data, in this area, as shown in Figure 2.8, there are three isolated tall trees surrounded by very low vegetation. This should increase locally vertical structure, but the impact of these trees in the three maps appears to be very different. In the field data, in most of the sliding windows covering these trees, the number of tall trees is low with respect to the number of smaller trees. On the contrary, for the Lidar data, since big trees produce more returns than the smaller ones, their presence will be exaggerated and spread over the area of the structure window. Lastly, in the tomographic SAR reconstruction, the tall trees could not be detected (see Figure 2.8), essentially because of insufficient spatial resolution after multilook (6 x 6.6 m).

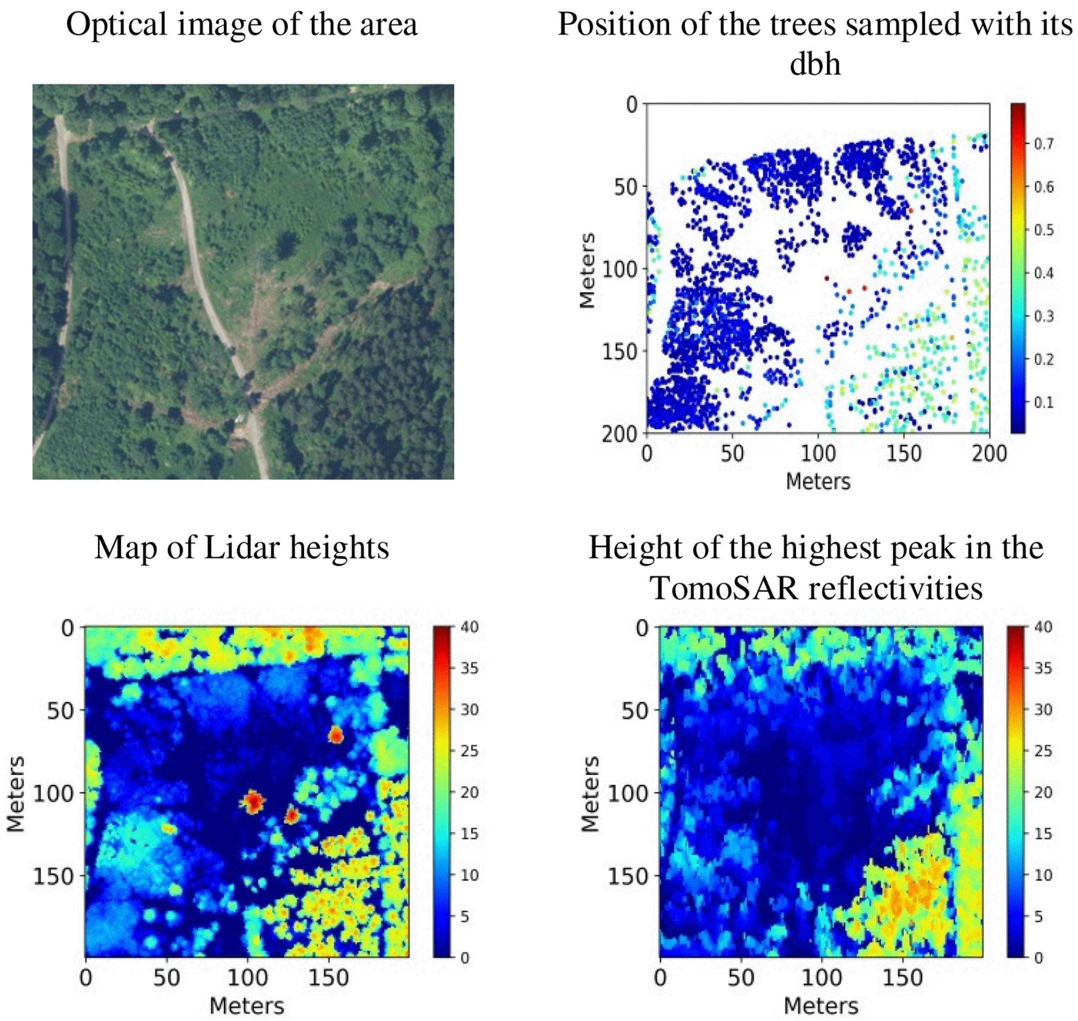
Optical image of the area

Position of the trees sampled with its dbh

Map of Lidar heights

Height of the highest peak in the TomoSAR reflectivities

FIGURE 2.8: Area in the white square in Figure 2.4.

The correlations between the different maps are shown in Figure 2.9. Correlations are slightly better for the horizontal than for the vertical structure estimators, which are reasonable because the vertical measure involves a second-order moment, whereas the horizontal one reflects first-order statistics. It can be observed from the maps and the correlation plots that across the site, structure types are unevenly distributed: Both for the horizontal and the vertical, most of the site exhibits similarly low values and very high values are concentrated in a small area. Also, especially for the vertical structure, transitions between areas with different structure are smoother than with Lidar and TomoSAR. In this sense, the higher sensitivity of the field data to vertical structure variations is due to the difference in accuracy of the measurements involved: Vertical structure estimated from field data according to 2.2 is sensitive to variations of dbh in the range of cms, whereas Lidar and especially TomoSAR are constrained by the vertical resolution of the system, which is on the order of several meters. Besides this, it can be observed that the structure estimated from Lidar shows a better correlation with the field data than the one estimated from TomoSAR for the horizontal dimension (r = 0.87 versus r = 0.83), but slightly worse for the vertical one (r = 0.75 versus r = 0.77).

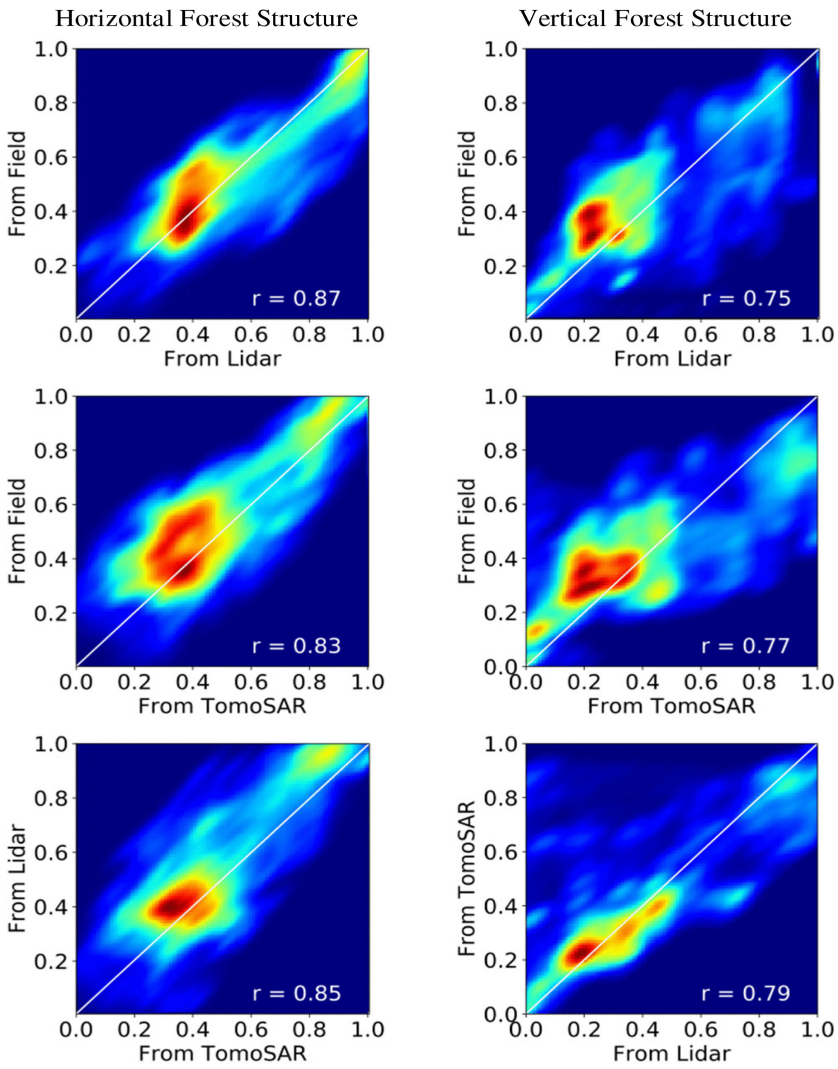

FIGURE 2.9: Correlations between horizontal (left column) and vertical (right column) forest structures as estimated from Field, Lidar, and TomoSAR data.

2.3.3 3-D Versus Height Only Forest Structure Estimation

In order to assess the advantages of employing tomographic SAR for forest structure estimation with respect to only height in the same conditions of spatial resolution, a simple test is carried out by estimating forest structure only taking into account the highest peak for each range and azimuth position instead of the complete vertical distribution of peaks. It is assumed here that the highest reflectivity peak is the closest one to the top of the canopy. Using the highest peaks only, horizontal and vertical structures can be estimated according to 2.3 and 2.4 following the same procedure as before. The maps of horizontal and vertical structure obtained are shown in Figure 2.10. A lower sensitivity when compared to the structures, estimated from the whole set of peaks (see Figures 2.6 and 2.7), can be observed essentially in the high vertical structure region, in the west part of the site. This is reflected as well in the correlation plots shown in Figure 2.11: Vertical structure is underestimated when considering only the highest peak and the underestimation is more important for higher structure values.

Four areas considered uniform in terms of structure according to field data and optical imagery available are defined. These four areas are shown in Figure 2.4 (top). From East to West, the area in the blue polygon is a monolayer dense stand. The orange polygon is of similar structure besides a few older trees to its western border increasing complexity. The green polygon is a very heterogeneous area with only a few scattered trees. Lastly, the red area comprises an older stand with a larger diversity in terms of trees dimensions and thus higher vertical structure.

Figure 2.12 shows the distribution of the indices in the HV plane for these four areas, considering the whole set of peaks and considering only the highest peak, at 50 x 50 m. When only the highest peak is considered, the reduction in sensitivity in the vertical dimension induces a vertical shrinkage of the signatures of the different areas, supporting the reduction of sensitivity to vertical structure observed from the maps in Figure 2.10 and the correlation plots in Figure 2.11.

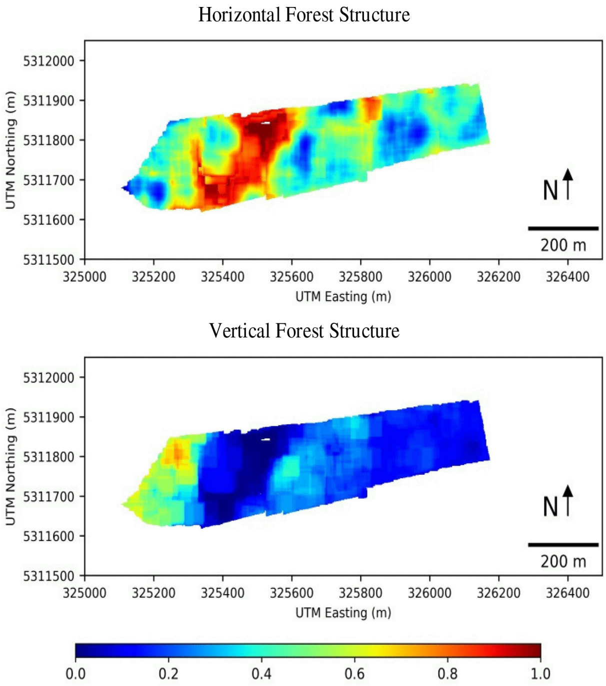

FIGURE 2.10: Maps of forest structure estimated from the highest peak of the reflectivity profiles. (Top) Horizontal and (bottom) vertical forest structure.

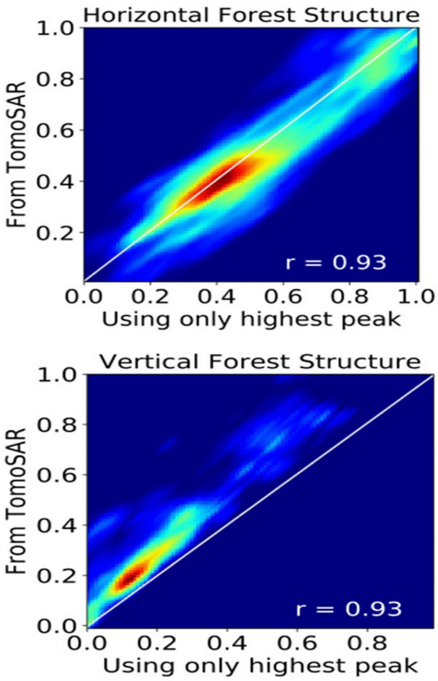

FIGURE 2.11: Correlations between the structures as estimated from the complete set of peaks of the TomoSAR reflectivity profiles and from only the highest one.

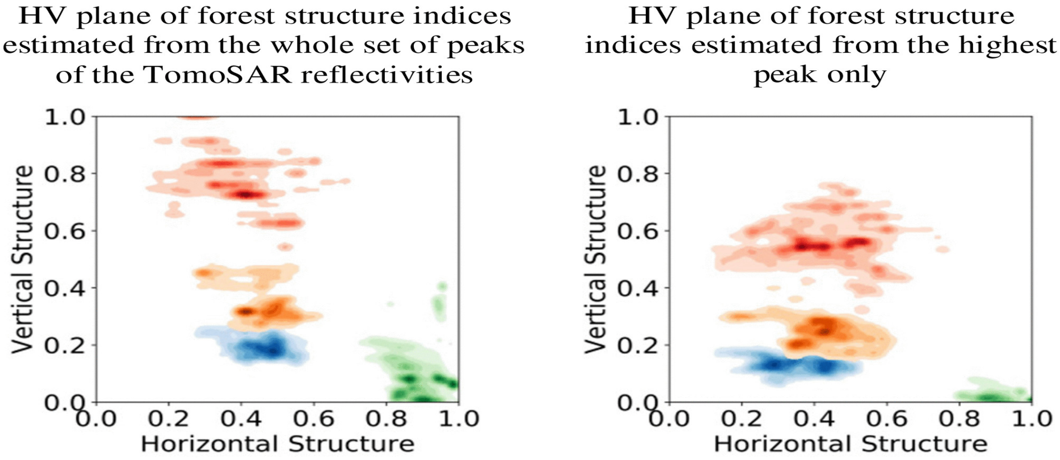

FIGURE 2.12: Signatures of the horizontal and vertical forest structure indices in the HV plane for four different polygons at different growth stages (young monolayer stand in blue, older mainly monolayer stand in orange, heterogeneous area with scattered trees in green, and multilayered stand in red), estimated using the whole set of peaks of the TomoSAR reflectivities (left) and using only the highest one (right), at 50 x 50 m.

2.3.4 Discussion on Scale

As already mentioned in Section 2.2.2.2, forest structure is inherently linked to scale and as a consequence the estimation of forest structure might vary with scale. Also, the measure of forest structure can be considered meaningful only within a range of scales. This range is bounded on the lower limit by the spatial variability of the scene and the spatial resolution of the sampling source. In fact, since the indices proposed rely on statistical measures, in order to ensure statistical significance, a minimum number of samples is required, both in terms of trees within the area considered and in terms of independent SAR observations. Too fine scales are not adequate to provide statistically significant values and, even within a uniform area, estimated forest structure may differ from sample to sample. On the other extreme, the upper limit of the valid scales is determined by the maximum correlation length of the stand. If the scales considered are larger than the size of the areas regarded as being uniform, the resulting estimates result from the mixing of diverse structures types and are therefore biased. Furthermore, besides the statistical considerations, ecological significance should also be accounted for. In that sense, it should be noted that the relations between forest species and 3-D vegetation structure may occur at spatial scales finer as 1 ha and therefore scales of 1 ha or finer are required for many ecological applications.

In order to illustrate the evolution of structure estimates across scales in the site considered, the indices of horizontal and vertical forest structure for the three sources available (field measurements, Lidar, and TomoSAR data) are estimated according to 2.1, 2.2, 2.3 and 2.4 at scales ranging from 25 x 25 m to 150 x 150 m. The distribution of the values of estimated forest structure in the HV plane for three different scales (25 x 25 m, 75 x 75 m, and 150 x 150 m) in the four areas regarded as uniform in terms of structure and defined in the previous section is shown in Figure 2.13.

Regardless of the source of data, it can be observed that at a scale of 25 x 25 m, the dispersion of values within polygons considered uniform in terms of structure is high. It can thus be deduced that especially in the red polygon with the highest vertical structure, cells of 25 x 25 m are too fine to sample its representative diversity. This large dispersion would hamper as well the classification of polygons, since the distribution of their values of horizontal and vertical structures appears close to each other or even overlapped in the HV plane. When the scale increases to 75 x 75 m, the dispersion of values within polygons is significantly reduced and the distributions for the different polygons drift apart from each other, favoring classification based on structure characterization. The standard deviation within the predefined polygons further decreases if the scale increases to 150 x 150 m, for the three sources of data. However, the four different signatures start to shrink again and become meaningfully less distinct. In fact, the elongated morphology of the test site considered in this paper together with its rapid spatial variability (see Figure 2.4) allows only a few windows larger than 1 ha still covering uniform trees distributions.

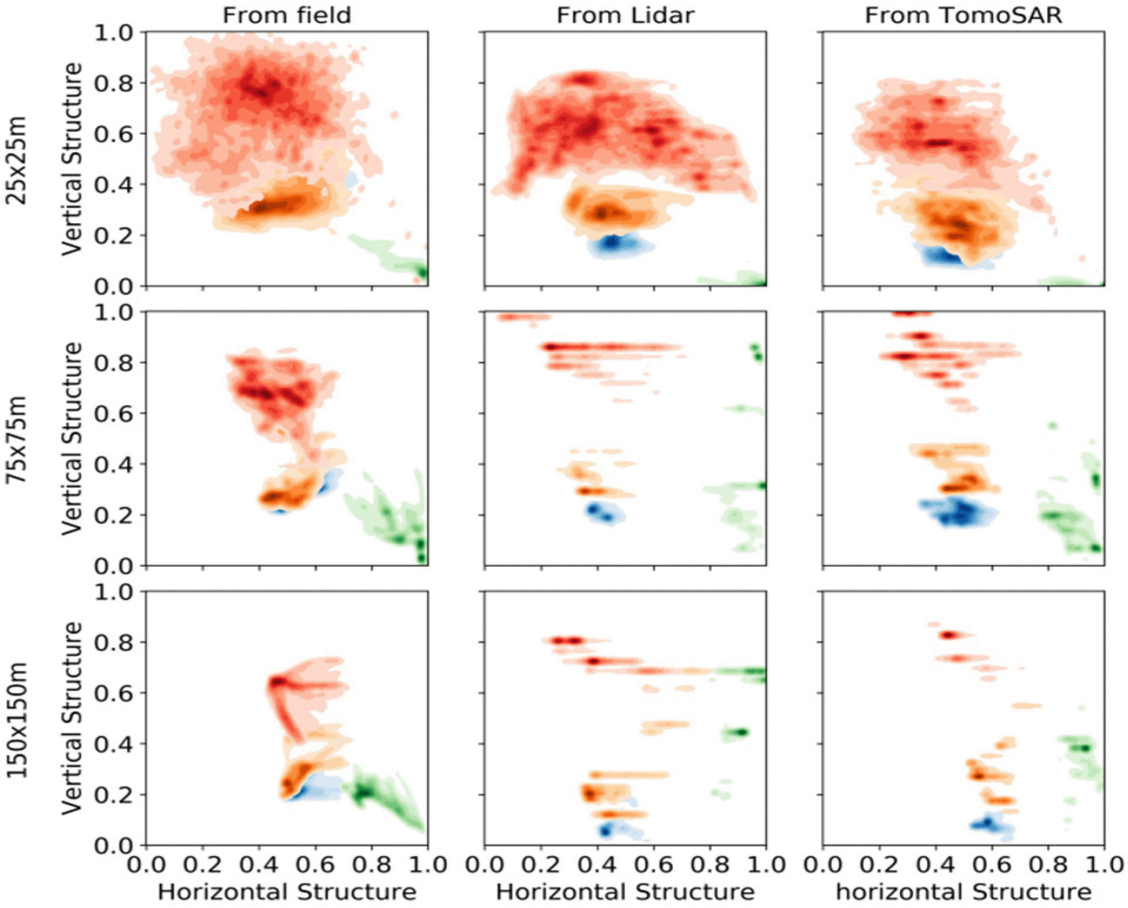

FIGURE 2.13: Signatures of the horizontal and vertical forest structure indices in the HV plane for four different polygons at different growth stages (young monolayer stand in blue, older mainly monolayer stand in orange, heterogeneous area with scattered trees in green and multilayered stand in red), as estimated from field, Lidar, and TomoSAR data, at three different scales.

2.4 Conclusions

A framework for qualitative and quantitative forest structure estimation from tomographic SAR measurements at L-band has been proposed. It is based on a pair of complementary indices for the characterization of horizontal and vertical structure. In order to ensure the physical interpretation and ecological relevance, the indices have been derived in correspondence to structure indices already established in forestry and ecology studies. The fact that the indices used in forestry and ecology are defined in terms of individual tree parameters while conventional SAR measurements are not able — in terms of spatial resolution — to distinguish single trees had to be accounted. A methodology to derive the two indices from 3-D radar reflectivity reconstructed by tomographic SAR techniques has been proposed and described step by step. The methodology relies on the evaluation of the location of the (local) maxima of the reconstructed vertical reflectivity profiles. The main reason for this is that the locations of the reflectivity maxima are less prone to variations induced by nonstructural effects as for example by changing seasonal and weather conditions than the reflectivity values itself.

The proposed methodology has been applied on airborne tomographic SAR data acquired at L-band over the temperate forest of Traunstein in Germany and validated against the structure indices obtained from airborne Lidar and field inventory data. The validation of the forest structure maps obtained from the radar data against the ones derived from the field inventory data revealed a meaningful correspondence. Reaching a good agreement between the maps generated from the two data sources is necessary to ensure the incorporation of the estimations generated by SAR systems in ecology studies, for example, through assimilation into existing models.

The framework as defined by the two indices allows:

1. the systematic interpretation of the 3-D radar reflectivity in terms of physical forest structure. This is not always an intuitive task because of the dependency of radar reflectivity on system parameters as well as on the geometric and dielectric properties of the forest;

2. the direct comparison of forest structure estimates from field inventory data to estimates derived from radar and even Lidar measurements.

Indeed, the proposed framework has proven to be suitable for Lidar measurements. The forest structure maps as estimated by means of radar and Lidar are comparable, despite the differences in resolution and acquisition geometry. This not only supports the significance of the proposed framework but also establishes a basis to combine the information provided by radar and Lidar.

It should be noted here that the quantitative characterization of forest structure by means of the proposed framework unavoidably incurs a loss of structure information, since a 3-D notion is projected into a 2-D space defined by the two indices, whose orthogonality is not guaranteed in any case (or scale). In this sense, further validation is necessary to entirely assess the limitations of the framework proposed when it comes to a complete representation of forest structure.

In order to assess the value added by the availability of full 3-D information when compared to the information provided by forest height alone, forest structure maps generated by accounting only the highest maximum of the reflectivity profiles have been generated. The considerable loss of sensitivity to vertical structure variations in these maps reinforces the importance of 3-D radar reflectivity estimates.

Finally, the evolution of the obtained forest structure estimates has been evaluated over a range of spatial scales. The main result was the understanding that the choice of scale has to be meaningful with respect to the structural complexity of the underlying stand or forest. For a complex highly heterogeneous stand, estimates at very fine scales (smaller than 25 x 25 m) are affected by a high dispersion. The dispersion decreases rapidly toward 50 x 50 m and beyond which is in agreement with the common understanding that the spatial distribution of trees at 0.5 to 1 ha scales renders a meaningful estimate of the complexity of a stand. The upper bound is given by the maximum scale at which the stand can still be considered uniform in terms of structure.

Further validation and possible refinements of the proposed methodology require sites and data with spatial and temporal diversity, i.e., a variety of forest scenarios with different characteristics and temporal variability. Regarding spatial variability, the proposed methodology has been already successfully validated in a number of tropical test sites in Gabon [36]. Temporal variability is important for assessing the sensitivity to temporal and spatial changes in forest structure and the robustness to nonstructural variations. In this context the proposed methodology has been tested on a time series of tomographic acquisitions conducted over temperate forests and proven to be robust enough to nonstructural variations and sensitive enough for tracking forest structure changes due to management practices [34].

2.5 Appendix. Principles of SAR Tomography and Compressive Sensing

Consider a tomographic acquisition composed by M (repeat-pass) tracks over the same scene. Given a range and azimuth coordinate, the SLC pixel amplitudes $y_m, m = 1, ..., M$ of a single-polarimetric channel can be arranged in a column vector y as follows:

$$y = [y_1, y_2, \ldots, y_M]^T . \tag{2.5}$$

In the multipolarimetric case, the same operation can be repeated for each one of the P available polarimetric channels ($P = 3$ for a fully polarimetric acquisition). Then, a PM-dimensional SLC data vector y_p is obtained by stacking the single-polarimetric data vectors one on top of the other.

Since each image is acquired from a slightly different angular position, a scatterer at a given height z introduces a phase difference among the acquisitions. The vertical sensitivity of the phase difference between two acquisitions is expressed by means of the vertical wavenumber defined as follows [37]:

$$k_z(m, n) = \frac{4\ \pi\ B_\perp}{\lambda\ r\ sin(\theta)} \tag{2.6}$$

where λ is the wavelength, r is the distance to the scatterer, θ is the incidence angle, and $B_\perp$ is the orthogonal distance between the tracks corresponding to the two acquisitions projected in the direction orthogonal to the line of sight. Let $k_{z\ max}$ be the wavenumber with maximum $B_\perp$, and $k_{z\ min}$ the one with minimum $B_\perp$. The value of $k_{z\ max}$ is related to the Rayleigh vertical resolution δ_z as [37]

$$\delta_z = \frac{2\pi}{k_{z\ max}} \tag{2.7}$$

which is conventionally used as a reference in SAR tomography. $k_{z\ min}$ gives the nonambiguous height interval h_{amb} as [37]

$$h_{amb} = \frac{2\pi}{k_{z\ min}} \tag{2.8}$$

In order to avoid ambiguities in the estimated vertical distribution of the backscattered power (reflectivity profile), h_{amb} should be higher than the maximum forest height of the scene.

The phase differences of each of the acquisitions are collected in the so-called z-dependent steering vector at a given height z defined as follows:

$$a(z) = [1, e^{jk_{z_2}z}, e^{jk_{z_3}z}, \cdots, e^{jk_{z_M}z}]^T \tag{2.9}$$

where k_{z_M} , $m = 1, ..., M$, is the vertical wavenumber for the mth acquisition with respect to the reference one, here placed in correspondence of the first image for which it results $k_{z_1} = 0$. In the multipolarimetric case, the $(PMxPM)$-dimensional covariance matrix R associated to y_p is as follows:

$$R = E\{y_p y_p^H\} \tag{2.10}$$

In 2.10, $E\{\cdot\}$ denotes the statistical expectation, and $(\cdot)^H$ the Hermitian (i.e., transpose conjugate) operator. It should be noted that the estimation of the expectation of a stochastic process requires several realizations of that process, which is generally not available in real datasets. Therefore, under the assumption of ergodicity, the statistical expectation in 2.10 is approximated by averaging neighboring pixels within a range-azimuth (multilook) cell.

Several (model-based and not) tomographic algorithms can be employed to estimate the reflectivity profiles using R and $a(z)$ [31], [38] on a set of heights $\{z_i\}_{i=1}^{H}$ within an interval of interest. In the general multipolarimetric case, it is of interest to estimate a set of (PxP)-dimensional polarimetric covariance matrices $\{T(z_i)\}_{i=1}^{H}$. Their P diagonal elements collected for the H heights form the reflectivity profiles in the P polarimetric channels. Different algorithms are characterized by different height resolution capabilities beyond the Rayleigh limit 2.7. However, the improvement in the achievable resolution can intrinsically reduce the radiometric accuracy, especially in the imaging of volume scatterers.

The estimation of the reflectivity profiles is based on the inversion of the Fourier relationship existing between them and the covariances in 2.10 [11], [37]. Following the derivation in [39], such relationship can be expressed by means of a linear system as follows:

$$R' = \phi T'. \tag{2.11}$$

In 2.11 R is (M^2xP^2)-dimensional matrix resulting from a proper permutation of the elements of the polarimetric-multibaseline covariance matrix 2.10: Each row represents for each of the M^2 interferometric pairs, the different P^2 polarization combinations, after ordering the elements of the (PxP)-dimensional polarimetric matrices as vectors. Further details on the permutation are given in [39]. ϕ is an (M^2xH)-dimensional matrix obtained by collecting the steering vectors 2.9 calculated for the H heights [39]. Finally, T' is an (HxP^2)-dimensional matrix that contains the elements of the unknown matrices $\{T(z_i)\}_{i=1}^{H}$ on each row [39]. Since in an usual tomographic configuration the number of acquisitions is limited, it results in $M^2 \ll H$. As a consequence, the linear system in 2.11 is highly underdetermined.

In order to estimate the vertical reflectivity profiles by solving the linear system in 2.11, in this paper we make use of an algorithm based on CS [40]. Essentially, the CS theory states that a signal can be reconstructed under the Nyquist sampling rate provided that it is sparse, meaning that it has a low number of nonzero coefficients, and the matrix ϕ fulfills the restricted isometry property [40]. Thus, a CS algorithm can cope with the underdetermination of the system 2.11 and can resolve scatterers at heights closer than the resolution limit in 2.7.

In general, the sparsity condition is too restrictive and most of the signals of interest do not fulfill it. However, the application of CS can be easily extended to compressible signals, which are signals that produce a sparse representation when projected in a fixed sparsifying basis.

Since some level of correlation is expected between adjacent rows in T' (i.e., consecutive heights), it is reasonable to assume that a sparse representation of T' may be obtained through a projection on a given basis. This has already been explored in [41], where it has been proven that the projection into an appropriate wavelet basis provides a sparse expansion of the reflectivity profiles in a forest scenario. Hence, by denoting with w the (HxH)-dimensional matrix of the wavelet projection, the vector of the sparse wavelet coefficients α results in the following:

$$\alpha = wT'. \tag{2.12}$$

With this, 2.11 can be rewritten as follows:

$$R' = \phi w^{-1}\alpha. \tag{2.13}$$

In this paper, we suggest to estimate α by solving 2.13 through a disciplined convex programming, which can be formalized by means of the following constrained minimization problem:

$$min\|\tilde{\alpha}\|_{2,1} \quad subject\ to \quad \|R' - \phi w^{-1}\tilde{\alpha}\|_F \leq \varepsilon \tag{2.14}$$

under the additional condition that every row of T' (i.e., each polarimetric covariance matrix) must be positive semidefinite. In 2.14, $\tilde{\alpha}$ are the estimated wavelet coefficients, ε is an upper bound for the error allowed in the estimation, $\|\cdot\|_{2,1}$ and $\|\cdot\|_F$ are a mixed (2,1) and a Frobenius norm, respectively. In the scope of this paper, the proposed approach has been implemented in Python and employs the CVXPY packages [42]. With the estimated coefficients $\tilde{\alpha}$ from 2.14, the estimated polarimetric covariance matrices $\tilde{T}$ and finally the reflectivity profiles can be obtained.

Acknowledgments

The authors would like to thank the Municipal Forest Administration of the City of Traunstein for making this project possible on their estate property and the F-SAR team for its invaluable effort during the data acquisition and processing. The Traunstein Forest Dynamics Plot is a collaborative project of the Chair for Forest Growth and Yield, Technische Universität München, the Department of Ecological Modelling at the Helmholtz Centre for Environmental Research UFZ, Leipzig, and the Microwaves and Radar Institute at the German Aerospace Center - DLR, Oberpfaffenhofen.

References

[1] M. Snyder, "What is forest stand structure and how is it measured?", *Northen Woodlands*, vol. 64, p. 15, 2010. [Online]. Available: `https://northernwoodlands.org/articles/article/what-is-forest-stand-structure-and-how-is-it-measured` (cited on page 24).

[2] T. A. Spies, "Forest structure: a key to the ecosystem", *Northwest Science*, vol. 72, no. 2, pp. 34–36, 1998. [Online]. Available: `http://andrewsforest.oregonstate.edu/pubs/pdf/pub2564.pdf` (cited on pages 24, 27).

[3] F. G. Hall, K. Bergen, J. B. Blair, R. Dubayah, R. Houghton, G. Hurtt, J. Kellndorfer, M. Lefsky, J. Ranson, S. Saatchi, H. Shugart, and D. Wickland, "Characterizing 3d vegetation structure from space: mission requirements", *Remote Sensing of Environment*, vol. 115, no. 11, pp. 2753–2775, 2011, DESDynI VEG-3D Special Issue, ISSN: 0034-4257. DOI: `10.1016/j.rse.2011.01.024` (cited on pages 24, 25).

[4] N. Brokaw and R. Lent, "Vertical structure. in 'maintaining biodiversity in forest ecosystems'", pp. 373–399, 1999. DOI: `10.1017/CBO9780511613029.013` (cited on pages 24, 27).

[5] C. McElhinny, P. Gibbons, C. Brack, and J. Bauhus, "Forest and woodland stand structural complexity: its definition and measurement", *Forest Ecology and Management*, vol. 218, no. 1, pp. 1–24, 2005. DOI: `10.1016/j.foreco.2005.08.034` (cited on pages 24, 26).

[6] F. J. Bohn and A. Huth, "The importance of forest structure to biodiversity–productivity relationships", *Royal Society open science*, vol. 4, no. 1, p. 160 521, 2017. DOI: `10.1098/rsos.160521` (cited on pages 24, 26).

[7] K. Bergen, S. Goetz, R. Dubayah, G. Henebry, C. Hunsaker, M. Imhoff, R. Nelson, G. Parker, and V. Radeloff, "Remote sensing of vegetation 3-D structure for biodiversity and habitat: review and implications for lidar and radar spaceborne missions", *Journal of Geophysical Research: Biogeosciences*, vol. 114, no. G2, 2009. DOI: `10.1029/2008JG000883` (cited on pages 24, 25).

[8] S. Goetz, D. Steinberg, R. Dubayah, and B. Blair, "Laser remote sensing of canopy habitat heterogeneity as a predictor of bird species richness in an eastern temperate forest, usa", *Remote Sensing of Environment*, vol. 108, no. 3, pp. 254–263, 2007. DOI: `10.1016/j.rse.2006.11.016` (cited on pages 24, 25).

[9] W. Turner, S. Spector, N. Gardiner, M. Fladeland, E. Sterling, and M. Steininger, "Remote sensing for biodiversity science and conservation", *Trends in ecology & evolution*, vol. 18, no. 6, pp. 306–314, 2003. DOI: `10.1016/S0169-5347(03)00070-3` (cited on pages 24, 25).

[10] S. Frolking, M. W. Palace, D. Clark, J. Q. Chambers, H. Shugart, and G. C. Hurtt, "Forest disturbance and recovery: a general review in the context of spaceborne remote sensing of impacts on aboveground biomass and canopy structure", *Journal of Geophysical Research: Biogeosciences*, vol. 114, no. G2, 2009. DOI: `10.1029/2008JG000911` (cited on pages 24, 25).

[11] S. Cloude and K. Papathanassiou, "Three-stage inversion process for polarimetric sar interferometry", *IEE Proceedings-Radar, Sonar and Navigation*, vol. 150, no. 3, pp. 125–134, 2003. DOI: `10.1049/ip-rsn:20030449` (cited on pages 25, 42).

[12] H. T. M. Dinh, S. Tebaldini, F. Rocca, C. Albinet, P. Borderies, T. Koleck, T. Le Toan, and L. Villard, "Tropiscat: multi-temporal multi-polarimetric tomographic imaging of tropical forest", in *2012 IEEE International Geoscience and Remote Sensing Symposium*, Jul. 2012, pp. 7051–7054. DOI: `10.1109/IGARSS.2012.6351947` (cited on page 25).

[13] M. Pardini, K. P. Papathanassiou, and F. Lombardini, "Impact of dielectric changes on L-band 3-D sar reflectivity profiles of forest volumes", *IEEE Transactions on Geoscience and Remote Sensing*, no. 99, pp. 1–14, 2018. DOI: `10.1109/TGRS.2018.2850357` (cited on pages 25, 29).

[14] T. Le Toan, S. Quegan, M. Davidson, H. Balzter, P. Paillou, K. Papathanassiou, S. Plummer, F. Rocca, S. Saatchi, H. Shugart, *et al.*, "The biomass mission: mapping global forest biomass to better understand the terrestrial carbon cycle", *Remote sensing of environment*, vol. 115, no. 11, pp. 2850–2860, 2011. DOI: `10.1016/j.rse.2011.03.020` (cited on page 25).

[15] A. Moreira, G. Krieger, I. Hajnsek, K. Papathanassiou, M. Younis, P. Lopez-Dekker, S. Huber, M. Villano, M. Pardini, M. Eineder, *et al.*, "Tandem-l: a highly innovative bistatic sar mission for global observation of dynamic processes on the earth's surface", *IEEE Geoscience and Remote Sensing Magazine*, vol. 3, no. 2, pp. 8–23, 2015. DOI: `10.1109/MGRS.2015.2437353` (cited on page 25).

[16] P. J. Clark and F. C. Evans, "Distance to nearest neighbor as a measure of spatial relationships in populations", *Ecology*, vol. 35, no. 4, pp. 445–453, 1954. DOI: `10.2307/1931034` (cited on page 26).

[17] F. Pastorella and A. Paletto, "Stand structure indices as tools to support forest management: an application in trentino forests (italy)", *Journal of Forest Science*, vol. 59, no. 4, pp. 159–168, 2013. DOI: `10.17221/75/2012-JFS` (cited on page 26).

[18] E. K. Zenner and D. E. Hibbs, "A new method for modeling the heterogeneity of forest structure", *Forest ecology and management*, vol. 129, no. 1-3, pp. 75–87, 2000. DOI: `10.1016/S0378-1127(99)00140-1` (cited on page 26).

[19] A. Pommerening, "Approaches to quantifying forest structures", *Forestry: An International Journal of Forest Research*, vol. 75, no. 3, pp. 305–324, 2002. DOI: `10.1093/forestry/75.3.305` (cited on page 26).

[20] H. Pretzsch, "Forest dynamics, growth, and yield", in *Forest Dynamics, Growth and Yield*, Springer, 2009, pp. 1–39. DOI: `10.1007/978-3-540-88307-4_1` (cited on page 26).

[21] M. Del Rio, H. Pretzsch, I. Alberdi, K. Bielak, F. Bravo, A. Brunner, S. Condes, M. J. Ducey, T. Fonseca, N. von Lupke, *et al.*, "Characterization of the structure, dynamics, and productivity of mixed-species stands: review and perspectives", *European journal of forest research*, vol. 135, no. 1, pp. 23–49, 2016. DOI: `10.1007/s10342-015-0927-6` (cited on page 26).

[22] C. D. Oliver, B. C. Larson, and C. Oliver, *Forest stand dynamics*. Wiley New York, 1996, ISBN: 9780471138334 (cited on page 26).

[23] L. H. Reineke, "Perfecting a stand-density index for even-aged forests", 1933. [Online]. Available: `https://naldc.nal.usda.gov/download/IND43968212/PDF` (cited on page 26).

[24] R. O. Curtis and D. D. Marshall, "Why quadratic mean diameter?", *Western Journal of Applied Forestry*, vol. 15, no. 3, pp. 137–139, Jul. 2000, ISSN: 0885-6095. DOI: `10.1093/wjaf/15.3.137` (cited on page 26).

[25] H. Pretzsch and P. Biber, "A re-evaluation of reineke's rule and stand density index", *Forest Science*, vol. 51, no. 4, pp. 304–320, Aug. 2005, ISSN: 0015-749X. DOI: `10.1093/forestscience/51.4.304` (cited on page 26).

[26] J. Liang, J. Buongiorno, R. A. Monserud, E. L. Kruger, and M. Zhou, "Effects of diversity of tree species and size on forest basal area growth, recruitment, and mortality", *Forest Ecology and Management*, vol. 243, no. 1, pp. 116–127, 2007. DOI: `10.1016/j.foreco.2007.02.028` (cited on page 26).

[27] I. Barbeito, I. Cañellas, and F. Montes, "Evaluating the behaviour of vertical structure indices in scots pine forests", *Annals of Forest Science*, vol. 66, no. 7, pp. 1–10, 2009. DOI: `10.1051/forest/2009056` (cited on page 26).

[28] M. Brolly and I. H. Woodhouse, "Vertical backscatter profile of forests predicted by a macroecological plant model", *International journal of remote sensing*, vol. 34, no. 4, pp. 1026–1040, 2013. DOI: `10.1080/01431161.2012.715777` (cited on page 29).

[29] L. Thirion, E. Colin, and C. Dahon, "Capabilities of a forest coherent scattering model applied to radiometry, interferometry, and polarimetry at P-and L-band", *IEEE Transactions on Geoscience and Remote Sensing*, vol. 44, no. 4, pp. 849–862, 2006. DOI: `10.1109/TGRS.2005.862523` (cited on page 29).

[30] Y.-C. Lin and K. Sarabandi, "A monte carlo coherent scattering model for forest canopies using fractal-generated trees", *IEEE Transactions on Geoscience and Remote Sensing*, vol. 37, no. 1, pp. 440–451, 1999. DOI: `10.1109/36.739083` (cited on page 29).

[31] O. Frey and E. Meier, "Analyzing tomographic sar data of a forest with respect to frequency, polarization, and focusing technique", *IEEE Transactions on Geoscience and Remote Sensing*, vol. 49, no. 10, pp. 3648–3659, 2011. DOI: `10.1109/TGRS.2011.2125972` (cited on pages 29, 42).

[32] V. Cazcarra-Bes, M. Tello-Alonso, M. Pardini, and K. P. Papathanassiou, "Assessment of tomographic sar processing techniques for forest structure estimation", in *EUSAR 2018; 12th European Conference on Synthetic Aperture Radar*, ISBN: 9783800746361, VDE, 2018, pp. 1–6 (cited on page 29).

[33] E. Assmann and P. Davis, *The Principles of Forest Yield Study: Studies in the Organic Production, Structure, Increment and Yield of Forest Stands*. Elsevier Science, 2013, ISBN: 9781483150932 (cited on page 29).

[34] V. Cazcarra-Bes, M. Tello-Alonso, R. Fischer, M. Heym, and K. Papathanassiou, "Monitoring of forest structure dynamics by means of L-band sar tomography", *Remote Sensing*, vol. 9, no. 12, p. 1229, 2017. DOI: `10.3390/rs9121229` (cited on pages 30, 40).

[35] R. Horn, A. Nottensteiner, A. Reigber, J. Fischer, and R. Scheiber, "F-sar—dlr's new multifrequency polarimetric airborne sar", in *Geoscience and Remote Sensing Symposium, 2009 IEEE International, IGARSS 2009*, IEEE, vol. 2, 2009, pp. II–902. DOI: `10.1109/IGARSS.2009.5418244` (cited on page 31).

[36] M. Pardini, M. Tello, V. Cazcarra-Bes, K. P. Papathanassiou, and I. Hajnsek, "L-and P-band 3-D sar reflectivity profiles versus lidar waveforms: the afrisar case", *IEEE Journal of Selected Topics in Applied Earth Observations and Remote Sensing*, no. 99, pp. 1–16, 2018. DOI: `10.1109/JSTARS.2018.2847033` (cited on page 40).

[37] A. Reigber and A. Moreira, "First demonstration of airborne sar tomography using multibaseline L-band data", *IEEE Transactions on Geoscience and Remote Sensing*, vol. 38, no. 5, pp. 2142–2152, 2000. DOI: `10.1109/36.868873` (cited on pages 41, 42).

[38] S. Tebaldini, "Single and multipolarimetric sar tomography of forested areas: a parametric approach", *IEEE Transactions on Geoscience and Remote Sensing*, vol. 48, no. 5, pp. 2375–2387, 2010. DOI: `10.1109/TGRS.2009.2037748` (cited on page 42).

[39] E. Aguilera, M. Nannini, and A. Reigber, "A data-adaptive compressed sensing approach to polarimetric sar tomography of forested areas", *IEEE Geoscience and Remote Sensing Letters*, vol. 10, no. 3, pp. 543–547, 2013. DOI: `10.1109/LGRS.2012.2212693` (cited on page 42).

[40] E. J. Candes, J. Romberg, and T. Tao, “Robust uncertainty principles: exact signal reconstruction from highly incomplete frequency information”, *IEEE Transactions on Information Theory*, vol. 52, no. 2, pp. 489–509, Feb. 2006, ISSN: 0018-9448. DOI: `10.1109/TIT.2005.862083` (cited on page 42).

[41] E. Aguilera, M. Nannini, and A. Reigber, “Wavelet-based compressed sensing for sar tomography of forested areas”, *IEEE Transactions on Geoscience and Remote Sensing*, vol. 51, no. 12, pp. 5283–5295, 2013. DOI: `10.1109/TGRS.2012.2231081` (cited on page 42).

[42] S. Diamond and S. Boyd, “Cvxpy: a python-embedded modeling language for convex optimization”, *The Journal of Machine Learning Research*, vol. 17, no. 1, pp. 2909–2913, 2016. [Online]. Available: `http://jmlr.org/papers/v17/15-408.html` (cited on page 43).

Chapter 3

Monitoring of Forest Structure Dynamics by Means of L-Band SAR Tomography

V. Cazcarra-Bes, M. Tello-Alonso, R. Fischer, M. Heym and K. P. Papathanassiou

Remote Sensing
Published in November 2017. DOI: 10.3390/rs9121229

Key findings/points:

- Validation of the forest structure framework for TomoSAR with realistic simulated forests.
- Qualitative classification of different ecological forest structure types.
- Quantitative and qualitative monitoring of forest structure changes using three TomoSAR data sets (2008,2012,2016) on a Temperate forest in Germany.

The author's contributions:

- Development and implementation of the tomographic algorithm, as well as of the forest structure algorithms.
- Interpretation of the results and main writing of the manuscript.

The co-author's contributions:

- M. Tello-Alonso contributed in the initial steps with ideas, helped on the interpretation of the results, and she supervised the whole work.
- R. Fischer provided the FORMIND simulations, contributed to Section 3.3.1 and helped in the interpretation of the results.
- M. Heym provided the ground data and contributed to Section 3.4.1 and Section 3.4.3 as well as in the interpretation of the results.
- K. P. Papathanassiou contributed to the main ideas and revised the work.

Monitoring of Forest Structure Dynamics by Means of L-Band SAR Tomography

V. Cazcarra-Bes[1,2], M. Tello-Alonso[2], R. Fischer[3], M. Heym[4] and K. Papathanassiou[2]

[1]Institute of Environmental Engineering, ETH Zürich, 8093 Zürich, Switzerland
[2]Microwaves and Radar Institute, German Aerospace Center (DLR), 82234 Wessling, Germany
[3]Department of Ecological Modelling, Helmholtz Centre for Environmental Research UFZ, Permoserstr. 15, 04318 Leipzig, Germany
[4]Faculty of Forest Science and Resource Management, Technical University of Munich, Hans-Carl-v.-Carlowitz-Platz 2, 85354 Freising, Germany

Abstract

Synthetic Aperture Radar Tomography (TomoSAR) allows the reconstruction of the 3D reflectivity of natural volume scatterers such as forests, thus providing an opportunity to infer structure information in 3D. In this paper, the potential of TomoSAR data at L-band to monitor temporal variations of forest structure is addressed using simulated and experimental datasets. First, 3D reflectivity profiles were extracted by means of TomoSAR reconstruction based on a Compressive Sensing (CS) approach. Next, two complementary indices for the description of horizontal and vertical forest structure were defined and estimated by means of the distribution of local maxima of the reconstructed reflectivity profiles. To assess the sensitivity and consistency of the proposed methodology, variations of these indices for different types of forest changes in simulated as well as in real scenarios were analyzed and assessed against different sources of reference data: airborne Lidar measurements, high resolution optical images, and forest inventory data. The forest structure maps obtained indicated the potential to distinguish between different forest stages and the identification of different types of forest structure changes induced by logging, natural disturbance, or forest management.

3.1 Introduction

Forests are three-dimensional (3-D) ecosystems whose 3D structure is strongly affected by dynamic processes such as growth, regeneration, decay and disturbance, and thus closely related to their history, diversity, function, microclimate and yield [1]. Accordingly, 3-D forest structure information is important for understanding and modelling the succession, function and development of forest ecosystems, and provides insight into ecological processes and forest dynamics. At the same time, forest structure information is essential for the development of accurate forest biomass estimators that are required to better understand and quantify the contribution of forest ecosystems to the global carbon cycle [2]–[4].

Forest structure monitoring has traditionally been performed by inventory measurements that provide accurate estimates of a number of (single) trees and stand parameters. However, inventory measurements are demanding in time and resources so that they are usually performed at smaller scales with rather low update rates. Given this, spaceborne Synthetic Aperture Radar (SAR) imaging configurations provide continuous forest mapping with global coverage at spatial and temporal resolutions relevant to the detection of changes on the forests. This, combined with the fact that radar signals—especially at lower frequencies—penetrate even dense forest canopies interacting with forest structure components at different heights, make SAR an important element in the context of global forest monitoring.

Indeed, in the last few years, a significant effort has been made to demonstrate and validate the potential of conventional SAR configurations to reflect spatial biomass distribution by means of SAR measurements [5]. The introduction of SAR interferometry was a critical step, as interferometric measurements have an increased sensitivity to vertical structure elements of forest. Indeed, the use of polarimetric interferometric measurements has allowed the model based estimation of vertical forest structure parameters such as forest height [6]–[9]. In order to reconstruct more detailed vertical distribution of scatterers, multi-baseline interferometric acquisitions have been used [10]. More recently, tomographic acquisitions (TomoSAR), that can be seen as an extension of multi-baseline interferometric acquisitions, have been used to reconstruct the 3-D radar reflectivity of forests, to explore for mapping 3-D forest structure, and to improve biomass estimators [11]–[16]. These activities were complemented by a number of ground-based [17]–[20] and airborne SAR experiments [21] aiming to quantify the impact of temporal decorrelation on the effect of weather and seasonal conditions on a temporal series of TomoSAR data rather than to analyse forest structure dynamics [22]–[24]. The promising results achieved initiated the implementation of TomoSAR acquisition modes in future spaceborne SAR missions, such as Biomass [25] or Tandem-L [26], for mapping at a global scale structural forest parameters and improving biomass estimations.

With respect to forest structure mapping, SAR configurations have a number of advantages when compared to other remote sensing techniques. Compared to optical and hyperspectral imaging configurations, SAR measurements provide significantly higher sensitivity to the vertical arrangement of forest elements due to the ability to penetrate through the vegetation layer and interact with forest structure components at different heights. Compared to Lidar configurations that allow accurate measurements of vertical forest structure, SAR configurations have the advantage of a higher penetration ability through clouds and into/through vegetation as well as in the realization of wide imaging swaths that allows large and global scale coverage at high temporal resolutions.

Motivated by this, this paper explores the potential of L-band TomoSAR data to monitor forest structure changes as induced by natural or anthropogenic disturbances such as logging, fire and forest management. To do this, a methodology for characterising physical forest structure by means of two descriptors that can be derived from TomoSAR data at L-band was used. First, a set of simulated data from a process-based forest model was used to demonstrate the concept of the proposed methodology. In a second step, real experimental datasets acquired over a temperate forest in the south of Germany were employed to test the robustness and consistency of the forest structure estimation methodology with respect to non-structural temporal changes in the forest, together with its sensitivity to structural variations. For the validation of the achieved results, different sources of reference data, including optical data, airborne Lidar measurements and forest inventory data, were used.

3.2 From Tomographic SAR Measurements to Forest Structure Estimation

Section 3.2.1 summarizes the principles of TomoSAR imaging for extracting vertical reflectivity profiles from a set of images [10]. Section 3.2.2 describes the link between the extracted vertical reflectivity profiles and physical forest structure.

3.2.1 Tomographic SAR Imaging

Provided that the frequency band employed is low enough to penetrate the canopy, multiple SAR acquisitions over the same area with a slightly different incidence angle can allow a 3-D reconstruction of the forest reflectivity at a given frequency and polarization. In the following, we refer to the resolution of the SAR images as SLC (single look complex) resolution in range and azimuth.

In particular, the set of M SAR images define vector $\boldsymbol{y}$:

$$\boldsymbol{y} = \left[y_1, y_2, \ldots, y_m \right]. \tag{3.1}$$

A scatterer at a given height z_0 introduces a phase difference in the set of interferometric pairs of the images in $\boldsymbol{y}$. These phase differences define the so called steering vector at a given height z_0 as:

$$a\left(z_0\right) = \left[1, e^{jk_{z1}z_0},\ e^{jk_{z2}z_0},\ \ldots, e^{jk_{zn}z_0}\right], \tag{3.2}$$

where k_{zi} is the vertical wavenumber for the ith pair of images and is defined as follows:

$$k_{zi} = -\frac{4\pi B_{\perp i}}{\lambda\ r\ \sin\left(\theta\right)}, \tag{3.3}$$

where λ is the wavelength; r is the distance to the scatterer; θ is the incidence angle; and $B_{\perp i}$ is the orthogonal distance between two acquisitions. The maximum value of k_{zi} gives the theoretical vertical resolution, while the minimum gives the non-ambiguous height interval [10].

From Equation 3.1, the multi-image covariance matrix R can be defined as:

$$R = \mathrm{E}\left\{\boldsymbol{y}\boldsymbol{y}^H\right\} \tag{3.4}$$

where $\mathrm{E}\left\{\right\}$ denotes the expectation; and $\left(\ \right)^H$ the Hermitian or transpose conjugate operator. It should be noted that the estimation of the expectation of a stochastic process requires several realizations of that process, which is generally not available in real datasets. Therefore, the process is assumed to be ergodic and $\mathrm{E}\left\{\right\}$ is approximated by spatial averaging. This spatial average or multilook operation degrades the SLC resolution. We will refer to tomographic resolution to the one achieved after multilook.

From the steering vector defined in Equation 3.2, the steering matrix ϕ is defined as:

$$\phi = a_z a_z^H\ . \tag{3.5}$$

Then, with Equations 3.4 and 3.5, the TomoSAR inversion problem can be expressed as [10], [27]:

$$R = \phi T, \tag{3.6}$$

where T is the reflectivity matrix whose number of rows equals the number of elements in height, and its number of columns is the number of available polarimetric channels. Since the number of measurements is usually lower than the number of scattering elements along the height, the system in Equation 3.6 is underdetermined. Several tomographic algorithms, parametric or non-parametric, can be applied to solve it and estimate the 3-D radar reflectivity. Among the non-parametric algorithms, Fourier beamforming is coherent, energy preserving, and does not require any a priori assumptions. However, it achieves limited vertical resolution and is prone to ambiguities if the number of baselines is low and/or they are irregularly distributed. With better vertical resolution capabilities, Capon beamforming is currently the standard algorithm most widely employed in the tomographic SAR community [28]–[30]. Aiming to achieve finer vertical resolutions, algorithms based on Compressive Sensing (CS) techniques have been proposed to solve the underdetermined system in Equation 3.6, and have been successfully applied to urban [31], [32] and forest scenarios [33].

It should be noted that different inversion algorithms lead to different reconstructed reflectivity profiles. Therefore, the ability to reflect forest structure variability is may be affected by the technique employed in the inversion [34]. In this paper, vertical reflectivity profiles were obtained through an algorithm based on CS [27], i.e., Equation 3.6 was solved by convex optimization as:

$$min||\alpha||_{2,1}\ \ s.t.\ \left\{\begin{array}{l} R = \ \phi W^{-1}\alpha \\ T_n\ is\ SDP\ \forall n \end{array}\right. , \tag{3.7}$$

where $T = \ W^{-1}\alpha$, W is a wavelet projection matrix; α are the wavelet coefficients $||\ ||_{2,1}$ stands for the mixed $l_{2,1}$ norm; and SDP indicates semi-definite positiveness. With this, matrix T contains for every pixel in range and azimuth a reflectivity profile representing the distribution of scatters along height.

3.2.2 Forest Structure Estimation

In the following, 3-D forest structure is understood as the vertical and horizontal arrangement of trees and/or tree elements in space. It is a critical parameter in forest ecology inherently related to ecological processes, forest stand dynamics and forest management practices [35], [36]. Furthermore, it is an indicator of biodiversity, disturbance, growth and yield [1]. Despite the difficulties in finding an appropriate characterization for forest structure for a wide range of applications, spatial scales and forest types, it is commonly assumed that two essential aspects of forest structure are the heterogeneity in the position and size of the trees within a stand. Based on this, a systematic framework for the discrimination of ecologically significant structure classes has recently been suggested [37], [38], which proposes two complementary measures: one for the horizontal, and one for the vertical structure. In the literature, different measures have been proposed for the estimation of horizontal and vertical forest structure from field data [39]–[44]. In the following the horizontal structure HS_{field} as the standard density index from [44] is used:

$$HS_{field} = N \left(\frac{25}{dg} \right)^{-1.605}, \tag{3.8}$$

where N is the number of trees per hectare; and dg is the mean diameter at breast height. Regarding the estimation of vertical structure VS_{field}, the standard deviation of individual tree heights H_i is used:

$$VS_{field} = std\left(H_i\right). \tag{3.9}$$

Essentially, the horizontal structure index mainly reflects the density of the tallest trees in the unit area considered, while the vertical structure index accounts for the diversity of tree heights. Therefore, according to its structural complexity, a forest stand can be classified in a horizontal/vertical plane (HV plane in the following) as shown in Figure 3.1.

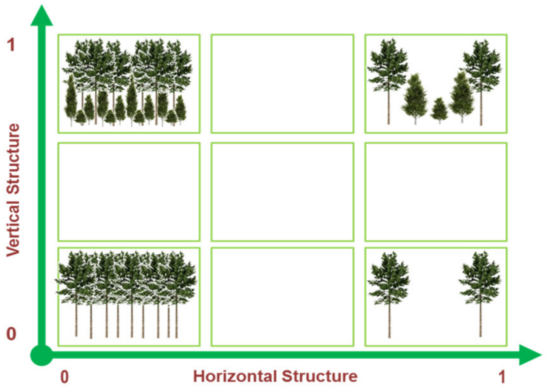

FIGURE 3.1: Horizontal/vertical structure plane proposed for forest structure classification.

Particular airborne SAR techniques such as multi-aspect TomoSAR [45] or holographic SAR [46] can reach higher resolutions and allow the estimation of individual tree profiles. However, this paper is focused on conventional spaceborne acquisitions at low frequencies. In this case, the achievable resolutions do not allow discriminating between individual trees and extracting single-tree parameters. Therefore, any individual-based measure such as HS_{field} and VS_{field} in Equations 3.8 and 3.9, cannot be directly estimated from the SAR data used in this paper and instead, indirect correspondences need to be explored to reflect forest structure. In this sense, the presence of a group of trees of similar height is reflected in the reflectivity profiles as a number of peaks (i.e., the maxima of the reconstructed vertical reflectivity profiles) in the range of heights occupied by the canopy [47]. Accordingly, the characterization of forest structure by means of the 3-D distribution of peaks in a statistical way appears sensible [34]. Following the characterization of structure from the field data, two complementary indices of structure were estimated from the 3-D distribution of reflectivity peaks, one for the horizontal and one for the vertical structure.

Therefore, as a first step, the peaks for every reflectivity profile in the range and azimuth were extracted from the radar reflectivity representing the distribution of scatters along height T. Then, a three-dimensional (range, azimuth, height) matrix B is the defined with ones at the position of every peak. From this matrix, the horizontal and vertical indicators were estimated.

The horizontal structure descriptor HS is related to the density of peaks in the upper layer of the forest for a given unit structure window. This upper layer was defined as the range of heights from H_{limit} to H_{max}, where H_{max} is defined as the height of the highest peak and H_{limit} is equal to 0.6 H_{max} or 5 m, when 60% of the maximum height was lower than 5. As an example, Figure 3.2 shows the peaks obtained from the reflectivity profile and the green dots represent the peaks in the top layer. The horizontal descriptor was then estimated for every pixel i, j in the image as the total number of peaks in the upper layer in the unit window centered on that pixel, divided by the area of this unit window:

$$HS_{i,j} = \frac{\sum_{i=0}^{n} \sum_{j=0}^{n} \sum_{k=H_{limit}}^{H_{max}} B_{i,j,k}}{A}, \tag{3.10}$$

where n represents the size of the unit structure window (50 m × 50 m); the sub-index k represents the height dimension; and A is the area in square meters of the unit structure window. It is worth mentioning that independent of the resolution of the SLC images, the peaks of matrix B were projected in a grid of 1 m × 1 m before counting the number of peaks in the unit structure window. This allows us to normalize the number of peaks when systems at different resolutions were employed.

Once the horizontal descriptor is computed for every pixel in the image, HS for the whole image is normalized as:

$$HS_{norm} = 1 - \frac{HS}{\max\left(HS\right)}, \tag{3.11}$$

where $\max\left(HS\right)$ represents the maximum in the image, or in the set of images to be compared.

Regarding the vertical structure descriptor VS, a mask of 5 m (empirically set) was first applied to avoid peaks produced by the ground (red peak in Figure 3.2). Then, the vertical descriptor is defined for every pixel i, j in the image as:

$$VS_{i,j} = \sum_{r=1}^{R} \left(S_i - \overline{S}\right)^2, \tag{3.12}$$

where S is a vector with the heights at which at least one peak is found in the unit structure window; R is the length of S; and $\overline{S}$ represents the mean of vector S. For example, if in a given area the heights in meters of the peaks are $[30, 25, 25, 10, 10, 10, 8, 2]$ then $S = [30, 25, 10, 8]$ and $R = 4$. Finally, the vertical descriptor is normalized by its maximum within the image (or within the set of images that are going to be compared). It is worth mentioning that since the vertical structure index is reflected by the dispersion of the heights of the peaks, it is not significantly affected by changes in the vertical resolution of the system employed. It should be mentioned that similar measures can be found in the literature for waveform Lidar [48], [49].

Furthermore, it is important to note here that system and, even more so, seasonal or environmental variability of the forest may affect the tomographic reflectivity and impact the estimation of structure indices. However, the location of the reflectivity peaks appears to be significantly more robust against system and environmental variability than other profile parameters [37]. This is the reason why the estimation of the structure indices relies only on the position of the peaks and ignores absolute or even relative intensity information.

The main steps to obtain the horizontal and vertical forest structure descriptors using multi-baseline SAR measurements are shown in Figure 3.2.

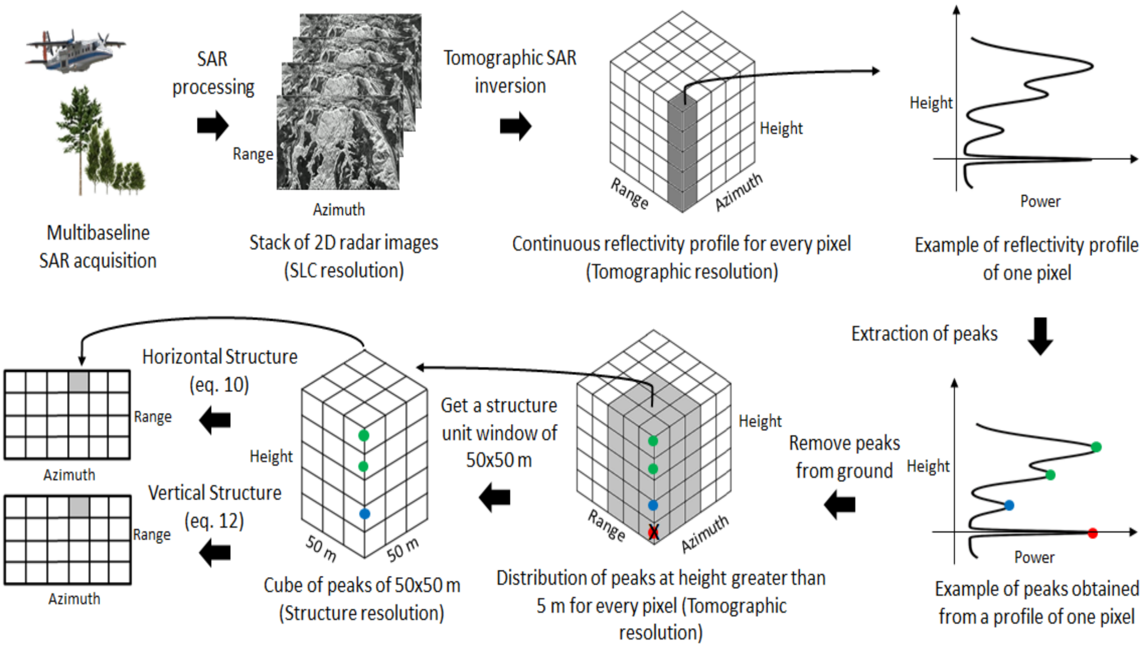

FIGURE 3.2: Steps to estimate forest structure using multibaseline Synthetic Aperture Radar (SAR) measurements.

3.3 Simulated Data

The proposed methodology was first applied on a set of simulated data. The data were generated in two steps. First, an individual-based forest model was used to generate the distribution of trees within stands for different forest conditions. Second, the multi-image covariance matrix was estimated for a set of vertical wavenumbers at a given spatial resolution. Both steps are described below.

3.3.1 The Forest Model

Forest-gap models are well-established tools used to investigate forest dynamics, and are able to account for processes such as growth, mortality and regeneration on the tree level, and thus able to simulate a wide range of different forest structure types [50], [51]. In this study, FORMIND, an individual and process-based forest gap model designed especially for tropical and temperate forests was used. A detailed description of the model can be found in [52], [53] where an African tropical forest parametrization was used for forest succession over 500 years on a scale of 100 hectares [54]. The advantage of employing complex tropical forest scenes in simulations is that they show higher complexity, mainly in the vertical structure, which allows for a better assessment of the effect of the different processes.

Six different scenarios were simulated and investigated. For each of them, FORMIND generated the full tree list including position, stem diameter and height for each individual tree. The normalized distribution of tree heights for each of the six scenarios is shown in Figure 3.3.

The first three scenarios represent three different stages from the long term forest evolution:

- The young forest represents an undisturbed early-succession forest at an age of 50 years (see Figure 3.4a). The majority of trees have heights between 10–18 m. The sharp mode at the height of 18 m is partly due to the fixed height-to-stem diameter relationship used by the forest model.

- The mature forest corresponds to an undisturbed old growth forest in a mature state that has reached 500 years of simulation time (see Figure 3.4b). The higher spread of the forest height distribution (see Figure 3.3a) reflects the higher structural heterogeneity when compared to the young forest.

- The forest after a fire event represents a forest 10 years after a fire event (which occurred in the year 490). For each tree, a (fire) survival rate is estimated depending on tree size and species-specific fire tolerance [52], which leads to a very heterogeneous forest landscape after the fire that consists of disturbed and undisturbed forest patches (see Figure 3.4c). The tree height distribution is now less uniform (see Figure 3.3a), and the number of tall trees is very low with respect to the number of trees below 20 m, as only a few old trees survived the fire. Moreover, in the 10 years after the fire, a dense homogeneous layer of young trees of around 15 m tall has grown beneath.

The latter three scenarios represent three different disturbance types of the mature forest:

- *Logging 1* corresponds to firewood removal or "thinning from below": all trees below 20 m are logged (see Figure 3.5b). The effect of cutting all trees below a certain threshold is clearly visible in the tree height distribution shown in Figure 3.3b.

- *Logging 2* is an example of diseased trees or "free thinning" where 60% of the trees (independent on their height) are randomly removed, as represented in Figure 3.5c. When 60% of the trees are randomly removed, the tree height distribution is also affected (see Figure 3.3b), as the more frequent heights are proportionally more penalized by the action.

- *Logging 3* is the selective logging of big trees or "thinning from above" case, where 50% of the trees above 25 m are cut, as shown in Figure 3.5d [55]. The distribution of tree heights varies, as shown in Figure 3.3b.

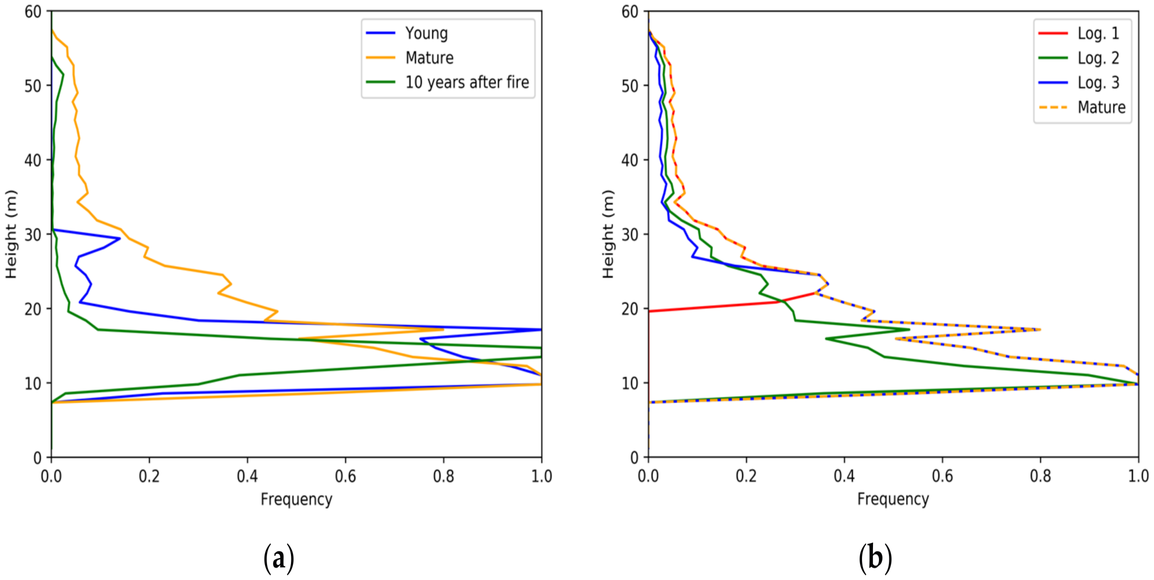

FIGURE 3.3: Distribution of heights for the simulated forest scenarios: (**a**) three scenarios derived from a young forest stand, after long term changes; and (**b**) three scenarios derived after performing a logging action on a mature forest.

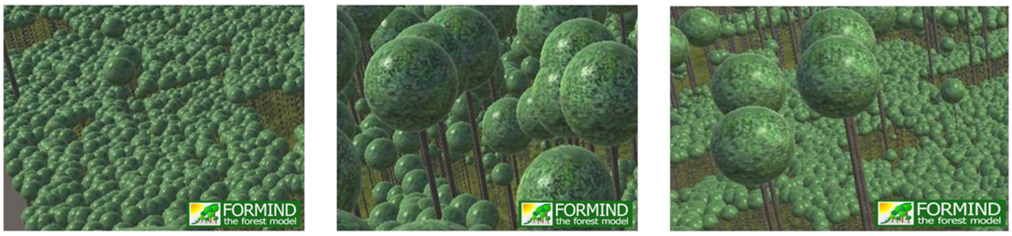

(**a**) (**b**) (**c**)

FIGURE 3.4: Representation of simulated forest: (**a**) young forest: example of undisturbed forest after 50 years; (**b**) mature forest: example of undisturbed forest after 500 years; and (**c**) mature forest 10 years after a fire event.

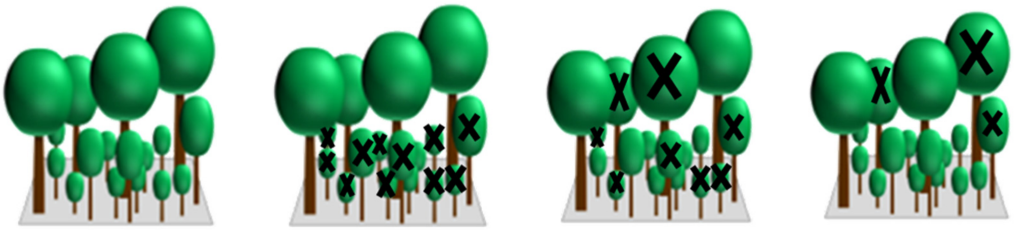

(**a**) (**b**) (**c**) (**d**)

FIGURE 3.5: Representation of simulated forest for logging actions: (**a**) mature undisturbed forest; (**b**) *Logging 1*: example of firewood removal or thinning from below; (**c**) *Logging 2*: example of diseased trees or free thinning; and (**d**) *Logging 3*: example of selective logging of big trees or thinning from above.

3.3.2 From Simulated Forest Stands to Reflectivity Profiles

Starting from the single tree parameters, vertical reflectivity profiles were simulated. This was implemented in a very pragmatic and simple way as the objective of this task was to demonstrate the underlying principle rather than to assess a given performance. Given the simplifications in the forest simulations and the modelling of the 3-D radar reflectivity, the results shown in this section provide a first consistency test, but do not pretend to constitute on their own a sufficient quantitative assessment of the proposed methodology.

The individual steps are described below and the flowchart is shown in Figure 3.6.

First, for every tree in the list, the distribution of biomass $B_{tree}(z)$ was estimated, taking into account the height of the tree as well as the diameter of its crown and stem. In the model, the tree canopies were assumed to be spherical and the stems cylinders for all trees. With this, the volume at each vertical slice at 0.5 m was computed to obtain the biomass from the volume, and different allometric equations were employed for the trunk, the crown, and tree species, using different wood densities. Once the vertical profile of the biomass for every tree was estimated, the scene was gridded to a given spatial resolution in range and azimuth. In the results below, a spatial resolution of 10 × 10 m was assumed. For each grid cell, the individual contributions of the different trees within the cell were added before applying an extinction factor σ:

$$B_{pixel}(z) = e^{-\sigma(Maximum\ height - z)} \sum\nolimits_{tree} B_{tree}(z). \tag{3.13}$$

In the results shown in this paper, the extinction was set to 0.05 m^{-1}. Neither interactions between the trees nor polarimetric diversity were accounted. Once the number and distribution of wavenumbers k_{zi} was set, the elements of the multi-image covariance matrix $R_{k_{zi}}$ were obtained as:

$$R_{k_{zi}} = \sum\nolimits_{z} B_{pixel}(z)\, e^{jk_{zi}z}. \tag{3.14}$$

Ten baselines were considered with k_z equally distributed between 0.05 and 0.4 rad/m and a spatial multilook of 5×5 px was employed for the estimation of the covariance matrix. No temporal decorrelation effects were taken into account. The reflectivity profiles T were reconstructed from $R_{k_{zi}}$, as discussed in Section 3.2.1.

It is worth noting that, despite much higher densities of shorter trees, tall trees produced significantly higher values of power density in the reconstructed vertical reflectivity profiles. This was not only due to the larger volume of taller trees, but was also a result of the applied attenuation that blurred the presence of shorter trees in the reconstructed 3-D reflectivity.

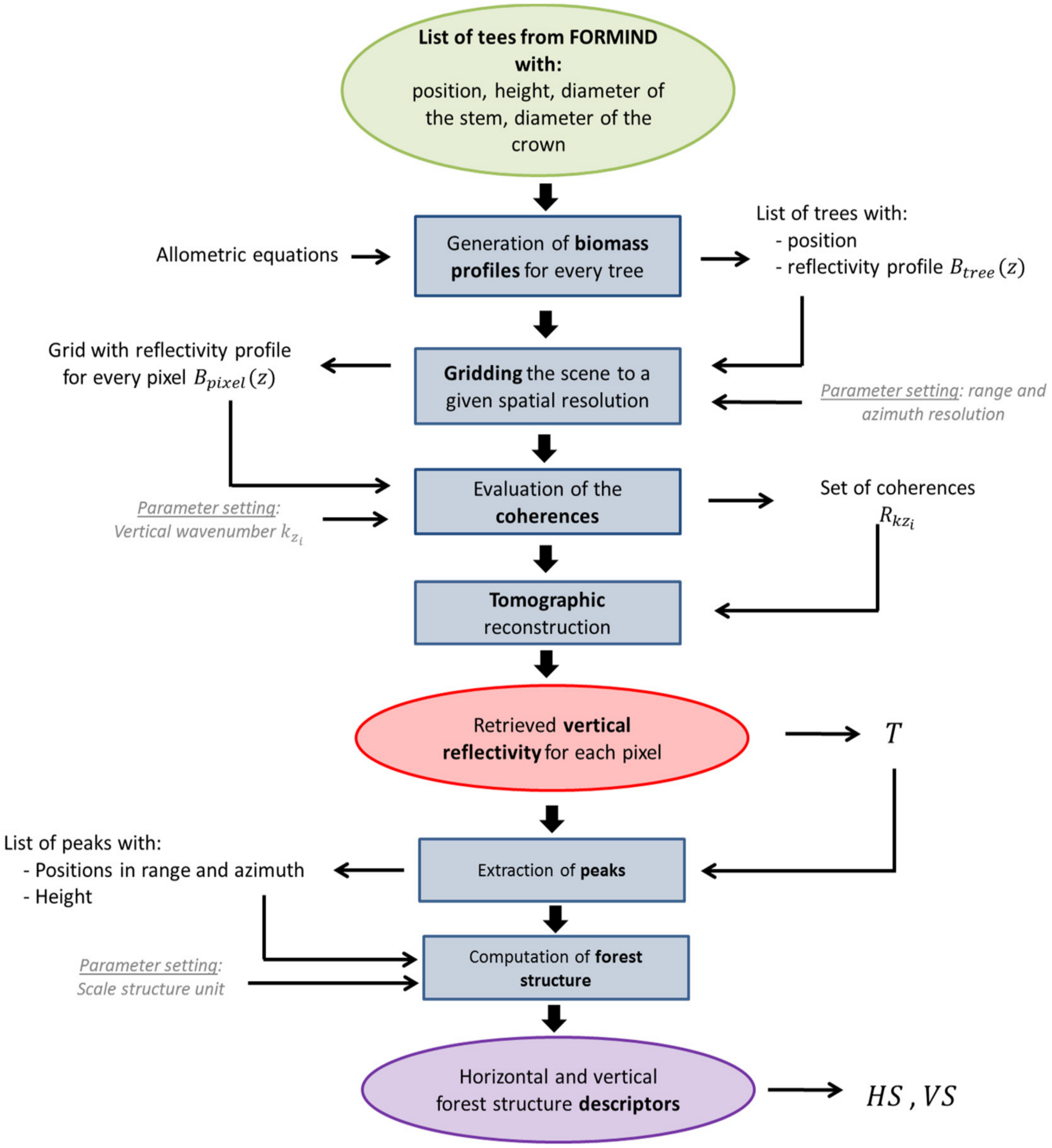

FIGURE 3.6: Flowchart of the simulation of vertical reflectivity profiles from forest stands simulated by FORMIND.

3.3.3 Results and Discussion

From the retrieved reflectivity profiles, the peaks were extracted and finally, the horizontal and vertical structure indices were estimated as per Equations 3.10–3.12. The density distribution of the obtained indices on the HV plane are shown in Figure 3.7.

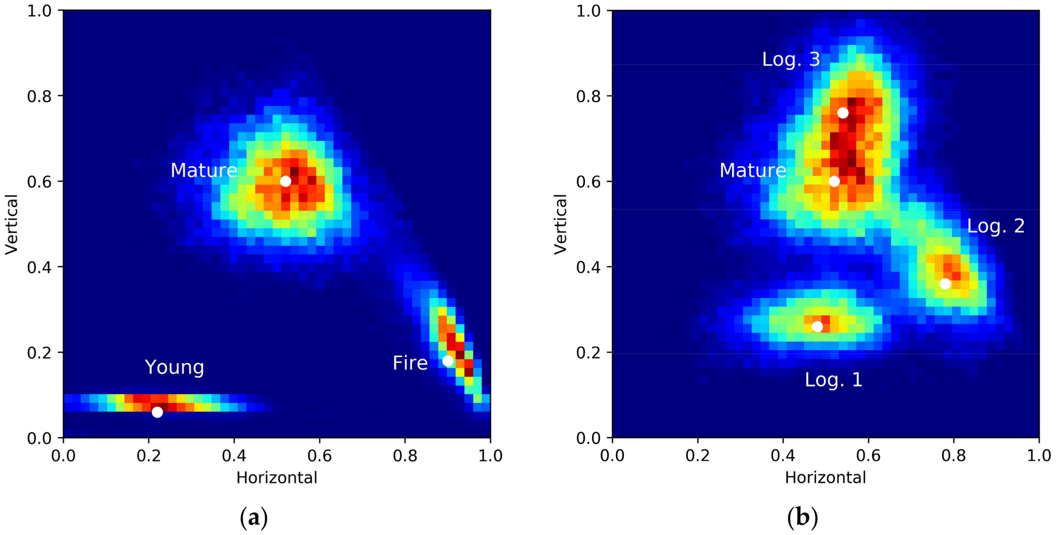

(**a**) (**b**)

FIGURE 3.7: Density distribution of the horizontal and vertical descriptors: (**a**) long-term simulations presented in Figure 3.4; and (**b**) logging activities presented in Figure 3.5.

Figure 3.7a shows the density distribution of the loci of the horizontal and vertical structure indices in the HV plane for the first three scenarios; the white dots indicate the location of the most frequent value in the histogram. The three scenarios can be clearly distinguished from each other. The structure complexity increased significantly in the evolution from young to mature forest (500 years later). The increase in the vertical complexity was predominant and was reflected by an increase of the vertical structure index. At the same time, the transition from a dense layer of younger trees to a less dense mature forest was also reflected by an increase of the horizontal structure index.

The mature forest 10 years after the major fire event significantly decreased the vertical structure as most of the younger trees had a similar height of around 15 m, and only a few (old) tall trees remained. As these tall trees were scattered across the stand, they increased the horizontal heterogeneity that is reflected by the increase of the horizontal structure index.

Figure 3.7b shows the density distribution of the loci of the horizontal and vertical structure indices in the HV plane for the three disturbance scenarios; the white dots indicate the location of the maximum density of each distribution. All three logging scenarios could be clearly distinguished from each other and from the undisturbed forest cases. The different ways that trees are removed induce different changes in the HV plane. For each change, the point cloud was translated to a different position in the plane. In the case of *Logging 1*, removing trees selectively to their height had a noticeable effect on the vertical structure complexity, which was reflected by a decrease in the vertical structure index (with respect to the undisturbed case). In the case of *Logging 2*, the random thinning increased the horizontal structure index (associated to a decrease of forest density) combined with a significant decrease of the vertical index; reflecting the fact that given the uneven original distribution of tree heights, the random logging affected more trees with a more frequent range of heights (in this case, the lower ones with heights below 20 m). Finally, when a number of tall trees with heights above a given threshold were removed, as in the case of *Logging 3*, the presence of lower trees was enhanced, thus leading to an increase in the vertical structure index.

3.4 Forest Structure Dynamics on a Real Scenario

3.4.1 Description of the Test Site

After the tests were performed using simulated data, the proposed approach was applied on real SAR data. To achieve this, we used three quad polarimetric multibaseline datasets acquired by DLR's (German Aerospace Center) airborne SAR system [56], [57] in a repeat pass interferometric mode over the same forest in 2008, 2012 and 2016. The forest selected is located in Traunstein in the south-eastern part of Germany and constitutes a managed forest in a temperate climate, with coniferous, deciduous and mixed stands. Due to the close-to-nature forest management approach, the forest stands are heterogeneous in terms of structure and species richness. Figure 3.8 shows a stand classification of development stages based on field inventory data. Five major stages were identified in this classification [58]. First, the *young stage* in this test site (represented in dark blue in Figure 3.8) is mainly constituted by stands of young trees with low density. The stands in the *growth stage* (represented in light blue) are fast-growing, constituted mainly by a dense layer of short trees. It should be noted that although the polygons were classified as growth stage, they show a high variability and in most of them, a few scattered tall trees still remain above the short trees. The *mature stage* in this forest (represented in green) is formed by tall trees that are densely and homogeneously distributed. In the *transition stage* (represented in orange), small trees grew under older taller trees where the older tall trees are significantly denser than in the growth stage. Finally, stands in the *plenter stage* (represented in red) have a high variety of tree heights. This *plenterwald* is the most noticeable feature in terms of structure in the forest under study, and is the result of decades of management practices aimed at boosting structure.

In terms of structure, the early stand stages, namely the young and the growth stages, refer to the low structural complexity describing the succession from established transition until the cumulation of growth. Increasing structural complexity is characteristic of the transition, particularly for the *plenter* stage, with the highest structural complexity. Regarding the mature stage stands in Traunstein, despite their age they exhibited a low complexity since most of the trees are of similar height.

3.4.2 Radar Data

As mentioned above, three multibaseline datasets at the L-band were acquired over the Traunstein area in a repeat pass interferometric mode. It should be noted that, besides taking place under different weather and seasonal conditions (as detailed in Table 3.1), different viewing geometries, resolutions and baseline distributions were employed for the different acquisitions. Since each of the tomographic sets was acquired by the same sensor and in the same day (separated only by minutes), system or environmental variability can be ignored within each of the sets. The three tomographic sets were then processed and calibrated (geometrically and radiometrically) to the same standards.

TABLE 3.1: Main parameters of the multibaseline L-band dataset over the Traunstein forest.

Time	System	Side Looking	Tracks	kz Distribution[1]	Height of Ambiguity[2]	Resolution		
						Vertical[2]	Range[3]	Azimuth[3]
06/2008	E-SAR	Left	5	$-0.12, -0.07, 0, 0.03, 0.15$	210 m	23 m	2.12 m	1.2 m
11/2012	F-SAR	Right	6	$-0.12, 0, 0.03, 0.04, 0.16, 0.31$	209 m	15 m	1.28 m	0.6 m
06/2016	F-SAR	Right	5	$-0.15, -0.04, 0, 0.06, 0.15$	157 m	20 m	1.28 m	0.6 m

[1]At the center of the SAR image; [2]theoretical values for beamforming approach; and [3]single look complex (SLC) resolution.

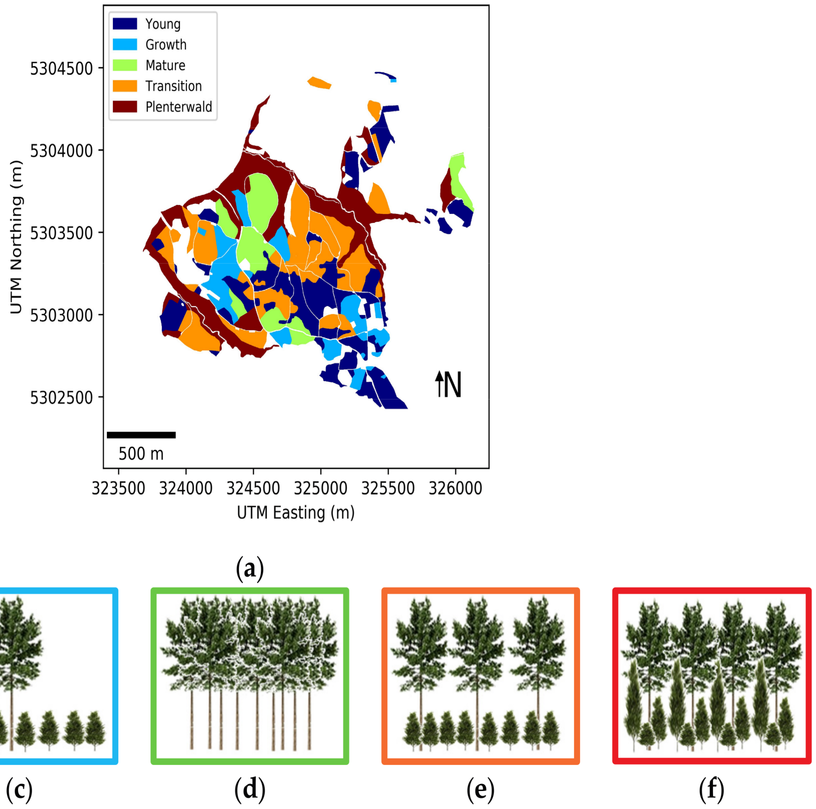

FIGURE 3.8: (**a**) Classification of the test site according to different development stages. Representation of trees distribution at the different development stages: (**b**) young; (**c**) growth; (**d**) mature; (**e**) transition; and (**f**) plenterwald.

3.4.3 Reference Data

To assess the validity of the results obtained, several sources of reference data were used. Their main specifications are summarized in Table 3.2. On the one hand, high resolution aerial optical images (2009, 2012) as well as airborne Lidar data (2008 and 2012) were available. On the other hand, in situ data acquired on the basis of inventory plots were considered. These sampled the area under study following a 100 m grid, recording at each grid node the most relevant trees inside a circular area of around 12.5 m radius. Not all trees were reported in the inventory plot, depending on their diameter at breast height and their distance to the center of the plot [58], [59]. It is worth mentioning that this scale is too small to allow a direct comparison on a local scale with the estimates from radar data obtained at a scale of 50 m × 50 m.

This set of inventory plots was employed to estimate the main development stages at different polygons previously determined and obtain the reference map shown in Figure 3.8. It should be noted that the polygons were defined following organizational divisions and not according to uniformity of forest type. Furthermore, the polygons included roads, paths, and other man-made targets that introduced important alterations of the estimated structure from the remote sensing data in the form of local discontinuities. Even if local, these discontinuities incurred significant variations that had a non-negligible effect on the structures averaged over the polygons.

Therefore, forest stands inside the predefined polygons were subject to high variability and this introduced uncertainties when averaging the estimated structures over the polygons.

TABLE 3.2: Main specifications of the different sources of reference data available in this study.

Source	Dates	Resolution	Coverage
Aerial optical image	2009, 2012	0.2 m	Dense
Lidar[1]	2008, 2012	1 m	Dense
In situ data	2009	12.5 m	Sparse

[1] This is the spatial resolution of the canopy height model derived from the point clouds of Lidar returns.

3.4.4 Results and Discussion

Following the proposed methodology, maps of horizontal and vertical structure were generated for 2008, 2012 and 2016, at a scale of 50 m × 50 m. First, the values of HS and VS were averaged over the polygons, classifying the stands in the five development stages shown in Figure 3.8, the results of which are shown in Figure 3.9. Figure 3.10 reflects how the mean values of horizontal and vertical structure for the five different polygons considered were distributed in the HV plane and how they varied across the three datasets.

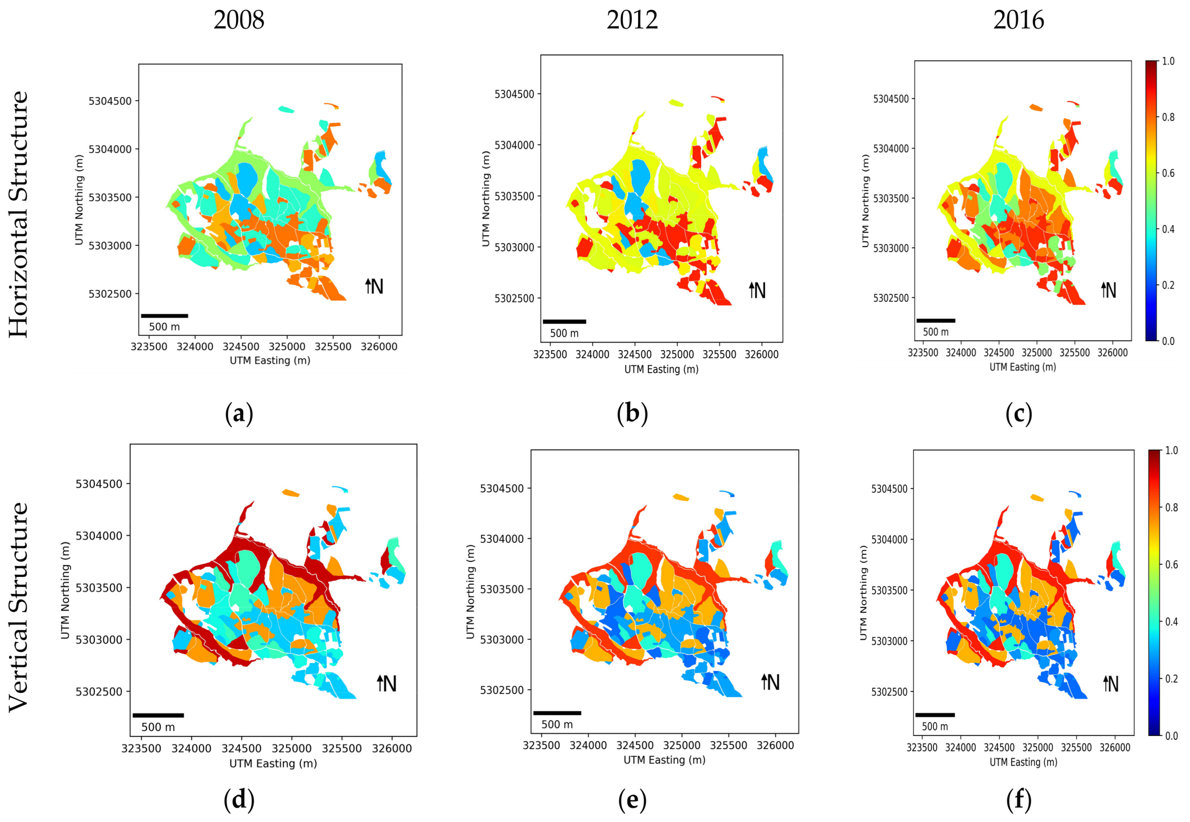

(**a**) (**b**) (**c**)

(**d**) (**e**) (**f**)

FIGURE 3.9: Horizontal and vertical forest structure in Traunstein averaged over the five predefined polygons, representing different growth stages. Horizontal structure in: (**a**) 2008; (**b**) 2012; and (**c**) 2016. Vertical structure in: (**d**) 2008; (**e**) 2012; and (**f**) 2016.

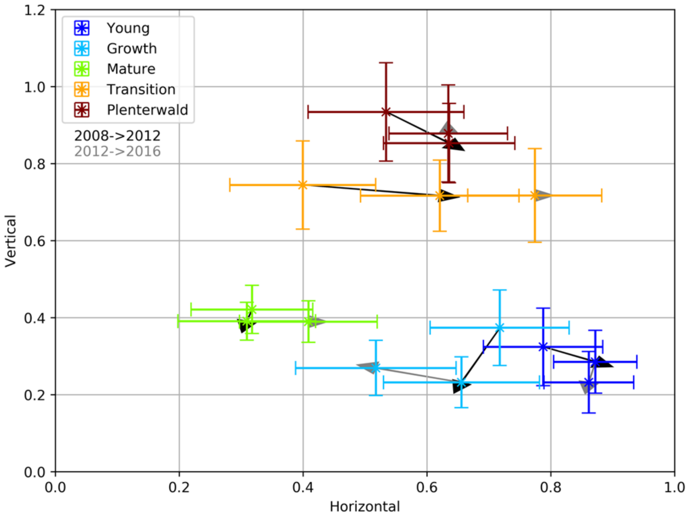

FIGURE 3.10: Distribution of the mean estimated structure in the horizontal/vertical (HV) plane for five polygons defined in Figure 3.8 at different development stages, and its temporal evolution between 2008 and 2016.

First, it was observed that the five development stages were characterized by different signatures in terms of structure and structure changes. They appeared at different positions in the HV plane and their evolution in this space across the three acquisitions was also different in terms of the magnitude and direction of the vectors representing the variations in structure. The complexity of the different development stages (introduced in Section 3.4.1) was effectively reflected through the vertical index. The forests at young, growth, and mature stages had low values in contrast to the transition and the *plenter* stages, whose complexity was reflected by significantly higher values. The horizontal index varies from 0.3 for the dense mature forest to 0.9 for the sparse young forest reflecting the difference in the density of the highest trees in each polygon.

Comparing the estimated structure indices for 2008, 2012 and 2016, it was seen that in general, they did not change significantly, given the range of variability within each stage except for the transition and the growth stands. These two types of forest were the ones most altered by the forest management practices and, therefore, were more dynamic in terms of structure change in such a relatively short time span. It was interesting to observe for these two stages the different direction of the vectors representing the variation in the values of the structure indices between 2008 and 2016. For the transition stand with an initial vertical high value and low horizontal structure value, the value of the horizontal index increased from 2008 to 2012, and further still in 2016. On the contrary, for the growth stage, the horizontal index decreased from 2008 to 2016.

However, to gauge the significance of these previous results, it should be observed that the high variability inside polygons produced by the way they were defined (already discussed in Section 3.4.1), resulted in a high dispersion of the indices around the mean values for the different stages represented in Figure 3.10. Furthermore, the variations in structure, essentially due to forest management actions, took place only locally and affected less than 10% of the area considered. This fact reduced the significance of the estimated structure changes when they were averaged over the polygons. The extent of the changes in the area were evaluated from differences in the maps of Lidar heights from 2008 and 2012 given that the changes were only due to forest management actions and, as a consequence, they necessarily produced a change in the height of the forest at high resolution. Figure 3.11 shows the map of Lidar heights in 2008 (see Figure 3.11a), in 2012 (see Figure 3.11b), and the map of absolute differences (see Figure 3.11c). In the latter, it was observed that most of the area remained undisturbed (represented in dark blue) and changes (represented in other colors) occurred only locally.

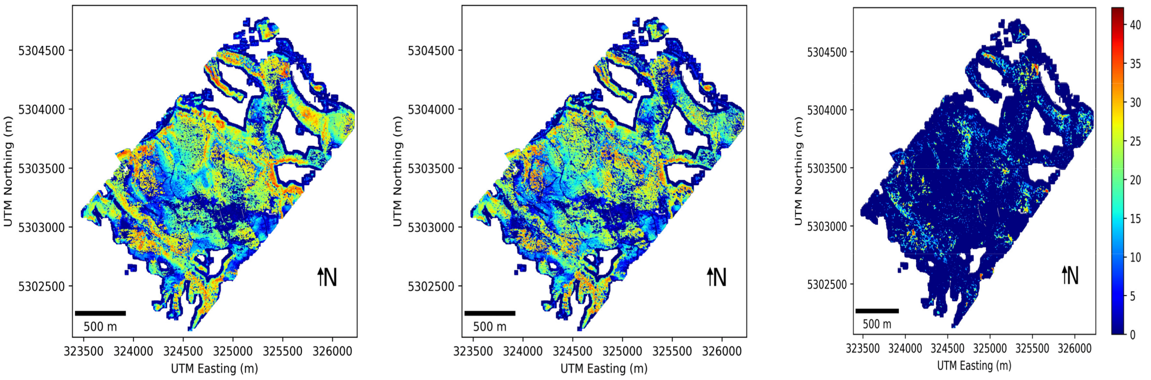

(a) (b) (c)

FIGURE 3.11: Map of Lidar height over the test site: (**a**) 2008; (**b**) 2012; and (**c**) the height difference between 2008 and 2012.

Similarly, the local extent of the variations in the forest structure was also observed in the maps generated from the TomoSAR data (see Figure 3.12). The main patterns in both the horizontal and vertical estimated structures were analogous, and significant variations occurred only locally. To compare the match between the intensity and location of logging action—as identified from the height variations with the Lidar measurements and by the changes in the maps of forest structure estimated from TomoSAR—two classes were defined (change and no change) both for the Lidar and TomoSAR maps. In particular, for the TomoSAR dataset, we extracted the map of change in horizontal (or vertical) forest structure by direct subtraction of horizontal (or vertical) forest structure estimated from the TomoSAR data in 2008 and 2012. We then estimated a single map of structure change by aggregating the changes in the horizontal and the vertical dimensions. To define the classes, a threshold was applied to keep only the most significant variations (the threshold was empirically set to 0.3 in the examples provided in this Section). Regarding the Lidar dataset, a map of change was also similarly estimated by applying a threshold (empirically to forest height differences greater than 10 m) to the map of height differences in Figure 3.11c. The two maps of forest change obtained from the TomoSAR data and the Lidar height were superimposed and are shown in Figure 3.13.

It was observed that both sources highlight the same areas as more affected by changes between 2008 and 2012. Regarding the discrepancies, the differences in the extension and orientation of the area affected by changes were mainly due to the different resolutions and geometries of the two sources. Both sources provided the same class in 92% of the cases.

In the forest structure estimated from the TomoSAR data, four cases were distinguished by considering the direction of the variation (horizontal or vertical):

-no change was identified either in the horizontal or in the vertical estimated structure;

-horizontal structure varied whereas vertical structure remained stable;

-vertical structure varied whereas horizontal structure remained stable;

-both horizontal and vertical structures varied simultaneously.

Results are shown in Figure 3.14. As already discussed in Section 3.3.3, different types of forest management action led to different directions of displacement of the loci of the values of horizontal and vertical structure in the HV plane: some changes were mostly noticeable as a variation in the horizontal structure (light blue areas in Figure 3.14), whereas others mainly affected the estimated vertical structure (yellow areas in Figure 3.14). To further assess the sensitivity of the proposed methodology to identify the type of forest structure change, two examples were considered in the following sub-sections: one for the horizontal structure change (highlighted by a black circle in Figure 3.12 and 3.14), and one for the vertical (highlighted by a grey circle in Figure 3.12 and 3.14).

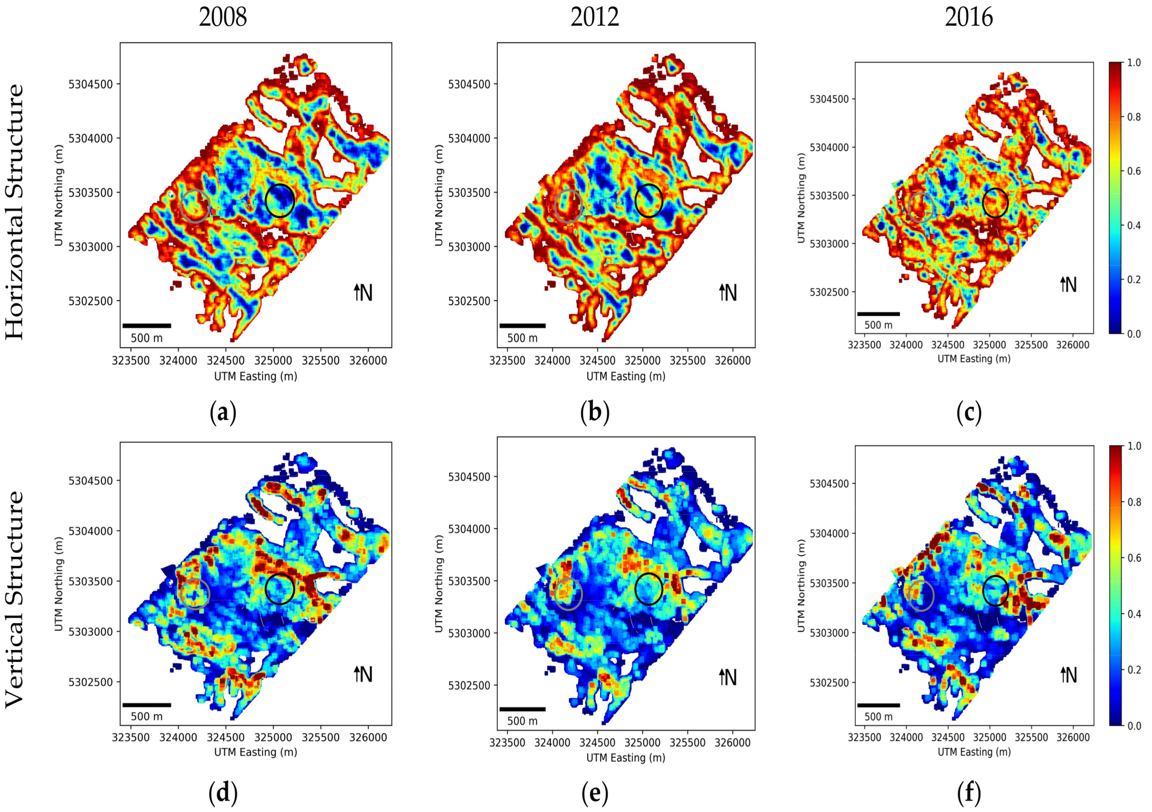

(a) (b) (c)

(d) (e) (f)

FIGURE 3.12: Forest structure maps estimated from TomoSAR. Horizontal structure in: (**a**) 2008; (**b**) 2012; and (**c**) 2016. Vertical structure in: (**d**) 2008; (**e**) 2012; and (**f**) 2016.

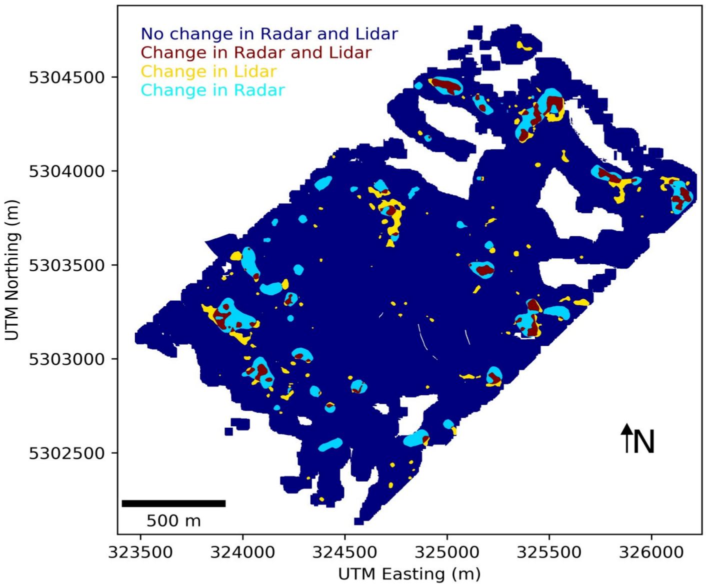

FIGURE 3.13: Map of forest change as identified from Lidar height and from forest structure estimated from TomoSAR data at the L-band.

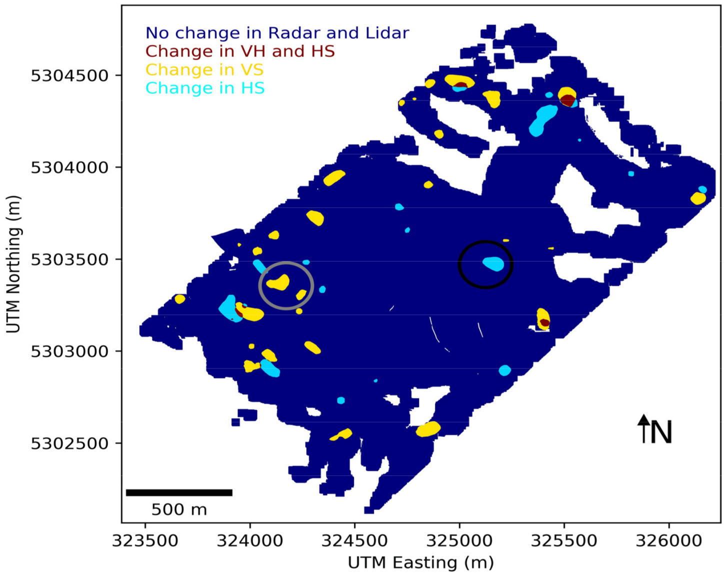

FIGURE 3.14: Map of forest change as identified from forest structure estimated from TomoSAR data at the L-band and discriminating between horizontal and vertical structure variations.

3.4.4.1 First Example of Local Forest Structure Change in the Area Under Study

The first example considered is a transition stand where between 2008 and 2012 a number of trees were logged, independent of their height, resulting in a clearing of a small area depicted in Figure 3.15d,e, and noticeable in the optical images (see Figure 3.15a,b). It should be noted that, even if less representative, other logging actions of different types occurred during this period and in the area considered. For example, it was observed (in the parts highlighted by white circles) that a few tall trees were removed, leaving the shorter trees below.

This type of logging, where trees are removed independently of their height, reduces the density of the highest trees, while the distribution of trees according to their height before and after the action remains essentially preserved. Figure 3.15c shows the histograms of Lidar heights within the plot in 2008 and 2012. This can be used as a proxy of tree-height frequency distribution for the stand. For accurate interpretation, it is worth noting that the height was estimated from the first Lidar return associated to the highest elements of the canopy. When these tall trees were removed, the vegetation below became apparent, which produced an increase in the number of samples at smaller heights. Bearing this in mind, the histograms reflect the reduction of a significant number of tall trees between 25–40 m that resulted in a flattening of the histogram, but the effect is rather small. In terms of structure, the logging action considered in the first example essentially produced a change mainly in the horizontal dimension, given that the density of trees in the top layer was significantly reduced. Regarding the vertical structure, it exhibited only a slight increase as the distribution of heights of the remaining trees was only slightly altered. This was reflected in the maps of the estimated forest structure, as shown in the area highlighted by a black circle in Figure 3.12, as well as in the representation of the evolution of structure indices in this area in the HV plane (see Figure 3.16). In Figure 3.16, the vector representing the variation in the values of the structure indices between 2008 and 2016 reflected an important increase in the horizontal direction. This increased the significance of the changes as estimated by the structure indices. Finally, it is worth mentioning that the results shown in this Section for this example of logging were consistent with the results obtained in Section 3.3.3 for the simulated scenario where a number of trees were removed randomly independent of their height (*Logging 2*).

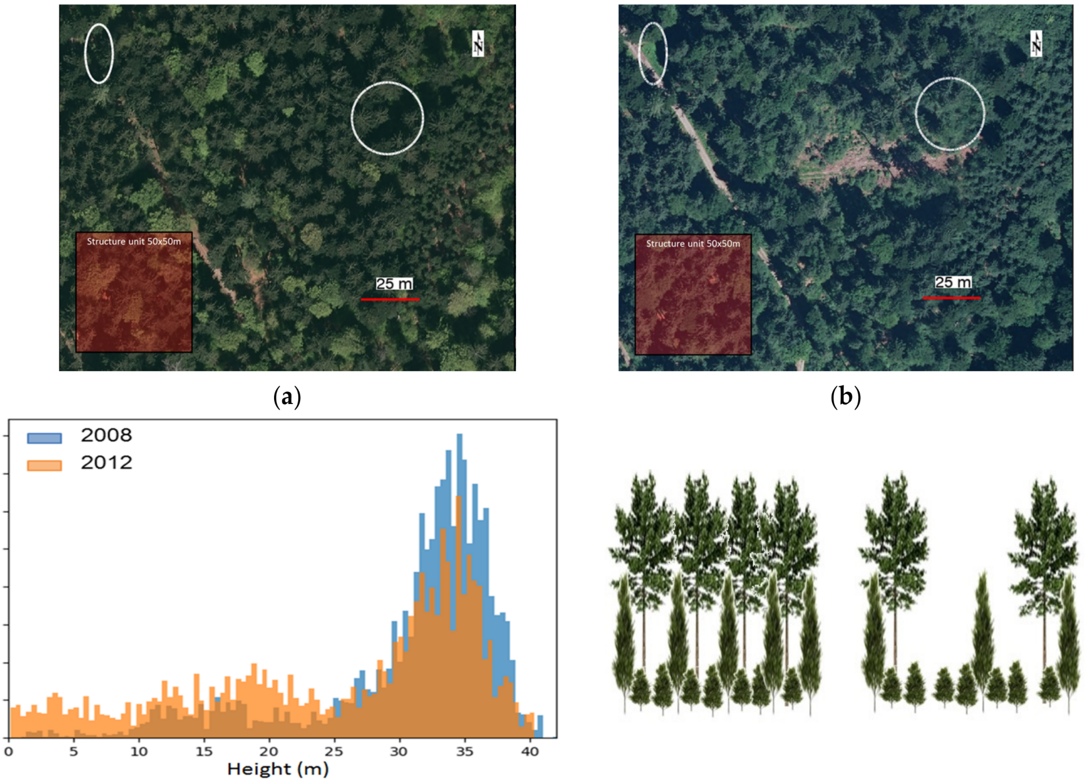

(a) (b) (c) (d) (e)

FIGURE 3.15: Main type of forest logging in the area considered in the first example of forest change. Optical images of the area in: (**a**) 2009; (**b**) 2012; and (**c**) a histogram of Lidar heights in the area considered in the first example of forest change in 2008 and 2012. Representation of local tree distributions (**d**) before; and (**e**) after logging.

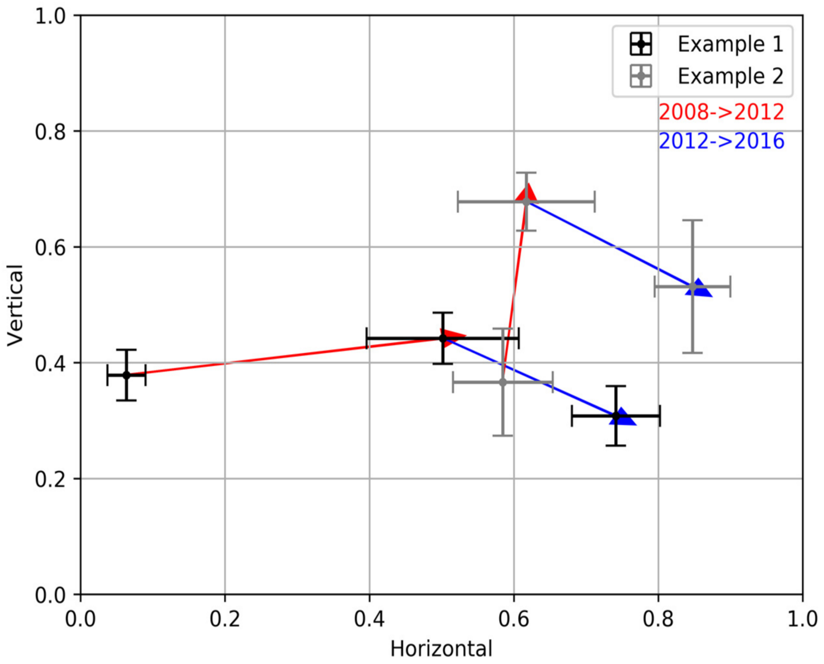

FIGURE 3.16: Evolution of the estimated structure for the two examples of local areas considered from 2008 to 2016.

3.4.4.2 Second Example of Local Forest Structure Change in the Area Under Study

In the second example, a number of tall trees were logged in a transition stand, leaving shorter trees mainly undisturbed. This can be observed in the optical images, particularly in the shadows of the tall trees on the road crossing the stand (see Figure 3.17a,b). As in the first example, it should be noted that other logging actions of different types have occurred in this area in the period considered. For example, a local clearing can be clearly observed (highlighted by a white circle).

In this case, the number of tall trees decreased; but, in contrast with the previous example, since the shorter trees were not removed the distribution of tree height was modified. Accordingly, Figure 3.17c shows the histograms of Lidar heights in 2008 and 2012 indicating a significant reduction in the tree heights ranging between 25–40 m, where at the same time there was a noticeable increase in the tree heights between 5–15 m: the presence of two modes was significantly enhanced. Consequently, this type of logging increased the vertical heterogeneity and hence the vertical structure index, as shown in Figure 3.16. Horizontal structure increased as long as some trees in the top layer were still preserved. This was also implied in the forest structure maps shown in Figure 3.12, and in the HV plane in Figure 3.16 by the difference in the direction of the structure change vector in the two examples considered. This result is consistent with the results obtained for the simulated scenario, defined as *Logging 3*, in Section 3.3.3.

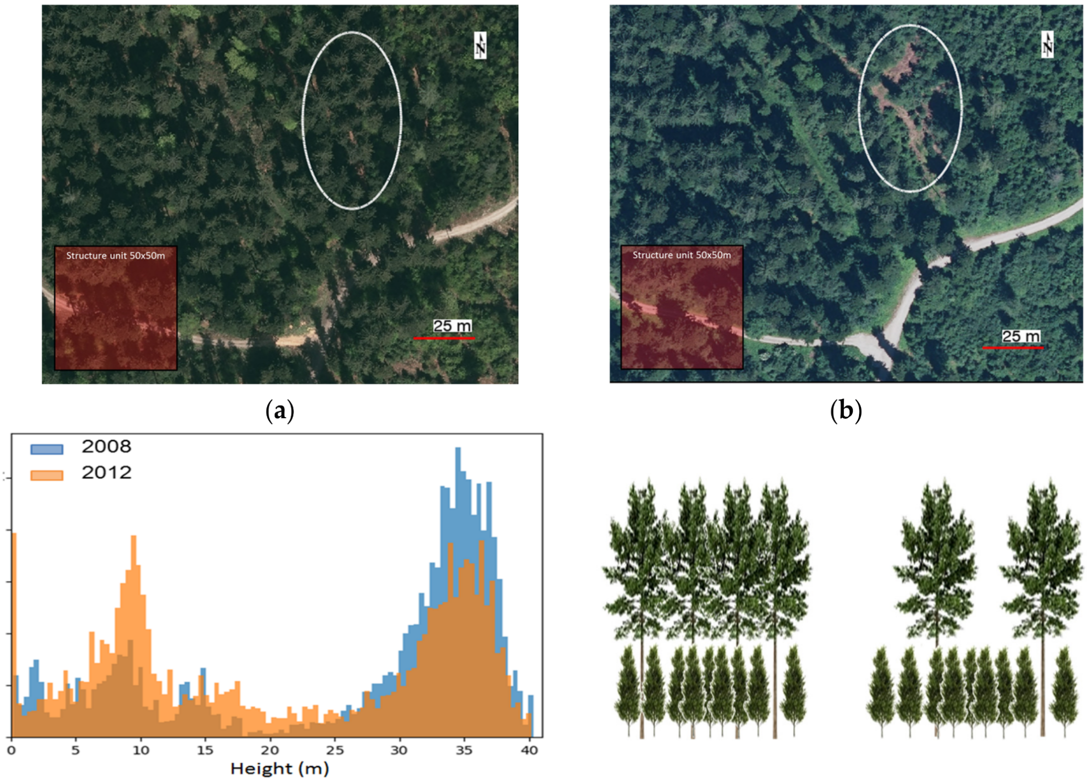

(a) (b)

(c) (d) (e)

FIGURE 3.17: Main type of forest logging in the area considered in the second example of forest change. Optical images of the area in: (**a**) 2009; (**b**) 2012; and (**c**) the histogram of Lidar heights in the area considered in the second example of forest change in 2008 and 2012. Representation of local tree distribution (**d**) before; and (**e**) after logging.

3.5 Conclusions

In this paper, a methodology to detect and interpret forest structure changes using L-band tomographic SAR acquisitions was proposed and tested. The link between the L-band tomographic-reconstructed 3-D forest reflectivity, which may depend on acquisition and instrument parameters, and the physical forest structure was established by using a recently introduced 2-D (i.e., horizontal and vertical) structure characterization concept [37], [38]. Accordingly, a pair of vertical and horizontal structure indices was defined derived from the 3-D distribution of the peaks of the reconstructed reflectivity function [34]. It was then possible to represent different forest structure conditions on a two-dimensional HV structure plane defined by these two indices. In this sense, different changes in forest structure can be represented on the HV structure plane by vectors with different directions and magnitudes. The length of the vector was associated to the extent (or amount) of structure change, while its direction represented the change in the distribution of trees occurring depending on their height.

The sensitivity and consistency of the proposed structure indices to natural or anthropogenic variations in forest structure was tested on simulated as well as real experimental data. The application of the proposed methodology on simulated data—despite the simplifications in the derivation of the 3-D reflectivity from the FORMIND simulations—allowed us to demonstrate the underlying principle for a large diversity of forest structure scenarios. Furthermore, it was shown that changes in forest structure caused either by natural (undisturbed) forest evolution, or by disturbances such as a fire event or different logging scenarios, impacted in different ways on the horizontal and vertical forest structure, and that these changes were projected into the two proposed structure indices.

The proposed methodology was then applied to three sets of tomographic L-band data acquired over the same temperate forest (Traunstein) in 2008, 2012 and 2016 with the aim of validating its ability to detect structural changes occurring in the time between the acquisitions. During this time, the main changes in the site were triggered by natural evolution as well as forest management in terms of logging selected trees and the opening of paths at local scales. For the interpretation and validation of the achieved results, different sources of reference data were available: airborne Lidar measurements, high resolution optical images, and forest inventory data. The results clearly showed that even subtle changes in the vertical as well as horizontal structure of the individual stands were reflected in the 3-D L-band reflectivity, and thus in the derived horizontal and/or vertical structure indices. The obtained forest structure maps were comparable and consistent; between them, they exhibited similar global behavior and the differences occurred only locally, as expected and confirmed by the reference data. Local changes were distinctly identified as variations in the estimated structure descriptors; and, consistent with the simulated scenarios, logging of different natures led to different directions of the change vectors on the HV structure plane, even by using data acquired by two different SAR sensors (E-SAR in 2008, and F-SAR in 2012 and 2016) with different viewing geometries, different spatial resolutions, and different spatial track distributions. It was then verified, at the L-band, that the fact that the definition of the two structure indices relied only on the 3-D location of the reflectivity peaks made them more robust against variations in the shape of the reflectivity profiles induced by non-structural variability, as long as the main scattering contributions associated with the reflectivity peaks did not change their location.

A drawback in the estimation of forest structure and forest structure changes in real scenarios through statistical measures like the ones employed in this paper is the non-uniformity of the stands that induces border effects. These discontinuities might be caused by the presence of contributions not due to vegetation, such as a road, path, or other man-made targets, but also by structure distributions changing rapidly in space. The extent of the variations introduced by these discontinuities in the forest structure indices was partly determined by the scale of the structure unit window employed. However, the dimensions of this window were difficult to set optimally with no a priori information, since this is site-dependent. Furthermore, a compromise exists between spatial resolution and accuracy of the indices, besides other considerations on system resolution. The effect of scale in the indices will be further addressed in future studies.

Finally, it should be pointed out that a critical point in forest studies with real data is validation. In this paper, field inventory data, Lidar measurements, and high resolution optical images were extensively cross-checked. However, as discussed and justified, the usability of the available field data for quantitative validation was insufficient. Other scenarios with field information at larger scales that are more compatible with remote sensing studies are available, but the temporal series of multibaseline SAR data have yet to be acquired.

Acknowledgments

This study was supported by the HGF Alliance HA-310 Remote Sensing and Earth Systems Dynamics.

References

[1] T. A. Spies, "Forest structure: a key to the ecosystem", *Northwest Science*, vol. 72, no. 2, pp. 34–36, 1998. [Online]. Available: `http://andrewsforest.oregonstate.edu/pubs/pdf/pub2564.pdf` (cited on pages 48, 51).

[2] J. Grace, "Understanding and managing the global carbon cycle", *Journal of Ecology*, vol. 92, no. 2, pp. 189–202, 2004. DOI: `10.1111/j.0022-0477.2004.00874.x` (cited on page 48).

[3] L. Gatti, M. Gloor, J. Miller, C. Doughty, Y. Malhi, L. Domingues, L. Basso, A. Martinewski, C. Correia, V. Borges, *et al.*, "Drought sensitivity of amazonian carbon balance revealed by atmospheric measurements", *Nature*, vol. 506, no. 7486, p. 76, 2014. DOI: `10.1038/nature12957` (cited on page 48).

[4] S. Frolking, M. W. Palace, D. Clark, J. Q. Chambers, H. Shugart, and G. C. Hurtt, "Forest disturbance and recovery: a general review in the context of spaceborne remote sensing of impacts on aboveground biomass and canopy structure", *Journal of Geophysical Research: Biogeosciences*, vol. 114, no. G2, 2009. DOI: `10.1029/2008JG000911` (cited on page 48).

[5] A. Beaudoin, T. Le Toan, S. Goze, E. Nezry, A. Lopes, E. Mougin, C. Hsu, H. Han, J. Kong, and R. Shin, "Retrieval of forest biomass from sar data", *International Journal of Remote Sensing*, vol. 15, no. 14, pp. 2777–2796, 1994. DOI: `10.1080/01431169408954284` (cited on page 48).

[6] R. N. Treuhaft and P. R. Siqueira, "Vertical structure of vegetated land surfaces from interferometric and polarimetric radar", *Radio Science*, vol. 35, no. 1, pp. 141–177, 2000. DOI: `10.1029/1999RS900108` (cited on page 49).

[7] F. Garestier, P. C. Dubois-Fernandez, D. Guyon, and T. Le Toan, "Forest biophysical parameter estimation using L-and P-band polarimetric sar data", *IEEE Transactions on Geoscience and Remote Sensing*, vol. 47, no. 10, pp. 3379–3388, 2009. DOI: `10.1109/TGRS.2009.2022947` (cited on page 49).

[8] S. R. Cloude and K. P. Papathanassiou, "Polarimetric sar interferometry", *IEEE Transactions on geoscience and remote sensing*, vol. 36, no. 5, pp. 1551–1565, 1998. DOI: `10.1109/36.718859` (cited on page 49).

[9] S. Cloude and K. Papathanassiou, "Three-stage inversion process for polarimetric sar interferometry", *IEE Proceedings-Radar, Sonar and Navigation*, vol. 150, no. 3, pp. 125–134, 2003. DOI: `10.1049/ip-rsn:20030449` (cited on page 49).

[10] A. Reigber and A. Moreira, "First demonstration of airborne sar tomography using multibaseline L-band data", *IEEE Transactions on Geoscience and Remote Sensing*, vol. 38, no. 5, pp. 2142–2152, 2000. DOI: `10.1109/36.868873` (cited on pages 49, 50).

[11] O. Frey and E. Meier, "Analyzing tomographic sar data of a forest with respect to frequency, polarization, and focusing technique", *IEEE Transactions on Geoscience and Remote Sensing*, vol. 49, no. 10, pp. 3648–3659, 2011. DOI: `10.1109/TGRS.2011.2125972` (cited on page 49).

[12] M. Neumann, L. Ferro-Famil, and A. Reigber, "Estimation of forest structure, ground, and canopy layer characteristics from multibaseline polarimetric interferometric sar data", *IEEE Transactions on Geoscience and Remote Sensing*, vol. 48, no. 3, pp. 1086–1104, 2010. DOI: `10.1109/TGRS.2009.2031101` (cited on page 49).

[13] A. T. Caicoya, M. Pardini, I. Hajnsek, and K. Papathanassiou, "Forest-above ground biomass estimation from vertical reflectivity profiles at L-band", *IEEE Geoscience and Remote Sensing Letters*, vol. 12, no. 12, pp. 2379–2383, 2015. DOI: `10.1109/LGRS.2015.2477858` (cited on page 49).

[14] S. Tebaldini and F. Rocca, "Multibaseline polarimetric sar tomography of a boreal forest at P-and L-bands", *IEEE Transactions on Geoscience and Remote Sensing*, vol. 50, no. 1, pp. 232–246, 2012. DOI: `10.1109/TGRS.2011.2159614` (cited on page 49).

[15] E. Aguilera, M. Nannini, and A. Reigber, "Wavelet-based compressed sensing for sar tomography of forested areas", *IEEE Transactions on Geoscience and Remote Sensing*, vol. 51, no. 12, pp. 5283–5295, 2013. DOI: `10.1109/TGRS.2012.2231081` (cited on page 49).

[16] M. Pardini and K. Papathanassiou, "Sub-canopy topography estimation: experiments with multibaseline sar data at L-band", in *Geoscience and Remote Sensing Symposium (IGARSS), 2012 IEEE International*, IEEE, 2012, pp. 4954–4957. DOI: `10.1109/IGARSS.2012.6352500` (cited on page 49).

[17] H. T. M. Dinh, S. Tebaldini, F. Rocca, T. Koleck, P. Borderies, C. Albinet, L. Villard, A. Hamadi, and T. Le Toan, "Ground-based array for tomographic imaging of the tropical forest in P-band", *IEEE Transactions on Geoscience and Remote Sensing*, vol. 51, no. 8, pp. 4460–4472, 2013. DOI: `10.1109/TGRS.2013.2246795` (cited on page 49).

[18] D. H. T. Minh, S. Tebaldini, F. Rocca, and T. Le Toan, "The impact of temporal decorrelation on biomass tomography of tropical forests", *IEEE Geoscience and Remote Sensing Letters*, vol. 12, no. 6, pp. 1297–1301, 2015. DOI: `10.1109/LGRS.2015.2394235` (cited on page 49).

[19] C. Albinet, T. Koleck, T. Le Toan, P. Borderies, L. Villard, A. Hamadi, G. V. Laurin, G. Nicolini, and R. Valentini, "First results of afriscat, a tower-based radar experiment in african forest", in *Geoscience and Remote Sensing Symposium (IGARSS), 2015 IEEE International*, IEEE, 2015, pp. 5356–5358. DOI: `10.1109/IGARSS.2015.7327045` (cited on page 49).

[20] A. R. Monteith, M. J. Soja, L. M. Ulander, and L. E. Eriksson, "Borealscat: a tower-based tomographic and polarimetric radar experiment in the boreal forest at P-, L-and C-band", in *Geoscience and Remote Sensing Symposium (IGARSS), 2016 IEEE International*, IEEE, 2016, pp. 7458–7461. DOI: `10.1109/IGARSS.2016.7730945` (cited on page 49).

[21] S.-K. Lee, F. Kugler, K. P. Papathanassiou, and I. Hajnsek, "Quantification of temporal decorrelation effects at L-band for polarimetric sar interferometry applications", *IEEE Journal of Selected Topics in Applied Earth Observations and Remote Sensing*, vol. 6, no. 3, pp. 1351–1367, 2013. DOI: `10.1109/JSTARS.2013.2253448` (cited on page 49).

[22] M. Simard, S. Hensley, M. Lavalle, R. Dubayah, N. Pinto, and M. Hofton, "An empirical assessment of temporal decorrelation using the uninhabited aerial vehicle synthetic aperture radar over forested landscapes", *Remote Sensing*, vol. 4, no. 4, pp. 975–986, 2012. DOI: `10.3390/rs4040975` (cited on page 49).

[23] M. Pardini, A. Cantini, F. Kugler, K. Papathanassiou, and F. Lombardini, "Monitoring dynamics in time of forest vertical structure with multibaseline polinsar data", in *Geoscience and Remote Sensing Symposium (IGARSS), 2014 IEEE International*, IEEE, 2014, pp. 3366–3369. DOI: `10.1109/IGARSS.2014.6947202` (cited on page 49).

[24] M. Pardini, A. Cantini, F. Lombardini, and K. Papathanassiou, "3-D structure of forests: first analysis of tomogram changes due to weather and seasonal effects at L-band", in *EUSAR 2014; 10th European Conference on Synthetic Aperture Radar; Proceedings of*, ISBN: 9783800736072, VDE, 2014, pp. 1–4 (cited on page 49).

[25] T. Le Toan, S. Quegan, M. Davidson, H. Balzter, P. Paillou, K. Papathanassiou, S. Plummer, F. Rocca, S. Saatchi, H. Shugart, *et al.*, "The biomass mission: mapping global forest biomass to better understand the terrestrial carbon cycle", *Remote sensing of environment*, vol. 115, no. 11, pp. 2850–2860, 2011. DOI: `10.1016/j.rse.2011.03.020` (cited on page 49).

[26] A. Moreira, G. Krieger, I. Hajnsek, K. Papathanassiou, M. Younis, P. Lopez-Dekker, S. Huber, M. Villano, M. Pardini, M. Eineder, *et al.*, "Tandem-l: a highly innovative bistatic sar mission for global observation of dynamic processes on the earth's surface", *IEEE Geoscience and Remote Sensing Magazine*, vol. 3, no. 2, pp. 8–23, 2015. DOI: `10.1109/MGRS.2015.2437353` (cited on page 49).

[27] V. Cazcarra-Bes, M. Tello, and K. Papathanassiou, "3d forest structure estimation from sar tomography by means of a full rank polarimetric inversion based on compressive sensing", in *Proceedings of PolInSAR*, ISBN: 9789292212933, 2015 (cited on page 50).

[28] J. Capon, "High-resolution frequency-wavenumber spectrum analysis", *Proceedings of the IEEE*, vol. 57, no. 8, pp. 1408–1418, 1969. DOI: `10.1109/PROC.1969.7278` (cited on page 50).

[29] F. Lombardini and A. Reigber, "Adaptive spectral estimation for multibaseline sar tomography with airborne L-band data", in *Geoscience and Remote Sensing Symposium, 2003. IGARSS'03. Proceedings. 2003 IEEE International*, IEEE, vol. 3, 2003, pp. 2014–2016. DOI: `10.1109/IGARSS.2003.1294324` (cited on page 50).

[30] M. Nannini, R. Scheiber, R. Horn, and A. Moreira, "First 3-D reconstructions of targets hidden beneath foliage by means of polarimetric sar tomography", *IEEE Geoscience and Remote Sensing Letters*, vol. 9, no. 1, pp. 60–64, 2012. DOI: `10.1109/LGRS.2011.2160329` (cited on page 50).

[31] A. Budillon, A. Evangelista, and G. Schirinzi, "Three-dimensional sar focusing from multipass signals using compressive sampling", *IEEE Transactions on Geoscience and Remote Sensing*, vol. 49, no. 1, pp. 488–499, 2011. DOI: `10.1109/TGRS.2010.2054099` (cited on page 50).

[32] X. X. Zhu and R. Bamler, "Tomographic sar inversion by l1-norm regularization-the compressive sensing approach", *IEEE Transactions on Geoscience and Remote Sensing*, vol. 48, no. 10, pp. 3839–3846, 2010. DOI: `10.1109/TGRS.2010.2048117` (cited on page 50).

[33] E. Aguilera, "Synthetic aperture radar tomography compressed sensing models and algorithms", PhD thesis, Technical University of Berlin, 2014. [Online]. Available: `https://elib.dlr.de/85764/` (cited on page 50).

[34] M. Tello, V. Cazcarra-Bes, M. Pardini, and K. Papathanassiou, "Assessment of forest structure estimation by means of sar tomography: potential and limitations", in *Geoscience and Remote Sensing Symposium (IGARSS), 2016 IEEE International*, IEEE, 2016, pp. 32–35. DOI: `10.1109/IGARSS.2016.7728999` (cited on pages 50, 51, 67).

[35] M. Snyder, "What is forest stand structure and how is it measured?", *Northen Woodlands*, vol. 64, p. 15, 2010. [Online]. Available: `https://northernwoodlands.org/articles/article/what-is-forest-stand-structure-and-how-is-it-measured` (cited on page 51).

[36] H. Pretzsch, "Forest dynamics, growth, and yield", in *Forest Dynamics, Growth and Yield*, Springer, 2009, pp. 1–39. DOI: `10.1007/978-3-540-88307-4_1` (cited on page 51).

[37] M. Tello, V. Cazcarra-Bes, M. Pardini, and K. Papathanassiou, "Structural classification of forest by means of L-band tomographic sar", in *Geoscience and Remote Sensing Symposium (IGARSS), 2015 IEEE International*, IEEE, 2015, pp. 5288–5291. DOI: `10.1109/IGARSS.2015.7327028` (cited on pages 51, 52, 67).

[38] F. J. Bohn and A. Huth, "The importance of forest structure to biodiversity–productivity relationships", *Royal Society open science*, vol. 4, no. 1, p. 160 521, 2017. DOI: `10.1098/rsos.160521` (cited on pages 51, 67).

[39] H. H. Shugart, *A theory of forest dynamics. The ecological implications of forest succession models.* The Blackburn Press, 1984, ISBN: 9781930665750 (cited on page 51).

[40] E. K. Zenner and D. E. Hibbs, "A new method for modeling the heterogeneity of forest structure", *Forest ecology and management*, vol. 129, no. 1-3, pp. 75–87, 2000. DOI: `10.1016/S0378-1127(99)00140-1` (cited on page 51).

[41] A. Pommerening, "Approaches to quantifying forest structures", *Forestry: An International Journal of Forest Research*, vol. 75, no. 3, pp. 305–324, 2002. DOI: `10.1093/forestry/75.3.305` (cited on page 51).

[42] M. Del Rio, H. Pretzsch, I. Alberdi, K. Bielak, F. Bravo, A. Brunner, S. Condes, M. J. Ducey, T. Fonseca, N. von Lupke, *et al.*, "Characterization of the structure, dynamics, and productivity of mixed-species stands: review and perspectives", *European journal of forest research*, vol. 135, no. 1, pp. 23–49, 2016. DOI: `10.1007/s10342-015-0927-6` (cited on page 51).

[43] R. F. Noss, "Indicators for monitoring biodiversity: a hierarchical approach", *Conservation biology*, vol. 4, no. 4, pp. 355–364, 1990. DOI: `10.1111/j.1523-1739.1990.tb00309.x` (cited on page 51).

[44] L. H. Reineke, "Perfecting a stand-density index for even-aged forests", 1933. [Online]. Available: `https://naldc.nal.usda.gov/download/IND43968212/PDF` (cited on page 51).

[45] M. Schmitt, M. Shahzad, and X. X. Zhu, "Reconstruction of individual trees from multi-aspect tomosar data", *Remote Sensing of Environment*, vol. 165, pp. 175–185, 2015. DOI: `10.1016/j.rse.2015.05.012` (cited on page 51).

[46] O. Ponce, P. Prats-Iraola, R. Scheiber, A. Reigber, and A. Moreira, "First airborne demonstration of holographic sar tomography with fully polarimetric multicircular acquisitions at L-band", *IEEE Transactions on Geoscience and Remote Sensing*, vol. 54, no. 10, pp. 6170–6196, 2016. DOI: `10.1109/TGRS.2016.2582959` (cited on page 51).

[47] M. Brolly and I. H. Woodhouse, "Vertical backscatter profile of forests predicted by a macroecological plant model", *International journal of remote sensing*, vol. 34, no. 4, pp. 1026–1040, 2013. DOI: `10.1080/01431161.2012.715777` (cited on page 51).

[48] M. W. Palace, F. B. Sullivan, M. J. Ducey, R. N. Treuhaft, C. Herrick, J. Z. Shimbo, and J. Mota-E-Silva, "Estimating forest structure in a tropical forest using field measurements, a synthetic model and discrete return lidar data", *Remote Sensing of Environment*, vol. 161, pp. 1–11, 2015. DOI: `10.1016/j.rse.2015.01.020` (cited on page 52).

[49] A. S. Whitehurst, A. Swatantran, J. B. Blair, M. A. Hofton, and R. Dubayah, "Characterization of canopy layering in forested ecosystems using full waveform lidar", *Remote Sensing*, vol. 5, no. 4, pp. 2014–2036, 2013. DOI: `10.3390/rs5042014` (cited on page 52).

[50] D. B. Botkin *et al.*, *Forest dynamics: an ecological model.* Oxford University Press on Demand, 1993, ISBN: 0195065557. DOI: `10.1017/S0266467400008166` (cited on page 53).

[51] H. Bugmann, "A review of forest gap models", *Climatic Change*, vol. 51, no. 3-4, pp. 259–305, 2001. DOI: `10.1023/A:1012525626267` (cited on page 53).

[52] R. Fischer, F. Bohn, M. D. de Paula, C. Dislich, J. Groeneveld, A. G. Gutiérrez, M. Kazmierczak, N. Knapp, S. Lehmann, S. Paulick, *et al.*, "Lessons learned from applying a forest gap model to understand ecosystem and carbon dynamics of complex tropical forests", *Ecological Modelling*, vol. 326, pp. 124–133, 2016. DOI: `10.1016/j.ecolmodel.2015.11.018` (cited on pages 53, 54).

[53] A. Huth, T. Ditzer, H. Bossel, *et al.*, *The rain forest growth model FORMIX3: model description and analysis of forest growth and logging scenarios for the Deramakot Forest Reserve (Malaysia).* E. Goltze, 1998, ISBN: 3884523856 (cited on page 53).

[54] R. Fischer, A. Ensslin, G. Rutten, M. Fischer, D. S. Costa, M. Kleyer, A. Hemp, S. Paulick, and A. Huth, "Simulating carbon stocks and fluxes of an african tropical montane forest with an individual-based forest model", *PLoS One*, vol. 10, no. 4, e0123300, 2015. DOI: `10.1371/journal.pone.0123300` (cited on page 53).

[55] G. P. Asner, D. E. Knapp, E. N. Broadbent, P. J. Oliveira, M. Keller, and J. N. Silva, "Selective logging in the brazilian amazon", *science*, vol. 310, no. 5747, pp. 480–482, 2005. DOI: `10.1126/science.1118051` (cited on page 54).

[56] R. Horn, "The dlr airborne sar project e-sar", in *Geoscience and Remote Sensing Symposium, 1996. IGARSS'96.'Remote Sensing for a Sustainable Future.', International*, IEEE, vol. 3, 1996, pp. 1624–1628. DOI: `10.1109/IGARSS.1996.516751` (cited on page 58).

[57] R. Horn, A. Nottensteiner, A. Reigber, J. Fischer, and R. Scheiber, "F-sar—dlr's new multifrequency polarimetric airborne sar", in *Geoscience and Remote Sensing Symposium, 2009 IEEE International, IGARSS 2009*, IEEE, vol. 2, 2009, pp. II–902. DOI: `10.1109/IGARSS.2009.5418244` (cited on page 58).

[58] S. Abdullahi, F. Kugler, and H. Pretzsch, “Prediction of stem volume in complex temperate forest stands using tandem-x sar data”, *Remote sensing of environment*, vol. 174, pp. 197–211, 2016. DOI: `10.1016/j.rse.2015.12.012` (cited on pages 58, 59).

[59] B. Staatsforsten, “Richtlinie für die mittel-und langfristige forstbetriebsplanung in den bayerischen staatsforsten, forsteinrichtungsrichtlinie fer 2011, bayerische staatsforsten, regensburg”, 2011 (cited on page 59).

Chapter 4

Comparison of Tomographic SAR Reflectivity Reconstruction Algorithms for Forest Applications at L-band

V. Cazcarra-Bes, M. Pardini, M. Tello-Alonso and K. P. Papathanassiou

IEEE Transactions on Geoscience and Remote Sensing
Published in September 2019. DOI: 10.1109/TGRS.2019.2934347

Key findings/points:

- Performance analysis of Capon beamforming, Fourier beamforming and compressive sensing algorithms for forest applications using simulated, as well as tomographic SAR data.
- Evaluation of the interpolation from a non-uniform to a uniform track distribution.
- Analysis of the temporal decorrelation effects for two TomoSAR implementations: tandem-like (bistatic) vs repeat-pass (monostatic).

The author's contributions:

- Development and implementation of the tomographic algorithms as well as the processing of the real and simulated data.
- Interpretation of the results and main writing of the manuscript.

The co-author's contributions:

- M. Pardini contributed with ideas, helped on the interpretation of the results, and he supervised the whole work.
- M. Tello-Alonso contributed in the initial steps of the paper, helped on the interpretation of the results, and she supervised some parts of the work.
- K. P. Papathanassiou contributed to the main ideas and revised the work.

Comparison of Tomographic SAR Reflectivity Reconstruction Algorithms for Forest Applications at L-band

V. Cazcarra-Bes[1,2], M. Pardini[2], M. Tello-Alonso[2] and K. Papathanassiou[2]

[1]Institute of Environmental Engineering, ETH Zürich, 8093 Zürich, Switzerland
[2]Microwaves and Radar Institute, German Aerospace Center (DLR), 82234 Wessling, Germany

Abstract

Forest structure is a key parameter for forest applications, but it is difficult to be estimated at the required spatial and temporal scales. In this context, synthetic aperture radar Tomography (TomoSAR) that allows, at lower frequencies, the 3-D imaging of natural volume scatterers with high spatial and temporal resolution may be a game changer. The aim of this article is to evaluate three TomoSAR algorithms, Fourier beamforming (FB), Capon beamforming (CB), and Compressive Sensing (CS) with respect to their performance in the reconstruction of the 3-D forest reflectivity. The implications of volumetric forest scattering, as well as the temporal decorrelation of scatterers, are analyzed. The algorithms are compared on a set of simulated scenarios and then evaluated on an experimental L-band data set composed by four acquisition dates, each one consisting of five tomographic tracks. The data were acquired in 2014, within a time span of two months, over the Traunstein forest (Germany) using the F-SAR system. Additionally, discrete airborne Lidar has been used for a qualitative evaluation. The results indicate that the CS reconstruction is, for many practical cases, superior when compared to FB or CB reconstructions as they achieve higher vertical resolution, especially in cases with a lower number of acquisitions and complex forest scenarios. By combining acquisitions performed at different days, the effect of temporal decorrelation on each algorithm for two different tomographic implementations (repeat-pass vs single-pass) has been assessed. The results indicate that simultaneously acquired image pairs allow a better reconstruction of the 3-D forest reflectivity.

4.1 Introduction

Forest structure is a critical forest parameter [1] that characterizes the successional stage, the development, the sustainability, the productivity [2], the biomass [3] and the biodiversity of a forest [4]–[6]. Moreover, the change of forest structure is an indicator of dynamic processes like the natural regeneration and growth, as well as the natural or human disturbances on it. The knowledge of forest structure and its evolution is important to model the development of forest ecosystems, e.g., in order to develop robust biomass estimators [7] or for assessing carbon fluxes associated with forest functionality [8].

Traditionally, forest structure characterization relies on sampling at local scales by means of field inventory plots. More recently, terrestrial laser scanning techniques able to catch the three-Dimentional (3-D) arrangement of vegetation compartments [9] have been used for this purpose as well. However, any extrapolation to larger scales depends on the ability of these measurements to represent their surrounding landscape. At the same time, the temporal continuity of such plot measurements is difficult to be established. Remote sensing techniques have the potential to overcome these limitations and to provide 3-D forest structure measurements over large areas. Nowadays, two remote sensing techniques allow the realization of 3-D forest measurements: Lidar (in full-waveform or high-density discrete-return configurations) [10]–[15] and synthetic aperture radar (SAR). In particular, for SAR configurations, Polarimetric SAR Interferometry (Pol-InSAR) [16] and SAR Tomography (TomoSAR) [17] are two techniques that allow extracting 3-D structure information. Pol-InSAR has been demonstrated in several experiments its value in the estimation of model-based forest structure parameters, e.g., forest height [18]. TomoSAR is an imaging technique that provides the full 3-D distribution of the backscattered power. Although studies of forest applications with TomoSAR are quite new, the potential of TomoSAR systems to estimate forest structure in temperate [19], [20] as well as tropical forest [21] in correspondence with Lidar and ground measurements have been pointed out. Therefore, in the present day, TomoSAR implementations at lower frequencies appear very attractive as they allow continuous 3-D forest structure measurements with high spatial and temporal resolution over large areas [22].

For the reconstruction of the 3-D radar reflectivity SAR Tomography relies on a set of multi-angular acquisitions acquired at the same (referred as single-pass TomoSAR) or at different times (referred as repeat-pass TomoSAR). One critical element in the tomographic processing chain is the selection of the reconstruction algorithm. The tomographic reconstruction algorithms can be separated into three main groups: model-based (or parametric), model-free (or nonparametric), and hybrid algorithms.

Model-based algorithms parameterize the vertical reflectivity profile, i.e. a vertical slice through the 3D reflectivity, in terms of geometrical and scattering properties [23]. The reflectivity profile is then calculated using the estimated individual model parameters. Examples are multiple signal classification (MUSIC) [24], [25], weighted subspace fitting (WSF) [26], and covariance matching estimator (COMET) [27], [28]. The assumed model is critical for the physical meaningfulness of the profiles and for avoiding interpretation ambiguities. However, more accurate parameterizations require higher dimensional models that may turn into underdetermined or ill-conditioned problems.

Model-free algorithms estimate the 3-D reflectivity without making assumptions on the structure of the data or using models to describe them. Algorithms in this category attempt to directly invert the Fourier relationship between data and the reflectivity profile. This allows the achievement of less constrained results, but makes their interpretation less straightforward. Fourier beamforming [29] and Capon beamforming [30] are probably the most used model-free tomographic algorithms. Their performance depends primarily, but not only, on the regularity of the available track distribution.

Finally, hybrid algorithms make no assumptions on the imaged scatterers, but they introduce constraints in the inversion. The coherence tomographic approach introduced in [31] expresses the reflectivity profiles as a weighted sum of a series of orthogonal functions, and the tomographic inversion consists in the estimation of the coefficients. Compressive sensing techniques follow a similar approach, with the additional constraint of sparsity (i.e. only few a nonzero coefficients) [32]–[37]. Other constraints can be imposed to improve the estimation of some profile features [38], [39].

In the particular case of forest scenarios, a vertical reflectivity profile is typically a continuous distribution of backscattered power due to the volumetric nature of scattering. In this context, the availability of a large number of images is a critical requirement for an accurate reconstruction of the reflectivity profile. However, TomoSAR data sets are typically constituted by a rather small number of images acquired with irregular track spacings, essentially due to flight or orbital time constraints. In this context, the TomoSAR inversion problem in forest scenarios becomes underdetermined in most cases. All available TomoSAR algorithms can also operate in the presence of this underdetermination, but the adopted design criteria reduce the reconstruction performance. This can result in increased ambiguities in the interpretation of the estimated profiles.

This article aims to evaluate the suitability and performance of three TomoSAR model-free algorithms, namely FB, CB and CS, to reconstruct the 3-D reflectivity for forest structure applications at lower frequencies. Simulated test scenarios and real tomographic SAR data at L-band are used to evaluate the performance of the three algorithms. FB and CB are selected because they do not rely on any data model or assumption, which allows a more general analysis. Moreover, they are widely used and very popular in the TomoSAR community. Regarding CS, it has been extensively used in urban scenarios (pointlike scatterers) with great results but its use over volumetric media is still not sufficiently understood.

An additional issue arises from the inability of actual tomographic (especially spaceborne) configurations to acquire the whole set of tomographic acquisitions simultaneously. This constraint introduces temporal decorrelation that, in most cases, compromises the reconstruction performance. For this, the effect of temporal decorrelation on the performance of the three reconstruction algorithms is also discussed. To analyze this, two different decorrelation scenarios, associated to different tomographic implementations are discussed. The first scenario refers to a conventional repeat-pass tomographic implementation where each acquisition is performed at a different time. The second scenario refers to a tandem-like tomographic implementation where each acquisition consists of a pair of images acquired simultaneously [22], and the tomographic data set is built-up by a number of such image pairs.

The article is organized as follows: Section 4.2 describes the basic principles of SAR tomography and the three TomoSAR algorithms addressed. In Section 4.3, the three algorithms are applied and evaluated on simulated scenarios. In Section 4.4, the three algorithms are applied and assessed on experimental TomoSAR data sets. In this section, the impact of a nonuniform acquisition distribution is discussed; moreover the effect of temporal decorrelation on the tomographic reconstruction performance is analyzed and evaluated for different tomographic configurations for all three algorithms. Finally, the conclusions are drawn in Section 4.5. Additionally, a ranking of the algorithms is given in the Appendix 4.6.

4.2 SAR Tomography

Due to their ability, especially at lower frequencies, to penetrate into and through the canopy and forest layers, radar pulses interact with different vegetation elements at different heights within the forest volume and with the underlying ground. A single SAR image however, represents only a two dimensional (2-D) projection of this 3-D scattering process [40]. The availability of a set of images acquired under slightly different incidence (or look) angles (see Figure 4.1) allows the reconstruction of the 3-D scattering process by means of the 3-D radar reflectivity employing tomographic techniques [17].

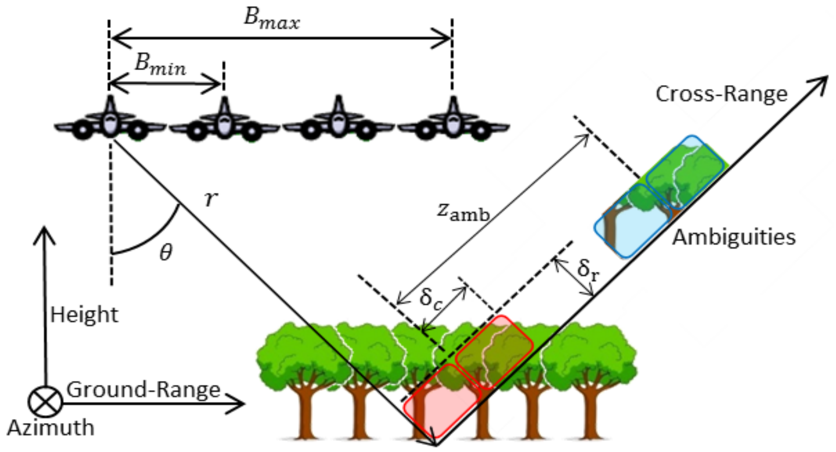

FIGURE 4.1: Geometry of the tomographic SAR configuration. B_{max} and B_{min} represent the maximum and minimum distance between each acquisition, respectively. The distance to the scatterer is represented by r and θ is the incidence angle. Red boxes: resolution cell, characterized by the vertical resolution δ_z (see 4.5), the cross range resolution δ_c and the slant-range resolution δ_r. Blue boxes: ambiguities of the desired signal that appear at the distance z_{amb} (see 4.6).

4.2.1 SAR Tomography: Problem Statement

A tomographic data set is composed by M, coregistred and phase calibrated [17], single-look complex (SLC) SAR images acquired with slightly different incidence (or look) angles along spatially displaced tracks (or orbits) [17]. For a given range-azimuth coordinate, the SLC image amplitudes $\{y_m\}_{m=1}^{M}$ can be arranged in form of a (column) data vector $\mathbf{y}$ as

$$\mathbf{y} = \; [y_1, \ldots, y_M]^T \tag{4.1}$$

where $(\cdot)^T$ denotes the transpose operator.

For each SLC image pair, the following Fourier relationship holds between the covariance and the vertical density of backscattered power $F(z)$, also called vertical reflectivity profile [16], [40]

$$E\{y_m y_n^*\} = \int F(z)\, e^{jk_z(m,n)z} dz \tag{4.2}$$

for $m, n = 1, \ldots, M$, where $E\{\cdot\}$ denotes the statistical expectation operator and $(\cdot)^*$ the complex conjugate. The socalled vertical wavenumber $k_z(m,n)$ expresses the sensitivity (i.e. the derivative) of the phase of $E\{y_m y_n^*\}$ to a height change [16], [17], [40] and can be expressed as

$$k_z(m,n) = \frac{4\,\pi\,\Delta\,\theta\,(m,n)}{\lambda\; sin(\theta)} \tag{4.3}$$

where $\Delta\theta\,(m,n)$ is the incidence-angle difference associated with the pair formed by the mth and the nth acquisitions, λ is the wavelength, and θ is the incidence angle. By increasing the spatial separation between the tracks $B\,(m,n)$, $\Delta\theta\,(m,n)$ and consequently $k_z\,(m,n)$ increase.

Equation 4.2 states that each image pair is associated with one spectral sample (i.e. a covariance) of $F(z)$ in the vertical wavenumber domain. Accordingly, the whole tomographic data set provides several spectral samples, that can be collected in an (MxM)-dimensional covariance matrix $R := E\{\mathbf{y}\mathbf{y}^H\}$ with

$$[\mathbf{R}]_{m,n} = E\{y_m y_n^*\} \tag{4.4}$$

where $(\cdot)^H$ indicates the Hermitian operator. It should be noted here that the estimation of the expectation of a stochastic process requires several realizations. This is in general not possible in real SAR data sets. However, assuming ergodicity, the statistical expectation is approximated by averaging neighboring samples within a range-azimuth (multilook) cell.

The TomoSAR inversion problem can be stated as the estimation of $F(z)$ through the inversion of the Fourier relationship 4.2 given a multilook estimate $\hat{\mathbf{R}}$ of $\mathbf{R}$.

With reference to Figure 4.1, two important parameters that characterize the TomoSAR inversion can be derived. The first one is the vertical Rayleigh resolution δ_z , which is inversely proportional to $k_{z,max} = max_{m,n}\{k_z(m,n)\}$ is given by [17]:

$$\delta_z = \frac{2\pi}{k_{z,max}}. \tag{4.5}$$

The second one is due to the finite sampling in the wavenumber domain, which causes the appearance of replicas of $F(z)$ in any of its estimates. The width of the non-ambiguous TomoSAR height interval is given by [17]:

$$z_{amb} = \frac{2\pi}{k_{z,min}} \tag{4.6}$$

where $k_{z,min} = min_{m,n}\{k_z(m,n)\}$. $k_{z,max}$ and $k_{z,min}$ are directly proportional to the maximum and minimum track displacements B_{max} and B_{min} , respectively.

4.2.2 Tomographic Algorithms

From 4.2, the TomoSAR inversion can be addressed as a spectral estimation problem [29], [30], [41]. The integral in 4.2 can be discretized on a set of H heights $\{z_i\}_{i=1}^{H}$, and estimates $\hat{F}(z_i)$ of $F(z_i)$ are obtained from the solution of a system of M^2 equations and H unknowns [34]

$$\mathbf{r} = \mathbf{A}\mathbf{f}. \tag{4.7}$$

In 4.7, $\mathbf{r} = vec(\mathrm{R})$ expresses the vectorization of $\mathbf{R}$, i.e. an M^2-dimensional column vector obtained as the stack of the columns of $\mathbf{R}$ each one on top of the other, and $\mathbf{f}$ is an H-dimensional column vector with generic element $[\mathbf{f}]_i = F(z_i)$. The $(M^2 xH)$-dimensional matrix $\mathbf{A}$ is the so-called steering matrix defined as

$$\mathbf{A} = \left[e^{jvec(\mathbf{K})z_1}, \cdots, e^{jvec(\mathbf{K})z_H}\right] \tag{4.8}$$

i.e. each column is obtained from the vectorization of the matrix (MxM)-dimensional matrix $\mathbf{K}$ with generic element $[\mathbf{K}]_{m,n} = k_z(m,n)$.

Volume scatterers are characterized by a continuous and extended vertical distribution of backscattered power. In this case, the number of available images M is in general too small to allow a determined inversion problem for the required H. In order to deal with this underdetermination, two approaches can be followed:

1. The first approach estimates the vertical reflectivity profile $F(z_i)$ as the output power of a filter, whose response is defined by a (height-varying) M-dimensional set of coefficients $\mathbf{h}(z_i)$. In this case $F(z_i) = E\{|\mathbf{h}^H(z_i)\mathbf{y}|^2\}$ leading to estimates of the form [29]

   $$\hat{F}(z_i) = \mathbf{h}(z_i)^H \hat{\mathbf{R}} \mathbf{h}(z_i). \tag{4.9}$$

   The generic $\mathbf{h}(z)$ should pass undistorted the backscattering contribution at z_i only, and at the same time cancel all the interfering contributions at the other heights. The rather small M prevents a complete cancellation. Thus, the choice of $\mathbf{h}(z)$ affects the final vertical resolution and the contrast (i.e. the sidelobe level) of $\hat{F}(z)$, as well as the estimation performance. FB and CB are such filter-based algorithms.

2. The second approach, to get the vertical reflectivity profile $F(z_i)$, directly inverts the system in 4.7, by assuming that $F(z)$ is sparse if expanded onto a given function basis. This means that only a low number of nonzero expansion coefficients are needed for the estimation of $\hat{F}(z_i)$ by means of CS techniques. In this way, the underdetermination is directly resolved.

4.2.2.1 Fourier Beamforming

In Fourier Beamforming (FB), a filter at a given height is designed assuming that the scattering contributions at all the other heights to be canceled are of equal power. This is equivalent to white noise, and therefore, from 4.9 the total power to be minimized is simply $\mathbf{h}^H\mathbf{h}$. As a consequence, the filter design criterion becomes [29], [30], [41]:

$$\mathbf{h}_{BF}(z) = arg\, min_h \quad [\mathbf{h}^H(z)\mathbf{h}(z)] \quad subject\, to \quad \mathbf{h}^H(z)\mathbf{a}(z) = 1. \tag{4.10}$$

In 4.10, $a(z)$ is the steering vector, calculated from the first column of K with the generic element:

$$[\mathbf{a}(z)]_m = e^{jk_z(m,1)z}. \tag{4.11}$$

$\mathbf{a}(z)$ contains the phase differences of all images (e.g. acquisitions) with respect to the first one, and represents the backscattered signal generated by an elementary (pointlike) scatterer at a generic height. The solution of 4.10 is

$$\mathbf{h}_{BF}(z) = \mathbf{a}(z)/M. \tag{4.12}$$

By using 4.12 in 4.9, it follows that the resulting estimate $\hat{F}_{FB}(z)$ is the squared absolute value of the discrete Fourier transform (DFT) of the data vector 4.1 averaged over the multiple looks [29], [41]. Similarly, $\hat{F}_{FB}(z)$ corresponds to the direct DFT of the covariance sample weighted by a (triangular shaped) Bartlett window [42]. It is worth noting that the equivalence to the DFT is strictly valid for uniformly distributed wavenumbers, and FB is the algorithm closest to a direct inversion of 4.2.

The FB estimation process is linear and stationary, i.e., the FB profile of a sum of scattering contributions equals the sum of the individual FB profiles obtained with the same filter 4.12. Accordingly, $\hat{F}_{FB}(z)$ can be interpreted as the convolution of $F(z)$ with the TomoSAR point spread function (PSF), i.e., the FB profile of a pointlike scatterer, that depends only on the wavenumber distribution. Thus, the vertical resolution of the FB estimate corresponds approximately to the Rayleigh resolution 4.5 [29]. The sidelobe level and the wavenumber distribution reflected in the PSF affects the radiometric accuracy. Especially for nonuniformly distributed wavenumbers, the resulting sidelobes complicate the geometric interpretation and bias the radiometry. Indeed, the main lobes of weak scatterers can be confused with or masked by the sidelobes of stronger ones depending on the height difference of the two scatterers compared to the vertical resolution.

4.2.2.2 Capon Beamforming

CB [43] allows a higher vertical resolution and lower sidelobes levels than FB [30]. Like FB, it is based on a filter design criterion, but in this case, the filters are defined adaptively to the data [29]

$$\mathbf{h}_{CB}(z) = arg\,min_{h} \quad [\mathbf{h}^{H}(z)\hat{\mathbf{R}}\mathbf{h}(z)] \quad subject\ to \quad \mathbf{h}^{H}(z)\mathbf{a}(z) = 1. \tag{4.13}$$

The adaptation to the data is guaranteed by the minimization of the true filter output power (see 4.9) which depends on R . The closed form solution of the minimization problem is [29], [43]

$$\mathbf{h}_{CB}(z) = \frac{\hat{\mathbf{R}}^{-1}\mathbf{a}(z)}{\mathbf{a}^{H}(z)\hat{\mathbf{R}}^{-1}\mathbf{a}(z)}. \tag{4.14}$$

The CB estimate of the reflectivity profile $F_{CB}(z)$ is obtained by using 4.14 in 4.9.

For each fixed height z , CB minimizes the interference of the contributions at different heights by placing proper nulls in the response of $\mathbf{h}_{CB}(z)$. From 4.14, it is apparent that the adaptation makes the filter response change with both height and distribution of scatterers. The vertical resolution changes accordingly, and it is typically better than the Rayleigh one. At the same time, the improvement in resolution is achieved at the cost of a poorer radiometric accuracy [44]. Inaccuracies in $\hat{\mathbf{R}}$ (e.g., due to a low number of looks) and/or residual phase errors may lead to a partial cancellation of meaningful scattering contributions [45]. In order to reduce these problems, the adaptation is reduced by applying a diagonal loading to the covariance matrix introducing a factor ρ as

$$\hat{\mathbf{R}}_{CB} = \hat{\mathbf{R}} + \rho\mathbf{I}_{M} \tag{4.15}$$

where $\mathbf{I}_{M}$ is the identity matrix of order M. $\hat{\mathbf{R}}_{CB}$ is then used in 4.14 for the calculation of the filter. The higher ρ , the closer becomes $\hat{F}_{CB}(z)$ to $\hat{F}_{FB}(z)$.

Radiometreically, especially for pointlike scatterers, CB can be even more accurate than FB as a direct consequence of the higher vertical resolution [29], [43]. However, CB is not optimized for volume scatterers where the nulling process of the filter becomes less effective, leading to less accurate power estimates. Depending on the wavenumber distribution, strong volume decorrelation levels may require the employment of larger loading factors, reducing the adaptation capability.

However, even in these critical situations, the use of CB may still be preferable to FB due to the better attenuation of sidelobes even for nonuniform wavenumber samplings with unfavorable PSF.

4.2.2.3 Compressive Sensing

More recently, approaches based on CS techniques [46] have been proposed to resolve the underdetermination of the equation system in 4.7 due to the limited amount of covariance samples [32]–[36]. According to CS theory, a TomoSAR profile can be reconstructed from a low number of covariance samples under the assumption that (1) the profiles are sparse, meaning that they have a low number of nonzero coefficients, and (2) the matrix **A** fulfills the restricted isometry property (RIP). This property essentially requires that matrix **A** approximately behaves like an orthonormal system [47]–[49].

The sparsity condition is too restrictive, and most of the profiles of interest do not fulfill it. However, the application of CS techniques can be extended to compressible profiles, i.e., profiles that produce a sparse representation when projected on an appropriate sparsifying basis. This is assumed to be the case for $F(z)$, as close-by power contributions are expected to be correlated. Indeed, the projection onto an appropriate wavelet basis provides a sparse expansion of the reflectivity profiles in forest scenarios [50]. With reference to 4.7, by denoting **W** the (HxH)-dimensional matrix whose columns are the first H functions of the wavelet basis evaluated at $\{z_i\}_{i=1}^{H}$, the H-dimensional vector of the sparse wavelet coefficients α results

$$\boldsymbol{\alpha} = \mathbf{Wf} \tag{4.16}$$

and 4.7 can be rewritten as

$$\mathbf{r} = \mathbf{AW}^{-1}\boldsymbol{\alpha}. \tag{4.17}$$

The estimation of **f** requires to obtain an estimate $\hat{\boldsymbol{\alpha}}$ of $\boldsymbol{\alpha}$, that can be formalized by means of the following constrained minimization problem:

$$\hat{\boldsymbol{\alpha}} = argmin_{\boldsymbol{\alpha}} \|\boldsymbol{\alpha}\|_{2,1} \quad subject\ to \quad \|\mathbf{r} - \mathbf{AW}^{-1}\boldsymbol{\alpha}\|_F \leq \varepsilon. \tag{4.18}$$

In this article, the minimization is performed by means of nonlinear reconstruction in the form of a disciplined convex programming [51] under the additional condition that all elements of **f** are positive. In 4.18 ε is an upper bound for the error allowed in the estimation (model mismatch), and $\|\cdot\|_{2,1}$ and $\|\cdot\|_F$ stand for the mixed (2,1) and Frobenius norm, respectively. Equation 4.18 can further be expressed as [49], [52]

$$\hat{\boldsymbol{\alpha}} = argmin_{\boldsymbol{\alpha}}[\tau \sum \|\alpha\|_{2,1} + \mu\|\mathbf{r} - \mathbf{AW}^{-1}\boldsymbol{\alpha}\|_F] \tag{4.19}$$

where τ and μ are two weighting parameters controlling the balance between sparsity and accuracy of the estimation. For the results presented in this paper τ is set to 2 and μ to 0.5. The minimization in 4.19 is associated with a higher computational cost compared to FB and CB.

Finally, after $\boldsymbol{\alpha}$ is estimated, the CS estimate of the reflectivity profiles $\hat{F}_{CS}(z)$ is obtained as $\mathbf{f} = \mathbf{W}^{-1}\boldsymbol{\alpha}$.

The most critical step of the application of CS inversion to forest volume scatterers is the choice of an appropriate (wavelet) basis that can guarantee a sufficiently sparse set of coefficients for a wide variety of reflectivity profiles. If sparsity in the expansion basis is achieved, the CS is expected to increase the probability of locating weak scatterers. On the contrary, if sparsity is not achieved, the estimated CS profile may not reflect a continuous distribution of scatterers. This can produce artifacts in the form of false local maxima in the estimated profiles, causing interpretation ambiguities. In this article, a Symmlet wavelet with four vanishing moments and two levels of decomposition is used [50].

4.3 Simulations

The three tomographic algorithms introduced in Section 4.2 are first compared by means of simulated analyses, that allow a direct comparison of individual isolated characteristics, which is often not possible with real data. The performance in the estimation of the reflectivity of extended volume scatterers is evaluated under certain constrains and acquisition geometry imposed by the capabilities of actual or near-future remote sensing tomographic missions.

The algorithms are compared on four scenarios defined to evaluate: the achieved vertical resolution, the ability to detect weak layers (scatterers), the stability with respect to an irregular wavenumber distribution and the performance loss as a consequence of a reduced number of acquisitions. The vertical reflectivity profiles consisting of different canopy layers are simulated using Gaussians. The power of the Gaussian refers to the density of scatterers in the canopy layer while its width refers to its vertical extension. Figure 4.2 shows an example of a forest with two canopy layers and its simulated reflectivity profile $F(z)$.

For computing the steering vector $\mathbf{a}(z)$, the number and distribution of tracks, as well as the interval of heights, need to be established. For all the simulations, H is equal to 128 samples from 0 to 64 m and five tracks with a uniform k_z distribution between 0 and 0.4 rad/m have been used providing a δ_z of 15.7 m and a z_{amb} of 63 m. These values have been chosen to be similar to the ones of the real data used in Section 4.4. The multibaseline covariance matrix $\mathbf{R}$ is then obtained according to (7), and then, the FB, CB, and CS algorithms have been applied to estimate the reflectivity profile $\hat{F}(z)$.

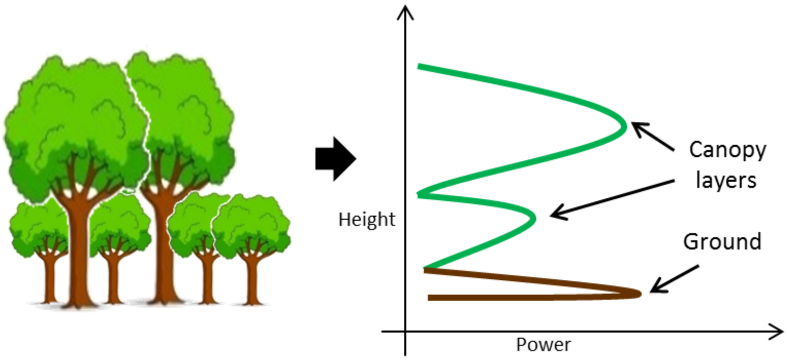

FIGURE 4.2: Simulation of the ideal reflectivity profile of a forest of two canopy layers and the ground.

4.3.1 Resolution: Two Layers at Varying Distance

The first simulation scenario aims to test the vertical resolution achieved by the three algorithms and their ability to distinguish layers with decreasing distance between them. Figure 4.3(a) shows the simulation scenario where two layers, a canopy layer, and a ground layer, both with the same power and a width with a standard deviation of 3 and 5 respectively, are coming closer to each other. The axes are given in terms of the Rayleigh resolution associated with the given number and distribution of vertical wavenumbers.

The reconstruction results achieved by the three algorithms, FB, CB, and CS, are shown in Figures 4.3(b),(c) and (d), respectively. In Figure 4.3(e), a (power) normalized vertical slice of the original and of the three reconstructions at 0.5 Rayleigh resolution are shown.

As expected, FB achieves the coarser resolution being able to distinguish the two layers only above the Rayleigh resolution. With CB the separation of the two layers is possible around 0.75 Rayleigh resolution, while CS is able to separate the two layers up to 0.45 Rayleigh resolution. This becomes clear in Figure 4.3(e): CS is able to distinguish clearly the two layers while CB and FB get only one.

CS also achieves a better contrast between the layers and the background. Due to the higher contrast of CS, very small local maxima could be interpreted as false layers. However, the power of these false layers is negligible compared to the main one and almost not visible. It is worth noting that the power ratio between the two layers is biased in all three reconstructions: FB and CB underestimate the power of the lower layer by 1.7 dB across the whole range of height distances. CS also underestimates the power of the lower layer on average about 0.8 dB, but the amount of underestimation varies with the distances of the two layers. When the layers are far from each other, the reconstructed reflectivity power is accurate. However, as soon as the layers are getting closer, the power estimates are becoming biased (up to -1.7 dB). Finally, for very close layers the reconstructed reflectivity power becomes accurate again.

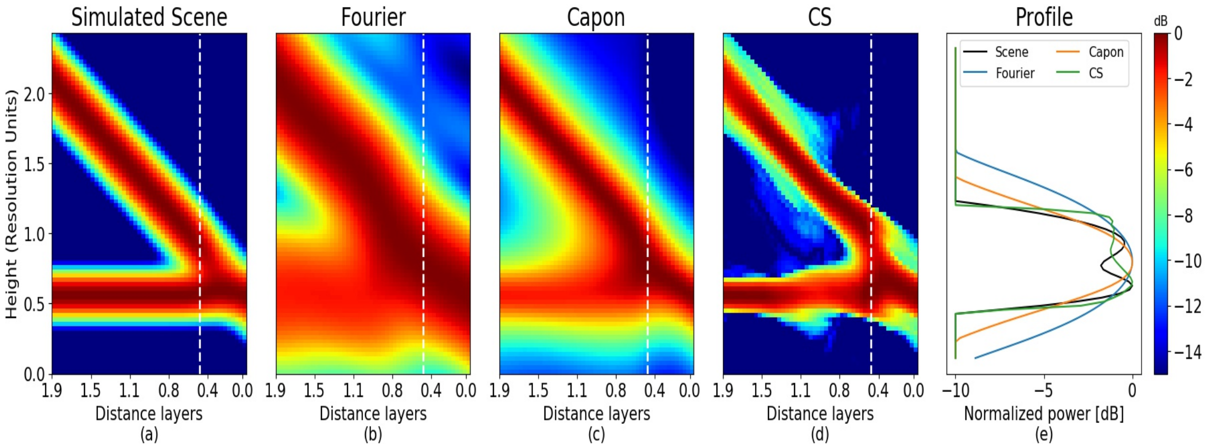

FIGURE 4.3: Simulated and estimated reflectivity profiles as a function of the distance between the layers. (a) Simulated scene, estimation provided by (b) FB, (c) CB and (d) CS. (e) Profile extracted from (a) to (d) in the simulation corresponding to the white dashed line. A Height resolution unit corresponds to 15.7 m.

4.3.2 Canopy Layers with Different Width and Relative Power

The second simulation scenario aims to test the ability of the three algorithms to detect a weaker layer (scatterer) in the presence of stronger ones. The simulation scenario is shown in Figure 4.4(a): Two canopy layers and one ground layer are considered. In the upper part a wide canopy layer is used, while for the lower heights a narrower one of the same power is simulated. In between these two layers, a second canopy layer of constant width but, from left to right, decreasing power is used. The x-axis indicates the power ratio between the middle and the lower (as well as higher) layer. The distance between the three layers remains constant at about Rayleigh resolution between neighboring layers.

The reconstruction results achieved by the three algorithms, FB, CB and CS, are shown in Figures 4.4(b), (c) and (d), respectively. In Figure 4.4(e), a (power) normalized vertical slice of the original and of the three reconstructions are shown. The profiles in Figure 4.4(e) correspond to the simulation where the middle layer has -3 dB less power than the other layers. For a power ratio bellow -3.8 dB, FB is not anymore able to detect the middle layer, while CB is able to detect it down to a power ratio of -4.15 dB. CS is able to detect the weaker middle layer up to a power ratio of -10 dB. The superior CS performance is clearly visualized with the profiles in Figure 4.4(e).

Similar as in the first scenario, the CS reconstruction achieves a better contrast between the layers and the background allowing a better discrimination of the canopy layers. With respect to the power reconstruction of the three layers all three algorithms provide biased results for the layer located at the bottom. More in detail, CS underestimates its power by 1.5 dB, which become 3 dB for FB and CB.

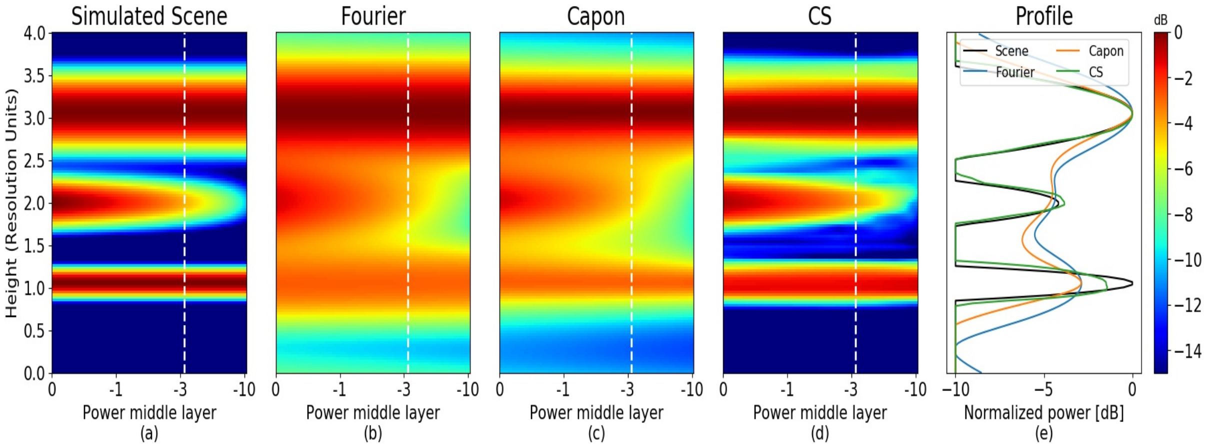

FIGURE 4.4: Simulated and estimated reflectivity profiles as a function of the different power between the layers. (a) Simulated scene, estimation provided by (b) FB, (c) CB and (d) CS. (e) Profile extracted from (a) to (d) in the simulation corresponding to the white dashed line. A Height resolution unit corresponds to 15.7 m.

4.3.3 Irregular Vertical Wavenumber Distribution

The third simulation scenario aims to test the stability of the three algorithms with respect to an irregular wavenumber distribution. The three layers have the same power and width and are separated by one Rayleigh resolution. By starting from the used baseline case of five uniformly distributed vertical wavenumbers between 0 and 0.4 rad/m, the distribution is distorted as shown in Figure 4.5(a). The reconstruction results achieved by the three algorithms, FB, CB, and CS, are shown in Figure 4.5(b), (c) and (d), respectively. In Figure 4.5(e), a (power) normalized vertical slice of the original and of the three reconstructions are shown. The FB results are strongly affected by the nonregular distribution of the available wavenumbers. The position and amplitude of the sidelobes of the PSF change with the wavenumber distribution. As a consequence, the visibility, width, and intensity of the main lobes of each scatterer are strongly affected by the superposition of the sidelobes of the other scatterers. Due to the limited vertical resolution and despite linearity, the radiometric accuracy can be lost even in the cases in which the three scatterers are visible. The CB results are more stable as the three layers are reconstructed at the right heights for all available wavenumber distributions. Even more, the relative power of the three layers is well preserved, but not their width. The CS reconstructions appear to be more stable with respect to the variation of the wavenumber distribution, allowing the reconstruction of the three layers at the right heights with the highest contrast between the layers and the background. In addition, the width of the layers is well preserved while the reconstruction of the power across all available wavenumber distributions shows a small, but larger than the one obtained by CB, variability. This behavior of the three reconstructions is clearly visible in the profiles in Figure 4.5(e).

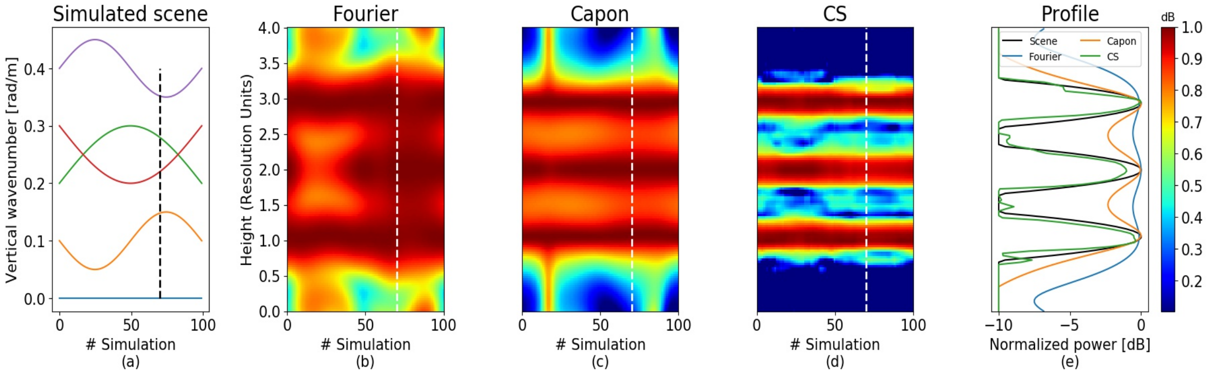

FIGURE 4.5: Simulated and estimated reflectivity profiles as a function of a nonuniform distribution of five vertical wavenumbers. (a) Vertical wavenumber distribution along the simulations, estimation provided by (b) FB, (c) CB and (d) CS. (e) Profile extracted from (a) to (d) in the simulation corresponding to the white dashed line. A Height resolution unit corresponds to 15.7 m.

4.3.4 Different Number of Vertical Wavenumbers

The fourth and last simulation scenario aims to test the robustness of the three algorithms with respect to the number of available acquisitions. For this, a scattering scenario consisting of two canopy layers of the same power and width separated by one Rayleigh resolution and a third ground layer of the same power, but smaller (half) width, located a half Rayleigh resolution below the lower canopy layer is considered (see Figure 4.6(a)). This scenario is reconstructed by the three algorithms for a changing number of vertical wavenumbers k_z: from 2 up to 14 uniformly distributed between 0 and 0.4 rad/m. The reconstruction results achieved by FB, CB and CS, are shown in 4.6(b), (c) and (d), respectively. In 4.6(e), a (power) normalized vertical slice of the original and of the three reconstructions are shown for the case of five vertical wavenumbers. For all numbers of vertical wavenumbers, FB gets the poorest vertical resolution resulting in a widening of the layers, followed by CB and CS. The higher contrast between the layers and the background characterize the CS results. The CS results are affected by artificial local maxima that could be interpreted as false layers. However, the power of these artificial maximas is about 10 dB lower than the true ones and allows a clear discrimination. For FB, the increase of the number of vertical wavenumbers beyond five has only a small effect on the retrieved profile. FB is not able to distinguish between the two lower layers as their distance is smaller than the Rayleigh resolution. In the case of CB and CS, the reconstructed layers become narrower with increasing the number of vertical wavenumbers. However, both CB and CS underestimate the power of the ground layer, i.e., in the case of the five vertical wavenumbers, the power of the ground for CB as well as CS is around -2 dB less than the expected one.

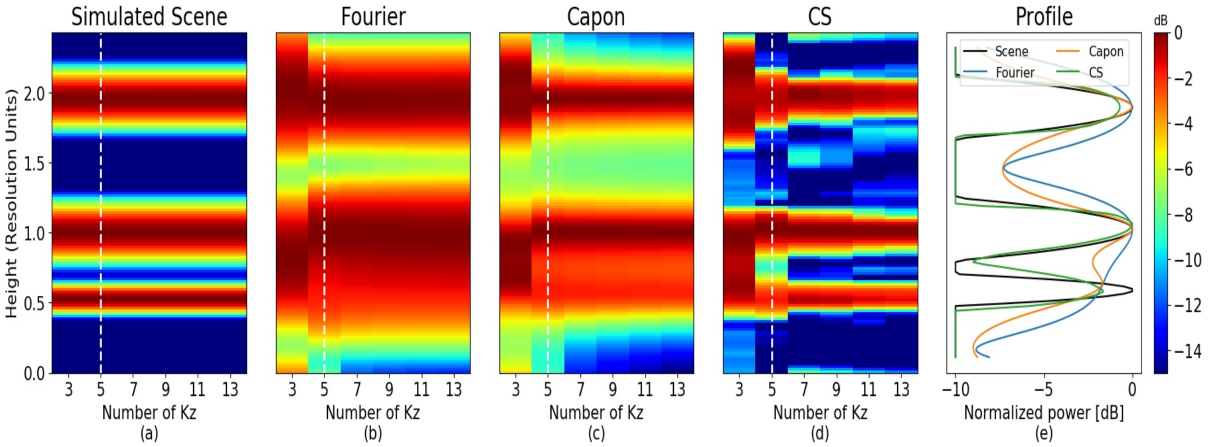

FIGURE 4.6: Simulated and estimated reflectivity profiles as a function of the number of uniform distributed vertical wavenumbers. (a) Simulated scene, estimation provided by (b) FB, (c) CB and (d) CS. (e) Profile extracted from (a) to (d) in the simulation corresponding to the white dashed line. A Height resolution unit corresponds to 15.7 m.

4.4 Real Data

4.4.1 Data Set

The data collected in the frame of a multi-temporal tomographic experiment in 2014 over the temperate forest of Traunstein (Germany) [19] were used to compare the performance of the three algorithms on a real data. The whole data set comprises four sets of fully polarimetric tomographic (i.e., multi-track) repeat pass acquisitions at L-band performed by the DLR's (German Aerospace Center) airborne F-SAR system [53]. Each of the four sets comprises five tracks acquired each time with the same geometry within a total time span of more than two months: on May 20, June 10, June 16 and July 28. The main parameters of the tomographic data set are summarized in Table 4.1. For comparison an airborne Lidar (LMS-Q 680i) data set (with a density of 25 points/m^2) of the site acquired on November 18, 2012 has also been used. Figure 4.7(a) shows the polarimetric Pauli RGB color composite image of the test site (generated from the acquisitions on May 20) and Figure 4.7(b) the Lidar derived top height map (first return) of the area.

TABLE 4.1: Main parameters of the tomographic SAR dataset.

Tracks	H_b[1]	V_b[1]	k_z[2]	z_{amb}[3]	Resolution (m)		
					δ_z[4]	Range[5]	Azimuth[5]
5	Refer.,7,15,20,25	Refer.,0,0,0,0	0,0.06,0.18,0.3,0.4	104.7	15.7	1.28	0.6

[1] H_b and V_b are the nominal horizontal (H_b) and vertical (V_b) track displacements (baselines) in meters respect to the reference one. Each track has an approximate deviation of ± 1.5 meters due to non-perfect flight path; [2] k_z is the vertical wavenumber at the centre of the image on May 20; [3] Height of ambiguity in meters; [4] Rayleigh resolution; [5] Slant range and azimuth resolution for the single look complex image before spatial averaging.

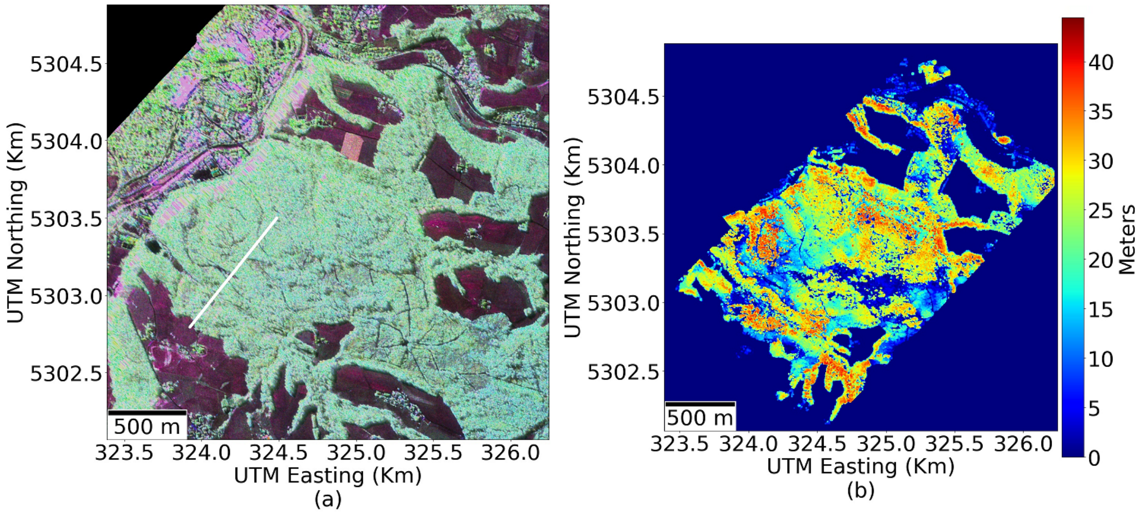

FIGURE 4.7: (a) F-SAR L-band Pauli RGB composite image, the white line indicates the area used in Figures 4.8 and 4.10. (b) Lidar top height (first return) over the Trauntein forest.

The resolutions in the slant-range and azimuth given in Table 4.1 refer to the original SAR SLC images. For the computation of the covariance matrix (see 4.4 in Section 4.2.1), a spatial averaging of 5 samples in slant-range and 11 in azimuth was used. Therefore, a final resolution of around 6.5 x 6.5 m in range and azimuth is obtained. No additional filtering of the data was applied.

The meteorological data collected from two local weather stations located within 20 km from the site at an hourly rate during the experiment indicate very similar conditions for all four campaign days [54]. There was no strong wind (< 1 m/s) and no precipitation neither during nor in the 24 hours before the acquisition. Only a negligible amount of rain was registered 48 hours before the acquisition on May 20 and July 28.

For each of the four tomographic data sets the temporal baseline between two consecutive tracks was about 10 minutes so that the whole set of five tracks was every time collected within less than one hour. Given also the low wind conditions on each of the campaign days, it is possible to assume that the temporal decorrelation within one single tomographic data set is rather small and can be neglected for the following investigations.

4.4.2 Original Vertical Wavenumber Distribution

Although the same geometry was attempted for each of the four tomographic data sets, deviations from the nominal flight track during the acquisitions distort the distribution of the vertical wavenumbers locally and introduce a small, but significant, variation of the acquisition geometry from day-to-day. In consequence, the vertical wavenumbers used to compute the steering vector $\mathbf{a}(z)$ (as in 4.11) are no longer uniformly distributed locally and vary across the four tomographic data sets. This may have an impact on the reconstructed reflectivity as indicated in Figure 4.8, where the impact of the non-ideal (i.e., distorted) real acquisition geometry on the reflectivity PSF for two (June 10 and July 28) of the four campaign days is shown. The left part of Figure 4.8 shows, in more detail, the PSF for around 1300 samples in azimuth over a line in range, highlighted with a white line in Figure 4.7(a), for the two mentioned days.

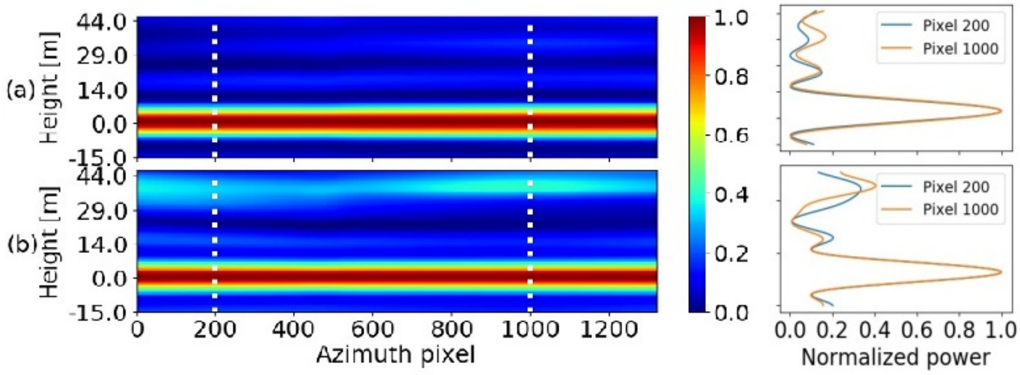

FIGURE 4.8: PSF over the area with a white line in Figure 4.7(a), for (a) July 28 with low error in the tracks and (b) for June 10 with high error in the tracks.

The PSF can be used as an indicator of the quality of the reconstructed reflectivity: all the power outside of the main lobe at 0 m contributes to the distortion of the reconstruction. As an example, the right part in Figure 4.8 shows the PSF profiles for two specific azimuth samples (indicated in white dashed lines), where the deviations on the distribution are clearly reflected on the big sidelobes of the PSF with around 4 dB less power than the main lobe. The k_z values for the two days are graphically represented in Figure 4.9. The July 28 acquisition geometry is only slightly distorted, characterized by a mean square error of 0.00040 rad/m with respect to a reference uniform distribution. The acquisition geometry on June 10 is significantly more distorted with a mean square error of 0.00875 rad/m with respect to a uniform distribution.

In order to assess better the distortion induced by the nonideal acquisition geometry, Figure 4.9(b) and (c) show the reflectivity profiles reconstructed by the three algorithms for the sum of the power of HH, 2HV and VV channels in correspondence of sample 1200 from Figure 4.10. A Lidar profile obtained from the Lidar point cloud is also plotted as a reference (black line) indicating the location of the ground at 0 m and a forest layer between 10 and 25 m. In order to obtain a continuous Lidar profile from the point cloud, a histogram of the heights of all returns in a resolution cell similar to the one obtained for the TomoSAR data (6.5 by 6.5 m.) is done. In that way, a continuous representation of the distribution of returns in height is obtained from the Lidar. Moreover, to compare the profiles from both systems, the Lidar profile is projected in slant-range geometry as in the case of the TomoSAR data.

For all three algorithms, it becomes obvious that the higher the error in the distribution of wavenumber, the worse the estimation of the reflectivity profile.

In Figure 4.9(b), the reconstructions for July 28, i.e., the day with the lower track deviations, are shown. All three algorithms are able to detect the two (ground and canopy) layers. FB introduces an additional third local maximum, as a consequence of a nonsuppressed sidelobe that could be misinterpreted as an additional layer. Although all three algorithms are able to detect the location of the two layers, CS performs significantly better. The higher resolution of CS allows better discrimination of closer layers, and the achieved higher contrast between the layers helps in their discrimination. Similar to the simulation results, here also reflectivity artifacts appear as local maxima close to the main maximum (that corresponds to the canopy layer) and could potentially be misinterpreted as layers. However, as in the simulations, these local maxima are very small allowing straightforward discrimination between the *false* and the *real* canopy layers.

In Figure 4.9(c), the reconstructions for June 10, i.e., the day with the higher track deviations, are shown. In the case of FB, the absolute and relative intensity of the third local maximum (i.e., the sidelobe) clearly increases. For the CB reconstruction, the main lobe associated with the forest layer becomes wider, and the sidelobes increase. The CS reconstruction appears more robust, with only a small increase of the sidelobe. This robustness of the CS approach with respect to the wavenumber distribution seen with the real data corresponds to what has been previously observed in the analysis on the simulated data in Figure 4.5 (see Section 4.3.3).

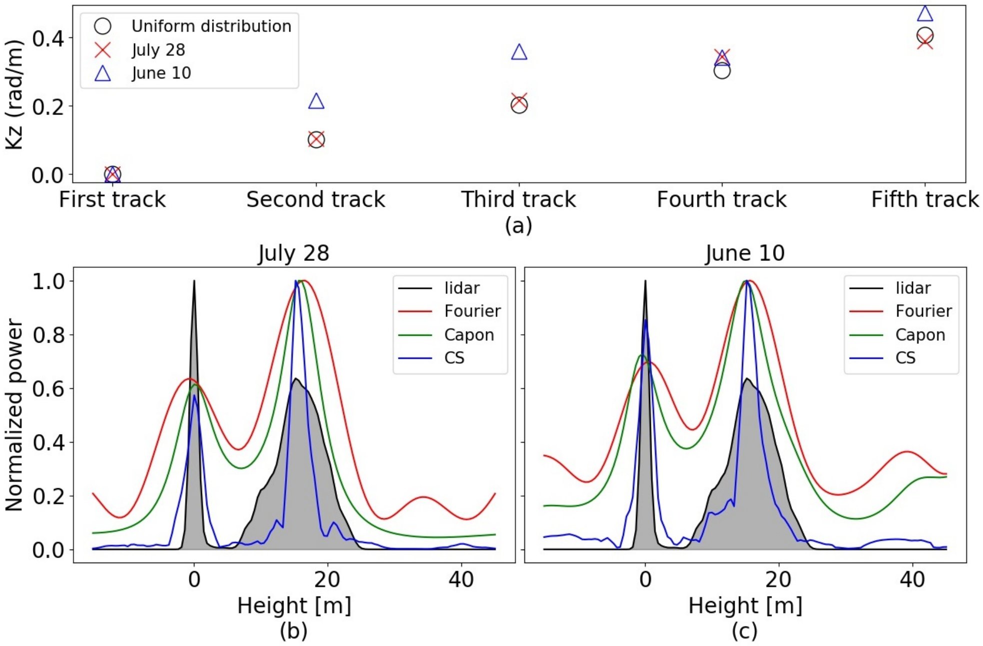

FIGURE 4.9: (a) Distribution of vertical wavenumber for a low (July 28) and high (June 10) track errors with respect to a uniform distribution for sample 1200 from Figure 4.10. (b) Vertical profiles for the same sample for July 28 with low error in the tracks. (c) June 10 with high error in the tracks.

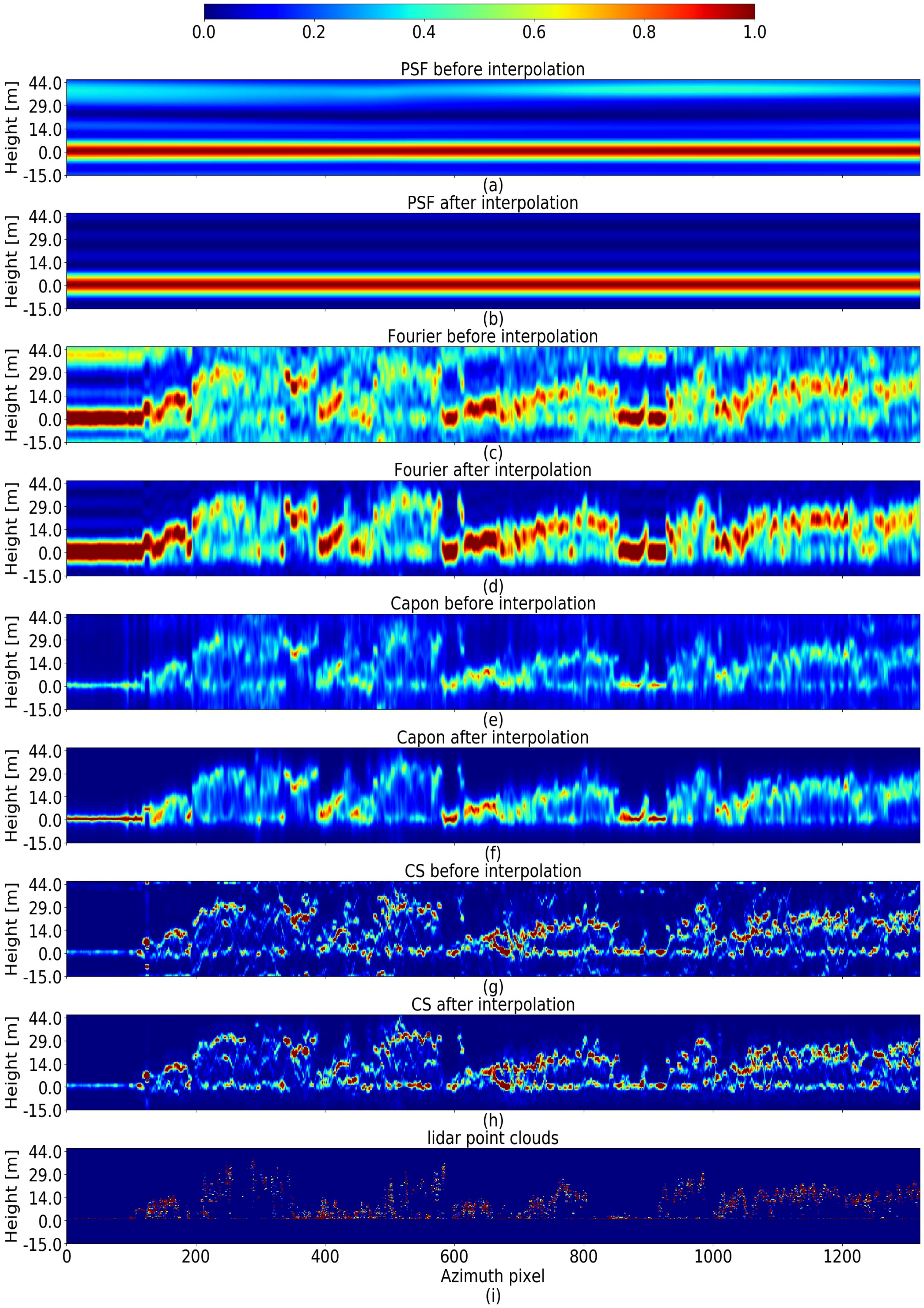

FIGURE 4.10: (a) PSF, (c) Fourier, (e) Capon and (g) CS for the sum of the power of HH, 2HV and VV channels over the area with a white line in Figure 4.7 before the interpolation and (b) PSF, (d) Fourier, (f) Capon and (h) CS over the same area after the interpolation. Color code: power of the radar reflectivity normalized along the transect. (i) Lidar point clouds from 2012, where the red values indicate high density and blue low density of returns. Each azimuth pixel represents a spacing of 0.8 m.

4.4.3 Interpolation to a Common and Uniform Wavenumber Distribution

A way to account for the distortions caused by the nonuniformly distributed vertical wavenumbers, and to minimize the performance variability of the tomographic reconstruction across the four data sets (induced by their different wavenumber distributions), is to interpolate the corresponding data vectors to a common uniform wavenumber distribution.

Let $\mathbf{a}_{int}(z)$ be the steering vector corresponding to the interpolated uniform tracks. As outlined in [55], [56] the interpolator is designed as a matrix $\mathbf{H}_{int}$ that linearly transforms $\mathbf{a}(z)$ into $\mathbf{a}_{int}(z)$ by minimizing the average interpolation error within the height interval $[z_{min}, z_{max}]$. This design criterion can be formalized as

$$\mathbf{H}_{int} = argmin_{H_{int}} \int_{z_{min}}^{z_{max}} \|\mathbf{a}_{int}(z) - \mathbf{H}_{int}\mathbf{a}(z)\|^2 dz. \tag{4.20}$$

The solution $\mathbf{H}_{int}$ can be calculated in closed form as in [56] after discretization of the height interval. A regularization factor has been included for increasing the interpolator robustness in the presence of noise and (small) residual phase calibration errors [57]. The interpolated data vector $\mathbf{y}_{int}$ and multi-look covariance matrix $\mathbf{R}_{int}$ are finally obtained as

$$\mathbf{y}_{int} = \mathbf{H}_{int}\mathbf{y}, \quad \hat{\mathbf{R}}_{int} = \mathbf{H}_{int}\hat{\mathbf{R}}\mathbf{H}_{int}^{H} \tag{4.21}$$

and used for the TomoSAR processing. The elements of $\hat{\mathbf{R}}_{int}$ are estimated by combining the elements of $\hat{\mathbf{R}}$ through $\mathbf{H}_{int}$.

It is worth noting that any attempt of using the interpolator as in 4.20 and 4.21 to obtain a larger maximum vertical wavenumber (i.e., better Rayleigh resolution) and/or larger number of vertical wavenumbers results into a meaningless extrapolation and / or interpolation. A larger maximum wavenumber in output does not increase the vertical resolution as the interpolator is linear. The increase of the number of vertical wavenumbers would provide a rank-deficient covariance matrix representing only a subspace of the information that could actually be obtained in the output covariance space in any scattering scenario.

Given a meaningful selection of the output wavenumber distribution, an inappropriate choice of the height interval $[z_{min}, z_{max}]$ can limit the interpolation performance. Indeed, the height interval constitutes a prior information exploited in the optimization of the matrix interpolator. For a fixed wavenumber distribution, the interpolation error is minimized if the interval is as tight as possible to the height interval occupied by the scattering components [55]. On the other hand, the interpolation becomes meaningless for narrower intervals [55], [56]. A second factor that can limit the performance of the interpolator in the case at hand is the irregularity of the input distribution of the vertical wavenumbers. Despite the matrix form, which provides a linear adaptive interpolation process, large gaps between consecutive wavenumbers might not be accurately resampled. In general, in the presence of inaccurate a prior information (i.e., larger height interval) and/or high wavenumber irregularity, the performance of the matrix interpolator is not superior to the one of a trivial bilinear or polynomial interpolator. However, this is not expected to be the case for the analysis in this article. Indeed, $[z_{min}, z_{max}]$ have been fixed according to the available Lidar digital terrain model and top canopy height, while the input wavenumber distributions do not exhibit large gaps, as shown in Figure 4.9.

Figure 4.10 shows the PSF and reflectivity transect as reconstructed by the three algorithms before and after the interpolation from the data set acquired on June 10 over the white line shown in Figure 4.7(a). As expected, the interpolation reduces the sidelobes of the PSF consistently along the whole transect, while the width of the main lobe remains unchanged (i.e., no change of vertical resolution). It is worth noting that the PSF main lobe amplitude does not change as well, i.e., the interpolation is radiometrically linear. The interpolation appears more effective for FB and CB rather than for CS, as CS is less affected (when compared to FB and CB) by the nonuniformity in the track distribution. As expected, the wide main lobe obtained by the FB algorithm indicates the rather poor resolution. The resolution is clearly improved by the CB and CS, as can be seen in the ground area on the left part of the transect. Concerning the forest areas, CS seems to differentiate between different scatterers that are mixed by CB and FB, although some small artifacts are expected as seen in the profiles analyzed in Figure 4.9, and in the simulation scenarios.

These effects can also be seen in Figure 4.11, where the profiles for the four days for the three algorithms before and after the interpolation for the sample 1200 of Figure 4.10 are shown. Independently of the algorithm that has been applied, the profiles of the four days are more similar between them after the interpolation. This similarity of the profiles for the four days is something expected, due to the fact that in the total period of two months no human activity or relevant environmental/seasonal changes have occurred. Figure 4.11 confirms the better resolution and the higher contrast for CS, which allow better detection of the position of the canopy layers. Moreover, CS shows the appearance of small artifacts with very low power with respect to the main lobe, which are reduced after the interpolation.

Finally, regarding the computational cost, CS is two to three orders of magnitude more expensive than FB and CB for the same hardware conditions.

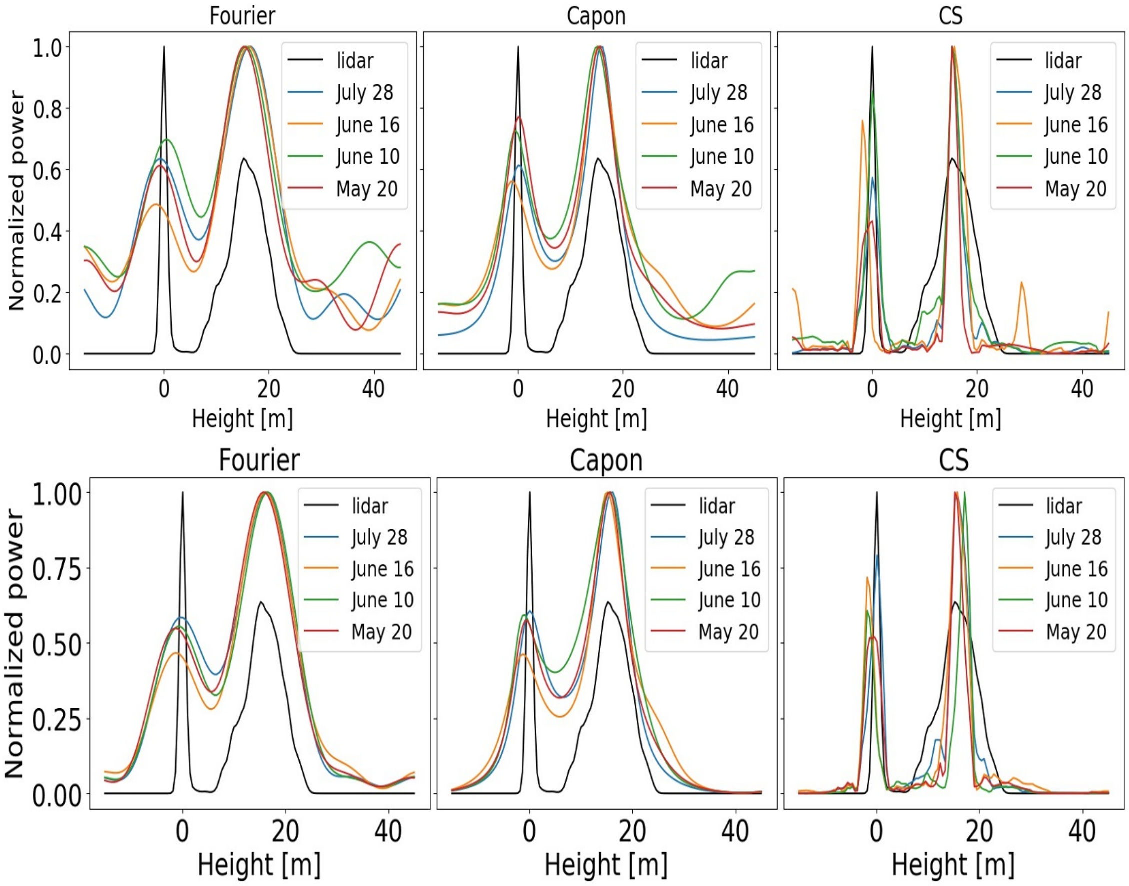

FIGURE 4.11: Vertical profiles for sample 1200 of the transect shown in Figure 4.10, (top) before the interpolation and (bottom) after the interpolation.

4.4.4 Temporal Decorrelation Effects on Different Tomographic Implementations

In this section, the three tomographic algorithms are compared with respect to their stability against different temporal decorrelation processes. Due to the inability of actual tomographic (especially spaceborne) implementations to acquire all tomographic acquisitions required simultaneously, temporal decorrelation between the tomographic acquisitions acquired at different times becomes an – in many cases critical – issue. In this context, two different decorrelation scenarios associated with different tomographic implementations are discussed.

The first scenario refers to a conventional repeat-pass tomographic implementation where each acquisition is performed at a different time. In order to process the data in a repeat-pass scenario, one of the data sets (i.e, the July 28) is selected as a reference. Then, the five acquisitions in that day are interpolated to a uniform wavenumber distribution. After that, the individual acquisitions (i.e., the SLC images) are replaced by equivalent (in terms of vertical wavenumber) ones extracted from the (interpolated) data sets acquired at one of the other available campaign days (i.e., on June 16, June 10 and on May 20). The fact that after interpolation, all four tomographic data sets have the same uniform wavenumber distribution, facilitates this exchange and allows a comparison with respect to temporal decorrelation effects only. The combinations used are summarized in Table 4.2.

TABLE 4.2: Combination of different days.

k_z	0	0.1	0.2	0.3	0.4
No combination	July 28	July 28	July 28	July 28	July 28
Combination 1	July 28	July 28	July 28	July 28	June 16
Combination 2	July 28	July 28	July 28	June 10	June 16
Combination 3	July 28	July 28	May 20	June 10	June 16
Combination 4	July 28	June 10	May 20	June 10	June 16

The second scenario refers to a tandem-like tomographic implementation [22], where each acquisition consists of a pair of images acquired simultaneously with a given vertical wavenumber. In this case, the tomographic data set is build-up by a number of such image pairs, each acquired on a different day and with a different vertical wavenumber. In order to investigate this case, starting from the acquisitions performed on the same day (i.e., on July 28), the elements of the covariance matrix are consecutively replaced by the equivalent elements of the tomographic covariance matrices formed using the acquisitions performed on the other days (i.e., on June 16, June 10, and May 20). The difference of the two scenarios is with respect to the effect of temporal decorrelation: While tandem-like tomographic implementations are affected only by the (temporal) variability of the underlying radar reflectivity function, conventional repeat-pass tomographic implementations are additionally affected by higher frequency decorrelation effects, as for example, wind-induced decorrelation.

4.4.4.1 Repeat-pass Tomographic Implementation

For simulating conventional repeat-pass tomographic implementation, acquisitions performed at different days are combined. Starting from the interpolated data vector $\mathbf{y}_{int}$ of the reference data set (i.e., the one acquired on July 28), one after another, the elements of $\mathbf{y}_{int}$ are replaced with the equivalent (in terms of vertical wavenumber) ones from the other (interpolated) data sets acquired at the other campaign days (i.e., on the June 16, June 10 and on May 20). Table 4.2 summarizes the different combinations used. Note that the data set acquired on July 28 has been selected to be the reference one as it is characterized by the lowest error in the wavenumber distribution (with respect to a uniform one), as well as, it is at one end of the timeline of the four acquisitions, which allows increasing the temporal difference linearly.

In Figure 4.12, the results of the three tomographic algorithms for the four different combinations are shown for a section of the transect from Figure 4.10. The first row corresponds to the reference case with the five acquisitions performed on the same day (July 28). Apparently moving from Combination 1 to 4, i.e., with increasing the number of acquisitions performed on different days, the reconstructed reflectivity profiles become more and more defocused (clearly visible on the ground reconstruction between samples 850 and 925). This is a direct consequence of the increasing temporal decorrelation between individual acquisitions. For evaluating this better, three different areas along the transect are discussed in the following.

The first area is situated between the samples 850 and 925 and is an area with only ground scattering contributions. The vertical profiles in correspondence of the green line in Figure 4.12 are shown in Figure 4.13(a). For all three algorithms, the reconstructed reflectivity profiles show a loss of power, as well as a significant loss in resolution with increasing temporal decorrelation between the individual acquisitions. In the CS reconstruction, the increase of temporal decorrelation is associated with some artifact contributions, although the main peak of the ground remains clearly dominant.

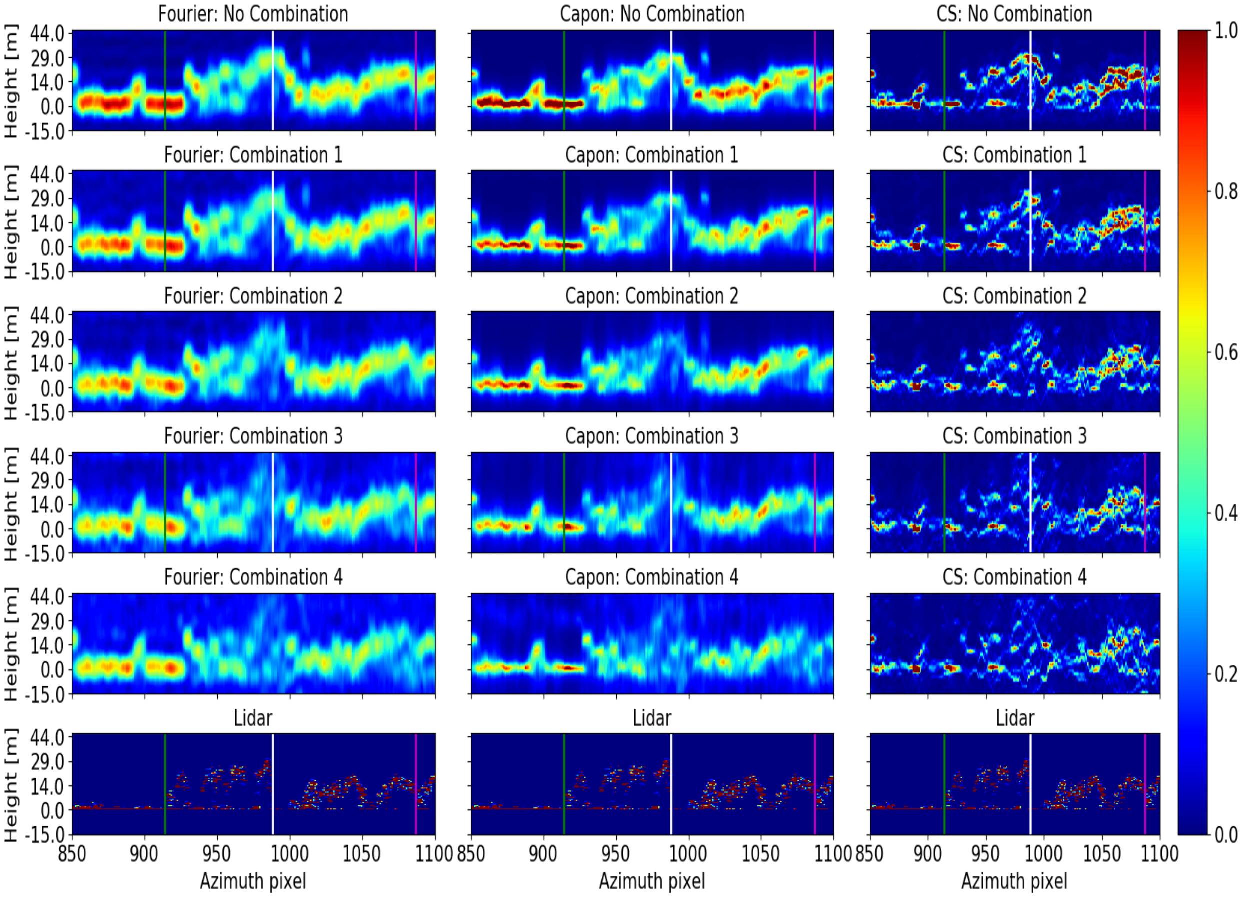

FIGURE 4.12: Profiles for Fourier (first column), Capon (second column) and CS (third column) for the combination of single SLC's (repeat-pass case) presented in Table 4.2 for the sum of the power of HH, 2HV and VV channels. Color code: power of the radar reflectivity normalized along the transect. Last row: Lidar point clouds from 2012, red indicates high density and blue low density of returns. The vertical lines correspond to the vertical profiles represented in Figure 4.13: The green line corresponds to a ground area, the white to a heterogeneous and not very dense forest and the purple one to a very homogenous and dense forest. Each azimuth pixel represents a spacing of 0.8 m.

The second area is between the samples 925 and 1000 and corresponds to a rather heterogeneous forest stand with a number of large trees and gaps. This is reflected in the higher amount of Lidar returns from the ground with respect to the canopy part. With increasing temporal decorrelation, the stand almost disappears in the reconstructed reflectivity. The vertical profiles in correspondence with the white line are shown in Figure 4.13(b). Without temporal decorrelation (orange line), FB and CB show no distinct maximum associated with the ground layer while CS detects the ground clearly. Further it becomes clear that temporal decorrelation severely distorts the structural interpretation of the reconstructed reflectivity. As soon as more days are combined, the power of the main lobe decreases for all three algorithms. For Combination 3 (red line) none of the algorithms are anymore able to reconstruct a meaningful profile.

Finally, the third area toward the end of the transect, between the samples 1050 and 1100, corresponds to a denser and more homogeneous forest stand. This is reflected in the higher amount of Lidar returns from the canopy. The increased homogeneity and density works in favor of the reflectivity reconstruction for all three algorithms. Only for Combination 4, the decorrelation effect on the reflectivity reconstruction becomes clearly visible. The vertical profiles in correspondence of the purple line are shown in Figure 4.13(c). Unlike the previous profile, the three algorithms are able to correctly reconstruct the profile for Combination 3. The defocusing is more pronounced for FB and CB. There is also a decrease in the power of the profile associated with the presence of temporal decorrelation. Similarly, as in other parts of the transect, in the case of CS, the increase of temporal decorrelation produces artifact contributions.

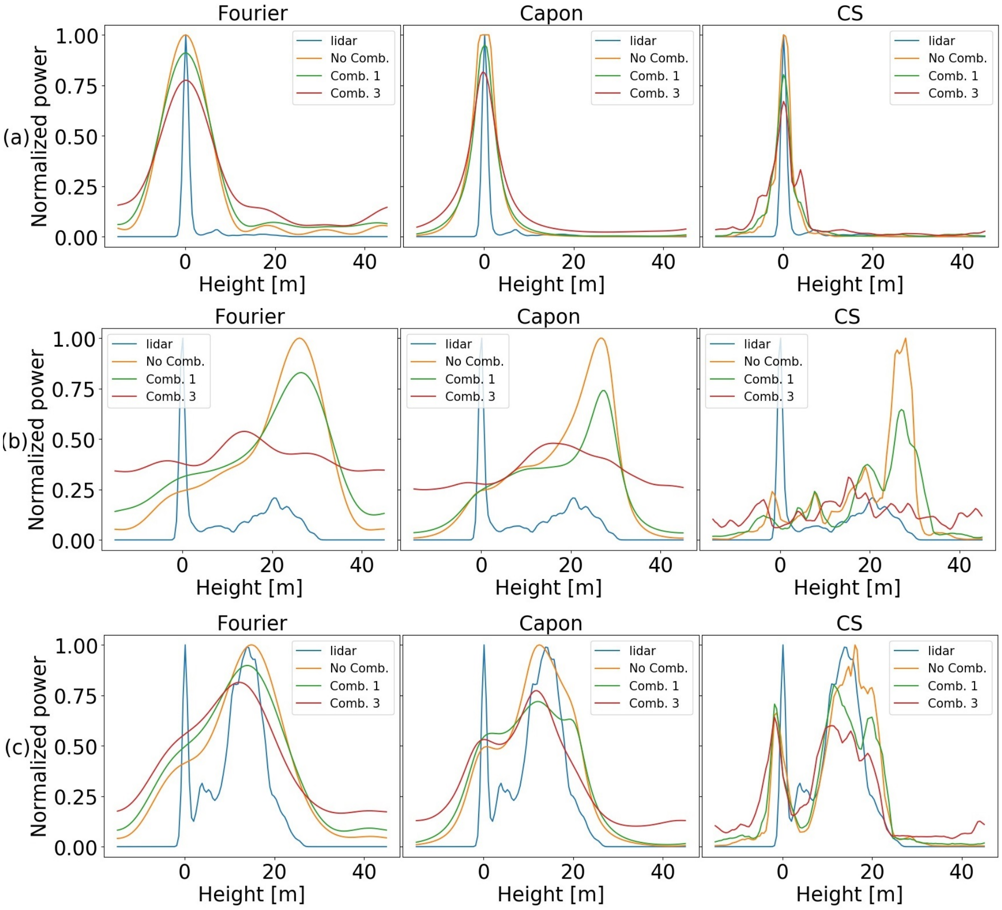

FIGURE 4.13: Vertical profiles for (a) green line, (b) white line, and (c) purple line from the transect in Figure 4.12.

4.4.4.2 Tandem-like Tomographic Implementation

In the tandem-like implementation each acquisition consists of a pair of images acquired simultaneously with a given vertical wavenumber. The tomographic data set is build-up by a number of such image pairs each acquired at a different day and with a different vertical wavenumber.

Starting from the interpolated data vector y_{int} of the reference data set (i.e., the one acquired on July 28) the corresponding covariance matrix $\mathbf{R}_{int}$ (see 4.4) for every day are obtained. From this, the coherence matrix is obtained as

$$\mathbf{C} = \mathbf{N}_R^{-\frac{1}{2}} \mathbf{R}_{int} \mathbf{N}_R^{-\frac{1}{2}} = \begin{bmatrix} 1 & \gamma_{12} & \cdots & \gamma_{1M} \\ \gamma_{12}^H & 1 & \cdots & \gamma_{1M} \\ \vdots & \vdots & \ddots & \vdots \\ \gamma_{1M}^H & \gamma_{2M}^H & \cdots & 1 \end{bmatrix} \tag{4.22}$$

where γ_{1M} represents the (complex) interferometric coherence (i.e., the normalized cross correlation) between the first and the Mth track. $\mathbf{N}_R$ is a diagonal matrix defined as follows:

$$\mathbf{N}_R = \begin{bmatrix} [\mathbf{R}_{int}]_{11} & 0 & \cdots & \cdots & 0 \\ 0 & [\mathbf{R}_{int}]_{22} & 0 & \cdots & \vdots \\ \vdots & \vdots & \ddots & \ddots & 0 \\ 0 & \cdots & \cdots & 0 & [\mathbf{R}_{int}]_{MM} \end{bmatrix} \tag{4.23}$$

Assuming that only two images are simultaneously acquired at each pass, zero coherence between images from different passes (days) is considered. Under this assumption, only the first row of the coherence matrix becomes available

$$\mathbf{c}_{first} = [1 \quad, \gamma_{12}, \quad \cdots \quad, \gamma_{1M}]. \tag{4.24}$$

In general, if there is not a complete temporal decorrelation, the coherence between images can be used to potentially improve the tomographic results [58].

Starting from the first row of the reference covariance matrix (i.e., on July 28), the row elements are consecutively replaced by the equivalent row elements of the other tomographic covariance matrices i.e., the ones formed using the acquisitions performed at the other days (i.e., on the June 16, June 10 and on May 20) following the combinations defined in Table 4.2.

As next, the complete coherence matrix $\mathbf{C}$ needs to be reconstructed from its first row $\mathbf{c}_{first}$. Due to the uniform wavenumber distribution (after resampling) the coherence matrix has a Toeplitz [59] form and can be reconstructed from $\mathbf{c}_{first}$ as

$$\mathbf{C}_{Toeplitz} = \begin{bmatrix} 1 & \gamma_{12} & \gamma_{13} & \cdots & \gamma_{1M} \\ \gamma_{12}^* & 1 & \gamma_{12} & \gamma_{13} & \vdots \\ \gamma_{13}^* & \gamma_{12}^* & 1 & \gamma_{12} & \gamma_{13} \\ \vdots & \gamma_{13}^* & \gamma_{12}^* & 1 & \gamma_{12} \\ \gamma_{1M}^* & \cdots & \gamma_{13}^* & \gamma_{12}^* & 1 \end{bmatrix} \tag{4.25}$$

where $(\cdot)^*$ indicates the complex conjugate. Finally, $\mathbf{C}_{Toeplitz}$ can be used for the tomographic reconstruction in all three algorithms in the same way as for the covariance matrix $\mathbf{R}_{int}$.

In Figure 4.14 the reflectivity profiles obtained by the three algorithms are shown for a section of the transect in Figure 4.10 for the four different combinations. The first row corresponds to the reference case with the five acquisitions performed on the same day (July 28). The improvement with respect to the results obtained using the repeat-pass configuration is for all three algorithms evident and can be assessed by looking again to the three scattering scenarios along the transect.

For the ground scattering case (situated in the transect between the samples 850 and 925) the vertical profiles in correspondence of the green line are shown in Figure 4.15(a). While the loss in resolution is obvious, more dramatic for FB than for CB and moderate for CS, the reflectivity power remains practically constant for all algorithms and all decorrelation combinations.

For the heterogeneous stand (situated between the samples 925 and 1000), the vertical profiles corresponding to the white line are shown in Figure 4.15(b). The results achieved are more stable than the ones in the equivalent repeat-pass case, and the combined FB and CB profiles are very similar to the reference ones. For Combination 3, CS is able to reconstruct the local maxima of the reference profile. However, the positions are shifted with respect to the reference ones, and a fourth reflectivity maximum appears, which could be considered as an artifact contribution.

Finally, the vertical profiles for the dense homogeneous stand (situated between the samples 1050 and 1100) in correspondence of the purple line are shown in Figure 4.15(c). Also here, the tandem-like results are more stable than the equivalent repeat-pass ones. There is no loss of reflectivity power for any combination in contrast to the repeat-pass case.

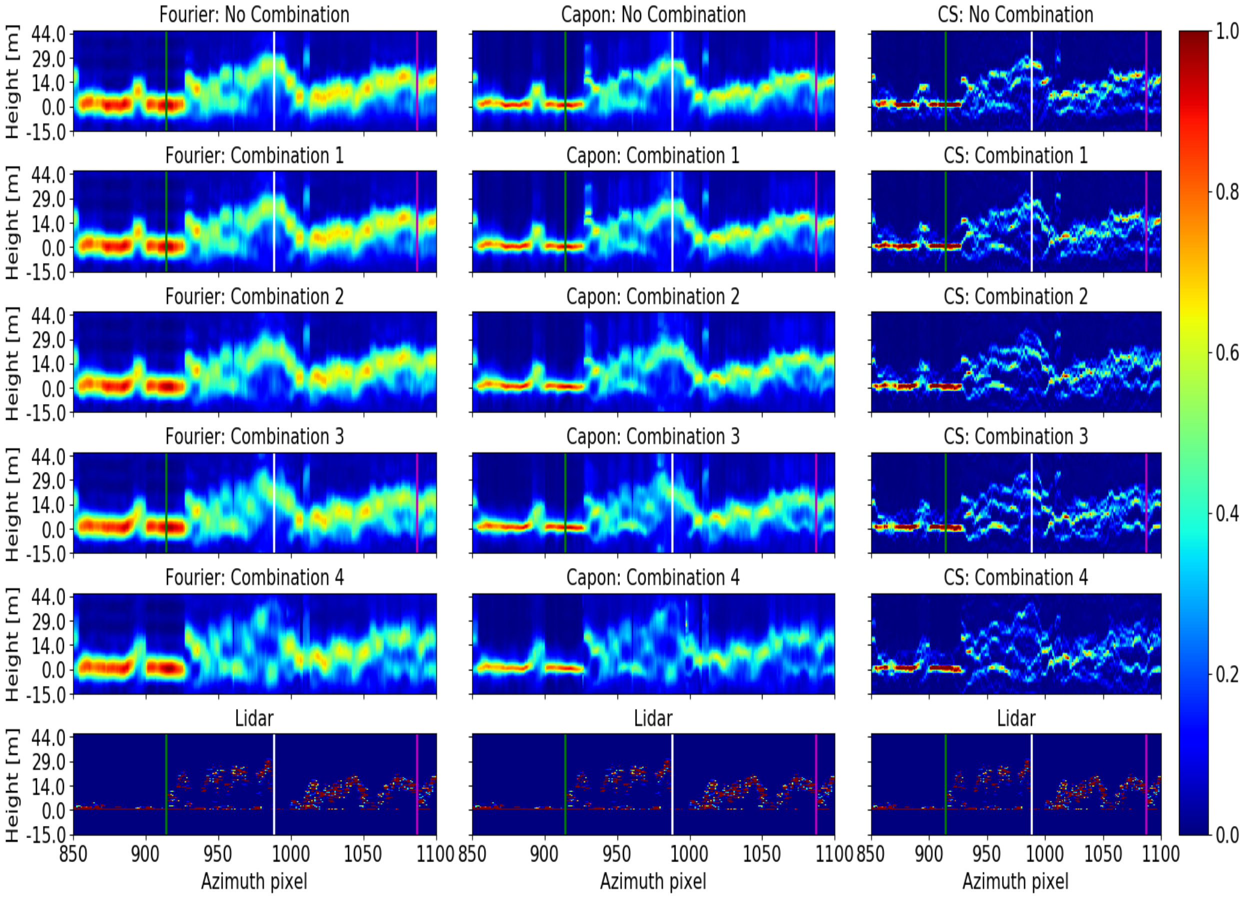

FIGURE 4.14: Profiles for Fourier (first column), Capon (second column) and CS (third column) for the combination of SLC's pairs (tandem-like configuration) presented in Table 4.2 for the sum of the power of HH, 2HV and VV channels. Color code: power of the radar reflectivity normalized along the transect. Last row: Lidar point clouds from 2012, red indicates high density and blue low density of returns. The vertical lines correspond to the vertical profiles represented in Figure 4.15: The green line corresponds to a ground area, the white to a heterogeneous and not very dense forest and the purple one to a very homogenous and dense forest. Each azimuth pixel represents a spacing of 0.8 m.

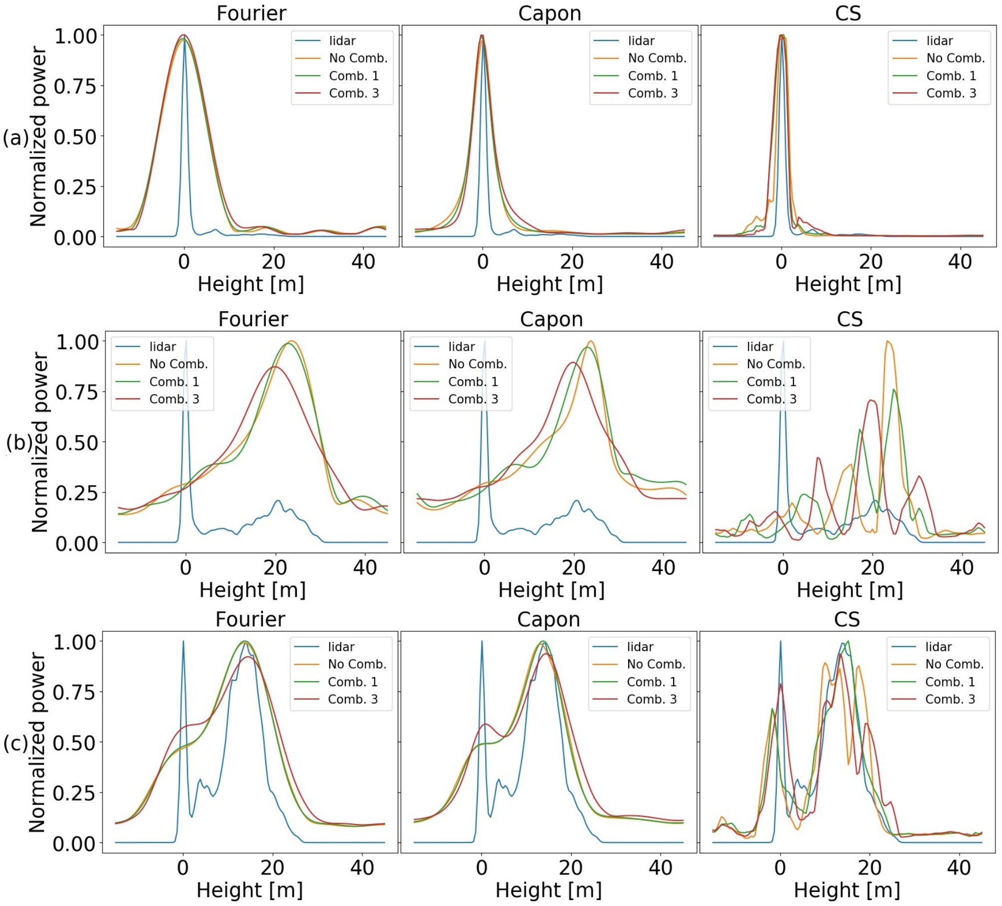

FIGURE 4.15: Vertical profiles for (a) green line, (b) white line, and (c) purple line from the transect in Figure 4.14.

4.5 Conclusions

In this article three tomographic algorithms widely used for the reconstruction of the 3-D radar reflectivity from tomographic SAR data, namely, Fourier beamforming (FB), Capon beamforming (CB), and compressive sensing (CS) are compared with respect to their performance in the reconstruction of the 3-D reflectivity of forests.

First, the algorithms have been compared on simulated data in order to assess the effects of the variation of individual parameters isolated from other effects. This is often not possible with real data. The intention was to compare the reconstruction performance under certain constraints in terms of the number of acquisitions and acquisition geometry as imposed by the design of actual or near-future tomographic implementations. The algorithms have been compared on four scenarios defined to evaluate the vertical resolution, the ability to detect weak scatterers, the stability against nonuniform wavenumber (i.e., track) distributions and the impact of a strongly reduced number of acquisitions.

The simulated scenarios confirm the poor (vertical) resolution of FB and its improvement by using CB and even more CS. CS also allows a better contrast between the layers and the background, due to the sparser reconstruction of the vertical profile with respect to CB and FB. Regarding the reconstruction of the layer amplitudes, the simulations indicate that CS provides the best amplitude ratio between layers. However, none of the algorithms is accordingly able to reconstruct the absolute power for volume scatterers. Furthermore, the effect of nonuniform distribution is more severe for FB, while CS remains more stable. Finally, an increase in the number of acquisitions produces a better focusing of the layers for the algorithms, but if the number is limited, only CS is able to detect clearly the layers.

The algorithms were applied and compared on a real multitemporal tomographic L-band SAR data set over a temperate forest in Traunstein (Germany). First, the impact of the nonuniform distribution of vertical wavenumber is evaluated. The results on real data show again that FB is the most affected one. Even small deviations from a uniform wavenumber distribution produce high sidelobes. On the contrary, CS is the least affected by deviations from a uniform wavenumber distribution, providing more stable results. In order to minimize the impact of the different and irregular wavenumber distributions at the different acquisition dates and to facilitate the multitemporal analysis, the tomographic data sets at each date have been interpolated. The objective of the interpolation is to provide the same equally distributed wavenumbers, imposing the same vertical resolution and nonambiguous height interval for all data sets. Such interpolation has been proven to be beneficial for all three algorithms compensating the performance loss caused by irregular wavenumber distributions.

Finally, the effect of temporal decorrelation on the performance of the three algorithms has been addressed. Two different tomographic implementations have been discussed: the conventional repeat-pass tomographic implementation and a tandem-like tomographic implementation. In the repeat-pass case, temporal decorrelation leads to a defocusing of the vertical reflectivity profile. The results indicate that temporal decorrelation severely distorts the structural interpretation of the reconstructed reflectivity in the case of repeat-pass acquisitions. For the tandem-like case, the estimated vertical profile tends to be more stable independently of the number of days combined. Furthermore, the profiles are more similar between them, although the number of different days increases. This similarity of the profiles indicates higher stability than in the case of combining single images acquired in repeat-pass mode.

It is important to note here that the interpolation becomes essential for FB and CB in tandem-like TomoSAR implementations, as it allows to build up a coherence matrix (required by FB and CB) from the acquired coherence vector. The matrix-based interpolation used in the experimental analysis to interpolate the SLC data vector can be used, as well to interpolate a coherence vector without formal changes. However, the interpolation performance, in this case, is more sensitive to the irregularity of the input wavenumber distribution, as the interpolation does not exploit the higher dimensional sampling and/or redundancy of a covariance matrix in input, but only a subset of its elements. As a result, the final covariance matrix after Toeplitz might be subject to ill-conditioning for a larger number of cases, leading to an inaccurate, if not meaningless, tomographic reconstruction. In contrast, the CS inversion does not necessarily need an interpolation of the coherence vector. However, the experimental results show that an interpolation to a uniform wavenumber distribution is beneficial to reduce artifacts in the reconstructed CS profiles. Thus, the design of estimators/interpolators of a full covariance matrix from a subset of its samples remains an open challenge that needs to be addressed for effective exploitation of tandem-like implementations of tomographic reconstructions.

As a general conclusion, for the reconstruction of forest reflectivity, all algorithms have their own strengths and weaknesses. It is important to know about them and to take appropriate account of them when it comes to the interpretation or further use of the results. Overall, CS seems more appropriate than CB or FB for forest applications in terms of detecting the position of canopy layers, i.e., the local maxima in the vertical reflectivity profile. CS can resolve higher vertical resolutions with a lower number of acquisitions, especially in complex structure scenarios. However, as the number of available acquisitions increases, CB unfolds its advantages in terms of susceptibility to false alarms and computational efficiency. Finally, for an appropriate Rayleigh resolution and not too irregular wavenumbers, the use of FB becomes advantageous as it provides a linear and accurate direct inversion of the relationship between the observed covariances and the vertical reflectivity profile.

4.6 Appendix. Ranking of the Algorithms

Table 4.3 shows a qualitative ranking of each algorithm (FB, CB, and CS) using 3 levels from A (more appropriate) to C (less appropriate), based on the results and discussions made along the whole manuscript for the simulated, as well as the real TomoSAR data. The ranking is independent for each aspect (each row in Table 4.3), described in the following list:

- *Vertical resolution*: The ability of the algorithm to detect layers closer in height than the Rayleigh resolution limit (Section 4.3.1).
- *Detection of weak layers*: The ability of the algorithm to distinguish weak canopy layers from the background noise (Section 4.3.2).
- *Non-Uniform wavenumber*: The robustness of the estimated profiles against irregular (non-uniform) wavenumber distributions (Sections 4.3.3, 4.4.2 and 4.4.3).
- *Number of wavenumbers*: The robustness of the estimated profiles against a reduction of the number of vertical wavenumbers (Section 4.3.4).
- *False alarms*: The distortion of the estimated profiles with local maxima that can be interpreted as false canopy layers. These local maxima of the profile are not present on the PSF defined by the vertical wavenumber distribution.
- *Absolute power*: The accuracy of the algorithm in the estimation of the absolute power profile.
- *Computational cost*: The processing time needed to process the same scene in each algorithm.
- *Temporal decorrelation*: The robustness of each algorithm (independently of the others) to obtain the profile (without temporal decorrelation) as soon as acquisitions from different days are combined. Note that, in this aspect, there is not a direct comparison between the algorithms (Section 4.4.4).

TABLE 4.3: Ranking of the TomoSAR algorithms

Algorithm	Fourier beamforming	Capon beamforming	compressive sensing
Vertical Resolution	C	B	A
Detection of weak layers	C	B	A
Nonuniform wavenumbers	C	B	A
Number of wavenumbers	C	B	A
False alarms	A	A	C
Absolute power	C	C	C
Computational cost	A	A	C
Temporal decorrelation	A	A	B

Acknowledgments

The authors would like to thank the F-SAR team for its invaluable effort during the data acquisition and processing as well as the Municipal Forest Administration of the city of Traunstein for making this project possible on their estate property. They would also like to thank the anonymous reviewers whose feedback improved this article.

References

[1] T. A. Spies, “Forest structure: a key to the ecosystem”, *Northwest Science*, vol. 72, no. 2, pp. 34–36, 1998. [Online]. Available: `http://andrewsforest.oregonstate.edu/pubs/pdf/pub2564.pdf` (cited on page 74).

[2] F. J. Bohn and A. Huth, “The importance of forest structure to biodiversity–productivity relationships”, *Royal Society open science*, vol. 4, no. 1, p. 160 521, 2017. DOI: `10.1098/rsos.160521` (cited on page 74).

[3] R. Fischer, N. Knapp, F. Bohn, H. H. Shugart, and A. Huth, “The relevance of forest structure for biomass and productivity in temperate forests: new perspectives for remote sensing”, *Surveys in Geophysics*, pp. 1–26, 2019. DOI: `10.1007/s10712-019-09519-x` (cited on page 74).

[4] K. Bergen, S. Goetz, R. Dubayah, G. Henebry, C. Hunsaker, M. Imhoff, R. Nelson, G. Parker, and V. Radeloff, “Remote sensing of vegetation 3-D structure for biodiversity and habitat: review and implications for lidar and radar spaceborne missions”, *Journal of Geophysical Research: Biogeosciences*, vol. 114, no. G2, 2009. DOI: `10.1029/2008JG000883` (cited on page 74).

[5] S. Goetz, D. Steinberg, R. Dubayah, and B. Blair, “Laser remote sensing of canopy habitat heterogeneity as a predictor of bird species richness in an eastern temperate forest, usa”, *Remote Sensing of Environment*, vol. 108, no. 3, pp. 254–263, 2007. DOI: `10.1016/j.rse.2006.11.016` (cited on page 74).

[6] W. Turner, S. Spector, N. Gardiner, M. Fladeland, E. Sterling, and M. Steininger, “Remote sensing for biodiversity science and conservation”, *Trends in ecology & evolution*, vol. 18, no. 6, pp. 306–314, 2003. DOI: `10.1016/S0169-5347(03)00070-3` (cited on page 74).

[7] S. Frolking, M. W. Palace, D. Clark, J. Q. Chambers, H. Shugart, and G. C. Hurtt, “Forest disturbance and recovery: a general review in the context of spaceborne remote sensing of impacts on aboveground biomass and canopy structure”, *Journal of Geophysical Research: Biogeosciences*, vol. 114, no. G2, 2009. DOI: `10.1029/2008JG000911` (cited on page 74).

[8] E. Rödig, M. Cuntz, A. Rammig, R. Fischer, F. Taubert, and A. Huth, “The importance of forest structure for carbon fluxes of the amazon rainforest”, *Environmental Research Letters*, vol. 13, no. 5, p. 054 013, 2018. DOI: `10.1088/1748-9326/aabc61` (cited on page 74).

[9] M. Del Rio, H. Pretzsch, I. Alberdi, K. Bielak, F. Bravo, A. Brunner, S. Condes, M. J. Ducey, T. Fonseca, N. von Lupke, *et al.*, “Characterization of the structure, dynamics, and productivity of mixed-species stands: review and perspectives”, *European journal of forest research*, vol. 135, no. 1, pp. 23–49, 2016. DOI: `10.1007/s10342-015-0927-6` (cited on page 74).

[10] M. A. Wulder, J. C. White, R. F. Nelson, E. Næsset, H. O. Ørka, N. C. Coops, T. Hilker, C. W. Bater, and T. Gobakken, “Lidar sampling for large-area forest characterization: a review”, *Remote Sensing of Environment*, vol. 121, pp. 196–209, 2012. DOI: `10.1016/j.rse.2012.02.001` (cited on page 74).

[11] S. Goetz and R. Dubayah, “Advances in remote sensing technology and implications for measuring and monitoring forest carbon stocks and change”, *Carbon Management*, vol. 2, no. 3, pp. 231–244, 2011. DOI: `10.4155/cmt.11.18` (cited on page 74).

[12] R. O. Dubayah and J. B. Drake, “Lidar remote sensing for forestry”, *Journal of Forestry*, vol. 98, no. 6, pp. 44–46, 2000. DOI: `10.1093/jof/98.6.44` (cited on page 74).

[13] *Global ecosystem dynamics investigation (gedi) mission. high resolution laser ranging of earth's forests and topography from the international space station (iss)*. [Online]. Available: `https://gedi.umd.edu/` (cited on page 74).

[14] S. Hancock, J. Armston, M. Hofton, X. Sun, H. Tang, L. I. Duncanson, J. R. Kellner, and R. Dubayah, “The gedi simulator: a large-footprint waveform lidar simulator for calibration and validation of spaceborne missions”, *Earth and Space Science*, vol. 6, no. 2, pp. 294–310, 2019. DOI: `10.1029/2018EA000506` (cited on page 74).

[15] Y. Wang, H. Weinacker, and B. Koch, “A lidar point cloud based procedure for vertical canopy structure analysis and 3d single tree modelling in forest”, *Sensors*, vol. 8, no. 6, pp. 3938–3951, 2008. DOI: `10.3390/s8063938` (cited on page 74).

[16] K. P. Papathanassiou and S. R. Cloude, “Single-baseline polarimetric sar interferometry”, *IEEE Transactions on Geoscience and Remote Sensing*, vol. 39, no. 11, pp. 2352–2363, 2001. DOI: `10.1109/36.964971` (cited on pages 74, 77).

[17] A. Reigber and A. Moreira, “First demonstration of airborne sar tomography using multibaseline L-band data”, *IEEE Transactions on Geoscience and Remote Sensing*, vol. 38, no. 5, pp. 2142–2152, 2000. DOI: `10.1109/36.868873` (cited on pages 74, 76, 77).

[18] S. Cloude and K. Papathanassiou, “Three-stage inversion process for polarimetric sar interferometry”, *IEE Proceedings-Radar, Sonar and Navigation*, vol. 150, no. 3, pp. 125–134, 2003. DOI: `10.1049/ip-rsn:20030449` (cited on page 75).

[19] V. Cazcarra-Bes, M. Tello-Alonso, R. Fischer, M. Heym, and K. Papathanassiou, "Monitoring of forest structure dynamics by means of L-band sar tomography", *Remote Sensing*, vol. 9, no. 12, p. 1229, 2017. DOI: `10.3390/rs9121229` (cited on pages 75, 86).

[20] M. Tello, V. Cazcarra-Bes, M. Pardini, and K. Papathanassiou, "Forest structure characterization from sar tomography at L-band", *IEEE Journal of Selected Topics in Applied Earth Observations and Remote Sensing*, vol. 11, no. 10, pp. 3402–3414, Oct. 2018. DOI: `10.1109/JSTARS.2018.2859050` (cited on page 75).

[21] M. Pardini, M. Tello, V. Cazcarra-Bes, K. P. Papathanassiou, and I. Hajnsek, "L-and P-band 3-D sar reflectivity profiles versus lidar waveforms: the afrisar case", *IEEE Journal of Selected Topics in Applied Earth Observations and Remote Sensing*, no. 99, pp. 1–16, 2018. DOI: `10.1109/JSTARS.2018.2847033` (cited on page 75).

[22] A. Moreira, G. Krieger, I. Hajnsek, K. Papathanassiou, M. Younis, P. Lopez-Dekker, S. Huber, M. Villano, M. Pardini, M. Eineder, *et al.*, "Tandem-l: a highly innovative bistatic sar mission for global observation of dynamic processes on the earth's surface", *IEEE Geoscience and Remote Sensing Magazine*, vol. 3, no. 2, pp. 8–23, 2015. DOI: `10.1109/MGRS.2015.2437353` (cited on pages 75, 76, 92).

[23] S. Tebaldini, "Algebraic synthesis of forest scenarios from multibaseline polinsar data", *IEEE Transactions on Geoscience and Remote Sensing*, vol. 47, no. 12, pp. 4132–4142, 2009. DOI: `10.1109/TGRS.2009.2023785` (cited on page 75).

[24] O. Frey and E. Meier, "Analyzing tomographic sar data of a forest with respect to frequency, polarization, and focusing technique", *IEEE Transactions on Geoscience and Remote Sensing*, vol. 49, no. 10, pp. 3648–3659, 2011. DOI: `10.1109/TGRS.2011.2125972` (cited on page 75).

[25] M. Nannini, R. Scheiber, and A. Moreira, "Estimation of the minimum number of tracks for sar tomography", *IEEE Transactions on Geoscience and Remote Sensing*, vol. 47, no. 2, pp. 531–543, 2009. DOI: `10.1109/TGRS.2008.2007846` (cited on page 75).

[26] Y. Huang, L. Ferro-Famil, and A. Reigber, "Under-foliage object imaging using sar tomography and polarimetric spectral estimators", *IEEE transactions on geoscience and remote sensing*, vol. 50, no. 6, pp. 2213–2225, 2012. DOI: `10.1109/TGRS.2011.2171494` (cited on page 75).

[27] S. Tebaldini, "Single and multipolarimetric sar tomography of forested areas: a parametric approach", *IEEE Transactions on Geoscience and Remote Sensing*, vol. 48, no. 5, pp. 2375–2387, 2010. DOI: `10.1109/TGRS.2009.2037748` (cited on page 75).

[28] B. Ottersten, P. Stoica, and R. Roy, "Covariance matching estimation techniques for array signal processing applications", *Digital Signal Processing*, vol. 8, no. 3, pp. 185–210, 1998. DOI: `10.1006/dspr.1998.0316` (cited on page 75).

[29] P. Stoica, R. L. Moses, *et al.*, *Spectral analysis of signals*. Pearson Prentice Hall Upper Saddle River, NJ, 2005, ISBN: 9780131139565 (cited on pages 75, 78, 79).

[30] F. Lombardini and A. Reigber, "Adaptive spectral estimation for multibaseline sar tomography with airborne L-band data", in *Geoscience and Remote Sensing Symposium, 2003. IGARSS'03. Proceedings. 2003 IEEE International*, IEEE, vol. 3, 2003, pp. 2014–2016. DOI: `10.1109/IGARSS.2003.1294324` (cited on pages 75, 78, 79).

[31] S. R. Cloude, "Polarization coherence tomography", *Radio Science*, vol. 41, no. 04, pp. 1–27, 2006. DOI: `10.1029/2005RS003436` (cited on page 75).

[32] X. X. Zhu and R. Bamler, "Tomographic sar inversion by l1-norm regularization-the compressive sensing approach", *IEEE Transactions on Geoscience and Remote Sensing*, vol. 48, no. 10, pp. 3839–3846, 2010. DOI: `10.1109/TGRS.2010.2048117` (cited on pages 75, 80).

[33] A. Budillon, A. Evangelista, and G. Schirinzi, "Three-dimensional sar focusing from multipass signals using compressive sampling", *IEEE Transactions on Geoscience and Remote Sensing*, vol. 49, no. 1, pp. 488–499, 2011. DOI: `10.1109/TGRS.2010.2054099` (cited on pages 75, 80).

[34] E. Aguilera, M. Nannini, and A. Reigber, "A data-adaptive compressed sensing approach to polarimetric sar tomography of forested areas", *IEEE Geoscience and Remote Sensing Letters*, vol. 10, no. 3, pp. 543–547, 2013. DOI: `10.1109/LGRS.2012.2212693` (cited on pages 75, 78, 80).

[35] X. Li, L. Liang, H. Guo, and Y. Huang, "Compressive sensing for multibaseline polarimetric sar tomography of forested areas", *IEEE Transactions on Geoscience and Remote Sensing*, vol. 54, no. 1, pp. 153–166, 2016. DOI: `10.1109/TGRS.2015.2451992` (cited on pages 75, 80).

[36] Y. Huang, J. Levy-Vehel, L. Ferro-Famil, and A. Reigber, "Three dimensional imaging of objects concealed below a forest canopy using sar tomography at L-band and wavelet-based sparse estimation", *IEEE Geoscience and Remote Sensing Letters*, vol. 14, no. 9, pp. 1454–1458, 2017. DOI: `10.1109/LGRS.2017.2709839` (cited on pages 75, 80).

[37] H. Aghababaee, G. Ferraioli, L. Ferro-Famil, G. Schirinzi, and Y. Huang, “Sparsity based full rank polarimetric reconstruction of coherence matrix t”, *Remote Sensing*, vol. 11, no. 11, 2019. DOI: `10.3390/rs11111288` (cited on page 75).

[38] G. M. del Campo, M. Nannini, and A. Reigber, “Towards feature enhanced sar tomography: a maximum-likelihood inspired approach”, *IEEE Geoscience and Remote Sensing Letters*, no. 99, pp. 1–5, 2018. DOI: `10.1109/LGRS.2018.2858571` (cited on page 75).

[39] X. Peng, X. Li, C. Wang, H. Fu, and Y. Du, “A maximum likelihood based nonparametric iterative adaptive method of synthetic aperture radar tomography and its application for estimating underlying topography and forest height”, *Sensors*, vol. 18, no. 8, p. 2459, 2018. DOI: `10.3390/s18082459` (cited on page 75).

[40] R. Bamler and P. Hartl, “Synthetic aperture radar interferometry”, *Inverse problems*, vol. 14, no. 4, R1, 1998. DOI: `10.1088/0266-5611/14/4/001` (cited on pages 76, 77).

[41] F. Gini, F. Lombardini, and M. Montanari, “Layover solution in multibaseline sar interferometry”, *IEEE Transactions on Aerospace and Electronic Systems*, vol. 38, no. 4, pp. 1344–1356, 2002. DOI: `10.1109/TAES.2002.1145755` (cited on pages 78, 79).

[42] S. Tebaldini and L. Ferro-Famil, “Sar tomography from bistatic single-pass interferometers”, in *2017 IEEE International Geoscience and Remote Sensing Symposium (IGARSS)*, IEEE, 2017, pp. 133–136. DOI: `10.1109/IGARSS.2017.8126912` (cited on page 79).

[43] J. Capon, “High-resolution frequency-wavenumber spectrum analysis”, *Proceedings of the IEEE*, vol. 57, no. 8, pp. 1408–1418, 1969. DOI: `10.1109/PROC.1969.7278` (cited on page 79).

[44] P. Stoica, J. Li, and X. Tan, “Spatial power spectrum and signal estimation using the pisarenko framework”, *IEEE Transactions on Signal Processing*, vol. 56, no. 10, pp. 5109–5119, 2008. DOI: `10.1109/TSP.2008.928935` (cited on page 79).

[45] F. Lombardini, M. Pardini, G. Fornaro, F. Serafino, L. Verrazzani, and M. Costantini, “Linear and adaptive spaceborne three-dimensional sar tomography: a comparison on real data”, *IET radar, sonar & navigation*, vol. 3, no. 4, pp. 424–436, 2009. DOI: `10.1049/iet-rsn.2008.0171` (cited on page 79).

[46] E. J. Candès and M. B. Wakin, “An introduction to compressive sampling”, *IEEE signal processing magazine*, vol. 25, no. 2, pp. 21–30, 2008. DOI: `10.1109/MSP.2007.914731` (cited on page 80).

[47] E. J. Candes and T. Tao, “Decoding by linear programming”, *IEEE Transactions on Information Theory*, vol. 51, no. 12, pp. 4203–4215, Dec. 2005. DOI: `10.1109/TIT.2005.858979` (cited on page 80).

[48] E. J. Candes and T. Tao, “Near-optimal signal recovery from random projections: universal encoding strategies?”, *IEEE transactions on information theory*, vol. 52, no. 12, pp. 5406–5425, 2006. DOI: `10.1109/TIT.2006.885507` (cited on page 80).

[49] E. Aguilera, “Synthetic aperture radar tomography compressed sensing models and algorithms”, PhD thesis, Technical University of Berlin, 2014. [Online]. Available: `https://elib.dlr.de/85764/` (cited on page 80).

[50] E. Aguilera, M. Nannini, and A. Reigber, “Wavelet-based compressed sensing for sar tomography of forested areas”, *IEEE Transactions on Geoscience and Remote Sensing*, vol. 51, no. 12, pp. 5283–5295, 2013. DOI: `10.1109/TGRS.2012.2231081` (cited on page 80).

[51] S. Diamond and S. Boyd, “Cvxpy: a python-embedded modeling language for convex optimization”, *The Journal of Machine Learning Research*, vol. 17, no. 1, pp. 2909–2913, 2016. [Online]. Available: `http://jmlr.org/papers/v17/15-408.html` (cited on page 80).

[52] V. Cazcarra-Bes, M. Tello, and K. Papathanassiou, “3d forest structure estimation from sar tomography by means of a full rank polarimetric inversion based on compressive sensing”, in *Proceedings of PolInSAR*, ISBN: 9789292212933, 2015 (cited on page 80).

[53] R. Horn, A. Nottensteiner, A. Reigber, J. Fischer, and R. Scheiber, “F-sar—dlr’s new multifrequency polarimetric airborne sar”, in *Geoscience and Remote Sensing Symposium, 2009 IEEE International, IGARSS 2009*, IEEE, vol. 2, 2009, pp. II–902. DOI: `10.1109/IGARSS.2009.5418244` (cited on page 86).

[54] [Online]. Available: `http://www.wetter-by.de` (cited on page 86).

[55] F. Lombardini and M. Pardini, “3-D sar tomography: the multibaseline sector interpolation approach”, *IEEE Geoscience and Remote Sensing Letters*, vol. 5, no. 4, pp. 630–634, 2008. DOI: `10.1109/LGRS.2008.2001283` (cited on page 90).

[56] F. Bordoni, A. Jakobsson, F. Lombardini, and F. Gini, “Multibaseline cross-track sar interferometry using interpolated arrays”, *IEEE transactions on aerospace and electronic systems*, vol. 41, pp. 1473–1482, 2005. DOI: `10.1109/TAES.2005.1561898` (cited on page 90).

[57] F. Lombardini, M. Pardini, and L. Verrazzani, “A robust multibaseline sector interpolator for 3d sar imaging”, in *7th European Conference on Synthetic Aperture Radar*, ISBN: 9783800730847, VDE, 2008, pp. 1–4 (cited on page 90).

[58] M. Pardini and K. Papathanassiou, “Spaceborne sar tomography over forests: performance and trade-offs for repeated single pass polinsar acquisitions”, in *2015 IEEE International Geoscience and Remote Sensing Symposium (IGARSS)*, Jul. 2015, pp. 1551–1554. DOI: `10.1109/IGARSS.2015.7326077` (cited on page 95).

[59] M. Pardini, A. Torano-Caicoya, F. Kugler, and K. Papathanassiou, “Estimating and understanding vertical structure of forests from multibaseline tandem-x pol-insar data”, in *2013 IEEE International Geoscience and Remote Sensing Symposium-IGARSS*, IEEE, 2013, pp. 4344–4347. DOI: `10.1109/IGARSS.2013.6723796` (cited on page 95).

Chapter 5

Optimization of Tomographic SAR Configurations for Forest Structure Applications at L-band

V. Cazcarra-Bes, M. Pardini and K. P. Papathanassiou

IEEE Geoscience and Remote Sensing Letters
Submitted in October 2019

Key findings/points:

- Analysis of different TomoSAR acquisition configurations.
- Evaluation of the requirements of TomoSAR acquisitions for distinguishing different structure types in terms of vertical resolution, height of ambiguity and peak side-lobe level of the point spread function.
- If the number of tracks is limited, a uniform distribution is not always the best choice.
- A non-uniform distribution of the tracks with low vertical resolution (10 to 15 m) is the best compromise to avoid higher values of the peak sidelobe level that would degrade the quality of the TomoSAR profiles and their interpretation.

The author's contributions:

- Development and implementation of the tomographic algorithms and the different tomographic configuration scenarios.
- Interpretation of the results and main writing of the manuscript.

The co-author's contributions:

- M. Pardini contributed with ideas, helped on the interpretation of the results, and he supervised the whole work.
- K. P. Papathanassiou contributed to the main ideas and revised the work.

Optimization of Tomographic SAR Configurations for Forest Structure Applications at L-band

V. Cazcarra-Bes[1,2], M. Pardini[2] and K. Papathanassiou[2]

[1]Institute of Environmental Engineering, ETH Zürich, 8093 Zürich, Switzerland
[2]Microwaves and Radar Institute, German Aerospace Center (DLR), 82234 Wessling, Germany

Abstract

Synthetic Aperture Radar Tomography (TomoSAR) at lower frequencies allows the reconstruction of the 3-D radar reflectivity of volume scatterers providing access to their physical 3-D structure. The performance of the reconstruction depends on the number and (spatial) distribution of the tomographic acquisitions (tracks). This dependency is addressed in this letter for the case of tomographic acquisitions for forest applications at L-band. Tomographic configurations of different number of tracks and distributions are compared against reconstruction requirements typical for forest structure mapping applications. For the reconstruction, three different TomoSAR algorithms (Fourier Beamforming, Capon Beamforming, and Compressive Sensing) have been used and compared to each other. For the analysis, a tomographic data set consisting of fifteen tracks acquired by the DLR's F-SAR system at L-band over the Traunstein test site in Germany is used. The results show that a higher vertical resolution plays a small role when the number and distribution of tracks is not adequate to avoid a degradation of the reconstructed 3-D radar reflectivity (i.e. vertical profiles) due to sidelobe effects.

5.1 Introduction

Synthetic Aperture Radar (SAR) tomography (TomoSAR) allows the reconstruction of the 3-D radar reflectivity of volume scatterers by combining multiple SAR images acquired with slightly different incidence (or look) angles along spatially displaced tracks (or orbits) [1]. At lower frequencies (L- or P-band) the reconstructed 3-D radar reflectivity allows characterising the 3-D forest structure [2], [3]. This potential to provide forest structure information [4], at high spatial and temporal resolution(s) as SAR systems, makes TomoSAR a key element of future space-borne SAR missions aiming forest applications, as for ESA's BIOMASS [5] and DLR's Tandem-L [6].

In the absence of unique solutions for the general TomoSAR reconstruction problem, different reconstruction algorithms (model-based, model-free or hybrid ones) have been proposed and used in the literature [7], [8]. The most popular ones are the Fourier beamforming (FB) [9], the Capon beamforming (CB) [9] (model-free algorithms) and compressive sensing (CS) [10] (hybrid algorithms) relying on sparsity bases. For volume scatterers, each algorithm has its strengths and weaknesses depending on the application requirements and system limitations. A detailed comparison of the three algorithms can be found in [11].

Besides the choice of the algorithm, the reconstruction performance for forest structure applications depends critically on the number and the spatial distribution (of the tracks or orbits) of the tomographic acquisitions. This is because they define three important reconstruction parameters. The first one is the vertical resolution, which is associated with the ability to resolve individual forest layers. The second one is the unambiguous reconstruction range, also known as the height of ambiguity. Finally, the third one is the Peak Sidelobe Level (PSL), that expresses the non-desired energy outside the main lobe of the Point Spread Function (PSF). The dependency of these three parameters on the number and the spatial distribution of the tomographic acquisitions can, at least in a first order, be assessed by using the PSF, which is given by the FB response to a point scatterer.

Each image pair y_m, y_n for $m, n = 1, ..., M$ from a TomoSAR data set consisting of M SAR images, is characterised by the so-called vertical wavenumber k_z that expresses the sensitivity (i.e. the derivative) of the phase (of the complex conjugate product of two Single Look Complex (SLC) images) to a height change [1]:

$$k_z(m,n) = \frac{4\,\pi\,\Delta\,\theta\,(m,n)}{\lambda\,sin(\theta)}, \tag{5.1}$$

where $\Delta\theta\,(m,n)$ is the incidence-angle difference associated with the pair formed by the mth and the nth acquisitions, λ is the wavelength, and θ is the incidence angle. The PSF is defined by all the vertical wavenumbers k_z of the TomoSAR acquisition.

The vertical resolution and the height of ambiguity can be defined as:

$$\delta_z = \frac{2\pi}{k_{z,max}}, \quad z_{amb} = \frac{2\pi}{k_{z,min}} \tag{5.2}$$

where $k_{z,min} = min_{m,n}\{k_z(m,n)\}$ and $k_{z,max} = max_{m,n}\{k_z(m,n)\}$. $k_{z,max}$ and $k_{z,min}$ are directly proportional to the maximum and minimum track displacements B_{max} and B_{min} , respectively.

Regarding the PSL, if the number of tracks is large and the tracks are uniformly displaced, the PSF becomes a $sinc^2$ function, and therefore the PSL is equal to -13.26 dB. However, if the number of tracks is low, the PSL becomes:

$$PSL = 10\,log_{10}\left(\frac{sin^2(1.4311\pi)}{M^2 sin^2\left(\frac{1.4311\pi}{M}\right)}\right). \tag{5.3}$$

However, the expression 5.3 holds only for a uniform displacement of tracks; if the distribution of k_z becomes non-uniform the PSL will change. Note that in 5.3 the position of the first side lobe has been approximated to be always in the same position, which is not strictly true as the position of the first side lobe slightly changes with M.

Optimized tomographic configurations have been addressed in previous studies, especially with respect to the minimum number of tracks [12]. However, they use the specific model-based algorithm MUSIC to define the number of phase centers on the vertical profile before the tomographic inversion.

This letter aims to evaluate the effect of the number and distribution of tracks on the vertical resolution, the height of ambiguity and the PSL of the reconstructed radar reflectivity in volume scenarios. Requirements on these three parameters are derived with respect to forest structure applications at L-band. The analysis relies on the PSF and experimental real TomoSAR data over a temperate forest. For the tomographic reconstruction, three tomographic algorithms are used and compared: FB and CB as non-modeled ones and the hybrid CS.

5.2 Test Site and Tomographic Data Set

The test site is a temperate forest located in Traunstein, Germany, containing different forest structure types. In May 2017, a fully polarimetric L-band tomographic repeat-pass data set has been acquired by the DLR's F-SAR airborne sensor consisting of fifteen uniformly distributed tracks with a horizontal distance of about 5 m between them. This results in a uniformly distributed set of vertical wavenumbers (k_z) from 0 rad/m to 1.05 rad/m associated with a vertical Rayleigh resolution of 6 m and a height of ambiguity of about 85 m. The resolutions of the SLC images are 1.28 m and 0.6 m in slant-range and azimuth respectively.

As additional data for comparison, airborne Lidar data also acquired in 2016 are used. Figure 5.1 shows the Lidar derived forest top height map of the site that visualizes the heterogeneity in the site: The west part (left) is composed by multi-layer forest stands (indicated by the black polygon), in the middle there is a gap with a few scattered trees (red polygon), and towards the east (right) there are mainly mono-layer and more homogeneous stands (orange and blue polygons).

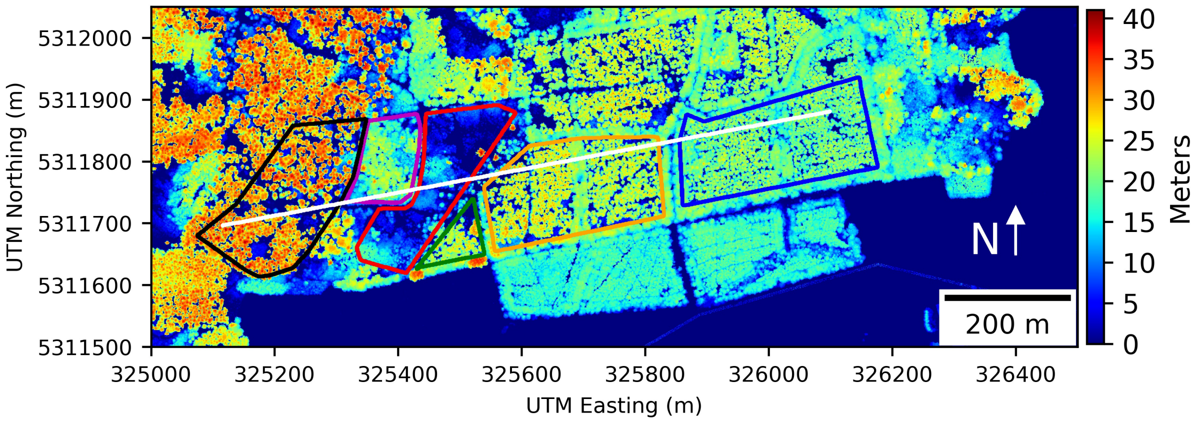

FIGURE 5.1: Lidar height over the Traunstein forest. Each polygon represents a homogeneous forest structure type.

5.3 Full Stack of Tracks

After SAR processing, the fifteen SLC SAR images (coregistered and phase calibrated with respect to each other) are ready to be used for tomographic processing [1]. The M tomographic images are arranged in form of a (data) vector $\mathbf{y} = [y_1, \ldots, y_M]^T$, where $(\cdot)^T$ denotes the transpose operator, and it is used to form the covariance matrix $R = E\{\mathbf{yy}^H\}$, where $(\cdot)^H$ indicates the Hermitian operator and $E\{\cdot\}$ is the statistical expectation approximated by the mean value of neighboring samples. The three tomographic algorithms are applied on the covariance matrix R using the associated vertical wavenumber k_z (see expression in (5.1)).

5.3.1 Forest Structure from Profiles: Agreement Lidar - Radar

Figure 5.2 shows the tomographic profile across the transect indicated by the white line in Figure 5.1 for FB (a), CB (b) and CS (c). Also, in (d) the Lidar profiles over the same area are shown. The visual qualitative good quality of the reconstructions is confirmed by looking on the PSF shown in Figure 5.3(a) characterised by a very low sidelobe of about -13 dB (with respect to the main lobe). FB and CB show very similar results with a slightly better resolution for CB, as confirmed by the narrower reflectivity layers. The CS results are more sparse characterized by an increase of the vertical resolution, but it also introduces some wrong maxima in the reflectivity profiles compared to FB and CB [11].

In order to evaluate better the achieved performance, Figure 5.4 (a) shows the mean profiles over the polygons highlighted in Figure 5.1. There is a consistent qualitative agreement between the Lidar profile (black line) and the tomographic reconstructions. There are differences between the algorithms, for example, the better discrimination of the maxima in the CS profile (blue line), but in general, the three algorithms can reconstruct the same structure as in the Lidar profile. Therefore, it can be concluded that using the full stack of fifteen tracks, first the different forest structure areas can be characterised with TomoSAR and second, the algorithm is not a crucial issue under this very favourable conditions.

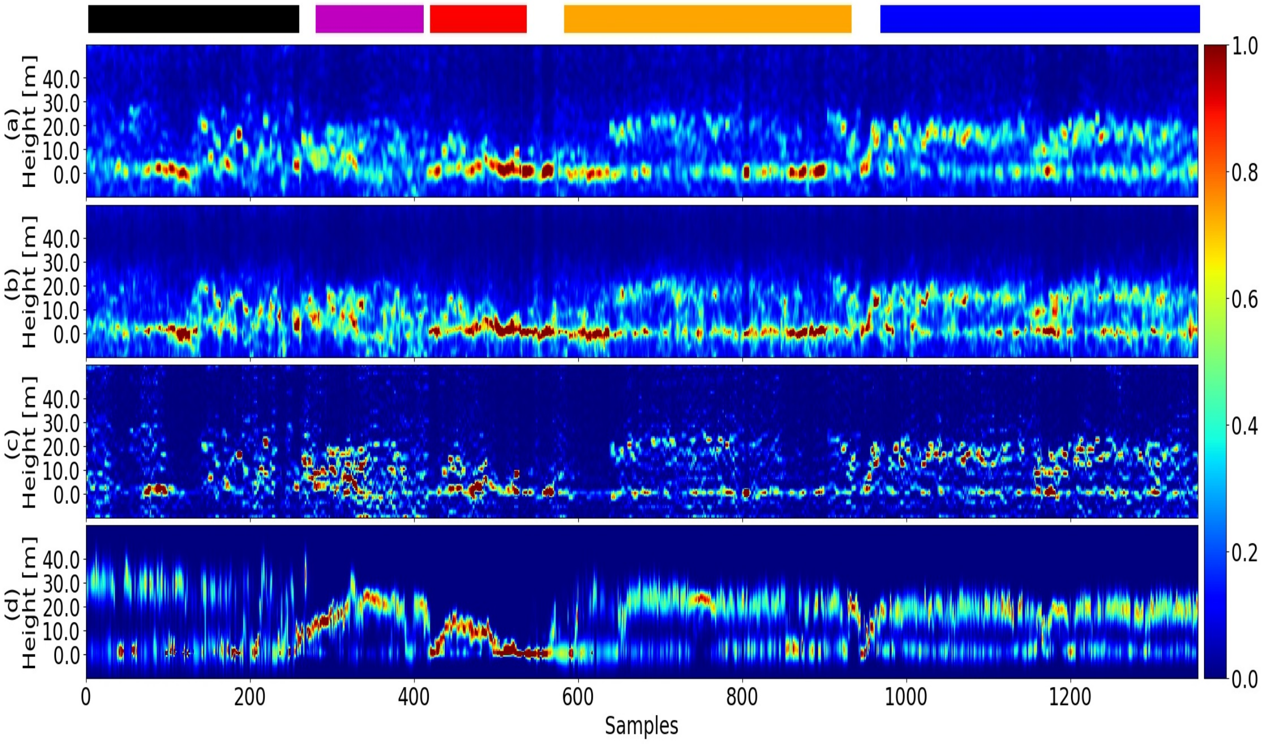

FIGURE 5.2: (a) Fourier Beamforming, (b) Capon Beamforming, (c) compressive sensing tomographic results for the HV channel and (d) Lidar profiles over the white line from Figure 5.1. Each figure is normalized by its own maximum. One sample represents a spacing of 0.8 meters. The colored rectangles on the upper part refer to the areas defined in Figure 5.1.

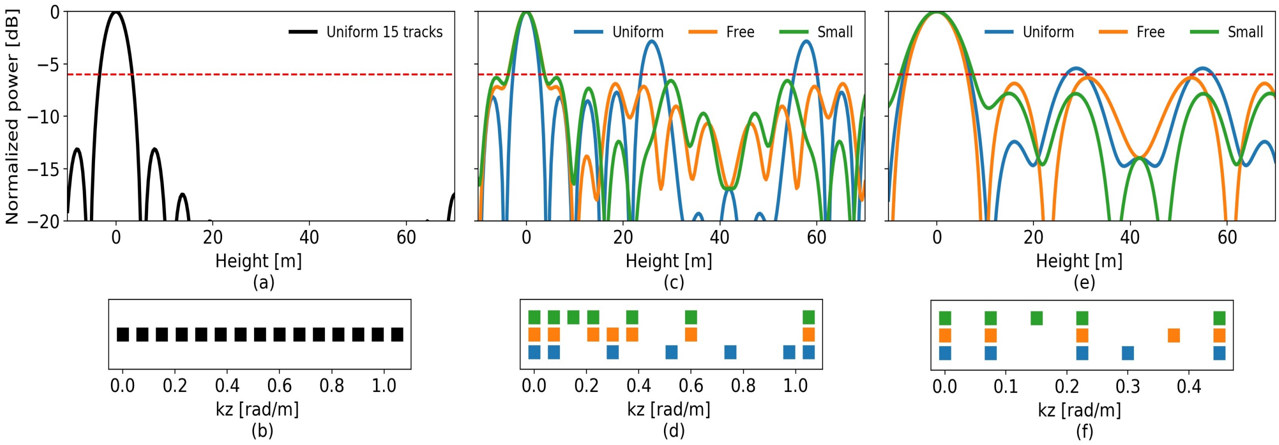

FIGURE 5.3: (a) Point Spread Function and (b) k_z distribution for fifteen tracks; (c) Point Spread Function and (d) k_z distributions for seven tracks; (e) Point Spread Function and (f) k_z distributions for five tracks.

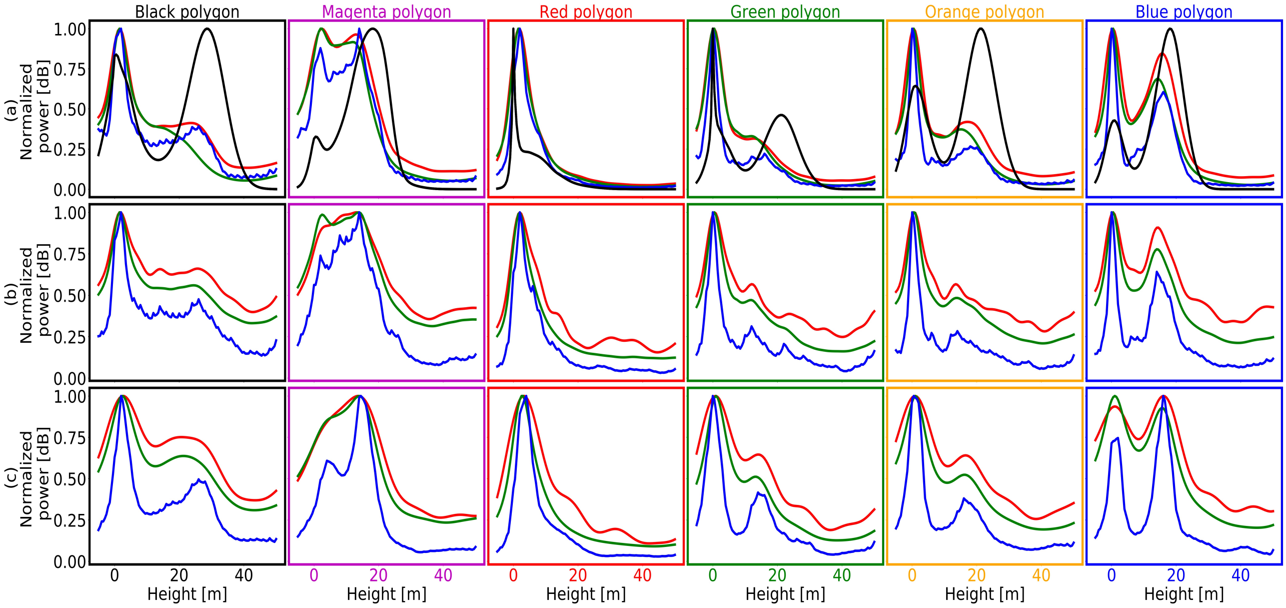

FIGURE 5.4: Mean profiles over the polygons (each column represents one) defined in Figure 5.1 for lidar point cloud (black) and the Tomographic SAR algorithms: Fourier beamforming (red), Capon beamforming (green) and Compressive Sensing (Blue) for the HV channel. Each row represents a different distribution of tracks: (a) Fifteen uniform tracks (see Figure 5.3(b)), (b) *small* distribution scenario with seven tracks (see green colour Figure 5.3(d)) and (c) *small* distribution scenario with five tracks (see green colour Figure 5.3(f)).

5.3.2 Requirements for Forest Structure Applications

While the requirements on vertical resolution (on the order of 5-15 m depending on the application requirements) and height of ambiguity (higher than the tallest trees in the scene) are well understood, the sidelobe levels are not. High sidelobes can be confused with the mainlobe maximas of weaker scattering contributions. For example, high sidelobes of the ground scattering component may be misinterpreted as real canopy layers. Accordingly, a requirement in terms of the power difference between the main lobe and the maximum sidelobe (i.e the PSL) appears appropriate. In the context of forest structure applications, where the local maxima of the reconstructed reflectivity are understood as canopy layers [2], [3], the power of the sidelobes should be lower than the reflectivity maxima induced by the canopy layers.

In order to derive such a requirement, the power difference between the two main reflectivity maxima, within the height interval of interest, in the reconstruction based on the fifteen tracks is evaluated. Table 5.1 shows the power difference values in dB for each of the polygons (i.e. structure types) of Figure 1, for the three algorithms (FB, CB and CS) in the different polarizations. Except the red polygon, where only one scattering contribution (i.e. the ground) dominates, all the rest differences lie between 2 and 5 dB. Accordingly, a 6 dB difference between the maxima and the highest sidelobe, appears sufficient to separate the canopy layers in the different forest structure areas. Note that, the ratios for CB, FB and CS are similar. This confirms that the posed requirement in terms of PSL (-6 dB) is independent of the selection of the TomoSAR algorithm and it can be analyzed through the PSF.

TABLE 5.1: Power difference in dB between the two main canopy layers

Algorithm,Channel	Blue polygon	Orange polygon	Green polygon	Magenta polygon	Black polygon
FB,HH	-2.84 (±1.37)	-3.67 (±1.31)	-5.09 (±1.25)	-2.92 (±1.37)	-3.1 (±1.43)
FB,HV	-1.87 (±1.02)	-2.52 (±1.25)	-3.47 (±1.37)	-2.22 (±1.31)	-2.37 (±1.31)
FB,VV	-2.37 (±1.19)	-3.28 (±1.25)	-4.2 (±1.31)	-2.44 (±1.31)	-2.68 (±1.37)
FB,HH+HV+VV	-2.01 (±1.08)	-3.1 (±1.25)	-4.32 (±1.31)	-2.44 (±1.37)	-2.68 (±1.37)
CB,HH	-2.92 (±1.25)	-3.87 (±1.31)	-5.09 (±1.31)	-2.6 (±1.43)	-3.47 (±1.43)
CB,HV	-1.8 (±1.02)	-2.76 (±1.31)	-3.37 (±1.49)	-2.08 (±1.31)	-2.06 (±1.37)
CB,VV	-2.52 (±1.19)	-3.57 (±1.31)	-4.32 (±1.43)	-2.29 (±1.31)	-3.01 (±1.43)
CB,HH+HV+VV	-2.15 (±1.08)	-3.47 (±1.25)	-4.44 (±1.31)	-2.15 (±1.37)	-3.1 (±1.37)
CS,HH	-2.92 (±1.37)	-3.57 (±1.49)	-4.69 (±1.49)	-2.68 (±1.37)	-2.76 (±1.49)
CS,HV	-1.87 (±1.14)	-2.44 (±1.37)	-3.19 (±1.49)	-1.94 (±1.19)	-2.15 (±1.31)
CS,VV	-2.44 (±1.25)	-3.1 (±1.43)	-3.77 (±1.49)	-2.22 (±1.25)	-2.37 (±1.37)
CS,HH+HV+VV	-2.76 (±1.31)	-3.57 (±1.43)	-4.56 (±1.43)	-2.44 (±1.31)	-2.68 (±1.43)

The first number represents the mean value (in the polygon) of the power difference in dB between the two highest local maxima for the tomographic result using fifteen tracks. The number in brackets correspond to the standard deviation.

5.4 Scenarios with a Reduced Number of Tracks

Having established the requirements on the reconstructed reflectivity in terms of the height of ambiguity (>50m) and PSL (-6 dB), downscaled tomographic configurations still able to fulfil these requirements are investigated. For the requirement of the vertical resolution, two scenarios are evaluated: One with the maximum possible vertical resolution (6 m) and another one changing the vertical resolution (from 21 m to 6 m). In these two scenarios, three vertical wavenumber distributions are discussed:

1. *Uniform* wavenumber distribution with equidistant tracks.
2. *Free* wavenumber distribution optimized with respect to the posed requirements.
3. *Small* wavenumber distribution, i.e. distributions with three small vertical wavenumbers (up to 0.22 rad/m). This is an important constraint when the same tomographic data set is used for (model-based) forest height inversion [13]. The rest of the remaining vertical wavenumbers are freely distributed to fulfill the requirements.

Note here, that the definition of the possible configurations is constrained by the fifteen values of the vertical wavenumber k_z of the experimental data set described in Section 5.2 as well as the requirements in terms of height of ambiguity and vertical resolution. The minimum possible track separation corresponds to a height of ambiguity of 84 m. The next smaller possible separation corresponds to a height of ambiguity of only 42 m, which is almost the height of the tallest trees in the scene. To avoid any misinterpretation, the height of ambiguity is then fixed to 84 m. The maximum possible track separation available from the data set corresponds to a vertical (Rayleigh) resolution of 6 m. From this high vertical resolution provided by the fifteen tracks of data set, scenarios with a reduced number of tracks keeping constant the resolution or a reduced vertical resolution are evaluated.

5.4.1 Maximum Possible Vertical Resolution

Table 5.2 shows the level of the PSL (in dB) for the three distributions, with an increasing number of tracks and keeping constant the vertical resolution to 6 m (i.e. the same maximum track separation). One can see that, in order to fulfill the sidelobe requirement, at least seven tracks are required for the *free* and *small* wavenumber distribution. In the case of the *uniform* distribution, an increase to eleven tracks is needed to have a sidelobe lower than -6 dB.

TABLE 5.2: Peak sidelobe level in dB for the different distributions with maximum vertical resolution

# tracks	3	4	5	6	7	8	9	10	11	12	13	14	15
Uniform[1]	-0.2	-0.5	-1.2	-1.7	-2.8	-5.2	-5.1	-4.4	-7.6	-7.5	-8.3	-10.2	-13.13
Free	-0.2	-2	-4.4	-5.5	-6.9	-8.5	-9.8	-10.8	-11.3	-12.9	-13.4	-14.23	-13.13
Small	-	-	-1.1	-4.2	-6.3	-8.5	-9.7	-10	-11.3	-12.9	-13.4	-14.23	-13.13

[1] The uniform distributions are not always completely uniform as the k_z values are limited to the original positions and two fixed positions are needed to fulfil the requirements in terms of height of ambiguity and vertical resolution.

Figure 5.3 (c) and (d) show the PSF for the case of seven tracks and the associated k_z values for each distribution. As already indicated, the *uniform* wavenumber distribution does not fulfill the -6 dB sidelobe requirement for seven tracks. However, compared to the other distributions, the main lobe is narrower and has a larger distance to the sidelobe. In the case of *free* and *small* wavenumber distributions, the not so narrow main lobe with small distance to the sidelobes, goes in favour of lower sidelobes, that in both cases fulfil the requirement of -6 dB. The difference between the *free* and the *small* wavenumber distribution is not significant, with an irregular PSF and similar levels for the PSL. The fact that the *small* distribution is of advantage for forest height estimation makes it in our view, the preferred one.

Figure 5.4 (b) compares the profiles obtained from the three reconstruction algorithms FB, CB and CS, in the case of the *small* wavenumber configuration for seven tracks with a vertical resolution of 6 m. The main difference to the fifteen tracks scenario (Figure 5.4 (a)) is the increase in the sidelobe level. Especially affected is the FB reconstruction (in red) making the identification of local reflectivity maxima more difficult. Anyhow, the reflectivity profile appears correct (compared to the Lidar) for all polygons, except for the green polygon where the reconstruction appears distorted. A possible explanation for this polygon is the small amount of samples to characterize this area. The use of the highest possible vertical resolution is reflected in the magenta polygon, where the two principal local maxima are separated in the CB and CS reconstructions, but not in the FB reconstruction. For FB, the increase of the sidelobes mix the two maxima, making impossible to distinguish the two layers.

5.4.2 Tomographic Scenario with Five Acquisitions

A conventional space borne tomographic data set may consist of a maximum of four to five acquisitions. From Table 5.2 follows that five acquisitions do not allow sidelobe levels bellow -6 dB keeping the vertical resolution at 6 m. A better PSL performance can only be achieved at the cost of the vertical resolution (i.e. by reducing the maximum track separation). Table 5.3 shows the PSL values depending on the vertical resolution for the three wavenumber distributions associated to five tracks. In order to fulfill the -6 dB requirement for the PSL, the vertical resolution has to be reduced to 14 m for the *free* and *small* distributions and to 16.7 m for the *uniform* one.

TABLE 5.3: Peak sidelobe level in dB for the different distributions with five tracks

Vertical Res.[1]	21	16.7	14	12	10.5	9.3	8.4	7.6	7	6.4	6
Uniform[2]	-12	-8.3	-5.4	-4.4	-3	-5.5	-2	-4.2	-2.8	-1.2	-1.2
Free	-12	-6.9	-6.3	-5.2	-5.3	-5.4	-4.5	-4.7	-5.16	-4.7	-4.4
Small	-12	-8.3	-7.8	-5.3	-3.8	-2.9	-2.3	-1.8	-1.5	-1.2	-1.1

[1] Rayleigh resolution in meters .[2] The uniform distributions are not always completely uniform as the k_z values are limited to the original positions and two fixed positions are needed to fulfil the requirements in terms of height of ambiguity and vertical resolution.

Figure 5.3 (e) and (f) show the PSF for a vertical resolution of 14 m using five tracks and the corresponding vertical wavenumbers. The lower resolution is reflected on a wider main lobe respect to the one obtained in Figure 5.3 (c). The loss of resolution goes in favour of a reduction of the PSL. The performance across the three distributions is now more similar, with slightly higher values of the PSL for the *uniform* distribution. Also here, the *small* distribution case appears the favoured one. Figure 5.4 (c) shows the profiles obtained by the three algorithms for the *small* distribution. In contrast to the results in Figure 5.4 (b), the profiles appear cleaner (less gradated) allowing a better localization of local maxima. However, the profiles show a wider shape compare to the scenarios with seven and fifteen tracks due to the reduction of the vertical resolution. Nevertheless, for this specific data set, only the magenta polygon appears to be affected by the degraded resolution. In that polygon, while CS is able to detect the two layers, FB and CB fail mixing both maxima. Regarding the difference between the algorithms, FB shows again the lower contrast between the maxima as well as with the sidelobes, while CS shows the higher contrast that allows a better discrimination of the maxima.

5.5 Conclusions

This letter analyzes the impact of different number and distributions of acquisitions in SAR tomography for forest structure applications. Starting from a data set with fifteen tracks, three wavenumber distributions associated to a reduced number of tracks have been discussed: A *uniform* wavenumber distribution, a *free* distribution of wavenumbers optimized with respect to the sidelobe level and a *small* wavenumber distribution. Temporal decorrelation, either in form of high (temporal) frequency changes (e.g. wind effects) or slower changes of the underlying reflectivity function has not been accounted.

Constraining the wavenumber distribution to achieve the maximum possible vertical resolution of 6 m, the obtained results indicate that a minimum number of seven tracks is necessary to suppress the sidelobes lower than -6 dB. For a tomographic scenario with only five acquisitions, a sidelobe suppression better than -6 dB can be achieved by reducing the vertical resolution (i.e. reducing the maximum track separation) down to 14 m. For both scenarios, the results have been discussed by means of three different TomoSAR reconstruction algorithms (Fourier beamforming, Capon beamforming and compressive censing) indicating the effect of the choice of the the reconstruction algorithm.

For a reduced number of acquisitions, a decrease of the vertical resolution is necessary (in the actual case from 6 to 14 m) to reduce the PSL bellow -6 dB. Such a significant reduction of the vertical resolution, may be problematic for areas with multiple canopy layers as it compromises the discrimination of the different forest structure types. In this sense, a possible compromise would be to use 6 tracks to increase the vertical resolution to 10.5 m and, at the same time, keep the PSL bellow -6 dB for all distributions. For 5 and 4 tracks, at 10.5 m of resolution, even with a *free* distribution, the PSL increases to -5.3 and -3.6 dB, respectively.

Acknowledgments

This study was supported and funded by the HGF Alliance. The authors would like to thank the F-SAR team for its invaluable effort during the data acquisition and processing.

References

[1] A. Reigber and A. Moreira, "First demonstration of airborne sar tomography using multibaseline L-band data", *IEEE Transactions on Geoscience and Remote Sensing*, vol. 38, no. 5, pp. 2142–2152, 2000. DOI: `10.1109/36.868873` (cited on pages 104–106).

[2] M. Tello, V. Cazcarra-Bes, M. Pardini, and K. Papathanassiou, "Forest structure characterization from sar tomography at L-band", *IEEE Journal of Selected Topics in Applied Earth Observations and Remote Sensing*, vol. 11, no. 10, pp. 3402–3414, Oct. 2018. DOI: `10.1109/JSTARS.2018.2859050` (cited on pages 104, 108).

[3] V. Cazcarra-Bes, M. Tello-Alonso, R. Fischer, M. Heym, and K. Papathanassiou, "Monitoring of forest structure dynamics by means of L-band sar tomography", *Remote Sensing*, vol. 9, no. 12, p. 1229, 2017. DOI: `10.3390/rs9121229` (cited on pages 104, 108).

[4] T. A. Spies, "Forest structure: a key to the ecosystem", *Northwest Science*, vol. 72, no. 2, pp. 34–36, 1998. [Online]. Available: `http://andrewsforest.oregonstate.edu/pubs/pdf/pub2564.pdf` (cited on page 104).

[5] T. Le Toan, S. Quegan, M. Davidson, H. Balzter, P. Paillou, K. Papathanassiou, S. Plummer, F. Rocca, S. Saatchi, H. Shugart, *et al.*, "The biomass mission: mapping global forest biomass to better understand the terrestrial carbon cycle", *Remote sensing of environment*, vol. 115, no. 11, pp. 2850–2860, 2011. DOI: `10.1016/j.rse.2011.03.020` (cited on page 104).

[6] A. Moreira, G. Krieger, I. Hajnsek, K. Papathanassiou, M. Younis, P. Lopez-Dekker, S. Huber, M. Villano, M. Pardini, M. Eineder, *et al.*, "Tandem-l: a highly innovative bistatic sar mission for global observation of dynamic processes on the earth's surface", *IEEE Geoscience and Remote Sensing Magazine*, vol. 3, no. 2, pp. 8–23, 2015. DOI: `10.1109/MGRS.2015.2437353` (cited on page 104).

[7] S. Tebaldini, "Single and multipolarimetric sar tomography of forested areas: a parametric approach", *IEEE Transactions on Geoscience and Remote Sensing*, vol. 48, no. 5, pp. 2375–2387, 2010. DOI: `10.1109/TGRS.2009.2037748` (cited on page 104).

[8] O. Frey and E. Meier, "Analyzing tomographic sar data of a forest with respect to frequency, polarization, and focusing technique", *IEEE Transactions on Geoscience and Remote Sensing*, vol. 49, no. 10, pp. 3648–3659, 2011. DOI: `10.1109/TGRS.2011.2125972` (cited on page 104).

[9] P. Stoica, R. L. Moses, *et al.*, *Spectral analysis of signals*. Pearson Prentice Hall Upper Saddle River, NJ, 2005, ISBN: 9780131139565 (cited on page 104).

[10] E. Aguilera, M. Nannini, and A. Reigber, "A data-adaptive compressed sensing approach to polarimetric sar tomography of forested areas", *IEEE Geoscience and Remote Sensing Letters*, vol. 10, no. 3, pp. 543–547, 2013. DOI: `10.1109/LGRS.2012.2212693` (cited on page 104).

[11] V. Cazcarra-Bes, M. Pardini, M. Tello, and K. Papathanassiou, "Comparison of tomographic sar reflectivity reconstruction algorithms for forest applications at L-band", *IEEE Transactions on Geoscience and Remote Sensing*, vol. 58, no. 1, pp. 147–164, Jan. 2020. DOI: `10.1109/TGRS.2019.2934347` (cited on pages 104, 106).

[12] M. Nannini, R. Scheiber, and A. Moreira, "Estimation of the minimum number of tracks for sar tomography", *IEEE Transactions on Geoscience and Remote Sensing*, vol. 47, no. 2, pp. 531–543, 2009. DOI: `10.1109/TGRS.2008.2007846` (cited on page 105).

[13] F. Kugler, S. Lee, I. Hajnsek, and K. P. Papathanassiou, "Forest height estimation by means of pol-insar data inversion: the role of the vertical wavenumber", *IEEE Transactions on Geoscience and Remote Sensing*, vol. 53, no. 10, pp. 5294–5311, Oct. 2015. DOI: `10.1109/TGRS.2015.2420996` (cited on page 109).

Chapter 6

Conclusions

This section summarises the whole work through the research questions raised in Section 1.3 and synthesizes the outcomes and open issues of the thesis. The main findings, as well as the key points investigated for each of the four chapters (i.e. the peer-reviewed publications), are summed up in Section 6.1. Moreover, the implications and limitations are presented and linked with the outlook of the work in Section 6.2.

6.1 Summary

The first main research question addressed in this thesis refers to the interpretation of TomoSAR vertical profiles to characterize physical 3-D forest structure. Chapters 2 and 3 have shown that it is possible to define indices that are not only able to quantify forest structure from TomoSAR profiles, but also to characterize structure changes. The second main research question is related to the TomoSAR imaging performance and has been addressed in Chapters 4 and 5. Different tomographic algorithms and configurations have been analyzed with a focus on forest structure applications.

6.1.1 Findings and Key Points Related to Forest Structure Estimation from TomoSAR Profiles

- *In which way 3-D forest structure can be quantified from TomoSAR profiles?*

This question has been addressed in Chapter 2, where the characterization of forest structure (crucial parameter of the forest ecosystem [1]), in terms of horizontal and vertical heterogeneity, have been investigated according to forestry studies. Following this idea, two indices to quantify the 3-D forest structure from TomoSAR profiles have been proposed. In contrast to ground measurements, TomoSAR reflectivity profiles do not provide direct physical structure information. Instead of that, TomoSAR profiles provide the radar reflectivity within an area of the forest rather than a physical forest parameter. The variability of the position and the number of local maxima of the profiles within an area have been used as key attributes of TomoSAR to quantify (by means of two indices) the horizontal and vertical forest structure. The proposed indices have been applied on real TomoSAR data at L-band over two temperate forests, using a compressive sensing algorithm (described in Sections 2.5 and 4.2.2.3). Additionally, the framework has also been tested in a tropical forest using L- and P- band TomoSAR acquisitions (see Appendix B).

- *How does the forest structure derived from inventory data (i.e ground measurements) is related to the structures derived from Lidar and TomoSAR measurements?*

The values of the forest structure indices obtained from TomoSAR have been compared with the horizontal and vertical indices from ground measurements based on single-tree information. From the wide range of indices available in the literature [2], [3], the standard density index [4] and the standard deviation of the diameter at breast height [5] have been selected as the horizontal and vertical structure indices, respectively. A temperate forest in Traunstein (Germany) has been chosen as a test site, where more than 16000 trees in an area of 25 hectares were measured. This is an ideal condition, as the continuous and extended measurements of the trees in the test site allows a direct comparison of the forest structure maps obtained from ground measurements and TomoSAR. In addition, it overcomes the limitation of the standard sparse ground measurements of forests. The results show that there is a good agreement between the structure indices obtained from inventory data (i.e. ground measurements) and TomoSAR profiles, which indicates the ecological significance of the result obtained from TomoSAR.

In order to further explore the capabilities of the structure framework, high-resolution airborne Lidar over the same area have been used to generate Lidar profiles. Afterwards, these Lidar profiles have been used to compute the horizontal and vertical structure indices. The structure results from Lidar and its correlations with the maps obtained with radar and ground measurements indicate that the concept is also valid for Lidar. Therefore, the high similarity between ground, Lidar and TomoSAR measurements confirms the validity of the horizontal-vertical framework to relate different structure measurements.

- *Is it possible to monitor forest structure changes with TomoSAR? Are these changes the same as the ones seen by Lidar, optical images or ground measurements?*

An application example of the proposed 3-D horizontal and vertical forest structure framework is the observation of structure changes. In Chapter 3, from single tree information provided by the FORMIND forest simulator [6], a simple methodology is proposed to generate radar profiles based on their relationship with biomass [7]. The use of a simulator allowed testing the sensitivity and consistency of the forest structure indices to changes due to natural forest evolution or disturbances, such as a fire event or logging activities. The results show that the horizontal and vertical indices, not only allow to differentiate different forest structure types, but also to observe the transition between structure types (e.g. transition from a young to a mature forest) through the changes in both indices. The concept has been applied to three TomoSAR data sets (in 2008, 2012 and 2016) at L-band over a temperate forest in Traunstein (Germany) using the same compressive sensing algorithm as in Chapter 2. The horizontal and vertical structure indices (for each of the years individually) show different values for each of the (previously known) delimited forest structure types. This result confirms again the ecological significance of the framework and the ability to distinguish different forest structure types. Taking into account the period of eight years, changes reported in external data (Lidar, high-resolution optical images and ground measurements) were retrieved in the horizontal and vertical structure indices as well. Therefore, the use of such a framework to get 3-D forest structure from TomoSAR data allows also continuous monitoring of forests to track different structure changes.

6.1.2 Findings and Key Points Related to TomoSAR Algorithms and Configurations

- *Which are the strengths and weaknesses of the most common tomographic algorithms for imaging forest volumes?*

In Chapter 4 two non-model (or model-free) tomographic algorithms (Fourier beamforming (FB) [8] and Capon beamforming (CB) [9]) and one hybrid (compressive sensing (CS) [10]–[12]) have been deeply analyzed for forest volumes in terms of forest structure. The achieved vertical resolution, the ability to detect weak scatterers (canopy layers), the impact of errors in the tracks and the imaging performance for a reduced number of acquisitions have been discussed. The results on simulated data show the better resolution of the CS approach compared to CB and FB, allowing to distinguish closer canopy layers. This feature goes in favour of estimating forest structure based on the position of the maxima, rather than the shape of the profile. Regarding the power, none of the algorithms is able to get the correct absolute power. However, they are able to reconstruct the power ratios between the different scatterers. In terms of robustness to non-uniform tracks, the FB profiles are affected by large lobes as soon as the tracks become not uniform, while CB and especially CS profiles are less affected. However, CS can produce artefacts in the profiles as a consequence of the violation of the assumption of the sparsity in the chosen representation basis.

The algorithms have also been evaluated on four L-band TomoSAR data sets of five images each one, with a total acquisition period of two months over a temperate forest in Traunstein (Germany). In order to improve the quality of the data, an interpolation of the original acquisition tracks to a uniform track distribution has been applied [13]. The results show that the interpolation is beneficial for compensating the instabilities in the tracks for the three algorithms, but FB is the one with the most significant improvement thanks to the interpolation.

The results for the different algorithms on real data also confirm the findings of the analysis with simulated data. CS seems the most appropriate candidate for the estimation of forest structure based on the position of local maxima of the profiles. Moreover, CS is the most robust algorithm against non-uniform tracks or with a reduced number of tracks compared to CB and FB. However, if the number of tracks is sufficiently high in a favourable distribution, approaches like CB or FB could be a better choice as they do not produce artefacts in the profiles and their computational cost is considerably lower than CS.

- *How do different TomoSAR implementations from space (single-pass such as DLR's Tandem-L mission vs repeat-pass such as ESA BIOMASS mission) affect the TomoSAR profiles?*

Unlike airborne TomoSAR implementations, where the images are acquired usually on the same day with some minutes of difference, in space borne implementations temporal gaps of days or weeks are expected between consecutive acquisitions. In Chapter 4 the effect of these temporal gaps in terms of two different space borne implementations, repeat-pass (only one satellite, monostatic) and tandem-like (two simultaneous satellites, bistatic), have been evaluated. The results show that, with the increase of the temporal gap, the use of a tandem-like system allows a better reconstruction of the radar reflectivity. The lower resolution of FB and CB goes in favour of a higher robustness of the imaging than CS. The increase of temporal decorrelation makes the CS profile more unstable in time, incurring in a higher number of artefacts and a general degradation of the profiles compare to the ones without temporal decorrelation.

- *How does the configuration (i.e. number and distribution of tracks) of a TomoSAR acquisition affect the 3-D radar reflectivity estimates and the discrimination among different forest structures?*

Independently of the algorithm used for the reconstruction, the configuration of the TomoSAR system (i.e. the number and the spatial distribution of tracks) affect directly the quality of the TomoSAR profiles and therefore the capability to distinguish different forest structure types. In Chapter 5 different TomoSAR configurations have been evaluated by posing three main requirements on vertical resolution, height of ambiguity and peak sidelobe level (PSL) of the TomoSAR point spread function (PSF). By using an over-sampled scenario of fifteen uniform distributed tracks, the L-band TomoSAR profiles in different forest structure areas of a temperate forest in Traunstein (Germany) have been used to establish a requirement in terms of PSL. From the TomoSAR profiles at each area, the power difference between the two main local maxima has been analyzed, and a PSL of -6 dB is founded sufficient to differentiate the canopy layers from the sidelobes of the PSF. Three reduced distributions of tracks with a reduced number of tracks have been analyzed: Uniform distribution, non-uniform (free) distribution optimized to a PSL level and a distribution with an imposed number of small vertical track displacements. The last type of distribution is optimized also for a (model-based) forest height inversion [14].

The results show that a uniform distribution is not a good option for scenarios with a reduced number of tracks, together with a high vertical resolution, as the PSL increases. In this case, it becomes necessary to distribute the tracks freely. As a consequence, the resulting track distribution is non-uniform, but the resulting PSL level is low enough to characterize the different forest structure areas. The difference in terms of PSL between a completely free distribution and one with constrained small track displacements is not significant. Therefore, the one with small track displacements is preferred as it also allows forest height inversion methodologies.

In the specific case of a temperate forest in Traunstein (Germany), different scenarios have been evaluated to analyze the trade-off between the number of tracks and resolution. Taking into account the limitation of the number of tracks in realistic scenarios, the results show that a reduction of the resolution (and the PSL) is preferred in contrast to a higher vertical resolution. Although a low vertical resolution can be problematic to characterize multi-layer canopy scenarios accurately, the reduction in resolution and PSL goes in favour to a better quality of the TomoSAR profiles and a robust discrimination of the different forest structure types.

6.2 Open Issues and Outlook

The main achievements described in the previous Section 6.1 raise new issues and questions that could be faced and answered in future research.

The principal assumption used in the estimation of forest structure from TomoSAR is the physical significance of the distribution of local maxima in terms of the distribution of trees. Some models and experiments support this assumption [15]–[17], but there is still not a direct validation at all frequencies, forest types and spatial scales. On the other hand, the radar signal depends not only on the structure parameters but also on the dielectric properties of the forest. In order to deal with these characteristics of radar, this thesis supports the idea that the relative position of maxima is, in general, more stable than their power. However, positions of local maxima from the same area could exhibit differences in dry and wet conditions [18] that may affect the horizontal and vertical forest structure indices. Therefore, the robustness of the forest structure estimation approach should be further tested under different weather and seasonal conditions, as well as different types of forests. The analysis on different areas has been started in the work presented in Appendix B for a tropical forest, but the availability of suitable coincidence of TomoSAR and continuous ground data limits the validation to only few test sites. Because of this, the estimation of forest structure from TomoSAR is very promising, but it is not yet fully established and validated. Studies with tower-based radars [19], [20] can help in the interpretation of the radar profiles under different conditions, but the reduced area of these experiments limits a complete and proper validation of the forest structure.

The horizontal-vertical structure plane (see Figure 1.1) has been found to be able to link ground, Lidar and TomoSAR structure measurements, but the representation in a 2-D plane of a 3-D quantity incurs on an intrinsic loss of information. Moreover, the conceptual orthogonality on the original idea of the horizontal-vertical plane is not assured for the suggested indicators from TomoSAR profiles. This non-orthogonality could lead to some ambiguities for some forest structure types. Moreover, the two indices are not absolute measurements, i.e. in order to compare maps from two different areas, a suitable normalization needs to be done. At the same time, if different TomoSAR sets are used, the number of local maxima in the scene could vary. This fact is not problematic for the vertical index, as it accounts for the relative positions of the local maxima. However, the horizontal index could exhibit lower values with systems with lower resolutions. Future research could focus on improving the indices to reduce the limitations of the proposed ones.

The structure indices are obtained by aggregating ground measurements or local maxima from profiles at a particular spatial scale. This statistical principle allows reducing small uncertainties and errors at the expenses of resolution, as the number of samples should be significant enough to have a meaningful result. With this, it is assumed that the forest inside the spatial scale used to compute the structure indices is as much uniform as possible. In general, forest structure estimation has been done for a fixed size of the spatial scale, and only a small analysis of different scales have been discussed in Section 2.3.4. The simultaneous use of indices calculated at multiple scales could allow a better characterization and distinction of forest structure types [21].

The test sites considered during the thesis are located in flat areas with almost no topography. However, the effect of slopes has an impact on the incidence angle which is translated into a different geometric projection of the scatterers distribution (TomoSAR profile) in the elevation direction. As a consequence, this distortion of the profiles may have an impact on the structure indices obtained in the slopes. The estimation and interpretation of the profiles in these areas is still an open issue to be further investigated.

The initialization of the CS algorithm for the TomoSAR inversion has some degrees of freedom, such as the wavelet basis [22] or the minimization algorithm [23], [24]. These settings can change the TomoSAR profiles, it would be interesting to investigate if these settings could be fixed adaptively to the data to achieve the best possible result. An additional issue to be further investigated in CS algorithms is the reduction of the high computational cost, which could limit the use in real applications where a huge amount of data would need to be processed.

The importance of biomass has been stressed as one of the main parameters of interest of the forest [25]. The use of structure indices to constrain the relationships for (a better) estimation of biomass should be investigated along the line of previous works [26], [27]. Besides, the ESA BIOMASS and DLR's Tandem-L missions will provide for the first time unique TomoSAR data sets over the forests around the Earth that will open the door to further analysis and improvements of 3-D forest structure applications from TomoSAR data.

References

[1] T. A. Spies, “Forest structure: a key to the ecosystem”, *Northwest Science*, vol. 72, no. 2, pp. 34–36, 1998. [Online]. Available: `http://andrewsforest.oregonstate.edu/pubs/pdf/pub2564.pdf` (cited on page 115).

[2] A. Pommerening, “Approaches to quantifying forest structures”, *Forestry: An International Journal of Forest Research*, vol. 75, no. 3, pp. 305–324, 2002. DOI: `10.1093/forestry/75.3.305` (cited on page 116).

[3] H. Pretzsch, “Forest dynamics, growth, and yield”, in *Forest Dynamics, Growth and Yield*, Springer, 2009, pp. 1–39. DOI: `10.1007/978-3-540-88307-4_1` (cited on page 116).

[4] L. H. Reineke, “Perfecting a stand-density index for even-aged forests”, 1933. [Online]. Available: `https://naldc.nal.usda.gov/download/IND43968212/PDF` (cited on page 116).

[5] N. Brokaw and R. Lent, “Vertical structure. in ‘maintaining biodiversity in forest ecosystems’”, pp. 373–399, 1999. DOI: `10.1017/CBO9780511613029.013` (cited on page 116).

[6] R. Fischer, F. Bohn, M. D. de Paula, C. Dislich, J. Groeneveld, A. G. Gutiérrez, M. Kazmierczak, N. Knapp, S. Lehmann, S. Paulick, S. Pütz, E. Rödig, F. Taubert, P. Köhler, and A. Huth, “Lessons learned from applying a forest gap model to understand ecosystem and carbon dynamics of complex tropical forests”, *Ecological Modelling*, vol. 326, pp. 124–133, 2016, Next generation ecological modelling, concepts, and theory: structural realism, emergence, and predictions, ISSN: 0304-3800. DOI: `10.1016/j.ecolmodel.2015.11.018` (cited on page 116).

[7] A. T. Caicoya, M. Pardini, I. Hajnsek, and K. Papathanassiou, “Forest-above ground biomass estimation from vertical reflectivity profiles at L-band”, *IEEE Geoscience and Remote Sensing Letters*, vol. 12, no. 12, pp. 2379–2383, 2015. DOI: `10.1109/LGRS.2015.2477858` (cited on page 116).

[8] P. Stoica, R. L. Moses, *et al.*, *Spectral analysis of signals*. Pearson Prentice Hall Upper Saddle River, NJ, 2005, ISBN: 9780131139565 (cited on page 117).

[9] J. Capon, “High-resolution frequency-wavenumber spectrum analysis”, *Proceedings of the IEEE*, vol. 57, no. 8, pp. 1408–1418, 1969. DOI: `10.1109/PROC.1969.7278` (cited on page 117).

[10] A. Budillon, A. Evangelista, and G. Schirinzi, “Three-dimensional sar focusing from multipass signals using compressive sampling”, *IEEE Transactions on Geoscience and Remote Sensing*, vol. 49, no. 1, pp. 488–499, 2011. DOI: `10.1109/TGRS.2010.2054099` (cited on page 117).

[11] E. Aguilera, M. Nannini, and A. Reigber, “Wavelet-based compressed sensing for sar tomography of forested areas”, *IEEE Transactions on Geoscience and Remote Sensing*, vol. 51, no. 12, pp. 5283–5295, 2013. DOI: `10.1109/TGRS.2012.2231081` (cited on page 117).

[12] X. X. Zhu and R. Bamler, “Tomographic sar inversion by l1-norm regularization-the compressive sensing approach”, *IEEE Transactions on Geoscience and Remote Sensing*, vol. 48, no. 10, pp. 3839–3846, 2010. DOI: `10.1109/TGRS.2010.2048117` (cited on page 117).

[13] F. Lombardini and M. Pardini, “3-D sar tomography: the multibaseline sector interpolation approach”, *IEEE Geoscience and Remote Sensing Letters*, vol. 5, no. 4, pp. 630–634, 2008. DOI: `10.1109/LGRS.2008.2001283` (cited on page 117).

[14] F. Kugler, S. Lee, I. Hajnsek, and K. P. Papathanassiou, “Forest height estimation by means of pol-insar data inversion: the role of the vertical wavenumber”, *IEEE Transactions on Geoscience and Remote Sensing*, vol. 53, no. 10, pp. 5294–5311, Oct. 2015. DOI: `10.1109/TGRS.2015.2420996` (cited on page 118).

[15] M. Brolly and I. H. Woodhouse, “Vertical backscatter profile of forests predicted by a macroecological plant model”, *International journal of remote sensing*, vol. 34, no. 4, pp. 1026–1040, 2013. DOI: `10.1080/01431161.2012.715777` (cited on page 118).

[16] L. Thirion, E. Colin, and C. Dahon, “Capabilities of a forest coherent scattering model applied to radiometry, interferometry, and polarimetry at P-and L-band”, *IEEE Transactions on Geoscience and Remote Sensing*, vol. 44, no. 4, pp. 849–862, 2006. DOI: `10.1109/TGRS.2005.862523` (cited on page 118).

[17] Y.-C. Lin and K. Sarabandi, “A monte carlo coherent scattering model for forest canopies using fractal-generated trees”, *IEEE Transactions on Geoscience and Remote Sensing*, vol. 37, no. 1, pp. 440–451, 1999. DOI: `10.1109/36.739083` (cited on page 118).

[18] M. Pardini, K. P. Papathanassiou, and F. Lombardini, “Impact of dielectric changes on L-band 3-D sar reflectivity profiles of forest volumes”, *IEEE Transactions on Geoscience and Remote Sensing*, no. 99, pp. 1–14, 2018. DOI: `10.1109/TGRS.2018.2850357` (cited on page 118).

[19] H. T. M. Dinh, S. Tebaldini, F. Rocca, C. Albinet, P. Borderies, T. Koleck, T. Le Toan, and L. Villard, “Tropiscat: multi-temporal multi-polarimetric tomographic imaging of tropical forest”, in *2012 IEEE International Geoscience and Remote Sensing Symposium*, Jul. 2012, pp. 7051–7054. DOI: `10.1109/IGARSS.2012.6351947` (cited on page 118).

[20] L. M. H. Ulander, A. R. Monteith, M. J. Soja, and L. E. B. Eriksson, “Multiport vector network analyzer radar for tomographic forest scattering measurements”, *IEEE Geoscience and Remote Sensing Letters*, vol. 15, no. 12, pp. 1897–1901, Dec. 2018. DOI: `10.1109/LGRS.2018.2865673` (cited on page 118).

[21] M. Tello, V. Cazcarra-Bes, R. Fischer, and K. Papathanassiou, “Multiscale forest structure estimation from sar tomography”, in *EUSAR 2018; 12th European Conference on Synthetic Aperture Radar*, ISBN: 9783800746361, Jun. 2018, pp. 1–4, ISBN: 9783800746361 (cited on page 119).

[22] E. Aguilera, “Synthetic aperture radar tomography compressed sensing models and algorithms”, PhD thesis, Technical University of Berlin, 2014. [Online]. Available: `https://elib.dlr.de/85764/` (cited on page 119).

[23] S. Diamond and S. Boyd, “Cvxpy: a python-embedded modeling language for convex optimization”, *The Journal of Machine Learning Research*, vol. 17, no. 1, pp. 2909–2913, 2016. [Online]. Available: `http://jmlr.org/papers/v17/15-408.html` (cited on page 119).

[24] B. O’Donoghue, E. Chu, N. Parikh, and S. Boyd, “Conic optimization via operator splitting and homogeneous self-dual embedding”, *Journal of Optimization Theory and Applications*, vol. 169, no. 3, pp. 1042–1068, Jun. 2016. [Online]. Available: `http://stanford.edu/~boyd/papers/scs.html` (cited on page 119).

[25] Food and A. O. of the United Nations, “Global forest resources assessment”, *Main report, FAO Forest paper 163*, 2010. [Online]. Available: `http://www.fao.org/3/i1757e/i1757e00.htm` (cited on page 119).

[26] A. T. Caicoya, “Allometric estimation of aboveground forest biomass using forest structure parameters estimated by means of multi-baseline sar measurements”, PhD thesis, Technische Universität München, 2016. [Online]. Available: `https://mediatum.ub.tum.de/?id=1284783` (cited on page 119).

[27] E. Blomberg, L. Ferro-Famil, M. J. Soja, L. M. H. Ulander, and S. Tebaldini, “Forest biomass retrieval from L-band sar using tomographic ground backscatter removal”, *IEEE Geoscience and Remote Sensing Letters*, vol. 15, no. 7, pp. 1030–1034, Jul. 2018. DOI: `10.1109/LGRS.2018.2819884` (cited on page 119).

Appendix A

Early Lessons on Combining Lidar and Multi-baseline SAR Measurements for Forest Structure Characterization

M. Pardini, J. Armston, W. Qi, S. Lee, M. Tello, V. Cazcarra-Bes, C. Choi, K. Papathanassiou, R. Dubayah, T. Fatoyinbo

Surveys in Geophysics
Published in July 2019. DOI: 10.1007/s10712-019-09553-9

Key findings/points:

- Review of the differences, commonalities, and complementarities of Lidar and SAR measurements.
- Analysis of a model-based framework where lidar-derived parameters are used to initialize SAR scattering models.
- Analysis of a structure-based framework based on the ability of lidar and SAR measurements to express physical forest structure by means of appropriate indices.
- Comparison of vertical profiles from TomoSAR at different frequencies and Lidar.
- Comparison of forest structure estimated from TomoSAR, Lidar and ground measurements.

The author's contributions:

- M. Pardini is the main author of the manuscript.

The co-author's contributions:

- V. Cazcarra-Bes helped in the processing of the Tomographic SAR data. He also obtained the forest structure maps and helped in the interpretation of the results.

Surveys in Geophysics
https://doi.org/10.1007/s10712-019-09553-9

Early Lessons on Combining Lidar and Multi-baseline SAR Measurements for Forest Structure Characterization

Matteo Pardini[1] · John Armston[2] · Wenlu Qi[2] · Seung Kuk Lee[2,3] · Marivi Tello[1] · Victor Cazcarra Bes[1] · Changhyun Choi[1] · Konstantinos P. Papathanassiou[1] · Ralph O. Dubayah[2] · Lola E. Fatoyinbo[3]

Received: 10 December 2018 / Accepted: 21 June 2019

Abstract
The estimation and monitoring of 3D forest structure at large scales strongly rely on the use of remote sensing techniques. Today, two of them are able to provide 3D forest structure estimates: lidar and synthetic aperture radar (SAR) configurations. The differences in wavelength, imaging geometry, and technical implementation make the measurements provided by the two configurations different and, when it comes to the sensitivity to individual 3D forest structure components, complementary. Accordingly, the potential of combining lidar and SAR measurements toward an improved 3D forest structure estimation has been recognised from the very beginning. However, until today there is no established framework for this combination. This paper attempts to review differences, commonalities, and complementarities of lidar and SAR measurements. First, vertical lidar reflectance and SAR reflectivity profiles at different wavelengths are compared in different forest types. Then, current perspectives on their combination for the generation of enhanced structure products are discussed. Two promising frameworks for combining lidar and SAR measurements are reviewed. The first one is a model-based framework where lidar-derived parameters are used to initialize SAR scattering models, and relies on both the validity of the models and on the physical equivalence of the used lidar and SAR parameters. The second one is a structure-based framework based on the ability of lidar and SAR measurements to express physical forest structure by means of appropriate indices. These indices can then be used to establish a link between the two kind of measurements. The review is supported by experimental results achieved using space- and airborne data acquired in recent relevant mission and campaigns.

Keywords Forest · Structure · Height · Lidar · Synthetic-aperture radar (SAR) · Full waveforms · Polarimetric SAR interferometry (Pol-InSAR) · SAR tomography (TomoSAR)

✉ Matteo Pardini
matteo.pardini@dlr.de

[1] Microwave and Radar Institute, German Aerospace Center, Wessling 82234, Germany

[2] Department of Geographical Sciences, University of Maryland, College Park, MD 20742, USA

[3] Biospheric Sciences Laboratory, NASA Goddard Space Flight Center, Greenbelt, MD 20771, USA

1 Introduction

The development and functionality of forests are widely reflected in their biophysical structure. According to a commonly used definition, forest (canopy) structure is “the organisation in space and time, including the position, extent, quantity, type and connectivity, of the aboveground components of vegetation” (Parker 1995; Lefsky et al. 1999; Spies 1998; Harding et al. 2001; Snyder 2010). Thus, it expresses forest state, functionality, biodiversity and evolution (Hall et al. 2011; Brokaw and Lent 1999; McElhinny et al. 2005). Accordingly, forest structure is an indicator of forest successional stage and development as well as sustainability and habitability, and is therefore an important parameter for assessing forest productivity (Bohn and Huth 2017), biomass and biodiversity (Bergen et al. 2009; Goetz et al. 2007; Turner et al. 2003). Forest structure changes are associated with dynamic processes such as growth, regeneration, decay, and natural or anthropogenic disturbance. Knowledge about such processes is important for modeling the function and development of forest ecosystems, and for developing accurate and robust forest biomass estimators (Frolking et al. 2009). Mapping forest structure is therefore critical for understanding the history, function, and future of forest ecosystems.

Traditionally, forest structure characterisation relies on sampling at local scales by means of either field inventory plots or more recently terrestrial laser scanning techniques able to catch the 3D arrangement of vegetation compartments. However, any extrapolation to larger scales is limited by the ability of these measurements to represent larger areas. Moreover, the fact that the temporal continuity of such plot measurements is in many cases difficult to be established limits even more their ability to characterise forest structure change. In this context, remote sensing techniques offer the potential to overcome, at least partially, these limitations (Hall et al. 2011; Bergen et al. 2009; Goetz et al. 2007; Turner et al. 2003; Frolking et al. 2009). Today, only two remote sensing techniques can provide 3D information and contribute to the characterisation of forest structure at large scales (Hall et al. 2011): lidar and synthetic-aperture radar (SAR).

Lidar systems are active configurations usually operating in the infrared or visible region of the electromagnetic spectrum at wavelengths in the nm range. They transmit laser pulses in nadir-looking geometry which “illuminate” a given footprint on the ground whose diameter is typically in the order of decimeters for small-footprint lidar up to tens of meters for large-footprint configurations. The transmitted pulses are reflected by the vegetation elements within the footprint back to the sensor, where they are usually “incoherently” recorded, i.e., only the energy (amplitude) of the reflected light is detected as a function of the signal runtime. A single transmitted laser pulse can be reflected by different vegetation elements located at different heights within the footprint, leading to multiple reflections and an extended distribution of light energy that returns to the sensor. The distribution of light energy that returns to the sensor is known as waveform and is directly related to the 3D distribution of the intercepted vegetation surfaces within the footprint (Dubayah and Drake 2000).

SAR configurations also transmit electromagnetic pulses, but differently from the lidar sensors in the microwave region of the electromagnetic spectrum (wavelengths in the order of cm to dm) in a side-looking geometry. The transmitted pulses interact with Earth’s surface, and only a portion of them is scattered back to the sensor. The backscattered pulses are “coherently” recorded by the receiver, i.e., both their amplitude and phase are measured. The amplitude and phase of the backscattered signal depend on the geometric and dielectric properties of the scatterers and their distribution within the antenna footprint, i.e., the illuminated area/volume. With increasing wavelength (decreasing frequency) radar pulses penetrate more and more into and through vegetation layers, and interact with vegetation elements located at different heights within the forest volume and with the underlying ground. However, a single SAR image, even if it results from the interaction of the transmitted pulse(s) with the whole 3D forest structure, does not allow a reconstruction of the 3D distribution of scatterers. For this, a set of SAR images acquired under (slightly) different angular directions (i.e., incidence angles) is required in the context of interferometric (InSAR) and tomographic SAR measurements (Moreira et al. 2013). The side-looking geometry complicates additionally the interpretation of a single SAR image, but at the same time, it allows the separation of the scatterers in the ground range direction and the realisation of wide swath widths up to hundreds of kilometers. Spaceborne SAR configurations of the latest generation can therefore realize revisit times between 1 and 2 weeks with resolution on ground between 1 m and 10 m.

Accordingly, the combined use of lidar and SAR data has the potential to enhance the quality of forest structure characterization by improving the accuracy of physical forest structure parameter estimates, (e.g., forest height and biomass). The combination of SAR and lidar data becomes even more relevant in view of a multitude of SAR and lidar spaceborne missions that are curently operational or planned to be launched and operated in the coming years to meet a number of forest-related objectives. Lidar missions like NASA’s GEDI (Dubayah 2015) and IceSAT-2 (Neuenschwander and Magruder 2018) or JAXA’s MOLI (Mitsuhashi et al. 2018) and SAR missions like ESA’s BIOMASS (Le Toan et al. 2011) NASA’s NISAR (Rosen et al. 2017) and/or DLR’s TanDEM-X (Krieger et al. 2013) and Tandem-L (Moreira et al. 2015) are expected to operate and acquire data simultaneously or contiguously in time. For this, the understanding of the complementarities and possible synergies between lidar and SAR (i.e., polarimetric SAR interferometry, Pol-InSAR, and/or SAR tomography, TomoSAR) measurements is required.

The similarity of information content of lidar and SAR measurements arises from their common sensitivity to the size and location of vegetation elements in the forest volume. The difference, thus complementarity, arises from the different wavelengths and the different acquisition geometries (i.e., nadir-looking vs. side-looking) defining the interaction of the transmitted pulses with the forest elements. For lidar, the penetration into and through the canopy layer is supported by the nadir-looking geometry that facilitates the penetration through vegetation gaps, while longer wavelengths allow SAR pulses to penetrate into and through canopy layers even in side-looking geometries. The structure information revealed by lidar measurements primarily implies the geometry of trunk and branch structure forming and supporting the canopy. On the other hand, the relative importance of the different tree components (e.g., leaves, branches, trunks) in SAR measurements depends on their vertical and horizontal distribution and the wavelength. Further, in contrast to lidar, SAR measurements are also sensitive to the dielectric properties of the forest which depend strongly on the amount and distribution of water across the vegetation elements (Hall et al. 2011; Moreira et al. 2013).

The difference in information content is one dimension that can be exploited for the development of lidar-SAR fusion algorithms. In this case, lidar and SAR data are combined in a commonly valid scattering or allometric model. One example is the direct use of lidar measurements or lidar-derived parameters to support and/or improve model-based inversions of forest structure parameters from SAR data. The use of lidar data allows to employ more complex physical models and to decouple the geometric from the dielectric information of the SAR data. This could be particularly important for instance to support smaller SAR observations spaces repeated in time to detect structural or dielectric changes. This concept has been demonstrated to estimate top height from X-band SAR interferometric coherence measurements by means of the Random-Volume-over-Ground (RVoG) model using the lidar ground topography (Kugler et al. 2014). Similarly, the use of lidar ground and top forest height in the RVoG model allows the estimation of the attenuation of SAR pulses through the vegetation again from interferometric coherences (Praks et al. 2012; Pardini et al. 2016; Qi and Dubayah 2016). Furthermore, higher-dimensional frameworks for the extraction of structure information from radar reflectivity profiles can benefit from the use of lidar vegetation profiles for parameterisation (Brolly et al. 2016). However, these approaches rely not only on the validity of the model(s) used to combine the two data sets, but also require that lidar and SAR configurations share a set of physically equivalent parameters. However, this is not always the case as, especially with increasing difference in the lidar and radar wavelengths, the differences in the scattering and propagation make lidar and SAR pulses interact differently with the physical vegetation elements. The loss of physical equivalence between SAR and lidar parameters makes the lidar-based parameterisation of SAR models lose significance (Treuhaft et al. 2009; Brolly et al. 2016; Pardini et al. 2018a, b).

The second dimension that can be used to combine lidar and radar data is their complementarity in terms of acquisition and measurement characteristics driven by the individual technologies and acquisition strategies. With particular reference to spaceborne implementations, lidar measurements are typically acquired by means of footprint samples along rather narrow stripes so that large scale coverage and short revisit times become challenging to achieve. In contrast, SAR measurements are continuous with high spatial resolution, and can be implemented by means of wide swaths that allow large scale coverage and short revisit times (Bamler and Hartl 1998; Moreira et al. 2013). At the same time, lidar configurations allow direct measurement of vegetation reflectance profiles with a fairly high vertical resolution, while SAR systems measure backscattering amplitudes and/or interferometric coherences at different polarizations (Pol-InSAR) or radar reflectivity profiles (TomoSAR) with a lower vertical resolution, which are not always straightforward to be interpreted in terms of physical forest structure.

In this case, the combination of lidar and SAR measurements strongly depends on the ability to establish a (physical or statistical) link between them at the different scales/resolutions performed. This link can be established by means of statistical regression(s), and several examples for such an approach have been reported in the literature, for example aiming at biomass estimation by combining lidar heights and SAR backscatter and/or interferometric parameters [see, e.g., (Kellndorfer et al. 2010; Sun et al. 2011; Tsui et al. 2013; Fatoyinbo and Simard 2013; Kaasalainen et al. 2015)]. On the other hand, lidar and SAR measurements can be linked more systematically by means of a scattering model or by means of common structure-dependent indices. The choice between the two frameworks strongly depends on the individual information content. The applicability of the *model-based* framework relies on the common sensitivity to geometric parameters. For instance, the lidar ground height has been used to bridge the spatial (Qi and Dubayah 2016, here together with forest heights at lidar footprint locations) or the temporal (Persson et al. 2017) dissimilarities of lidar and SAR measurements to obtain continuous estimates of forest height and of its changes over large scales. On the other hand, the *structure-based* framework aims at establishing a correspondence between lidar and Pol-InSAR/TomoSAR measurements by means of their capability in reflecting physical 3D forest structure through appropriate indices without necessarily exchanging parameters (Cazcarra-Bes et al. 2017; Tello et al. 2018; Pardini et al. 2018a). In this way, not only the commonalities, but also the complementarities of the different configurations and wavelengths can be exploited. Although promising, the latter framework is in a very early stage of development, considering also that the interpretation of 3D SAR reflectivity in terms of physical forest structure attributes is not as advanced as for lidar profiles.

The objective of this paper is to review (i) the differences, thus indicating the complementarities, in terms of information content of lidar and SAR measurements at different wavelengths, and (ii) the model-based and the structure-based frameworks in which their combination appears promising. Section 2 presents from a theoretical point of view how lidar and SAR measurements are linked to forest structure, and the factors affecting this relationship. The complementarity between the information content of lidar and SAR measurements is then addressed in Sect. 3 by using reflectance and reflectivity profiles in different forest types. The dependency of the SAR profiles on wavelength, dielectric properties, 3D structure, and temporal changes is shown. For this, real airborne SAR (DLR E-SAR and F-SAR platforms) and lidar data acquired over the temperate Traunstein forest (South of Germany) are used. As an example of a tropical forest site lidar and SAR results over the ForestGEO (Smithsonian Institution Forest Global Earth Observatories) plot in Rabi (Gabon) are also shown. The model-based framework is reviewed in Sect. 4 with a case study concerning forest height estimation. With reference to a spaceborne implementation, one InSAR coherence is used to fill the spatial gaps of a lidar acquisition that, in turn, parameterises the RVoG model. Different parameterisation strategies are compared. Concerning the structure-based framework, Sect. 5 reviews a case study on the Rabi plot in which indices expressing horizontal and vertical heterogeneity of structure are calculated from lidar waveforms and TomoSAR profiles, in correspondence to structure indices with the same meaning already established in forestry and ecology. Finally, Sect. 6 draws the conclusions.

2 Basics of Lidar and SAR Measurements of Forest Structure

2.1 Lidar Measurements

Lidar measurements rely on the transmission of laser pulses of finite length towards a scene. The pulses are intercepted, attenuated and reflected (i.e., backscattered) by the branches and leaves of the vegetation canopy, and by the ground, and return back to the sensor. The receiver records the reflected distribution of (light) energy (i.e., the waveform) as a function of time. The time a pulse takes after being transmitted to return to the sensor depends on the range and the scattering properties of intercepted objects within the illuminated part of the scene (i.e., the footprint) as well as the distance between the laser source and the receiver, and the actual atmospheric conditions. The range between the sensor and an intercepted object is calculated as $r_i = c(t_i - t_0)/2$, where c is the speed of light, t_0 is the timing of the transmitted pulse and t_i is the timing of a peak or discretised range bin of the received waveform. Accordingly, the received waveform depends directly on the 3D distribution of the intercepted vegetation elements within the footprint (Dubayah and Drake 2000).

The reflected energy from a vegetation layer of thickness (i.e., height) H_V located over a reference elevation z_G—ignoring for simplicity the propagation through the atmosphere and assuming a random distribution of scattering elements and penetration until the ground level z_G—can generally be modelled as

$$P(x, y, z) = P_0 \int_{z_G}^{z_G+H_V} \mathrm{d}z \iint \beta(x, y, z) \cdot \mathrm{e}^{-\tau(z-z_G)} \mathrm{d}y\mathrm{d}x, \tag{1}$$

where P_0 is the total returned power, where $\beta(x, y, z)$ is the volumetric reflection of the vegetation layer, τ the volumetric extinction coefficient that accounts for the two-way attenuation within the vegetation layer.

Vegetation lidar instruments use in general wavelengths of 1064 nm or 1550 nm and are designed to maximise the measurement signal-to-noise ratio considering atmospheric attenuation, eye-safey, and the reflectance of ground and vegetation elements at those wavelengths. The way the distribution of light energy that returns to the sensor is received and recorded categorises lidar instruments as discrete return or waveform:

1. “Discrete return” lidar systems record only individual (discrete) peaks (i.e., time-stamped ranges triggered real-time) of the waveform. They identify peaks and record a point at each peak location in the waveform curve. These individual or discrete points are called returns. A discrete system may record 1–4 (and sometimes more) returns from each laser pulse.
2. “Full-waveform” lidar systems record the distribution of transmitted and returned light energy. Accordingly, (full) waveform lidar data contain more information compared to discrete return lidar systems, but are more complex to process. Waveform lidar systems sample the returned waveform at a higher frequency and record the energy returned over equal time intervals.

Discrete return lidars are typically designed for fine-scale topographic airborne mapping, therefore their footprint is typically kept to 0.1 to 2 m by employing a small beam divergence angle. However, large-footprint (>5 m) waveform lidar have several advantages over small footprint ones for mapping vegetation (Dubayah and Drake 2000). First, with a footprint comparable to the average crown diameter (10–25 m), there is a higher probability to contain both ground and tree top at the same time in a waveform. Second, larger footprints can cover wider areas at a lower cost. Large-footprint full-waveform lidar systems from airborne platforms such as the NASA Laser Vegetation, and Ice Sensor (LVIS; Blair et al. 1999) are being used not only for many vegetation studies, but also for calibration and validation of structure parameter extraction algorithms for instruments on spaceborne platforms, like the GEDI (Global Ecosystem Dynamics Investigation).

Central to the use of lidar measurements for estimating vegetation structure parameters is the separation of reflections (returns) from canopy and ground surfaces. Simple waveforms are common from bare ground and complex waveforms from heterogeneous forest canopies. In addition to the characteristics of canopy structure, waveform shapes are affected by ground slope, pulse width and the spatial distribution of wavefront energy (Dubayah et al. 2000). The first and last modes along the profile of a recorded waveform are typically associated with the highest and lowest reflecting surfaces within the footprint, respectively. Identification of these modes within the waveform is required to precisely geolocate the corresponding reflecting surfaces and calculate statistical quantile metrics from the integrated waveform between these ranging points. These statistical quantiles are

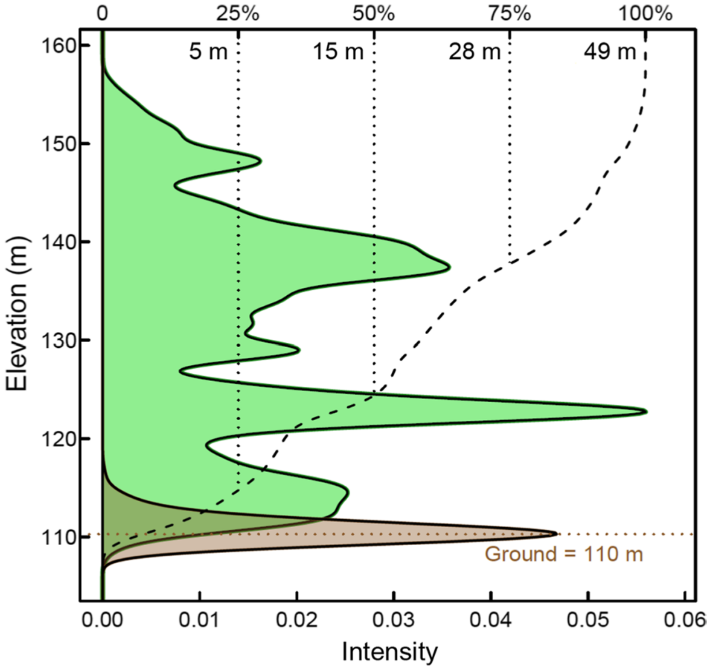

Fig. 1 Example of a lidar waveform simulated from airborne discrete return lidar data acquired over a complex rainforest canopy at La Selva Biological Station, Costa Rica, showing the energy returned from the ground surface (brown) and the energy returned from the canopy (green) as a function of elevation. The reference ground elevation is shown along with the 25th, 50th, 75th, and 100th percentile relative height (RH) metrics extracted from the cumulated energy profile (dashed line)

typically referred to as relative height (RH) metrics (sketched in Fig. 1), which are often used in models to predict aboveground biomass density (Dubayah et al. 2010). The derivation of vertical structure of vegetation canopies from lidar waveform data, though, depends on the knowledge of the relationship between lidar waveforms and the spatial structure and optical properties of vegetation canopies.

In addition to “lidar perceived” statistical metrics, large-footprint waveform lidars enable the estimation of biophysical metrics, as they are a direct measurement of the vertical distribution of the intercepted surfaces between the canopy top and the ground. In the absence of multiple scattering, a received waveform is the product of the projected area of canopy/background materials along the path of the laser pulse, their single scattering albedo, and phase function. The projected area of canopy/background materials is often expressed as the canopy gap probability (P_{gap}), which is a parameter that is fundamental to linking lidar measurements, vertical and horizontal canopy structure, and the radiation regime of a plant canopy (Armston et al. 2013; Ni-Meister et al. 2001). The directional gap probability, $P_{gap}(\theta)$, is defined as the probability of a beam of infinitesimal width at zenith angle θ to the local normal, being directly transmitted through a canopy. The vertical distribution of lidar-derived P_{gap} is indirectly related to the vertical distribution of plant area, enabling the estimation of Plant Area Index (PAI), vegetation cover and their vertical profiles (Ni-Meister et al. 2001; Tang et al. 2012).

Surface elevation, height, and vertical profiles of PAI and vegetation cover are all structure parameters that are being generated from GEDI waveform lidar measurements. However, in contrast to airborne scanning systems such as LVIS, spaceborne lidar instruments such as NASA’s ICESat/GLAS and GEDI are profiling instruments and may only measure a fraction of the Earth’s surface. For example, during GEDI’s 2-year mission life, waveform measurements are made over the Earth’s surface between 51.6°N and 51.6°S, resulting in approximately 10 billion observations of the Earth’s land surface in absence of clouds. The sampling pattern is optimised to maximise the geographic coverage of these observations. In the case of GEDI, shown in Fig. 2,

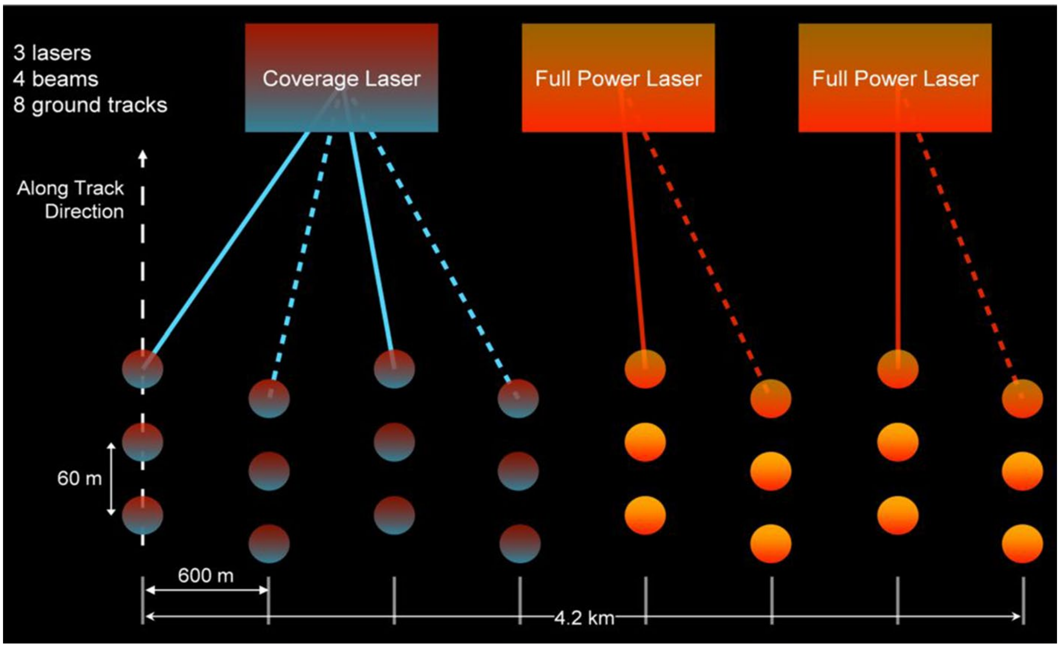

Fig. 2 The sampling pattern of the NASA Global Ecosystems Dynamics Investigation (GEDI) mission, illustrating the arrangement of ground tracks generated from the full power and coverage laser beams. Vertical and horizontal spacing of footprints are not to scale

three lasers (two full power and a coverage one) generate four beams that are dithered to allow data collection along 8 tracks separated by 600 m in across-track direction. This way, a total across-track width of 4.2 km is covered by a single GEDI overflight. Along each track, footprints with a nominal diameter of 25 m are illuminated on ground and separated by 60 m in the along-track direction.

Lidar acquisitions are limited by the presence of clouds and dense atmospheric haze: in these cases, the signal is often attenuated before it reaches the ground. In addition, the estimation of the sub-canopy topography, vegetation height and the interpretation of the waveform in terms of physical structure is affected directly by multiple scattering, sloped terrains and off-nadir pointing (Yang et al. 2011). Multiple scattering occurring in optically thick media distort the waveform making their interpretation more difficult. Additionally, off-nadir pointing and/or a sloped terrain may also deform the vertical waveform shape with respect to a nadir pointing and/or flat terrain. Sloped terrains typically extend the ground return and make it closer to, or even overlapping with, the vegetation returns. This effect becomes more critical at larger footprint sizes. For an off-nadir pointing angle, a larger amount of light energy tends to remain trapped in the upper canopy layers. If penetration to the ground occurs, the ground peak can disappear even on a flat terrain, similarly to the sloped terrain and nadir pointing case. However, in an off-nadir pointing lidar the path length is tilted with respect to the tree growth direction, and this has to be accounted for in the height estimation process. Finally, it is worth remarking that spaceborne lidar sensor are further limited due to the sampling on ground, that leads to a gapped coverage and hampers high spatial resolution (e.g., 1 ha) mapping of forest structure characteristics. In this case, high-resolution mapping can be achieved by combining the lidar data with those from different sensors (e.g., radar or optical).

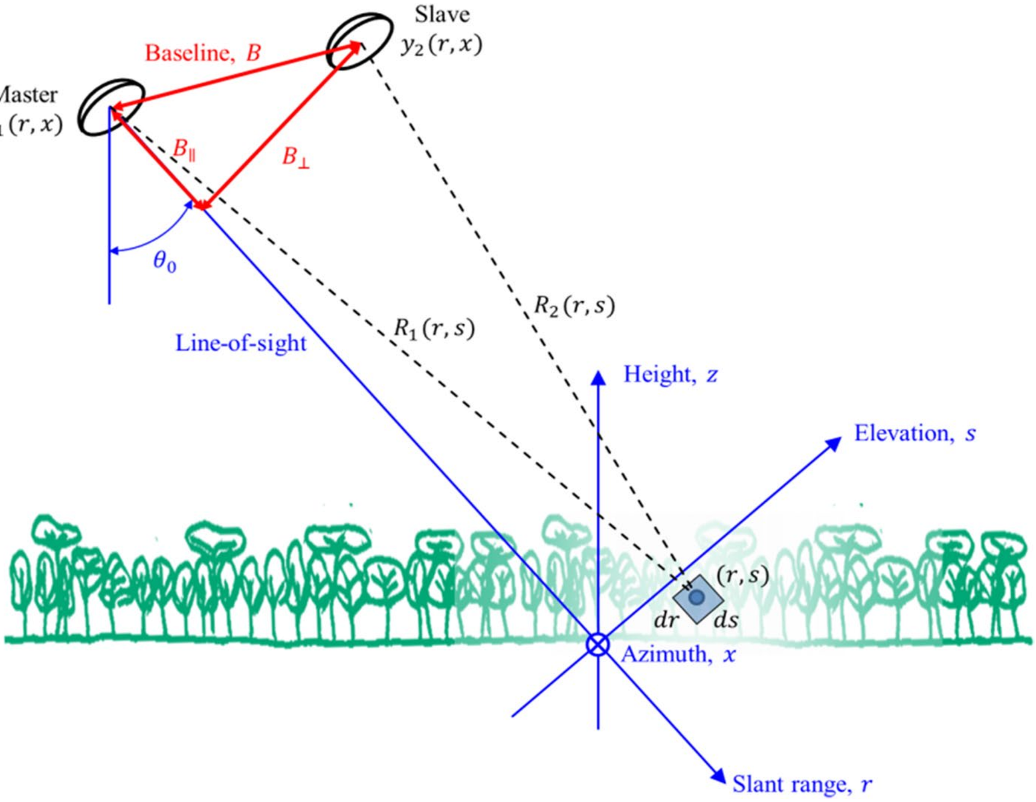

Fig. 3 SAR and (Pol-)InSAR acquisition geometry in the basic single baseline configuration. The azimuth axis is orthogonal to the plane of the page. Angles and distances are not to scale

2.2 SAR Measurements

SAR systems are installed on moving platforms, typically airborne or spaceborne, and transmit electromagnetic pulses in side-looking geometry (see Fig. 3). The radiation backscattered from the illuminated footprint is recorded continuously. The illuminated width of the footprint, i.e. the swath width, extends for 1–20 km in the airborne case and for 30–500 km in the spaceborne case, with typical resolution between 1 and 10 m (Moreira et al. 2013).

The received signals are coherently processed in order to focus 2D SAR (amplitude and phase) single-look complex (SLC) images in the slant range (r, parallel to the line of sight)—azimuth (x, parallel to the flight direction) plane. According to the Born approximation, the backscattered radiation is the linear superposition of the contributions arising from the individual scatterers (i.e., the physical vegetation elements). Multiple scattering phenomena from their mutual interactions are neglected. As a consequence, the SLC complex amplitude for a fixed polarization channel at the generic range–azimuth $\left(r',x'\right)$ coordinates can be expressed as a volume integral (Bamler and Hartl 1998; Fornaro et al. 2003):

$$y\left(r',x'\right) = \iiint h\left(r'-r,x'-x\right)\cdot\xi(r,x,s)\cdot \mathrm{e}^{-j\frac{4\pi}{\lambda}R(r,s)}\mathrm{d}r\mathrm{d}x\mathrm{d}s, \tag{2}$$

where s is the elevation coordinate, $R(r,s)$ is the distance between the antenna and the elementary volume defined by $\mathrm{d}r\mathrm{d}x\mathrm{d}s$, λ is the wavelength, and $h(r,x)$ is the (end-to-end) system point-spread function after focusing which depends on the range and azimuth resolutions (Bamler and Hartl 1998). $\xi(r, x, s)$ is the (unknown) 3D complex radar reflectivity, resulting from the interaction between the transmitted pulse and the scatterer. From (2), it is apparent that a SAR image alone contains backscatter amplitude information that depends on the full 3D forest structure, but it does not provide structure reconstruction capability as a consequence of the integration in s.

The sensitivity to the vertical dimension can be recovered in an InSAR configuration constituted by two SAR images $y_1\left(r', x'\right)$ and $y_2\left(r', x'\right)$ acquired under a (slight) angular diversity (incidence angle) from tracks or orbits separated in space by a baseline of length B. With reference to Fig. 3, InSAR can localize a scatterer by measuring the phase difference in the SLCs induced by the difference of the distances from the two SAR platform positions to the scatterer. The sensitivity (i.e., the derivative) of the InSAR phase difference with respect to the vertical height corresponds to the so-called vertical wavenumber, which is given by (Reigber and Moreira 2000; Papathanassiou and Cloude 2001):

$$k_Z := \frac{4\pi}{\lambda r} \frac{B_\perp}{\sin \theta_0}, \tag{3}$$

where $B_\perp$ is the orthogonal baseline, i.e., the length of the projection of the InSAR baseline in the direction orthogonal to the line of sight, and θ_0 is the incidence angle. As any phase value, the interferometric phase is ambiguous by integer multiples of 2π. As a consequence, the related height measurements are ambiguous over a height interval $\mathrm{HoA} = 2\pi / k_Z$.

The scattering from natural media, including forests, is typically regarded as a stochastic process. Although Gaussianity may not hold depending on wavelength and/or resolution, the use of second-order statistics has been proven to be valuable for the extraction of scatterer information. Thus, the complex coherence is considered and it is defined as:

$$\gamma_{1,2}\left(k_Z\right) := \frac{E\left\{y_1\left(r', x'\right) y_2^*\left(r', x'\right)\right\}}{\sqrt{E\left\{\left|y_1(r', x')\right|^2\right\} E\left\{\left|y_2(r', x')\right|^2\right\}}}, \tag{4}$$

where $E\{\cdot\}$ indicates the statistical expectation operator, and the asterisk indicates the complex conjugate. The dependence of the coherence on k_Z has been explicitly indicated at the left-hand side of (4), while range and azimuth have been dropped for simplicity. The estimation of $\gamma_{1,2}\left(k_Z\right)$ in (4) would require several realizations of the underlying stochastic process, which are generally not available in reality. Therefore, assuming spatial ergodicity, reliable measurements of the statistical expectations in (4) are typically obtained by averaging neighboring pixels within a range–azimuth (multilook) cell.

By following all the algebraic development (see Appendix 1), and by considering the presence of noise, the complex coherence (3) becomes (Zebker and Villasenor 1992; Bamler and Hartl 1998):

$$\gamma_{1,2}\left(k_Z\right) = \gamma_{\mathrm{Sys}} \gamma_{\mathrm{SNR}} \gamma_S\left(k_Z\right) \gamma_{\mathrm{vol}}\left(k_Z\right). \tag{5}$$

In (5), γ_{Sys} includes a wide range of decorrelation effects induced by the SAR system and processing inaccuracies (e.g., quantization, co-registration, range and azimuth ambiguities, …), while γ_{SNR} is the decorrelation induced by the presence of noise, and therefore by a finite signal-to-noise ratio. $\gamma_S(k_Z)$ is a (real-valued) decorrelation term that depends on $h(r, x)$ (Zebker and Villasenor 1992; Bamler and Hartl 1998). The former two terms can be compensated by exploiting the available SAR system characterisation, while $\gamma_S(k_Z)$ is compensated by applying the so-called spectral shift filtering (Bamler and Hartl 1998). The remaining term $\gamma_{\mathrm{vol}}(k_Z)$ is the volume decorrelation, and expresses the spectral decorrelation properties of the 3D reflectivity:

$$\gamma_{\mathrm{vol}}\left(k_Z\right) := \mathrm{e}^{jk_Z z_G} \frac{\int_0^{H_V} F_{\mathrm{vol}}(z)\mathrm{e}^{jk_Z z}\mathrm{d}z}{\int_0^{H_V} F_{\mathrm{vol}}(z)\mathrm{d}z}. \tag{6}$$

In (6), $F_{\mathrm{vol}}(z)$ is the spatial density of backscattered power along height (i.e., a projection of $\xi(r, x, s)$, see Appendix 1) for the fixed range cell, called also vertical reflectivity profile. z_G is a reference volume bottom height [see also (1)] and H_V is the volume extension above z_G. If the wavelength allows penetration down to the underlying ground, then z_G is the ground height with respect to the global or local height considered as a reference.

The vertical reflectivity $F_{\mathrm{vol}}(z)$ reflects the physical (geometric) 3D distribution of vegetation elements through scattering and attenuation processes that depend on the SAR wavelength, incidence angle, polarisation, and the dielectric properties of the canopy layers:

- The wavelength defines directly the scattering of and the propagation through the vegetation. Longer wavelengths (e.g., P- and L-bands) are more sensitive to larger vegetation elements. At the same time, a (high) penetration through them provides propagation and sensitivity down to the ground. The sensitivity to smaller elements, which can still be relevant from an ecological point of view, increases with decreasing wavelength (from S- up to X-band). However, the attenuation of the vegetation increases. Hence, at shorter wavelengths the propagation through (even small) vegetation gaps contributes to the penetration to a larger extent than at longer wavelengths.
- For a fixed slant range, wavefronts at steeper (i.e., closer to nadir) incidence angles have a wider projection on the horizontal plane, thus $F_{\mathrm{vol}}(z)$ results more sensitive to the projection of the horizontal distribution of the effective scatterers. In contrast, shallower incidence angles (i.e., far from nadir), increase the sensitivity to the vertical distribution. At the same time, the incidence angle defines the length of the propagation path through the vegetation volume, hence the (two-way) attenuation of the transmitted wave as a function of height. Steeper incidence angles are less attenuated than shallower ones for the same stand characteristics. Not only this, but steeper incidence angles facilitate penetration through gaps at shorter wavelengths.
- The orientation of the scattering vegetation elements as a function of height affects the related distribution of the backscattered power in the different SAR polarisation channels. Therefore, the relative power levels of scattering components at different heights in $F_{\mathrm{vol}}(z)$ can be changed by changing polarisation channel.
- The dielectric properties of the vegetation elements affect their scattering and attenuation, which depend on the water content of the tree tissuesand on its distribution. Dielectric changes can occur due to both environmental (e.g., rains, droughts, snowfalls…) and seasonal changes, and $F_{\mathrm{vol}}(z)$ can change accordingly although the extent and type of change can be wavelength-dependent (Pardini and Papathanassiou 2018; Bai et al 2018; Kugler et al 2014).

Equation (6) shows that the volume coherence $\gamma_{\mathrm{vol}}(k_Z)$ and the vertical reflectivity profile $F_{\mathrm{vol}}(z)$ form a Fourier pair, i.e., an InSAR acquisition corresponds to one Fourier component of the reflectivity profile at a spatial frequency equal to the vertical wavenumber. One single-baseline InSAR measurement makes it possible to extract the height of the backscattering phase center within the volume, i.e., the Digital Elevation Model

(DEM), corresponding (at first order) to the "center of mass" of $F_{\mathrm{vol}}(z)$. It is calculated as $z_{\mathrm{DEM}}(k_Z) = \varphi_{\mathrm{vol},u}(k_Z)/k_Z$, with $\varphi_{\mathrm{vol},u}(k_Z)$ being the phase of the volume coherence after unwrapping. In order to be able to estimate a larger number of parameters, one can increase the observation space by acquiring interferometric pairs in different polarisation channels, and/or by acquiring multiple images from multiple track/orbit displacements (multi-baseline acquisition). Two different approaches can then be followed:

(A1) The first one is to parameterise $F_{\mathrm{vol}}(z)$ in terms of geometrical and scattering properties and to use then the set of measured $\gamma_{\mathrm{vol}}(k_Z)$ to estimate the individual model parameters, as it is done with Pol-InSAR inversions (Papathanassiou and Cloude 2001). The scattering model, whose validity is in general frequency-dependent, is essential for the significance and accuracy of the estimated parameters. The model should contain enough physical structure to interpret the interferometric measurements, and at the same time, it must be simple in terms of number of parameters in order to be determinable with the available (in general limited) number of measured coherences.

(A2) The second approach is the most direct one, and attempts to invert the Fourier relationship (6) provided that a set of measurements of $\gamma_{\mathrm{vol}}(k_Z)$ is available at suitable k_Z, according to the TomoSAR imaging principle (Reigber and Moreira 2000). This approach is more expensive in terms of acquisitions needed, but it has the advantage that no assumption on the shape of $F_{\mathrm{vol}}(z)$ is required, allowing the reconstruction of arbitrary vertical reflectivity profiles. The smallest available HoA (i.e., the largest k_Z) is the TomoSAR vertical resolution (Rayleigh limit).

Pol-InSAR model-based inversion approaches have been demonstrated, e.g., for forest height estimation in boreal, temperate and tropical forests at multiple frequencies from P- up to X-band, considering both airborne and spaceborne platforms (Papathanassiou and Cloude 2001; Garestier et al. 2008; Neumann et al 2010; Lee et al. 2013; Kugler et al. 2014; Lavalle and Hensley 2015; Simard and Denbina 2018). The TomoSAR reconstruction of $F_{\mathrm{vol}}(z)$ has been demonstrated in airborne experiments across different forest types (Reigber and Moreira 2000; Frey and Meyer 2011; Tebaldini and Rocca 2012; Mariotti et al. 2012; Pardini et al. 2018a, b). Several algorithmic solutions have been found in the spectral estimation theory (Gini et al. 2002; Frey and Meyer 2011; Aguilera et al. 2013) to improve the imaging performance against the typical low number and the irregular distribution of the flight tracks/orbits. Among the several alternatives, the model-free Capon spectral estimator (Lombardini and Reigber 2003) is widely employed, and can provide vertical resolution beyond the Rayleigh limit (Cazcarra et al. 2019).

As a final remark, a fundamental prerequisite for a successful estimation of 3D structure parameters from SAR acquisitions is the stationarity of $F_{\mathrm{vol}}(z)$ within the total acquisition time. Changes can be induced by, e.g., the movement of the vegetation under the action of wind, or changes in the dielectric properties, and introduce an additional (wavelength-dependent) temporal decorrelation factor in (4). If not properly accounted for, the inversion problem may become ambiguous if not unfeasible (Lee et al. 2013; Lavalle and Hensley 2015). On the other hand, (bistatic) single-pass (Pol-)InSAR acquisitions provide temporal decorrelation-free measurements of $\gamma_{\mathrm{vol}}(k_Z)$, although dielectric changes may still occur between acquisitions. In this frame, a full separation between geometric and dielectric contributions within the same vertical reflectivity profile or its parameters would only be possible with single-pass multistatic TomoSAR constellations.

3 A Comparison Between Lidar and SAR Profiles at Different Wavelengths

In this Section, the dependency of the TomoSAR vertical reflectivity profiles on wavelength, dielectric properties, and structure types is discussed by comparing profiles extracted in the temperate Traunstein (Germany) and the tropical Rabi (Gabon) forest sites. Details on the used lidar and SAR data sets are reported in Appendix 2. TomoSAR vertical profiles have been estimated in the HV channel in square range–azimuth multilook cells measuring 20 m × 20 m, corresponding to the profile resolution in the horizontal range–azimuth plane. The profiles have been obtained by means of the Capon spectral estimator (Lombardini and Reigber 2003). Since lidar waveforms were available only in Rabi, lidar profiles have been generated in Traunstein as the histogram of all the recorded ALS returns as a function of height.

The profiles in Fig. 4 have been calculated in the Traunstein forest, and refer to different growth stages (“transition”, “close-to-nature”, “mature” and “young”) which are typical of this forest site. The profiles in Fig. 5 have been estimated in the Rabi forest in correspondence of a ForestGEO inventory plot (see Appendix 2).

The ability of the different wavelengths of penetrating into and through the canopy layers can be assessed directly by detecting the presence and measuring the power of the ground scattering in the profiles. In both Traunstein and Rabi, the ground scattering is well visible in almost all the P-band profiles (see Figs. 4a, 5a). A larger variation of ground power across forest stands occurs at L-band due to the higher sensitivity to the spatial variations of the attenuation levels induced by the changes of both canopy density and water content (see Figs. 4b, 5b). In Traunstein, the L-band profiles in Fig. 4c have been obtained with data acquired around 3.5 years after the ones used to generate the profiles in Fig. 4b, and show a change of ground power. This can be due to a change of canopy attenuation caused by a change of both canopy density, as a result of forest management, and dielectric properties, as a result of seasonality-induced redistributions of water content. The effect of forest management is particularly visible in the “transition” stands, in which old taller trees are cut to allow the growth of the younger shorter ones below. This is recognisable also in the sparsity of the lidar returns in Fig. 4e. The effect of seasonal dielectric changes is likely visible in the forest stand beyond a horizontal distance of 2 km (Autumn 2009 vs. Spring 2013). Indeed, an increase of ground power occurs in the presence of the thick canopy cover shown by the lidar profiles. Finally, the X-band profiles (Fig. 4d) are the ones characterized by the lowest ground contribution due to the largest attenuation of the shortest X-band wavelength. However, the ground scattering becomes dominant in the “transition” stands. Here, the sparser canopy facilitates penetration through its largest gaps even in the slanted SAR geometry.

In both Traunstein and Rabi, P- and L-band waves exhibit similar penetration, but different sensitivity to the physical canopy elements. In Traunstein, the P-band canopy contributions are weaker than the ground ones in many stands in contrast to L-band, similarly to other temperate and boreal forests (Frey and Meyer 2011; Tebaldini and Rocca 2012). However, there are cases in which the P- and L-band profiles are more similar (e.g., the forest stand beyond a horizontal distance of 2 km). The spatial variation of the canopy backscattering distribution (which in general occurs at very small scales) is reflected in different ways by the wavelengths. At P-band, the visibility of the canopy layers changes in space faster than at L-band. At L-band, canopy scattering contributions are either concentrated closer to the canopy top, or spread along the

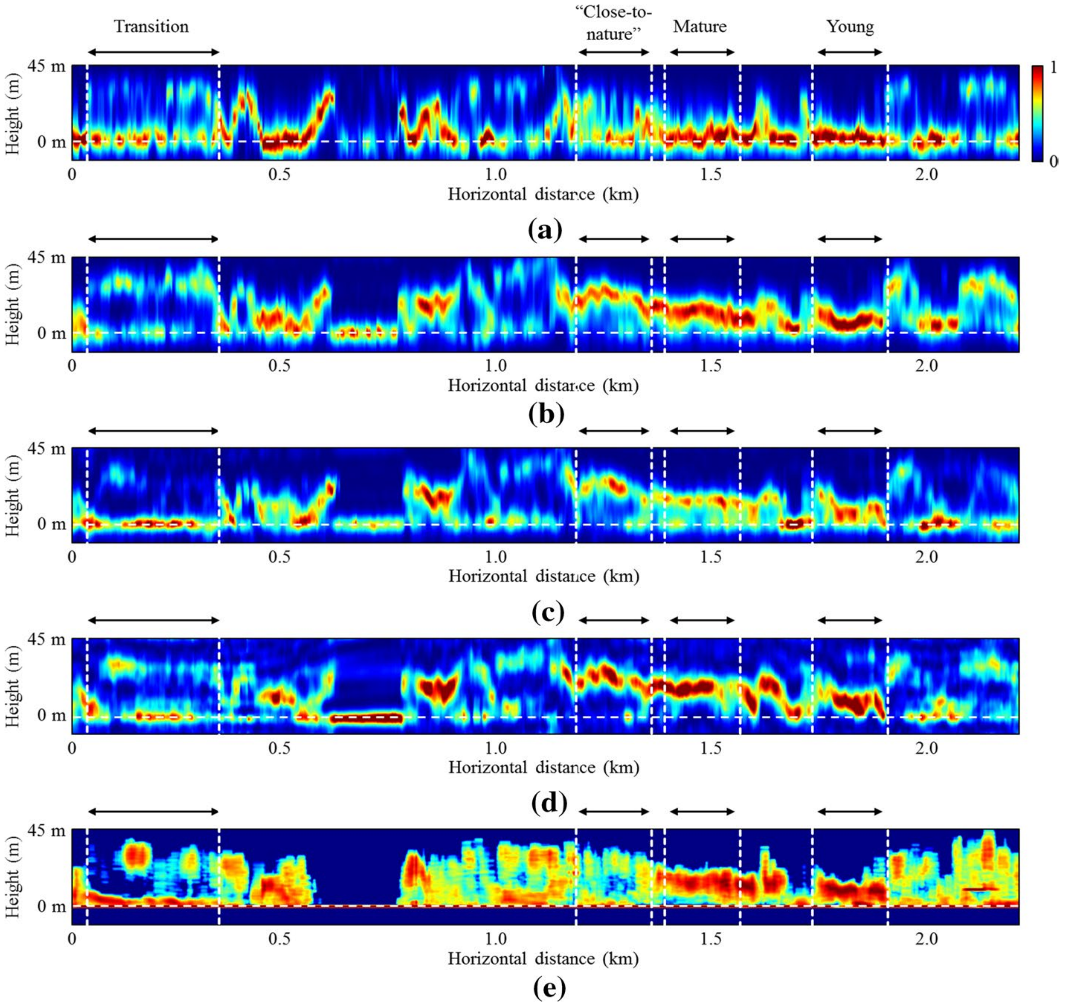

Fig. 4 Traunstein forest (south of Germany). SAR vertical reflectivity profiles and lidar profiles (histograms of the lidar returns as a function of height) over a representative azimuth transect at constant range, HV polarization channel. The height axis is relative to the ground height (0 m), indicated with the horizontal white dashed line. The vertical white dashed lines delimit stands of interest in different growth stages. SAR profile intensities are normalised by the total backscattered power. **a** P-band (2009); **b** L-band (2009); **c** L-band (2013); **d** X-band (2013); **e** lidar profiles

whole volume extension. Seasonal dielectric changes affect not only the distribution of the power at the ground, but also within the canopy layers (e.g., the forest stand beyond a horizontal distance of 2 km). Due to the larger attenuation, at X-band the canopy scattering contributions tend to be closer to the canopy top than at the other wavelengths. In contrast to Traunstein, P- and L-band profiles tend to be more similar in Rabi. However, large differences can occur, as shown for the stand corresponding to the horizontal distances between 600 and 800 m (delimited by the vertical dashed lines in Fig. 5). Here, stronger canopy contributions are close to the canopy top at P-band, while they are distributed along height at L-band. The distribution of the physical size of the involved scatterers might again explain this difference: the bigger ones might be close to the top, while smaller ones (which are semi-transparent at P-band) might be distributed down

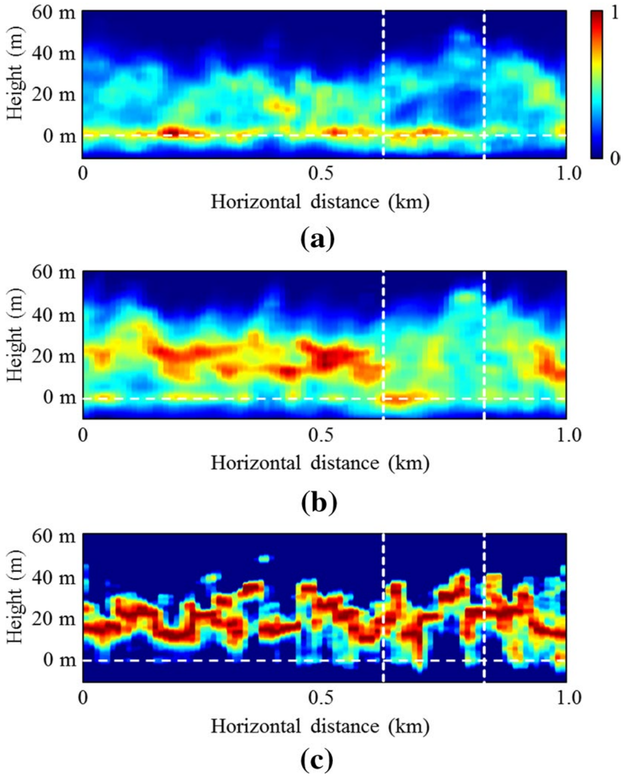

Fig. 5 Rabi ForestGEO plot (Gabon). Vertical profiles along a North–South transect. The height axis is relative to the ground height (0 m), indicated with the white dashed line. SAR profile intensities are normalised by the total backscattered power. **a** P-band and **b** L-band TomoSAR vertical reflectivity profiles, **c** LVIS waveforms

to the ground. On the contrary, the most powerful contributions in the lidar profiles are close to the canopy top due to a reduced penetration.

The profiles in Fig. 6 are extracted from Fig. 4 (Traunstein forest), and can be used to gain some additional insights about the capability of each wavelength to reflect 3D structure properties. Each plot shows 10 profiles extracted every 10 m in one of the four growth stages highlighted in Fig. 4:

- In the "transition" stands, all wavelengths show similar vertical profiles, with relevant vegetation backscattering contributions up to 10 m and between 20 and 40 m. However, the relative profile amplitudes and their spatial variation across profile coordinates are wavelength- and time-dependent. The contributions close to the canopy top appear in 2009 more heterogeneous at P- than at L-band. This might be due to electromagnetic semitransparency at P-band, affecting any interpretation in terms of horizontal heterogeneity. As a result of the sparsity induced at the canopy top by management activities, in 2013 the upper canopy scattering contributions become weak at L-band, but stronger at X-band. In addition, the sparsity of the vegetation elements makes X-band penetrate well down to the ground, and the related reflectivity profiles reflect closely the geometric distribution of the lidar returns.
- The "close-to-nature" stands are characterized by the largest heterogeneity in terms of tree species and heights. The resulting structural complexity is reflected by the lidar profiles, which are composed by returns at all heights. In parallel, all the SAR frequencies show this heterogeneity, but at different extents. P-band shows still large penetration capabilities, and the profiles contain larger or even dominant scattering contributions close to ground. These contributions are present also in the L-band

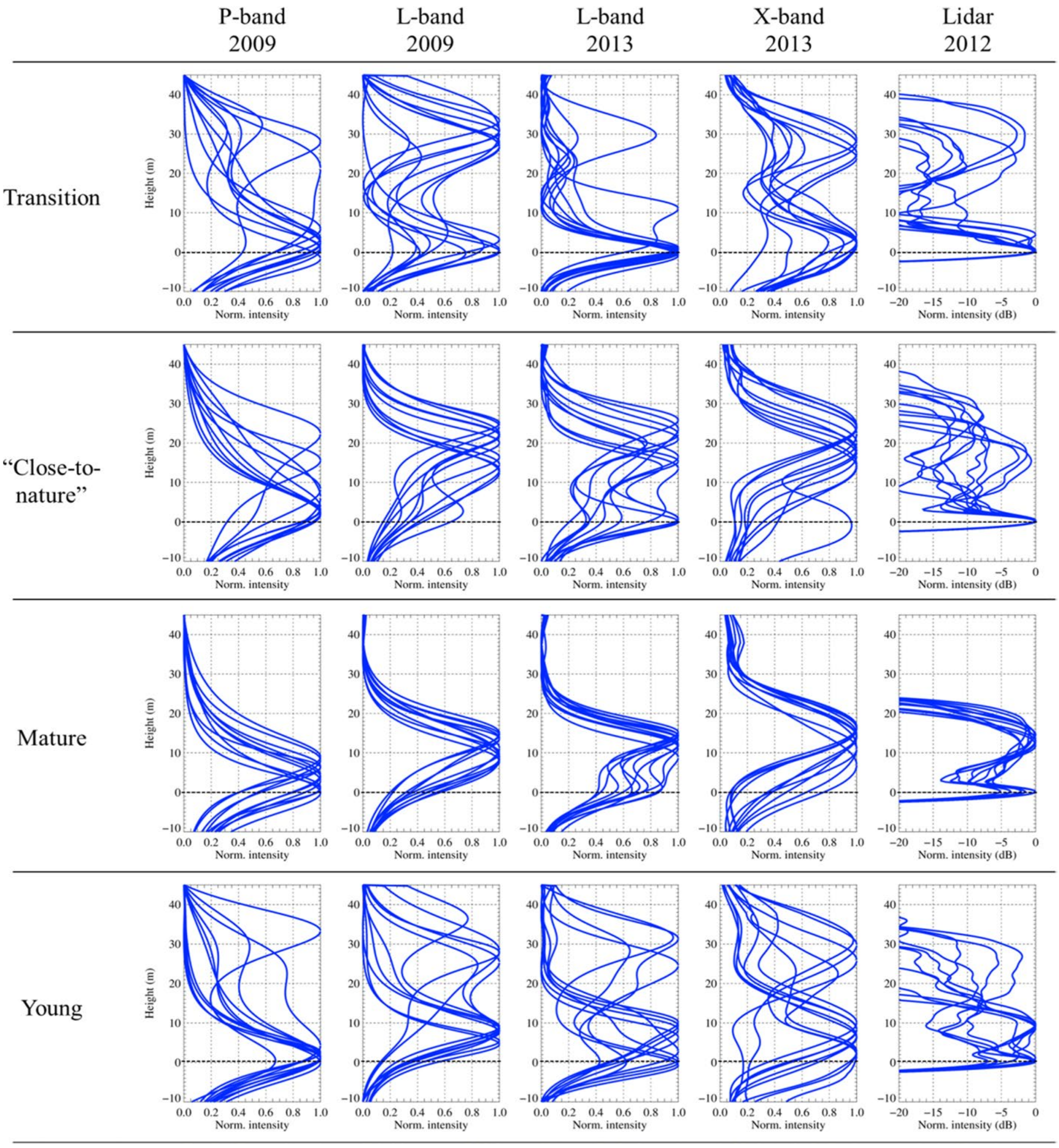

Fig. 6 Traunstein forest (south of Germany). Examples of lidar and TomoSAR profiles (HV channel) in the forest stands delimited in Fig. 4. The height axis is relative to the ground height (0 m), indicated with the horizontal black dashed line. For the sake of visualization the profiles have been normalized by their maximum

profiles together with additional stronger ones in correspondence of the upper canopy layers. The difference between the L-band profiles in 2009 and 2013 is probably caused by the difference in TomoSAR vertical resolution (better in 2013) and dielectric differences at a lower extent, as no management action is documented in these stands. At X-band, the reduced penetration makes the profiles sensitive to the upper canopy variations between 15 m and 30 m.

- The "mature" stands are constituted by (tall) trees uniformly distributed in space. This uniformity characterizes the lidar and SAR profiles at all wavelengths. The P-band profiles show the least sensitivity to the canopy top, having their main peak located closer to the ground. Similarly to the "close-to-nature" stands, the change of the L-band profiles from 2009 to 2013 is mostly due to an improvement in the vertical resolution and to dielectric changes. In 2013, beyond the difference in attenuation, the L- and X-band profiles convey similar structural (i.e., geometric) information.

- Finally, the "young" stands are composed of mainly a layer of short trees with low density and some sparser taller trees. The shorter trees are visible at all the frequencies, while the taller trees are less visible at P-band. In 2013, the L-band profiles show a significant spatial variability of the canopy layer close to the ground corresponding to the shorter trees. Such variability is not shown either by the lidar or the X-band profiles. The spatial distribution of the X-band profiles is very similar to the lidar ones, and once more this could indicate their increased sensitivity to the geometric properties of the canopy.

To summarize, these examples have shown that, together with lidar profiles, SAR profiles at all wavelengths contain information about 3D structure. P- and L-band can penetrate through the canopy layers down to the ground even in dense tropical forest environments, and can complement lidar profiles in mapping vertical heterogeneity. At P-band, vegetation elements can be semitransparent in some stands, and the fast and strong spatial changes of attenuation might make the canopy appear more heterogeneous horizontally. At L-band, the scattering from smaller vegetation elements becomes more significant, and different degrees of vertical heterogeneity could be more distinguishable than, e.g., at P-band. The complementarity between these two frequencies seems to depend on the imaged forest structures. The L-band examples clearly show also the dependency of the reflectivity profiles on the dielectric properties, which might affect the interpretation of the profiles and their spatial changes in terms of physical structure. Finally, the X-band profiles resemble more closely the geometric distribution of the canopy layers in the lidar profiles, at least in those sparser stands where penetration until the ground occurs. This might be an indication that penetration is facilitated by vegetation gaps along the SAR line of sight. In the absence of these, the resulting lower X-band penetration increases the sensitivity to the top canopy spatial variations, therefore complementing and improving the capability of longer wavelengths in the characterization of horizontal heterogeneity.

4 The Lidar-SAR Model-Based Framework for Forest Height Estimation

In this section, a case study is considered in which the common sensitivity of lidar and SAR measurements to geometric structure parameters is exploited in the parameterisation of the Random-Volume-over-Ground Pol-InSAR backscattering model using sparsely sampled lidar full waveforms for obtaining accurate, continuous and high-resolution forest (top) height estimates.

4.1 The Random-Volume-Over-Ground Model

The Random-Volume-over-Ground (RVoG) model describes the variation of the reflectivity profiles with the polarization channel $\boldsymbol{\omega}$ (Papathanassiou and Cloude 2001). First of all, it is assumed that $F_{\mathrm{vol}}(z)$ is the sum of the ground-only and the volume-only vertical reflectivity profiles (two-layer model). Next, it is assumed that the backscattered power at the ground level is the only component of $F_{\mathrm{vol}}(z)$ that changes with polarisation. In other words, the volume-only profile is the same across all polarimetric channels except for a scalar factor. Additionally, the ground-only profile is modelled by a Dirac-δ function (Papathanassiou and Cloude 2001). As a consequence:

$$\gamma_{\text{vol}}\left(k_Z, \boldsymbol{\omega}\right) = \mathrm{e}^{jk_Z z_G} \frac{\gamma_V\left(k_Z\right) + \mu(\boldsymbol{\omega})}{1 + \mu(\boldsymbol{\omega})} \tag{7}$$

where the dependency of the individual parameters on the polarisation channel $\boldsymbol{\omega}$ has been explicitly indicated. $\gamma_V(k_Z)$ is the (polarisation-independent) volume-only coherence and $\mu(\boldsymbol{\omega})$ is the ground-to-volume amplitude ratio. $\gamma_V(k_Z)$ is obtained from the volume-only vertical reflectivity profile $F_V(z)$ with a relationship formally identical to (6). The dependency of $\gamma_V(k_Z)$ on the forest top height H_V is made explicit by modeling $F_V(z)$. A widely and very successful model is an exponential distribution of scatterers, i.e.

$$F_V(z) = \mathrm{e}^{-2\left(H_V - z\right)\tau / \cos\theta_0} \quad \text{for} \quad 0 \le z \le H_V \tag{8}$$

where defines the attenuation rate of the profile, which is a function of both density of scatterers and their dielectric constant. The exponential profile tends to fit better at shorter wavelengths. At longer wavelengths, or more in general in the cases in which more effective scatterers are located closer to the ground, the exponential decay in (6) may not be valid. Different parameterisations might be used instead [see, e.g., (Garestier et al. 2008)].

4.2 Case Study: Fusion of GEDI Waveforms and TanDEM-X Coherences

The GEDI lidar acquires footprints according to the spatial sampling pattern illustrated in Fig. 2. The use of single-pass bistatic X-band InSAR coherences acquired during the DLR's TanDEM-X mission has been proposed to bridge the spatial gaps between the footprints in order to obtain continuous and high-resolution forest mapping, and the inversion of the RVoG model (7, 8) is a possible solution. Only one TanDEM-X coherence in one polarimetric channel is most typically available for inversion. On the other hand, fixed a polarimetric channel, the RVoG model (7) presents 4 unknown parameters, i.e., H_V, τ, $\mu(\boldsymbol{\omega})$ and z_G. As one complex coherence can account for only two real parameters, the inversion of a full RVoG model results underdetermined. Additionally, the X-band penetration is not guaranteed in all forest types, and the use of an external z_G is needed to avoid any penetration-dependent height estimation bias (Kugler et al. 2014). The spatially sparse set of GEDI footprints can then be used to initialize some of the RVoG parameters, thus making the inversion determined (Qi and Dubayah 2016, 2017) and correcting penetration-induced biases. Depending on the model assumptions, the following strategies can be adopted:

(S1) The sparse GEDI ground topography values are interpolated on the TanDEM-X spatial grid of the complex InSAR coherences. Given the interpolated topography, the RVoG model is fitted to the complex coherences to estimate H_V and τ assuming $\mu = 0$ (no ground contribution).

(S2) Assuming $\mu = 0$, the GEDI ground topography and top height are used in the RVoG model to estimate extinction values from TanDEM-X complex coherences in correspondence of the footprints. Then, both topography and extinction are interpolated over the TanDEM-X grid. Finally, a continuous and high-resolution estimate of H_V is obtained by fitting the RVoG to the coherences using the interpolated topography and extinction.

(S3) As in (S2), but allowing $\mu \neq 0$, i.e., values of μ and τ are jointly estimated in correspondence of the footprints, interpolated and used in the inversion of the remaining parameters.

The interpolation of the three parameters (i.e., ground topography, extinction and ground-to-volume ratio) estimated in correspondence of the footprints can be carried out, e.g., by means of a simple kriging interpolation (Qi et al. 2017; Oliver and Webster 1990), in which it is assumed that samples are correlated according to a negative exponential spatial correlation function. Alternatively, the TanDEM-X high-resolution DEM can be used to obtain a ground topography with higher resolution than the one that a simple interpolation would provide (Lee et al. 2018). A wavelet transformation is used to decompose the TanDEM-X DEM into three high spatial frequency components (describing local changes of topography) and a low-frequency one, according to the methodology outlined in (De Grandi et al. 2016). The low-frequency part of the TanDEM-X DEM is substituted by the GEDI interpolated ground topography, and a GEDI-TanDEM-X combined ground topography is obtained by inverting the wavelet transformation.

Real data results have been generated over the two tropical forest sites of La Selva (Costa Rica) and Lopé (Gabon) by using TanDEM-X HH acquisitions and simulated GEDI acquisition patterns (Qi and Dubayah 2016, 2017). Details about the radar and lidar data sets are reported in Appendix 2. Over La Selva, the lidar data were processed to simulate GEDI full waveforms following the method in Blair and Hofton (1999) with measurement noise added following Hancock et al. (2011). GEDI acquisition tracks were simulated also over the Lopé site. In both cases, the nominal lidar sampling after 2 years of mission has been considered. In the experiments, TanDEM-X interferometric coherences have been calculated over 25 m×25 m (ground range) multilook cell approximately corresponding to the GEDI footprint diameter (25 m). Therefore the TanDEM-X estimates of H_V have been obtained with 25 m resolution. To reduce statistical variations, the estimates have been averaged on a threefold bigger cell. As a consequence, the final resolution of the height map is 75 m. Figure 7 shows the estimated TanDEM-X height maps and their validation against the lidar top height (2D histograms) for different configurations of the model parameters over La Selva. The adoption of the strategy (S1) (Fig. 7b) improves both the estimation RMSE and the bias with respect to the case in which the TanDEM-X absolute coherence values alone are used to estimate H_V with $\tau = \tau_0$ fixed a priori (Fig. 7a). However, the overall estimation performance is not satisfactory, due to the still large bias (around 4 m). A noticeable improvement is obtained by applying (S2), as the bias reduces to around 0.5 m (Fig. 7c). The use of (S3) keeps almost unaltered the already very small bias and further reduces the RMSE to 4.3 m (13%) (Fig. 7d). Such estimation performance is definitely better than just interpolating the GEDI top heights over the TanDEM-X grid. Moreover, the residual RMSE can be reduced by averaging further the final estimates to a coarser resolution.

The combination strategy (S1) with the refined wavelet-based interpolation of the ground topography has been applied to the Lopé acquisition. The mean value of the interpolation error between the original topography and the interpolated one (Fig. 8a) is 0.8 m and the standard deviation is around 8 m. The forest height (Fig. 8b) could be estimated with a correlation coefficient of 0.81 and an RMSE of 5.47 m (i.e., around 10%) with respect to the lidar RH95 heights (Fig. 8c). This performance is still comparable to the one obtained for the forest height inverted using the original lidar fully sampled topography (correlation coefficient of 0.92 and RMSE of 3.58 m).

As a final remark, the effectiveness of the parameterisation of SAR interferometric models by means of lidar waveform parameters is influenced by the difference of wavelengths, the

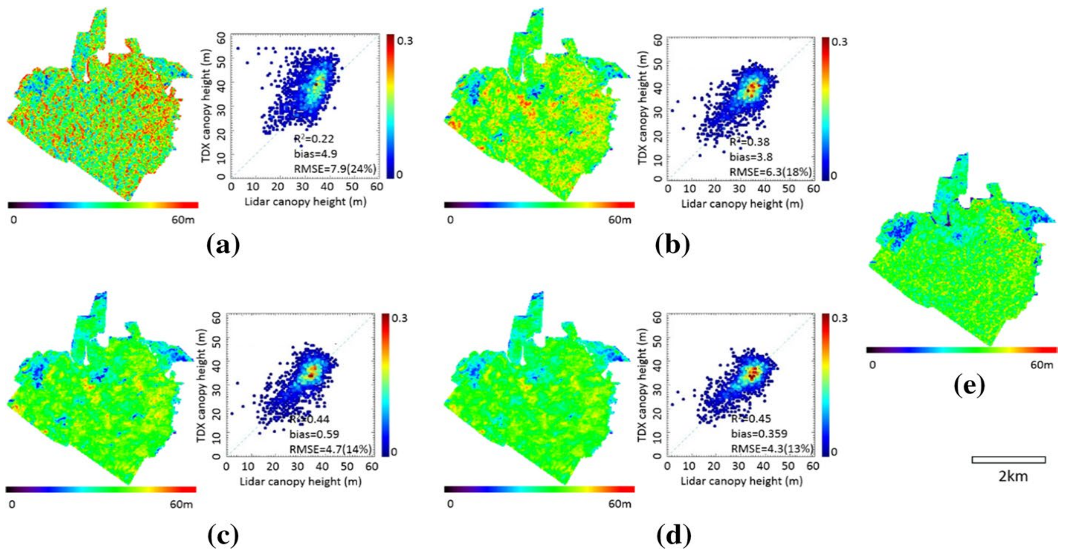

Fig. 7 La Selva Biological Station. TanDEM-X forest top height maps before and after combination with GEDI simulated data and 2D histograms against lidar canopy height **a** Inversion from TanDEM-X data only; **b** TanDEM-X inversion using the interpolated GEDI terrain height; **c** TanDEM-X inversion using the GEDI interpolated terrain height and σ, for $\mu = 0$; **d** TanDEM-X inversion using the GEDI interpolated terrain height, σ and μ; **e** reference lidar top height

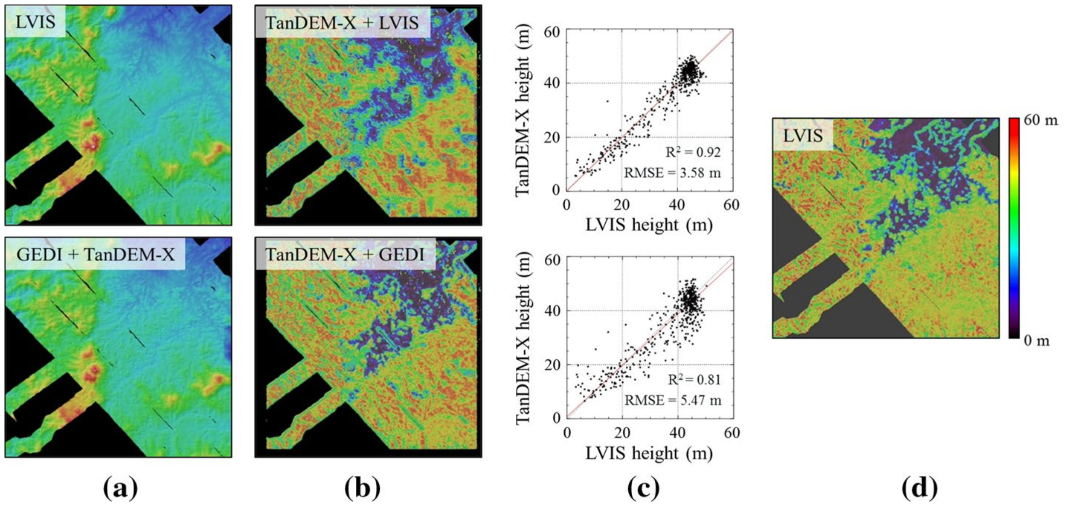

Fig. 8 Lopé test site. **a** LVIS terrain height (upper) and terrain height resulting from the simulated GEDI-TanDEM-X combination; **b** TanDEM-X top height inversion results from the LVIS terrain height (upper) and the one resulting from the GEDI-TanDEM-X combination (bottom); **c** validation plots against LVIS RH95; **e** reference LVIS RH95 canopy height

difference in the looking geometry, and the resolution of the parameterisation itself. Concerning the resolution of the parameterisation, in the example above τ and μ are radar reflectivity parameters, which depend on the (relatively) fast spatial variations of dielectric properties and physical arrangement of the vegetation elements. In general, any mismatch between the resolution of an external parameterisation and the resolution of the TanDEM-X height inversion causes a loss of estimation performance. A constant value of τ makes the inversion of forest height feasible even from single-baseline coherences without external parameterisations, but can lead to an unsatisfactory estimation performance. The interpolation of the values of τ and μ retrieved at the footprint locations improves the estimation performance, but it can track only a low-resolution component of these variations depending on the spatial sampling rate provided by the footprints. A way to reduce the consequential mismatch between the interpolated parameters and the SAR data could be to reduce the resolution of both the lidar parameterisation (for instance by aggregating multiple footprints) and at the same time of the inversion (multilook cell) from the interferometric coherences, for instance as noted by Brolly et al. (2016).

5 The Lidar-SAR Structure-Based Framework

The applicability of the lidar-SAR model-based framework presented in Sect. 4 becomes limited with increasing difference of the wavelength involved. This is a consequence of the fact that different wavelengths "see" different effective scatterers, as shown by the examples in Sect. 3. A direct relationship between lidar profiles and SAR vertical reflectivity profiles becomes difficult to be established at the increase of the wavelength difference, resolution and look angle (Brolly et al. 2016; Pardini et al. 2018a, b). In the structure-based framework, lidar and SAR measurements are used to calculate one or more structure indices independently, i.e., without exchanging a parametrization of the underlying backscattering models. The structure indices considered here are defined with the aim of describing (components of) physical structure, and they use features extracted from the vertical reflectance/reflectivity profiles that reflect physical heterogeneity within a certain scale. In this Section, we review meaningful structure indices both from field data and lidar and SAR profiles, and we show in an example with real data how they can be used to relate the structure information content of the profiles.

5.1 Structure from Ground Measurements

Forest structural information is often quantified by means of scalar indices whose definition depends on the specific application. Basing on field inventory data, structure indices are defined at plot level by means of single-tree attributes such as diameter, height, basal area, canopy dimension, species composition, and stand density. A number of indices have been proposed in the literature, like, e.g., the aggregation index (Clark and Evans 1954), the diametric differentiation index, the mingling index, the contagion index, or the complex stand index (Pastorella and Paletto 2013). However, there is not yet an overall and unequivocal measure able to express forest structure in terms of forestry and ecology appropriate for a wide variety of application, spatial scales, and forest types (Zenner and Hibbs 2000; Pommerening 2002; Pretzsch 2009; del Rio et al. 2016). Despite this difficulty, there is a common understanding that the structural heterogeneity in both the horizontal and the vertical dimensions are two complementary aspects that should be considered.

One way to quantify horizontal structure or heterogeneity is to use the concept of density. High density means low heterogeneity, and vice versa. The stand density index SDI (Reineke 1933) (measured in trees per hectare) links space utilization to tree size. It is closely related to basal area and by definition relates the stand density with the equivalent density of a stand with a quadratic mean diameter of 25 cm:

$$\mathrm{SDI} = N_S\left(\frac{D_g}{25}\right)^{1.605} \tag{9}$$

where N_S is the number of stems per hectare and D_g is the quadratic mean diameter at breast height (*dbh*) in cm within the scale at which SDI is calculated. A horizontal (dimensionless) structure index can be defined as

$$\mathrm{HS}_{\text{field}} := 1 - \mathrm{SDI}_{\text{norm}}, \tag{10}$$

where $\mathrm{SDI}_{\text{norm}}$ is the normalized SDI within an area. $\mathrm{HS}_{\text{field}}$ varies between 0 and 1, indicating the minimum and maximum horizontal heterogeneity, respectively. Additional refinements can be applied, e.g., considering the taller trees to better characterize canopy closure.

Quantifying vertical structure is often treated as quantifying the degree of heterogeneity in the vertical direction. In this sense, vertical structure has been expressed by means of indices such as the Gini coefficient, the Shannon index or the standard deviation of single tree heights (Liang et al. 2007; Barbeito et al. 2009; Bohn and Huth 2017). However, tree height measurements are often not performed so that these indices cannot be calculated directly from inventory data. An alternative way to express tree size variability is to use the diameter at breast height (*dbh*), which is a standard inventory measurement and can be related to tree height through models. Therefore, a vertical structure index can be defined as (McElhinny et al. 2005):

$$\mathrm{VS}_{\text{field}} := \mathrm{std}(\{\mathrm{dbh}\}), \tag{11}$$

in cm, where $\{\mathrm{dbh}\}$ is the ensemble of diameter at breast height of all the trees included in a stand, given in cm. Without loss of generality, the vertical structure index can be normalized to its maximum within the area under consideration, becoming a dimensionless index as the horizontal one.

5.2 Structure from Lidar and TomoSAR Profiles

The definition of indices from lidar and TomoSAR vertical profiles with the same structural meaning as the ones from field inventory data in Sect. 5.1 is challenged by the fact that the resolution of conventional remote sensing configurations (especially SAR) does not allow single trees to be distinguished directly. An additional complication in the interpretation of the profiles in term of geometric structure is caused by the specific dependencies of their information content (see Sect. 2). Consequently, the direct translation of the indices in Sect. 5.2 is not possible, and the use of physically significant profile features is desired to express the same heterogeneity. Recently, TomoSAR profiles have been interpreted in terms of forest structure by considering the distribution of their peaks. Even if the correspondence between the 3D distribution of peaks and the variability in the distribution of trees may not be given at all frequencies and/or spatial scales, it is supported in a number of models and experiments (Lin and Sarabandi 1999; Frey and Meyer 2011; Thirion et al. 2006; Brolly and Woodhouse 2013; Whitehurst et al. 2013; Cazcarra-Bes et al. 2017; Tello et al. 2018).

Canopy height variation above the ground height within a certain scale can be considered as a proxy for horizontal structure (Couteron et al. 2005; Carabajal and Harding 2006; Neumann et al. 2012; De Grandi et al. 2016). Here, this idea is applied to the top peaks (i.e.,

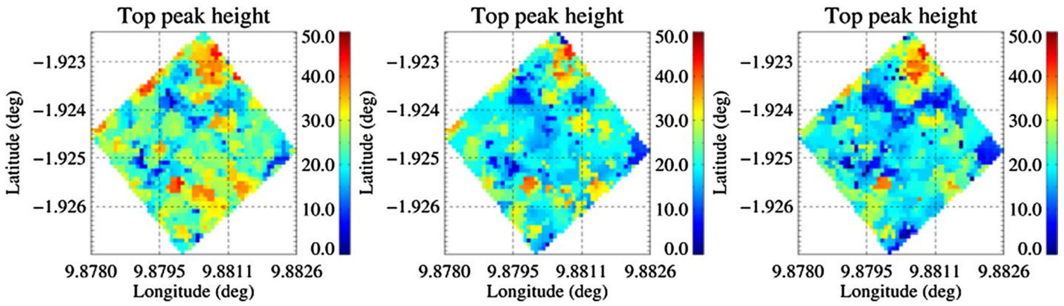

(a) (b) (c)

Fig. 9 Rabi ForestGEO plot. Top peak heights maps extracted from **a** LVIS waveforms, **b** L-band and **c** P-band vertical reflectivity profiles

the peaks at the highest height) of the waveforms and the vertical reflectivity profiles. Let $\mathrm{Z_{TOP}} = \left\{z_{T1}, z_{T2}, \ldots, z_{TM}\right\}$ be the ensemble of the M unique top peak heights within the structure window. The horizontal structure index HS can be calculated as:

$$\mathrm{HS} := \mathrm{var}\left\{Z_{\mathrm{TOP}}\right\}, \tag{12}$$

where var{·} denotes the variance of a set of values. Along this line, a way to quantify vertical structure is to consider the ensemble $Z = \left\{z_1, z_2, \ldots, z_N\right\}$ of all the unique peak heights (excluding the ground peak, if present) between the ground and the canopy top. Then, a vertical structure index can be calculated as:

$$\mathrm{VS} := N\mathrm{var}\{Z\}. \tag{13}$$

Similarly to $\mathrm{HS_{field}}$ and $\mathrm{VS_{field}}$, HS and VS can be normalized to their maximum value over an area. The increase in their values toward 1 corresponds to increasing heterogeneity.

5.3 Real Data Examples

The structure indices defined in the previous Sections have been applied to the field inventory measurements LVIS lidar and L- and P-band TomoSAR (Capon spectral estimator) profiles extracted over the ForestGEO plot in the Rabi test site (see Appendix 2). The profiles have horizontal resolution 20 m×20 m and have been used to calculate the structure indices within a window measuring 100 m×100 m. This means aggregating information from 25 statistically independent profile cells. A smaller window would reduce the statistical validity of the number of independent cells, while a larger window could provide biased values of the structure indicators as different structure types would be mixed together, and therefore lose ecological significance.

Figure 9 shows the maps of the top peak heights of LVIS profiles, and the L- and P-band TomoSAR profiles (Capon spectral estimator). Due to penetration differences, the L- and P-band top peak heights are in general lower than the LVIS ones, as shown by the profiles in Fig. 5. Nevertheless, there is a limited number of cases in which the L-band top peak height can be even higher than the LVIS one, and they are more likely focusing artifacts (e.g., sidelobes) coming from very high decorrelations. The generated $\mathrm{HS_{field}}$ and HS maps are shown in Fig. 10. All of them can well locate heterogeneous areas in the North and the South parts of the plot, and some discrepancies are visible in the remaining areas. The temporal difference (around 4 years) between the field measurements and the lidar and SAR

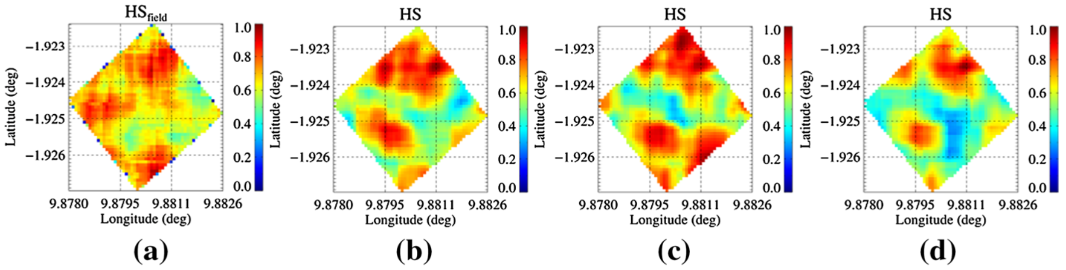

(a) **(b)** **(c)** **(d)**

Fig. 10 Rabi ForestGEO plot. Maps of **a** HS_{field}, and HS calculated from **b** LVIS waveforms, **c** L-band and **d** P-band vertical reflectivity profiles

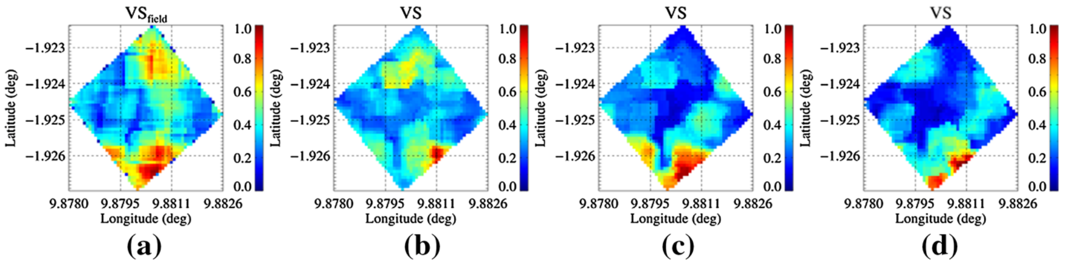

(a) **(b)** **(c)** **(d)**

Fig. 11 Rabi ForestGEO plot. Maps of **a** VS_{field}, and VS calculated from **b** LVIS waveforms, **c** L-band and **d** P-band vertical reflectivity profiles

acquisitions may also affect the comparison between field and remote sensing indices. The LVIS and the L-band HS maps are the most similar ones, although in some stands the L-band profiles lead to higher values of HS as a consequence of the mentioned artifacts. At P-band, many stands result in more homogeneity as a consequence of the lower sensitivity to the top canopy variations.

Figure 11 shows the VS_{field} and the VS maps. All maps highlight an area of high vertical structure at the southeastern part of the site, which seems to be the mean feature in the plot. More to the North, another high structure area is indicated in the map derived from the field data. This area is also visible in the LVIS map and in the L-band map, while it becomes hardly visible in the P-band one. The correlation plot of Fig. 12 clearly shows that L-band reconstructs the wider range and distribution of structure indices obtained from the field data. The profiles of Fig. 5 offer some insights to understand these differences. In the LVIS profiles, the majority of peaks appear within 20 to 45 m, while peaks below 20 m are rather seldom. On the other hand, the TomoSAR peaks at L- as well as at P-band are distributed across the whole canopy extent down to the ground. The peaks from the P-band TomoSAR profiles are particularly numerous closer to the ground level. Occasionally, gaps in the canopy layer become visible at P-band which are not noticeable at L-band or in the LVIS profiles. Therefore, LVIS profiles are more sensitive than TomoSAR reflectivity profiles to variations mostly concentrated in the highest part of the canopy and can better predict VS_{field} in those areas. However, TomoSAR long-wavelength profiles are more sensitive to variations of vertical structure when these are driven by the presence of sub-canopy elements.

Fig. 12 Rabi, ForestGEO plot. Comparison between VS and VS_{field}. The square symbols indicate (conditioned) mean values, while the vertical bars delimit the VS interval where 75% of values are found

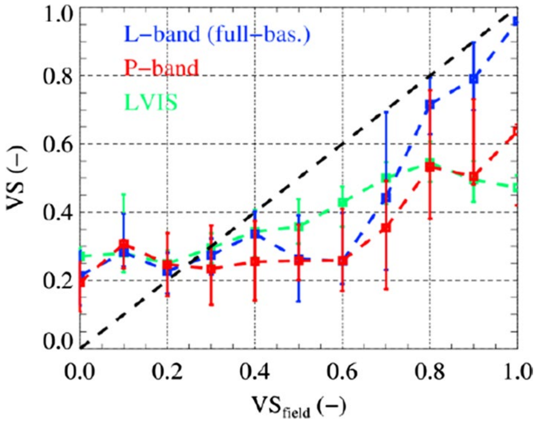

6 Conclusions

In this paper, first, a comparison between lidar waveforms and TomoSAR reflectivity profiles at multiple wavelengths has been attempted by means of real data in a temperate and a tropical test site. It has been shown that the wavelength affects directly penetration through the vegetation volume down to the ground. While lidar penetration occurs through vegetation gaps and is facilitated by the nadir-looking geometry, SAR penetration typically reduces from P- up to X-band, being however further affected by forest type, density, and dielectric properties (attenuation induced by water content). At the same time, it has been shown, even when the penetration is comparable, the measurements provided by lidar and by SAR systems at different wavelengths are sensitive to different components of forest structure, and therefore all of them can complement each other for structure characterization. This comparison has then be used as a basis to gain some early insights on the capabilities of two most promising combination frameworks, i.e., the model-based and the structure-based frameworks, based on two recent case studies.

The common sensitivity to geometric parameters drives the parameterisation of SAR backscattering models by means of lidar measurements in the model-based framework. A fusion algorithm could then be based on the complementarity of type and/or spatial distribution and resolution of the measurements. With reference to forest height estimation, some of the experimented model-based combination methodologies have been presented by means of a case study developed in the context of the NASA GEDI lidar mission. The TanDEM-X coherences can be used to continuously extend the coverage of the top heights measured by GEDI on the sparsely sampled waveform footprints. The RVoG model has been shown to be simple and representative enough to allow accurate parameterisation and inversion. Depending on the SAR wavelength and configurations, additional parameters can be accommodated (Simard and Denbina 2018). In general, (i) the choice of an appropriate backscattering model and its dimensionality, (ii) the choice a meaningful lidar parameterisation, and (iii) its interpolation from the lidar footprint to the continuous SAR coverage are three critical steps that contribute to the effectiveness of the combination.

The structure-based framework can directly accommodate both commonalities and complementarities in the information content of lidar and SAR measurements, bridging the limitations of the model-based framework in the cases in which the physical equivalence between lidar and SAR parameters is not given. An example has been shown in which indices expressing horizontal and vertical structure (heterogeneity) have been applied to lidar waveforms and TomoSAR vertical reflectivity profiles, in correspondence to structure indices established in ecology and forestry with ground inventory measurements. Lidar and P- and L-band wavelengths fully complement each other in both the horizontal and vertical structure if significant penetration differences exist and/or structural differences are driven by element sizes. For sure, the sensitivity of lidar waveforms to vertical structure variations mostly close to the canopy top is complemented by the higher sensitivity of long-wavelength TomoSAR profiles to variations closer to the ground. The definition of ecologically significant structure indices is of crucial importance. Nevertheless, the structure space defined by the two indices (whose independence is not guaranteed) seems to be able to relate lidar and SAR measurements and field measurements, therefore providing a biophysical interpretation. Limitations and ambiguities of this framework are still under investigation, remembering that indices might only describe an incomplete "subspace" of the whole structure information.

It is worth noting that a combination framework that unifies both the model-based and the structure-based ones might also be developed. For instance, the structure-based framework could be used to identify the spatial regions of validity of a certain parameterisation, thus defining models and supporting inversion strategies in the model-based framework.

A critical factor affecting both frameworks is the scale at which structure parameters and indices are retrieved. Indeed, it affects both the meaningfulness of the parameterisation with respect to the final inversion performance and the structure indices with respect to the underlying stand or forest. Highresolution sensors allow to explore multiple scales, representing an additional degree of freedom for structure characterisation to be exploited in the combination between lidar and SAR, and SAR at multiple wavelengths. Existing models, algorithms and indices should be assessed also in this perspective, and new ones developed, if necessary. At the present stage, addressing these issues and understanding the underlying relationships is a unique challenge that still needs to be mastered toward the development of effective fusion techniques for forest structure observation, and to optimize system and acquisitions configurations.

Acknowledgements This review originates from the workshop "Space-based Measurement of Forest Properties for Carbon Cycle Research" held at the International Space Science Institute in Bern in November 2017. We thank P. Biber and M. Heym (Technische Universität München, TUM, Munich, Germany), and A. Huth and R. Fischer (Helmholtz Zentrum für Umweltforschung, UFZ, Leipzig, Germany) for inputs and discussions on forest structure and structure metrics. Part of this work was supported by the Helmholtz Alliance Remote Sensing and Earth System Dynamics funded by the Initiative and networking Fund of the Helmholtz Association. Laser Vegetation and Ice Sensor (LVIS) data sets were provided by the team in the Laser Remote Sensing Branch at NASA Goddard Space Flight Center with support from the University of Maryland, College Park. Finally, we thank the two anonymous reviewers that helped to improve the manuscript with their constructive comments.

Appendix 1: Derivation of the Relationship Between InSAR Volume Coherences and Vertical Reflectivity Profile

The purpose of this Appendix is to summarize the algebraic steps that lead to the Fourier relationship between the InSAR coherence and the vertical reflectivity profile starting from the volume integral (2).

First of all, it is commonly assumed that the (end-to-end) system point-spread function after focusing is separable in the range and azimuth dimensions, i.e.

$$h(r, x) = h_r(r) \cdot h_x(x) \tag{14}$$

being $h_r(r)$ and $h_x(x)$ the range and azimuth system point-spread functions, usually approximated as ideal rectangular functions with width equal to the respective resolution. The formulation in (14) implies that the viewing geometry is independent of the azimuth coordinate,[1] therefore the integral on dx can be solved, and (1) becomes:

$$y(r') = \iint h_r(r' - r) \cdot \bar{\xi}(r, s) \cdot \mathrm{e}^{-j\frac{4\pi}{\lambda}R(r,s)} \mathrm{d}r\mathrm{d}s, \tag{15}$$

$\bar{\xi}(r, s)$ being the integral along azimuth of the complex reflectivity weighted by the azimuth point-spread function. The dependency on the azimuth has been dropped for notational simplicity. From (15), a single SAR image provides a single tomographic projection of the 3D reflectivity filtered by the range response (Bamler and Hartl 1998). The interpretation of the convolution integral in (15) is facilitated in the domain of the 2D range-elevation spatial frequencies after a Fourier transform. Indeed, the SAR image spectrum is a 2D slice out of the complete 3D reflectivity spectrum (Bamler and Hartl 1998).

In general, an additional 2D spectral slice with minimum overlap increases the amount of information available on the reflectivity spectrum toward its reconstruction. Conventional InSAR configurations realize this by varying the complex exponential in (15), i.e., by collecting one additional SAR image in spatial (incidence angle) diversity. First of all, the two images are co-registered, i.e., both images are resampled onto a common grid so that the co-registered pixels refer to a common position in the 3D space. After co-registration, and in absence of system (including noise) and processing non-idealities, the SLC complex amplitudes for the same pixel become:

$$\begin{aligned} y_1(r') &= \iint h_r(r' - r) \cdot \bar{\xi}(r, s) \cdot \mathrm{e}^{-j\frac{4\pi}{\lambda}R_1(r,s)} \mathrm{d}r\mathrm{d}s, \\ y_2(r') &= \iint h_r(r' - r) \cdot \bar{\xi}(r, s) \cdot \mathrm{e}^{-j\frac{4\pi}{\lambda}R_2(r,s)} \mathrm{d}r\mathrm{d}s, \end{aligned} \tag{16}$$

under the additional assumption that $\bar{\xi}(r, s)$ does not change with the difference of incidence angle induced by the track/orbit displacement and with the (possible) time difference between the two acquisition. The interferogram is defined as

$$\varphi(r') = \angle y_1(r') y_2^*(r'), \tag{17}$$

which for an ideal deterministic point scatterer located at (r', s') becomes:

$$\varphi(r') = \frac{4\pi}{\lambda}\left[R_2(r', s') - R_1(r', s')\right] \tag{18}$$

Let $B_{\|}$ and $B_{\perp}$ be the spatial track/orbit displacements in the direction parallel and orthogonal to the line of sight, respectively. Therefore, one can write:

$$R_2(r, s) = \sqrt{\left(r - B_{\|}\right)^2 + \left(s - B_{\perp}\right)^2}. \tag{19}$$

Some processing steps and approximations can be applied in order to reach a convenient formulation, which are detailed in Bamler and Hartl (1998) and Fornaro et al (2003). In

---

[1] The dependence on the azimuth direction can be readily included. Here it has not been considered for simplicity.

these operations, $y_1(r')$ is taken as a phase reference, and for this reason it is called master; $y_2(r')$ is then called slave. The small variation of look angle between the two acquisitions allows to retain the paraxial approximation. By developing (19), a residual s^2-dependent phase contribution is originated by the curvature of the wavefront which can be included in the complex reflectivity, as its (second-order) amplitude distribution is normally of interest. Alternatively, it can simply be neglected if the distance between the sensor and the scatterers is large enough (as it typically is) to make the plane-wave approximation hold. Finally, the phase of the slave image is "flattened" with respect to a reference height by using the interferometric phase (18). In this case, the reference height can be chosen constant for the entire scene, or varying locally according to a reference external DEM. After these manipulations, by further assuming $B_{\|} \ll r$, it results:

$$\begin{aligned} y_1(r') &= \iint h_r(r'-r) \cdot \xi'(r,z)\mathrm{d}r\mathrm{d}z, \\ y_2(r') &\cong \iint h_r(r'-r) \cdot \xi'(r,z) \cdot e^{jk_z z}\mathrm{d}r\mathrm{d}z. \end{aligned} \tag{20}$$

In (20), a change of variable from elevation to vertical height z has been performed, with $s = z/\sin\theta_0$. $\xi'(r,z)$ is the final complex reflectivity after the change of variables and the inclusion of phase residuals ψ, i.e., $\xi'(r,z) = \bar{\xi}(r, z/\sin\theta_0)\mathrm{e}^{j\psi}/\sin\theta_0$, being θ_0 the local incidence angle. k_Z is the so-called vertical wavenumber, defined in (3).

Being composed of distributed scatterers, the scattering from forest scenarios is better described by its statistics, particularly by the complex coherence defined in (4). This results in:

$$\begin{aligned} E\{y_1(r')\} &= E\{y_2(r')\} = 0, \\ E\left\{\left|y_1(r')\right|^2\right\} &= E\left\{\left|y_2(r')\right|^2\right\} = P_y, \\ E\{y_1(r')y_2^*(r')\} &= P_y\gamma_{1,2}(k_Z), \end{aligned} \tag{21}$$

and using (20):

$$E\{y_1(r')y_2^*(r')\} = \iint \left|h_r(r'-r)\right|^2 \cdot F_\xi(r,z) \cdot \mathrm{e}^{jk_z z}\mathrm{d}r\mathrm{d}z. \tag{22}$$

$F_\xi(r,z)$ represents the spatial density of backscattered power in the height-range plane. It is interesting to consider the case of surface scattering at a constant height $z = z_0$. Its complex reflectivity can be written as a Dirac-δ with power P_S. After appropriate algebraic manipulations, it provides the following interferometric coherence:

$$\gamma_{1,2}(k_Z) = \frac{E\{y_1(r')y_2^*(r')\}}{P_S} = \gamma_S(k_Z)\mathrm{e}^{jk_Z z_0}. \tag{23}$$

Therefore, the coherence phase is proportional to the surface of the height. $\gamma_S(k_Z)$ is a positive (real-valued) geometric decorrelation term that depends on the range point-spread function.[2] However, forest scatterers are distributed within a volume, that can be seen as the coherent superposition of the number of surfaces with different total powers. As a consequence, it simply follows:

$$E\{y_1(r')y_2^*(r')\} = \gamma_S(k_Z) \sum_n P_S(z_n) \mathrm{e}^{jk_Z z_n}. \tag{24}$$

In the most general case, by letting the number of surfaces tend to infinity, the sum in (24) becomes an integral, and it is readily obtained

$$\gamma_{1,2}(k_Z) = \gamma_S(k_Z)\gamma_{\mathrm{vol}}(k_Z), \tag{25}$$

where:

$$\gamma_{\mathrm{vol}}(k_Z) := \mathrm{e}^{jk_Z z_G} \frac{\int_0^{H_V} F_{vol}(z)\mathrm{e}^{jk_Z z}\mathrm{d}z}{\int_0^{H_V} F_{\mathrm{vol}}(z)\mathrm{d}z}, \tag{26}$$

which provides the Fourier relationship between vertical reflectivity profile and volume coherence anticipated in Sect. 2.1.

Appendix 2: Descriptions of Test Sites and Data Sets

Traunstein Forest (South of Germany)

This temperate forest site is located close to the city of Traunstein in the South of Germany. Most forest stands are structurally complex due to species richness and management practices, with a majority of conifer stands (around 70%). The forest top height can reach 40 m, and mean biomass level is about 200 t/h, significantly higher than other managed forests in the same ecological zone. In this test site, TomoSAR data sets at different frequencies have been collected by means of the German Aerospace Center (DLR) E-SAR and F-SAR airborne platforms since 2008. The data sets used in this paper were acquired at P- and L-band in 2009, and at X-band in 2013 with approximately the same flight tracks and viewing (master) geometry. Due to the 4-year time difference between the P- and X-band data sets, an additional L-band TomoSAR data set of 2013 has been considered. In this way, two direct comparisons can be performed, i.e., P- versus L-band in 2009, and L- versus X-band in 2013. All acquisitions share the same (master) geometry. While the acquisitions at P- and L-band are in repeat-pass mode, the one at X-band is in repeated single-pass mode (with changing k_Z for different passes) to avoid temporal decorrelation (Pardini et al. 2018b). The most relevant acquisition parameters are reported in Table 1. On November 18, 2012, discrete return lidar data have been acquired as well. During the total 4-year time, structural changes occurred in some stands due to forest management activities. Additionally, all acquisitions are in leaf-off conditions, but differences of water content and of its distribution in the tree trunk (Gates 1991) could have affected the SAR backscattering.

---

[2] If the dependence of the problem on the azimuth coordinate is taken into account, a similar term would arise also in azimuth. However, the related decorrelation is normally lower than the range one, thus it is considered negligible.

Table 1 Summary of parameters characterizing the airborne SAR acquisitions over the Traunstein and Rabi forests

Test site	Traunstein (Germany)	Traunstein (Germany)	Traunstein (Germany)	Traunstein (Germany)	Rabi (Gabon)	Rabi (Gabon)
Platform	E-SAR	E-SAR	F-SAR	F-SAR	F-SAR	F-SAR
Frequency	P-band	L-band	L-band	X-band	P-band	L-band
Wavelength (m)	0.85	0.23	0.23	0.031	0.69	0.23
Acquisition date	05/11/2009	28/10/2009	04/04/2013	22/03/2013	07/02/2016	
Resolution range × azimuth (m)	6.64 × 2.4	2.12 × 1.2	1.28 × 0.6	0.96 × 0.5	3.84 × 2	1.92 × 0.64
Number of tracks	6	4	5	6	10	10
Total acquisition time[a]	~ 1 h	< 1 h	~ 1 h	~ 1 h	~ 2 h	~ 2 h
Vertical resolution, m[b]	20	20	10	20	15	5

[a] Time needed to fly all the acquisition tracks

[b] Average Rayleigh TomoSAR vertical resolution (defined in Sect. 2.2) for the considered transect

Rabi and Lopé (Gabon)

The Rabi forest site is located at the southwestern Gamba Complex of Gabon, and consists of a diverse mix of upland and wet-forest with a mean tree height of about 40 m on a fairly flat topography. Within this forest site, a ForestGEO (Smithsonian Institution Forest Global Earth Observatories) plot was established between 2010 and 2012 in which the position and the diameter at breast height (*dbh*) of more than 175,000 trees belonging to 340 species with $dbh \geq 1$ cm were inventoried across 25 ha. P- and L-band TomoSAR acquisitions were carried out with the F-SAR airborne platform during the AfriSAR campaign in 2016 (see Table 1 for the relevant acquisition parameters) (Pardini et al. 2018a). During the same campaign, the Rabi site has been covered also by NASA LVIS lidar waveforms. For AfriSAR, LVIS operated at 7315 m altitude, with a wavelength equal to 1064 nm, ~20 m footprint diameter and 10 m footprint spacing along latitude and longitude. Together with the waveforms, ground topography (Digital Terrain Model, DTM) and relative height metrics have been processed.

The Lopé site lies within the Lopé National Park, and it consists of a mosaic of savannah and (dense) forest, with varying species richness and tree density across stands. The maximum tree height exceeds 50 m in many stands. The forest (above ground) biomass ranges between 10 t/ha in savanna areas up to ~400 t/ha in mature forest stands. The terrain is hilly, with many local slopes steeper than 20°. This test site was covered during the AfriSAR campaign by both airborne SAR and LVIS lidar acquisitions similarly to the Rabi site. For the experiments in Sect. 4, a TanDEM-X bistatic single-pass single polarisation (HH) interferometric acquisition has been considered (see Table 2) that was performed a few weeks apart from the LVIS acquisitions.

La Selva (Costa Rica)

La Selva Biological Station (LSBS) forest site is located in northeastern Costa Rica. The site is a protected low-land region of tropical rain forest, covering an area of 1600 ha. The area contains a mixture of old-growth, secondary and selectively logged forests with height up to 60 m. The mean biomass of old-growth forest, which is the major components of total LSBS biomass, is around 169 t/ha (Clark et al. 2011). Airborne discrete return lidar data were collected over LSBS in September and October 2009. In 2011, the LSBS was covered by a dual polarisation (HH/VV) TanDEM-X bistatic acquisition on December 5, whose characteristic parameters are reported in Table 2.

Table 2 Summary of parameters characterizing the TanDEM-X SAR acquisitions over Lopé and La Selva

Test site	Lopè (Gabon)	La Selva (Costa Rica)
Acquisition date	14/12/2015	05/11/2011
Acquisition mode	Bistatic	
Polarization	HH	HH/VV
Resolution range × azimuth (m)	1.7 × 3.3	1.7 × 6.6
incidence angle (°)	45	38
HoA (m)	80	70

References

Aguilera E, Nannini M, Reigber A (2013) Wavelet-based compressed sensing for SAR tomography of forested areas. IEEE Trans Geosci Remote Sens 51(12):5283–5295

Armston J, Disney M, Lewis P, Scarth P, Phinn S, Lucas R, Bunting P, Goodwin N (2013) Direct retrieval of canopy gap probability using airborne waveform lidar. Remote Sens Environ 134:24–38

Bai Y, Tebaldini S, Minh DHT, Yang W (2018) An empirical study on the impact of changing weather conditions on repeat-pass SAR tomography. J Sel Top Appl Earth Obs Remote Sens 11(10):3505–3511

Bamler R, Hartl P (1998) Synthetic aperture radar interferometry. Inverse Probl 14:R1–R54

Barbeito I, Montes F, Canellas I (2009) Evaluating the behavior of vertical structure indices in Scots pine forests. Ann For Sci 66(710):1–10

Bergen KM, Goetz SJ, Dubayah RO, Henebry GM, Hunsaker CT, Imhoff ML, Nelson RF, Parker GG, Radeloff VC (2009) Remote sensing of vegetation 3-D structure for biodiversity and habitat: review and implications for lidar and radar spaceborne missions. J Geophys Res 114:1–13

Blair JB, Hofton MA (1999) Modeling laser altimeter return waveforms over complex vegetation using high-resolution elevation data. Geophys Res Lett 26:2509–2512

Blair J, Rabine D, Hofton M (1999) The laser vegetation imaging sensor: a medium altitude, digitization-only, airborne laser altimeter for mapping vegetation and topography. ISPR J Photogramm Remote Sens 54(2/3):115–122

Bohn FJ, Huth A (2017) The importance of forest structure to biodiversity-productivity relationships. R Soc Open Sci 4(1):160521

Brokaw N, Lent R (1999) Vertical structure. In: Maintaining biodiversity in forest ecosystems. Cambridge University Press, Cambridge, UK

Brolly M, Woodhouse IH (2013) Vertical backscatter profile of forests predicted by a macroecological plant model. Int J Remote Sens 34(4):1026–1040

Brolly M, Simard M, Tang H, Dubayah R (2016) A lidar-radar framework to assess the impact of vertical forest structure on interferometric coherence. IEEE J Sel Top Appl Earth Obs Remote Sens 9:5830–5841

Carabajal CC, Harding DJ (2006) SRTM C-band and ICESat laser altimetry elevation comparisons as a function of tree cover and relief. Photogramm Eng Remote Sens 72(3):287–298

Cazcarra Bes V, Tello M, Fischer R, Heym M, Papathanassiou K (2017) Monitoring forest structure dynamics by means of L-band SAR tomography. Remote Sens 9(12):1229

Cazcarra Bes V, Pardini M, Tello M, Papathanassiou K (2019) Comparison of tomographic SAR reflectivity reconstruction algorithms for forest applications at L-band. IEEE Trans Geosci Rem Sensing (Accepted for publication)

Clark P, Evans C (1954) Distance to nearest neighbor as a measure of spatial relationships in populations. Ecology 35(4):445–452

Clark ML, Roberts DA, Ewel JJ, Clark DB (2011) Estimation of tropical rain forest aboveground biomass with small-footprint lidar and hyperspectral sensors. Remote Sens Environ 115:2931–2942

Couteron P, Pelissier R, Nicolini EA, Paget D (2005) Predicting tropical forest stand structure parameters from Fourier transform of very high-resolution remotely sensed canopy images. J Appl Ecol 42:1121–1128

De Grandi EC, Mitchard E, Hoekman D (2016) Wavelet based analysis of TanDEM-X and LiDAR DEMs across a tropical vegetation heterogeneita gradient driven by fire distrurbance in Indonesia. Remote Sens 8:641–667

Del Rio M (2016) Characterization of structure, dynamics, and productivity of mixed species stands: review and prespectives. Eur J For Res 135(1):23–49

Dubayah RO (2015) The global ecosystem dynamics investigation (GEDI) lidar. In: Proceedings of 1st BIOMASS science workshop

Dubayah RO, Drake JB (2000) Lidar remote sensing for forestry. J For 98(6):44–46

Dubayah RO, Sheldon SL, Clark DM, Hofton MA, Blair JB, Hurtt GC, Chazdon RL (2010) Estimation of tropical forest height and biomass dynamics using lidar remote sensing at La Selva, Costa Rica. J Geophys Res 115:1–17

Fatoyinbo TE, Simard M (2013) Height and biomass of mangroves in Africa from ICESat/GLAS and SRTM. Int J Remote Sens 34(2):668–681

Fornaro G, Serafino F, Soldovieri F (2003) Three-dimensional focusing with multipass SAR data. IEEE Trans Geosci Remote Sens 41(3):507–517

Frey O, Meyer E (2011) Analyzing tomographic SAR data of a forest with respect to frequency, polarization, and focusing techniques. IEEE Trans Geosci Remote Sens 49(10):3648–3659

Frolking S, Palace MW, Clark DB, Chambers JQ, Shugart HH, Hurtt GC (2009) Forest disturbance and recovery: a general review in the context of spaceborne remote sensing of impacts on aboveground biomass and canopy structure. J Geophys Res: Biogeosci 114:1–27

Garestier F, Dubois-Fernandez P, Champion I (2008) Forest height inversion using high resolution P-band Pol-InSAR data. IEEE Trans Geosci Remote Sens 46(10):3544–3559

Gates DM (1991) Water relations of forest trees. IEEE Trans Geosci Remote Sens 29(6):836–842

Gini F, Lombardini F, Montanari M (2002) Layover solution in multibaseline SAR interferometry. IEEE Trans Aerosp Electron Syst 38(4):1344–1356

Goetz S, Steinberg D, Dubayah RO, Blair B (2007) Laser remote sensing of canopy habitat heterogeneity as a predictor of bird species richness in an eastern temperate forest. Remote Sens Environ 108:254–263

Hall FG, Bergen K, Blair JB, Dubayah R, Houghton R, Hurtt G, Kellndorfer J, Lefsky M, Ranson J, Saatchi S, Shugart HH, Wickland D (2011) Characterizing 3D vegetation structure from space: mission requirements. Remote Sens Environ 115:2753–2775

Hancock S, Disney M, Muller JP, Lewis P, Foster M (2011) A threshold insensitive method for locating the forest canopy top with waveform lidar. Remote Sens Environ 115:3286–3297

Harding DJ, Lefsky MA, Parker GG, Blair JB (2001) Laser altimeter canopy height profiles: methods and validation for closed-canopy, broadleaf forest. Remote Sens Environ 76(3):283–297

Kaasalainen S, Holopainen M, Karjalainen M, Vastaranta M, Kankare V, Karila K, Osmanoglu B (2015) Combining lidar and synthetic aperture radar data to estimate forest biomass: status and prospects. Forests 6:252–270

Kellndorfer JM, Walker WS, LaPoint E, Kirsch K, Bishop J, Fiske G (2010) Statistical fusion of lidar, InSAR, and optical remote sensing data for forest stand height characterization: a regional-scale method based on LVIS, SRTM, Landsat ETM+, and ancillary data sets. J Geophys Res 115:G00E08

Krieger G, Zink M, Bachmann M, Bräutigam B, Schulze D, Martone M, Rizzoli P, Steinbrecher U, Antony JW, De Zan F, Hajnsek Papathanassiou K, Kugler F, Rodriguez Cassola M, Younis M, Baumgartner S, López Dekker P, Prats P, Moreira A (2013) TanDEM-X: a radar interferometer with two formation-flying satellites. Acta Astr 89:83–98

Kugler F, Schulze D, Hajnsek I, Pretzsch H, Papathanassiou K (2014) TanDEM-X Pol-InSAR performance for forest height estimation. IEEE Trans Geosci Remote Sens 52(10):6404–6422

Lavalle M, Hensley S (2015) Extraction of structural and dynamic properties of forests from polarimetric-interferometric SAR data affected by temporal decorrelation. IEEE Trans Geosci Remote Sens 53(9):4752–4767

Le Toan T, Quegan S, Davidson MJW, Baltzer H, Paillou P, Papathanassiou K, Plummer S, Rocca F, Saatchi S, Shugart S, Ulander L (2011) The BIOMASS mission: mapping global forest biomass to better understand the terrestrial carbon cycle. Remote Sens Environ 115:2850–2860

Lee SK, Kugler F, Papathanassiou K, Hajnsek I (2013) Quantification of temporal decorrelation effects at L-band for polarimetric SAR interferometry applications. IEEE J Sel Top Appl Earth Obs Remote Sens 6(3):1351–1367

Lee SK, Fatoyinbo T, Qi W, Hancock S, Armston J, Dubayah R (2018) GEDI and TanDEM-X fusion for 3D forest structure parameter retrieval. In: Proceedings of international symposium of geoscience and remote sensing (IGARSS)

Lefsky MA, Harding DJ, Cohen WB, Parker GG, Shugart HH (1999) Surface lidar remote sensing of basal area and biomass in deciduous forests of eastern Maryland, USA. Remote Sens Environ 67(1):83–98

Liang J, Buongiorno J, Monserud RA, Kruger EL, Zhou M (2007) Effects of diversity of tree species and size on forest basal area growth, recruitment, and mortality. Forest Ecol Manag 243(1):116–127

Lin Y, Sarabandi K (1999) A Monte Carlo coherent scattering model for forest canopies using fractal-generated trees. IEEE Trans Geosci Remote Sens 37(1):440–451

Lombardini F, Reigber A (2003) Adaptive spectral estimation for multibaseline SAR tomography with airborne L-band data. In: Proceedings of international symposium of geoscience and remote sensing (IGARSS)

Mariotti d'Alessandro M, Tebaldini S, Rocca F (2012) Phenomenology of ground scattering in a tropical forest through polarimetric synthetic aperture radar tomography. IEEE Trans Geosci Remote Sens 51(8):4430–4437

McElhinny C, Gibbons P, Brack C, Bauhus J (2005) Forest and woodland stand structural complexity: its definition and measurement. For Ecol Manag 218(1–3):1–24

Mitsuhashi R, Murooka J, Sakaizawa D, Imai T, Kimura T, Hayashi M, Mizutani K, Sawada Y, Endo T, Kajiwara K, Honda Y, Asai K (2018). The development of vegetation Lidar mission 'MOLI'. In: Proceedings of forest SAT

Moreira A, Prats-Iraola P, Younis M, Krieger G, Hajnsek I, Papathanassiou KP (2013) A tutorial on synthetic aperture radar. IEEE Geosci Remote Sens Mag 1(1):6–43

Moreira A, Krieger G, Hajnsek I, Papathanassiou K, Younis M, Lopez Dekker P, Huber S, Villano M, Pardini M, Eineder M, De Zan F, Parizzi A (2015) Tandem-L: a highly innovative bistatic SAR mission for global observation of dynamic processes on the Earth's surface. IEEE Geosci Remote Sens Mag 3(2):8–23

Neuenschwander A, Magruder L (2018) Mapping global forests using data from NASA's ICESat-2 Mission. In: Proceedings of Forest SAT

Neumann M, Ferro-Famil L, Reigber A (2010) Estimation of forest structure, ground, and canopy layer characteristics from multibaseline polarimetric interferometric SAR data. IEEE Trans Geosci Remote Sens 48(3):1086–1104

Neumann M, Saatchi S, Clark DB (2012) Quantifying spatial and temporal dynamics of tropical forest structure using high resolution airborne lidar. In: Proceedings of international symposium of geoscience and remote sensing (IGARSS)

Ni-Meister W, Jupp DLB, Dubayah R (2001) Modeling lidar waveforms in heterogeneous and discrete canopies. IEEE Trans Geosci Remote Sens 39(9):1943–1958

Oliver MA, Webster R (1990) Kriging: a method of interpolation for geographical information systems. Int J Geogr Inf Syst 4:313–332

Papathanassiou K, Cloude S (2001) Single-baseline polarimetric SAR interferometry. IEEE Trans Geosci Remote Sens 39(11):2352–2363

Pardini M, Papathanassiou K (2018) TomoSAR vertical profiles at multiple frequencies: an experimental analysis. In: Proceedings of European SAR conference (EUSAR)

Pardini M, Qi W, Dubayah R, Papathanassiou KP (2016) Exploiting TanDEM-X Pol-InSAR data for forest structure observation and potential synergies with NASA's Global Ecosystem Dynamics Investigation Löidar (GEDI) mission. In: Proceedings of European SAR conference (EUSAR)

Pardini M, Tello M, Cazcarra-Bes V, Papathanassiou K, Hajnsek I (2018a) L- and P-Band 3-D SAR reflectivity profiles versus lidar waveforms: the AfriSAR case. IEEE J Sel Top Appl Earth Obs Remote Sens 11(10):3386–3401

Pardini M, Papathanassiou K, Lombardini F (2018b) Impact of dielectric changes on L-band 3-D SAR reflectivity profiles of forest volumes. IEEE Trans Geosci Remote Sens 56(12):7324–7337

Parker GG (1995) Structure and microclimate of forest canopies. In: Lowman M, Nadkarni N (eds) Forest canopies: a review of research on a biological frontier. Academic press, New York, pp 73–106

Pastorella F, Paletto A (2013) Stand structure indices as tools to support forest management: an application in Trentino forests (ItalyO). J For Sci 59(4):159–168

Persson HJ, Ollson H, Soja MJ, Ulander LMH, Fransson JES (2017) Experiences from large-scale forest mapping of Sweden using TanDEM-X data. Remote Sens 9(12):1253

Pommerening A (2002) Approaches to quantifying forest structures. Forestry 75(3):305–324

Praks J, Antropov O, Hallikainen M (2012) LIDAR-aided SAR interferometry studies in Boreal forest: scattering phase center and extinction coefficient at X- and L-band. IEEE Trans Geosci Remote Sens 50(10):3831–3843

Pretzsch H (2009) Forest dynamics, growth and yield. Springer, Berlin

Qi W, Dubayah R (2016) Combining Tandem-X InSAR and simulated GEDI lidar observations for forest structure mapping. Remote Sens Environ 187:253–266

Qi W, Dubayah R (2017) Forest structure modelling of a coniferous forest using TanDEM-X InSAR and simulated GEDI lidar data. In: Proceedings of IEEE international symposium of geoscience and remote sensing (IGARSS)

Reigber A, Moreira A (2000) First demonstration of airborne SAR tomography using multibaseline L-band data. IEEE Trans Geosci Remote Sens 38(5):2142–2152

Reineke R (1933) Perfecting a stand-density index for even aged forests. J Agric Res 46(7):627–638

Rosen P, Kim Y, Kumar R, Misra T, Bhan R, Raju Sagi T (2017) Global persistent SAR sampling with the NASA-ISRO SAR (NISAR) mission. In: Proceedings of IEEE radar conference

Simard M, Denbina M (2018) An assessment of temporal decorrelation compensation methods for forest canopy height estimation using airborne L-band same-day repeat-pass polarimetric SAR interferometry. IEEE J Sel Top Appl Earth Obs Remote Sens 11(1):95–111

Snyder M (2010) What is forest stand structure and how is it measured? North Woodl 64:15

Spies TA (1998) Forest structure: a key to the ecosystem. Northw Sci 72:34–36

Sun G, Ranson KJ, Guo Z, Zhang Z, Montesano P, Kimes D (2011) Forest biomass mapping from lidar and radar synergies. Remote Sens Environ 115:2906–2916

Tang H, Dubayah R, Swatantran A, Hofton M, Sheldon S, Clark DB, Blair B (2012) Retrieval of vertical LAI profiles over tropical rain forests using waveform lidar at La Selva, Costa Rica. Remote Sens Environ 124:242–250

Tebaldini S, Rocca F (2012) Multibaseline polarimetric SAR tomography of a boreal forest at P- and L-bands. IEEE Trans Geosci Remote Sens 50(1):232–246

Tello M, Cazcarra-Bes V, Pardini M, Papathanassiou K (2018) Forest structure characterization from SAR tomography at L-band. IEEE J Sel Top Appl Earth Obs Remote Sens 11(10):3402–3414

Thirion L, Colin E, Dahon C (2006) Capabilities of a forest coherent scattering model applied to radiometry, interferometry, and polarimetry at P- and L-Band. IEEE Trans Geosci Remote Sens 44(4):849–862

Treuhaft RN, Chapman BD, dos Santos JR, Gonçalves FG, Dutra LV, Graça PMLA, Drake JB (2009) Vegetation profiles in tropical forests from multibaseline interferometric synthetic aperture radar, field, and lidar measurements. J Geophys Res 114:D23110

Tsui OW, Coops NC, Wulder MA, Marshall P (2013) Integrating airborne LiDAR and space-borne radar via multivariate kriging to estimate above-ground biomass. Remote Sens Environ 139:340–352

Turner W, Spector S, Gardiner N, Fladeland M, Sterling E, Steininger M (2003) Remote sensing for biodiversity science and conservation. Trend Ecol Evol 18:306–314

Whitehurst AS, Swatantran A, Blair JB, Hofton MA, Dubayah R (2013) Characterization of canopy layering in forested ecosystems using full waveform lidar. Remote Sens 5(4):2014–2036

Yang W, Ni-Meister W, Lee S (2011) Assessment of the impacts of surface topography, off-nadir pointing, and vegetation structure on vegetation structure on vegetation lidar waveforms using an extended geometric optical and radiative transfer model. Remote Sens Environ 115:2810–2822

Zebker HA, Villasenor J (1992) Decorrelation in interferometric radar echoes. IEEE Trans Geosci Remote Sens 30(5):950–959

Zenner EK, Hibbs D (2000) A new method for modelling the heterogeneity of forest structure. For Ecol Manag 129:75–87

Appendix B

L- and P-Band 3-D SAR Reflectivity Profiles Versus Lidar Waveforms: The AfriSAR Case

M. Pardini, M. Tello, V. Cazcarra-Bes, K. P. Papathanassiou, I. Hajnsek

IEEE Journal of Selected Topics in Applied Earth Observations and Remote Sensing
Published in August 2018. DOI: 10.1109/JSTARS.2018.2847033

Key findings/points:

- Presentation of the AfriSAR campaign.
- Comparison of TomoSAR profiles at L- and P-band, and Lidar profiles over different tropical forests.
- Analysis of the ground and volume contributions for TomoSAR acquisitions at L- and P-band, as well as the performance to estimate the location of the ground.
- Comparison of vertical forest structure descriptors estimated from TomoSAR (at L- and P-band), Lidar and ground measurements.

The author's contributions:

- M. Pardini is the main author of the manuscript.

The co-author's contributions:

- V. Cazcarra-Bes helped in the processing of the Tomographic SAR data and the preparation of the LVIS data. He also obtained the forest structure maps and helped in the interpretation of the results.

L- and P-Band 3-D SAR Reflectivity Profiles vs. Lidar Waveforms: The AfriSAR Case

Matteo Pardini, *Member, IEEE*, Marivi Tello, *Member, IEEE*, Victor Cazcarra-Bes, Konstantinos Papathanassiou, *Fellow, IEEE*, and Irena Hajnsek, *Fellow, IEEE*

***Abstract*—The aim of this paper is to compare L- and P-band vertical backscattering profiles estimated by means of Synthetic Aperture Radar (SAR) Tomography (TomoSAR) and full LIght Detection And Ranging (lidar) waveforms in terms of their ability to distinguish different tropical forest structure types. The comparison relies on the unique DLR F-SAR and NASA LVIS lidar data sets acquired in 2016 in the frame of the AfriSAR campaign. In particular, F-SAR and LVIS data over three different test sites complemented by plot field measurements are used. First, the SAR and lidar 3-D data sets are compared and discussed on a qualitative basis. The ability to penetrate into and through the canopy down to the ground is assessed at L- and P-band in terms of both the ground-to-volume power ratio and the performance to estimate the location of the underlying ground. The effect of polarimetry on the visibility of the ground is discussed as well. Finally, the 3-D measurements for each configuration are compared with respect to their ability to derive physical forest structure descriptors. For this, vertical structure indices derived from the volume-only 3-D radar reflectivity at L- and P-band and from the LVIS profiles are compared against each other as well as against plot-derived indices.**

***Index Terms*—Tropical forest, forest structure, synthetic aperture radar (SAR), SAR tomography (TomoSAR), light detection and ranging (lidar), full waveforms.**

I. INTRODUCTION

REMOTE sensing systems have been demonstrated to be a powerful source of information for monitoring tropical forest ecosystems. In particular, Synthetic Aperture Radar (SAR) and LIght Detection And Ranging (lidar) systems provide measurements sensitive to 3-D forest structure parameters at high spatial resolutions. This is of critical importance given the high spatial heterogeneity and complexity of tropical forests.

Exploiting the concept of altimetry, lidar sensors emit laser pulses that are reflected by vegetation and/or ground elements within the footprint illuminated and return to the sensor. Depending on the number of the reflective elements within the footprint one emitted laser pulse generates one or multiple returns. Waveform lidar allows to estimate the continuous distribution of the returned laser energy for each pulse (where discrete return lidar does not). Metrics derived from the lidar waveforms are used to estimate structural forest attributes as forest height and biomass [1], [2]. Concerning SAR, the development of approaches for the estimation of parameters related to forest structure has been boosted in the last years by the introduction of Polarimetric SAR Interferometry (Pol-InSAR) [3] and SAR Tomography (TomoSAR) [4]. Pol-InSAR model-based inversion approaches have been successfully demonstrated e.g. for forest height estimation in boreal, temperate and tropical forests at multiple frequencies from P- up to X-band, considering both airborne and space borne platforms [5]-[8]. TomoSAR techniques rely on the angular diversity of SAR images acquired under slightly different incidence angles (e.g., along slightly displaced tracks or orbits) to estimate the 3-D distribution of the backscattered power, also known as the 3-D radar reflectivity. Its reconstruction by TomoSAR techniques is today established and has been demonstrated in several experiments across different forest ecosystems [9]-[13]. However, the interpretation of the reconstructed 3-D radar reflectivity in terms of physical forest structure is not as well established and still in a rather early stage of development. Although first experiments to determine this interpretation have been carried out in temperate forests and especially at L-band [14]-[15], they have been hampered in tropical forest due to the lack of suitable TomoSAR data and adequate reference data sets. Previous interferometric SAR campaigns like INDREX-II (2004) [5] and TropiSAR (2009) [16] provided unique data sets, but the collected data are sub-optimal for assessing multi-frequency TomoSAR performance for forest structure monitoring.

To fill this gap, the AfriSAR campaign was successfully carried out in 2015 and 2016 as a joint effort among space agencies (ESA, NASA, ONERA, DLR and AGEOS) over the African tropical forests of Gabon [17], [18]. The objective of the campaign was to acquire Pol-InSAR and TomoSAR data sets, lidar full waveforms and ground measurements for the development, calibration and validation of tropical forest structure and biomass estimation algorithms. This activity is especially relevant to future planned and under study SAR missions like BIOMASS (ESA) [19], NISAR (NASA) [20],

---

This work was supported by the Helmholtz Alliance Remote Sensing and Earth System Dynamics funded by the Initiative and Networking Fund of the Helmholtz Association.

M. Pardini, M. Tello and K. Papathanassiou are with the German Aerospace Center (DLR), Microwaves and Radar Institute, 82234 Wessling, Germany.

V. Cazcarra-Bes and I. Hajnsek are with the German Aerospace Center (DLR), Microwaves and Radar Institute, 82234 Wessling, Germany, and also with the Institute of Environmental Engineering, Swiss Federal Institute of Technology (ETH) Zurich, 8093 Zurich, Switzerland.

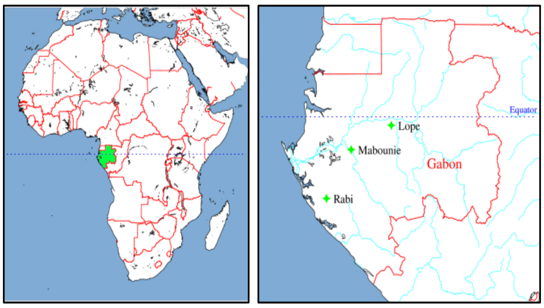

Fig. 1. Location of Gabon in the African continent (indicated in green in the map on the left) and locations (green stars in the map on the right) of the three AfriSAR test sites considered in this paper. The latitude axis is on the vertical direction.

Tandem-L (DLR) [21] and the full waveform GEDI lidar (NASA) mission [22]. The AfriSAR data set allows not only to evaluate the potentials of each sensor and frequency and to optimize their use, but also to characterize synergies and complementarities among them towards unified observation strategies for the generation of biophysical products.

Within this framework, the objective of this paper is to compare TomoSAR L-, P-band profiles and lidar waveforms with respect to their ability and complementarity to distinguish among different vertical forest structure types. The experimental results have been obtained by processing multi-baseline SAR data acquired by DLR's F-SAR platform and NASA's LVIS (Land, Vegetation and Ice Sensor) lidar in February and March 2016. Test sites and data sets are described in Section II. The used TomoSAR algorithms are briefly reviewed in Section III. In Section IV, the SAR penetration through the vegetation volume is directly assessed by evaluating the ground-to-volume power ratio. The impact of the ground-to-volume level on the localization of the ground scattering component in the TomoSAR data is discussed as well. In Section V, SAR and lidar vegetation profiles are firstly compared to each other in a qualitative way. In a second step, their performance to derive physical (i.e. ecologically meaningful) forest structure descriptors is evaluated. For this, vertical structure indices calculated from the volume-only 3-D radar reflectivity at L- and P-band and from the LVIS profiles are compared against each other and against indices derived from plot measurements. Finally, Section VI summarizes the results and draws the conclusions.

II. TEST SITES AND DATA SETS

A. Test sites

During the AfriSAR campaign, fully polarimetric F-SAR L- and P-band acquisitions were carried out over a total of six test sites, namely Lopé, Mondah, Rabi, Mabounie, Pongara and Nkok. In particular, TomoSAR data sets have been acquired by means of a multi-track implementation over Lopé, Rabi and Mabounie. The location of the three sites is shown in Fig. 1. The tracks configurations have been properly designed in order to allow the same vertical resolution and thus a fair performance comparison.

The Lopé site is located within the homonymous National Park, consisting of a mosaic of savannah and (dense) forest, with varying species richness and tree density across stands. The maximum tree height exceeds 50 m in many stands. The forest (above ground) biomass ranges between 10 t/ha in savanna areas up to ~400 t/ha in mature forest stands. The terrain is hilly, with many local slopes steeper than 20°. Twelve inventory plots with size between 0.5 to 1 ha were sampled between January and August 2016 [17].

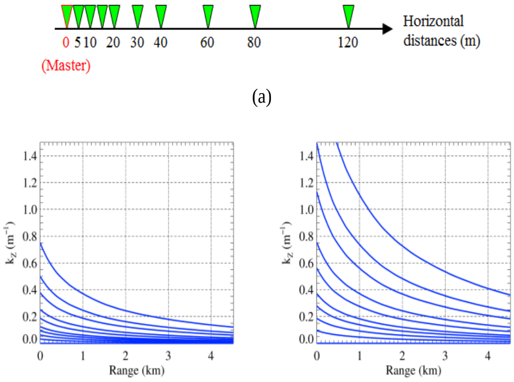

(a)

(b)

Fig. 2. Lopé and Mabounie test sites: (a) Nominal distribution of the horizontal distances among tracks; (b) corresponding vertical wavenumbers resulting from the acquisition as a function of slant range at P-band (left) and L-band (right).

Mabounie is known for being a mining exploration site. Most of the test site is covered by mature primary forest stands (with tree heights between 40 and 50 m) and degraded forest (with tree heights around 20 m). The terrain is rather flat with few gentle slopes.

Finally, the Rabi test site, located at the southwestern Gamba Complex of Gabon, is the site with the highest biodiversity and consists of a diverse mix of upland and wet-forest with a mean tree height of about 40 m. The topography is fairly flat. Within the site, a 25 ha ForestGEO (Smithsonian Institution Forest Global Earth Observatories) plot is located. Between 2010 and 2012 the position and the diameter at breast height (dbh) of more than 175,000 trees belonging to 340 species with dbh ≥ 1 cm were inventoried across 25 ha.

B. TomoSAR acquisitions

SAR data were acquired and processed with an off-nadir angle range between 20° (near-range) and 50° (far-range). The P-band was operated with a 50 MHz bandwidth centered at 435 MHz (equivalent to a wavelength of 69 cm), while the L-band was operated with a 100 MHz bandwidth centered at 1.325 GHz (equivalent to a wavelength of 23 cm). The flight level of 20000 ft (6096 m) was chosen to ensure an above the clouds operation in order to reduce turbulences. For each TomoSAR data acquisition, the tracks were horizontally displaced in order to minimize deviations from the nominal flight tracks.

In (Pol-)InSAR and TomoSAR applications, the vertical sensitivity of the phase difference between two acquisitions is expressed through the vertical wavenumber k_z [4], [7]:

$$k_z = \frac{2\pi}{\text{HoA}} \approx \frac{4\pi}{\lambda}\frac{B}{R\sin\theta\cos\theta}, \tag{1}$$

where θ is the nominal incidence angle, λ is the radar wavelength, R is the slant-range distance, and B is the horizontal distance between the two acquisitions. According to (1), the Height of Ambiguity (HoA) is then the height difference in the scene that causes a 2π phase difference. If the horizontal distances between the tracks are integer multiples of the smallest one, then the largest HoA (corresponding to the smallest horizontal distance) is equal to the TomoSAR HoA [4]. On the other hand, the smallest HoA (corresponding to the largest horizontal distance) equals the vertical TomoSAR resolution. However, as indicated by (1), for a given acquisition configuration the TomoSAR HoA and the vertical resolution vary with the wavelength. This may be critical for simultaneous multi-frequency acquisitions, as track spacings optimized for one frequency can be sub-optimal for another. For example, a multi-track acquisition configuration optimized for L-band will result into a three-time smaller HoA (i.e. corresponding to the ratio between the wavelengths) and a three-time worse vertical resolution at P-band.

With this in mind and referring to (1), the baseline distribution has been designed according to the following considerations:

- For a maximum tree height of about 45 m, a minimum TomoSAR HoA of 90 m is desired. In order to meet this requirement for L-band at an off-nadir angle of 25° (i.e. at near range), a minimum horizontal distance of 5 m is required. At P-band, the same horizontal distance leads to a three times larger minimum HoA (i.e. increased by the ratio of the wavelengths) that becomes 270 m.
- For a maximum horizontal separation of 120 m, the TomoSAR vertical resolution at P-band is around 20 m at mid range. For a maximum tree height of about 45 m, this allows resolving two independent vertical resolution cells for the tallest stands. At L-band, the same geometry leads to a vertical resolution better than 10 m.

Note that due to the inherent dependency on the off-nadir angle the TomoSAR HoA becomes smaller in near range and larger in far range. The same happens to the TomoSAR vertical resolution, which is therefore better in near range and worse in far range.

The total number of tracks flown over each site was limited by the maximum operation time and the time required for a single track including aircraft maneuvers. For AfriSAR, up to 10 tracks per sites have been flown. A non-uniform distribution of horizontal distances between the tracks has been chosen with increasing distance between consecutive tracks from a minimum of 5 m up to maximum of 120 m as shown in Fig. 2(a). Such a configuration has several advantages. First, it leads to a (nominal) uniform distribution of k_z between the minimum and the maximum values, for a better conditioned TomoSAR imaging. Secondly, it provides a certain redundancy of the critical (nominal) k_z values. Finally, the first seven tracks (i.e. horizontal distances up to 40 m) correspond at L-band to a similar k_z set as the one provided at P-band by using the full set (i.e., all 10 tracks). Accordingly, the reduced 7-track L-band and the full 10-track P-band set offer the same vertical TomoSAR resolution. It has already been argued that from a theoretical point of view the difference in the number of tracks has only a negligible impact on the TomoSAR processing [23].

The track setup has been flown over Lopé and Mabounie within a two-hour time window on February 10 and 20, 2016, respectively. The resulting k_z values averaged along azimuth are plotted in Fig. 2(b) as a function of slant range. The standard deviation of the flown tracks with respect to the nominal ones was within 1 m. The variation of k_z with range

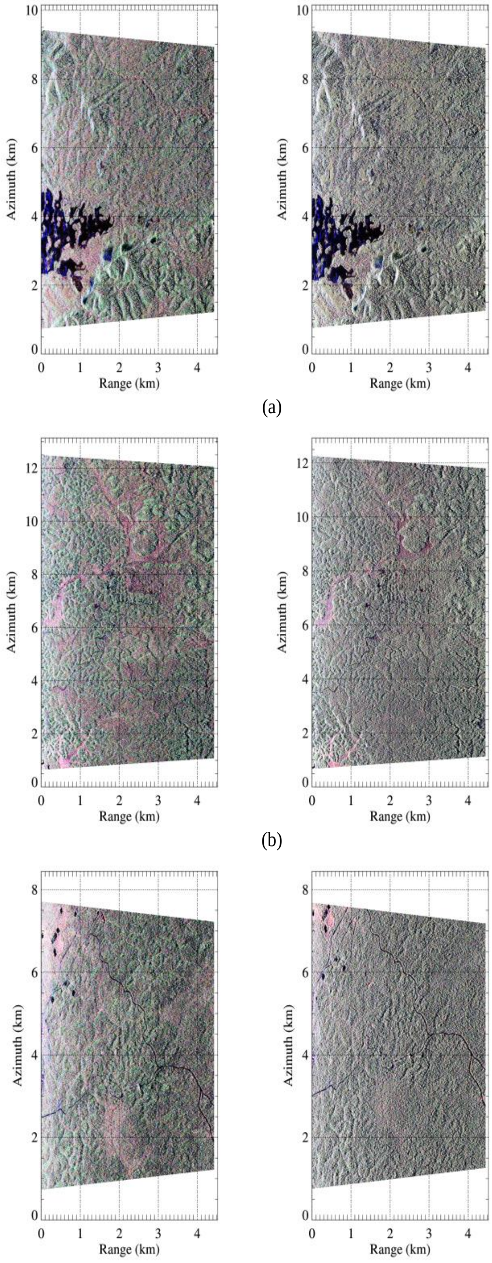

(a)

(b)

(c)

Fig. 3. Pauli RGB composite images in range-azimuth geometry for (a) Lopé, (b) Mabounie, (c) Rabi. Left panel: P-band; right panel: L-band.

is apparent. For Rabi, only 8 tracks have been flown on February 7, 2016: the tracks associated to the horizontal distance of 30 m and 120 m have been missed. In order to counteract the implied non-negligible loss of vertical resolution, especially at P-band, due to the loss of the larger vertical separation, two additional tracks flown on the same day but at different flight heights (up to 30 m above the standard tracks) [17] have been used. The polarimetric Pauli RGB color-composite images at L- and P-band for the three test sites are shown in Fig. 3.

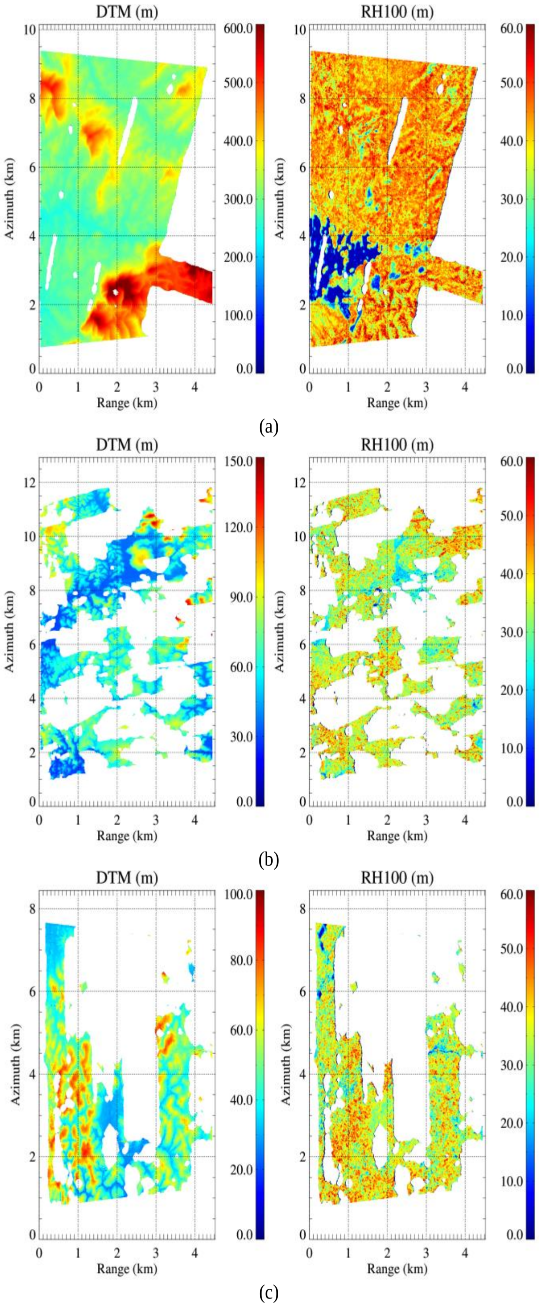

(a)

(b)

(c)

Fig. 4. LVIS DTM (left panel) and RH100 (right panel) in meters for (a) Lopé, (b) Mabounie, (c) Rabi, project on the L-band range-azimuth geometry.

C. LVIS acquisitions

In parallel to the F-SAR acquisitions, the NASA's LVIS sensor also covered the same sites [18]. LVIS is a medium/high altitude (flight altitude between 10 and 20 km), medium footprint (diameter from 5 to 25 m) waveform digitizing lidar. For AfriSAR, LVIS operated with a 18 m footprint.

Similarly to TomoSAR profiles, each waveform is just a proxy to the canopy profiles due to the attenuation of the beam through the vegetation elements. However, the waveforms are acquired in nadir-looking configuration, and the different geometry has to be accounted when comparing LVIS and TomoSAR profiles.

Together with the waveforms, ground topography (Digital Terrain Model, DTM) and relative height (RH) estimates have been processed and provided by the team at NASA Goddard and University of Maryland (USA). Each RH metric expresses the height interval in which a certain percentage of energy is received above the noise level and with respect to the ground height. For instance, the RH100 corresponds to the height interval above the ground in which the total energy is received. RH metrics have been largely used to estimate biomass and to describe canopy vertical structure [1], [2].

In Fig. 4, the LVIS DTM and RH100 are shown for Lopé, Mabounie and Rabi, projected in the L-band range-azimuth geometry. Lopé presents the largest and most continuous LVIS coverage, which becomes patchy in the other two test sites mostly due to the presence of clouds.

III. TOMOSAR ALGORITHMS

The TomoSAR data stacks have been processed by means of the standard F-SAR repeat-pass interferometric processing chain including focusing of the single-look complex images, calibration, co-registation, flat-Earth and terrain phase compensation, spectral shift filtering, and finally a two-step data-driven TomoSAR phase calibration to correct for residual baseline errors [17]. After calibration, the residual phase errors are within 10° (standard deviation) at L-band and 5° at P-band [17], well within the requirements for accurate TomoSAR imaging [24]. TanDEM-X DEM's have been used as topographic reference for focusing [17]. The main characteristics of the TomoSAR data are summarized in Tab. I.

A TomoSAR stack is composed by K images in N_P polarimetric channels (here, $N_P = 3$). The steering vector $\mathbf{a}(z)$ contains the height-dependent phase (difference) with respect to a generic height z for each of the tracks. Its $k-$th $(k = 1,\ldots,K)$ element is $[\mathbf{a}(z)]_k = \exp\{jk_{Z,k}z\}$, where $k_{Z,k}$ is the vertical wavenumber associated to the $k-$th image with respect to the reference (master) track.

For a fixed range-azimuth coordinate, the complete TomoSAR acquisitions are represented by the $N_P K-$dimensional vector $\mathbf{y}_P$ obtained by stacking the single-pol data vectors one on top of the other. The associated TomoSAR covariance matrix is denoted with $\mathbf{R}_P := E\{\mathbf{y}_P \mathbf{y}_P^H\}$, where

TABLE I
SUMMARY OF F-SAR DATA PARAMETERS

Frequency	L-band	P-band
Resolution Range × azimuth, m	1.92 × 0.64	3.84 × 2
[min, max] incidence angle, deg	[20, 50]	
Number of tracks	10	10
Max. vertical wavenumber, rad/m (at mid range)	0.66	0.22
Vert. resolution, m (at mid range)	~ 6.7	~ 20

$E\{\cdot\}$ indicates the statistical expectation operator. The estimation of the volume-only interferometric coherences and the ground and volume polarimetric covariances has been implemented assuming the validity of the Random-Volume-over-Ground (RVoG) model [3], [25], i.e. assuming that the volume-only reflectivity is but for a scaling factor the same across all polarimetric channels, and that the ground reflectivity is described by a Dirac-δ function. Thus, $\mathbf{R}_P$ is modelled as:

$$\mathbf{R}_P = \mathbf{C}_G \otimes \mathbf{\Gamma}_G + \mathbf{C}_V \otimes \mathbf{\Gamma}_V \,, \tag{2}$$

where "$\otimes$" denotes the Kronecker matrix product, $\mathbf{\Gamma}_G$ and $\mathbf{\Gamma}_V$ are the polarization-independent ground and volume interferometric coherence matrices, and $\mathbf{C}_G$ and $\mathbf{C}_V$ are the (k_Z-independent) ground and volume polarimetric covariance matrices, respectively. Under the Dirac-δ assumption, the ground-only coherence matrix becomes

$$\mathbf{\Gamma}_G = \mathbf{a}(z_G)\mathbf{a}^H(z_G) \,. \tag{3}$$

The $(l,m)-$th element of $\mathbf{C}_G$ and $\mathbf{C}_V$ is estimated as [26]:

$$\begin{bmatrix} [\mathbf{C}_G]_{l,m} \\ [\mathbf{C}_V]_{l,m} \end{bmatrix} = (\mathbf{U}^H \mathbf{W} \mathbf{U})^{-1} \mathbf{U}^H \mathbf{W} \hat{\mathbf{r}}_P^{(l,m)} \,, \tag{4}$$

where $\mathrm{vec}(\cdot)$ denotes the vectorization operator, $\mathbf{U} = [\mathrm{vec}(\mathbf{\Gamma}_G), \mathrm{vec}(\mathbf{\Gamma}_V)]$, $\hat{\mathbf{r}}^{(l,m)} = \mathrm{vec}(\hat{\mathbf{R}}_P^{(l,m)})$, with $\hat{\mathbf{R}}_P^{(l,m)}$ the $(l,m)-$th $K \times K$ block of the sample covariance estimate $\hat{\mathbf{R}}_P$ of $\mathbf{R}_P$, and $\mathbf{W} = (\hat{\mathbf{R}}_P^{(l,m)})^{-T} \otimes (\hat{\mathbf{R}}_P^{(l,m)})^{-1}$ is a weight matrix.

$\mathbf{\Gamma}_G$ and $\mathbf{\Gamma}_V$ must be estimated before the evaluation of (4). Concerning $\mathbf{\Gamma}_G$, it is sufficient to know the ground height z_G. In principle, z_G can be estimated from the TomoSAR data themselves. However, for consistency in the comparison, the LVIS DTM has been used. $\mathbf{\Gamma}_V$ has been estimated by applying the Sum-of-Kronecker-Product decomposition [25] and by using again z_G to regularize the estimation. A detailed description and discussion of the methodology is in [27].

Once $\mathbf{C}_G$ and $\mathbf{C}_V$ are estimated, classical Pol-InSAR contrast optimization can be used to find the polarimetric channel with the maximum and minimum ground-to-volume ratio $\mu_{\max}$ and $\mu_{\min}$ by solving the eigen-problem [28]:

$$\mathbf{C}_V^{-1} \mathbf{C}_G \mathbf{w} = \mu \mathbf{w} \,. \tag{5}$$

$\mu_{\max}$ and $\mu_{\min}$ correspond to the maximum and minimum eigenvalues μ, respectively, while the associated polarimetric channels $\mathbf{w}$ are given by the corresponding eigenvectors.

Finally, TomoSAR vertical profiles of the backscattered power have been estimated by using the Capon spectral estimator [29]. The volume-only Capon power profile $P_C(z)$ is obtained as:

$$P_C(z) = \frac{1}{\mathbf{a}^H(z) \mathbf{\Gamma}_V^{-1} \mathbf{a}(z)} \,. \tag{6}$$

The vertical super-resolution performance of the Capon spectral estimator is well known [29]-[31]. As an intrinsic consequence of super-resolution, the radiometric accuracy is penalized when it comes to volume scatterers [29], [30]. The heights of the vertical (reflectivity) profile peaks (i.e., maxima) are intuitively interpreted as the positions of the dominant (back-) scattering contributions, although a clear relationship to physical forest structure attributes is in general not a-priori given. In contrast, ground scattering as described by (3) is expected to appear as a peak close to z_G.

In the following, TomoSAR parameters and profiles have been estimated on square 20 × 20 m multilook cells associated to approximately 325 looks at L-band and more than 50 looks at P-band.

IV. VISIBILITY OF THE GROUND

The penetration through the canopy down to the ground at L- and P-band can be assessed by addressing the visibility of the ground. This can be performed by means of the ground-to-volume power ratio and/or by evaluating the localization accuracy of the ground height.

A. Analysis of the ground-to-volume ratios

The maximum ground-to-volume ratio $\mu_{\max}$ has been estimated with the algorithm outlined in Section III. The results obtained at both frequencies are shown in Fig. 5, together with the terrain slopes in range derived from the LVIS DTM. The dependency of $\mu_{\max}$ on the local slope is shown in Fig. 6. Positive slopes indicate a terrain inclination towards the radar, while negative slopes indicate an inclination away from the radar. As expected, at both frequencies $\mu_{\max}$ is in general smaller for negative slopes with no relevant variation with the off-nadir angle. For flat terrain (i.e. slopes around 0°), $\mu_{\max}$ becomes maximum as expected for a ground scattering component consisting of both surface and dihedral contributions. The highest $\mu_{\max}$ is achieved in near range and

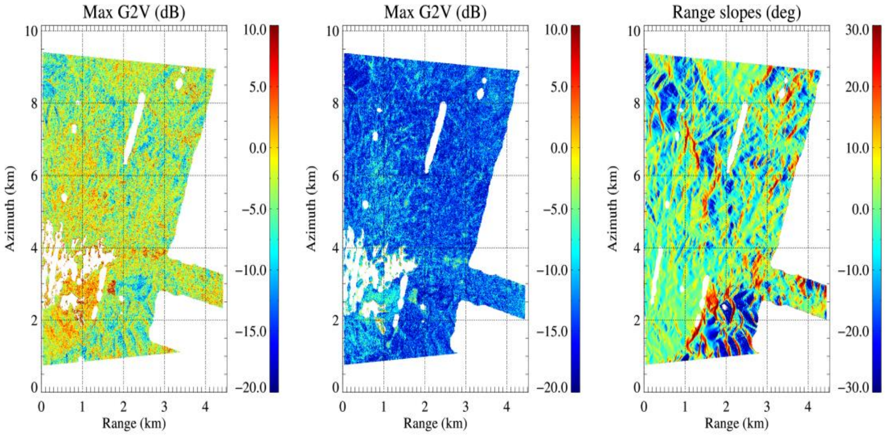

(a) (b) (c)

Fig. 5. Lopé: Maximum ground-to-volume ratio $\mu_{\max}$ over the LVIS coverage in the range-azimuth plane at (a) P-band and (b) L-band, and (c) terrain range slopes.

decreases when moving to far range as the path through the vegetation increases, progressively attenuating the dihedral component. For positive slopes, $\mu_{\max}$ gently decreases again, being about 2 dB higher in near range than in far range for slopes up to 15°. The trends are similar at both frequencies and reflect the modulation of $\mu_{\max}$ by the variation of the ground scattering power. At L-band the attenuation of the ground scattering by the volume is higher, resulting in $\mu_{\max}$ values of about 10 dB smaller in average than those at P-band.

In addition to $\mu_{\max}$ and $\mu_{\min}$, the ground-to-volume ratio in the HH (μ_{HH}) and the HV (μ_{HV}) channel have been estimated for all test sites, and the histograms for flat terrains are shown in Fig. 7. The effect of polarimetry becomes evident and appears consistent across all sites: it increases the ground-to-volume ratio range by more than 10 dB at both frequencies. At P-band, μ_{HH} and μ_{HV} differ by 5 dB (values measured at the histogram maxima), while $\mu_{\max}$ is greater than μ_{HH} by 3 dB. At L-band, the difference between μ_{HH} and μ_{HV} is only 1.5 dB, and $\mu_{\max}$ is by around 2 dB greater than μ_{HH}. At both frequencies, $\mu_{\min}$ is about 10 dB lower than μ_{HV}.

B. Localization of the ground

Next, the performance of estimating the ground location at L- and P-band is addressed. Similar to the ground estimation from the LVIS waveforms, where the ground is estimated as the location of the last returned pulse [1], [32], the ground location was estimated by detecting the peak corresponding to the ground scattering of the Capon profiles for $\mu_{\max}$. In order to reduce the probability of erroneously detecting a sidelobe in the TomoSAR profiles, only significant peaks, i.e. the ones with amplitude larger than 10% of the profile maximum and appearing within a meaningful height range, are considered. The TanDEM-X DEM has been used for defining the meaningful height range. The location of the ground is given by the lowest significant peak within the height interval $z_{DEM} - 50\text{ m} \le z \le z_{DEM} + 20\text{ m}$ where z_{DEM} is the TanDEM-X DEM height accounting for the fact that the associated X-band phase center is located closer to the canopy top than to the ground. The definition of the meaningful height range is rather relaxed and does not impose hard constraints on the used DEM. Alternatively, the phase center DEM derived from the TomoSAR data set itself can be used.

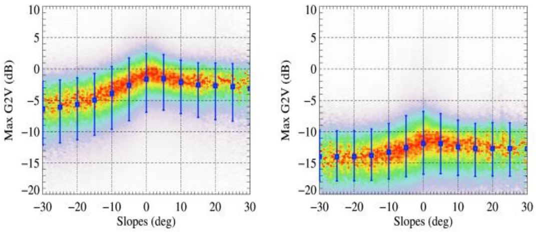

(a) (b)

Fig. 6. Lopé: variation of $\mu_{\max}$ at (a) P-band and (b) L-band as a function of terrain range slopes. For the selected values of slopes, the blue square symbols indicate mean values, while the vertical bars delimit the $\mu_{\max}$ interval where 75% of the estimates are found.

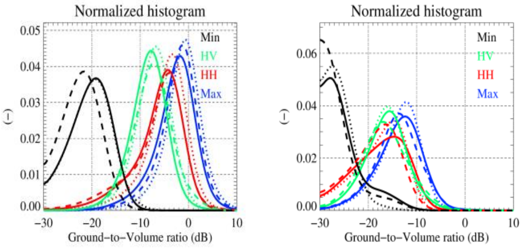

(a) (b)

Fig. 7. Histograms of the ground-to-volume ratios for all test sites and for different polarization channels at (a) P-band and (b) L-band. Continuous line: Lopé; dashed line: Rabi; dotted line: Mabounie.

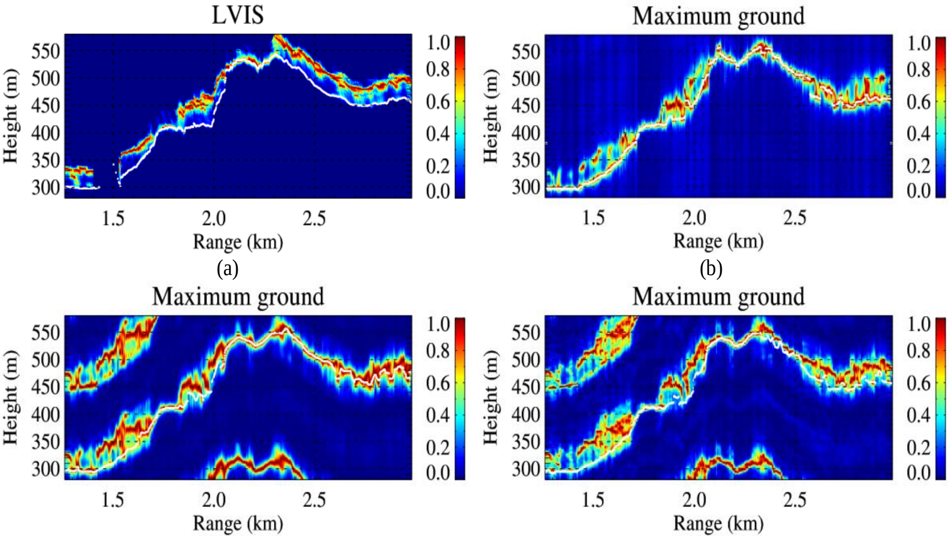

(a) (b)

(c) (d)

Fig. 8. Lopé: representative LVIS and TomoSAR Capon profiles (polarization channel with maximum ground) in presence of terrain slopes for a fixed azimuth coordinate and varying range coordinates. The LVIS profiles have been projected into the slanted radar geometry. Profile amplitudes have been normalized to the maximum of each coordinate. (a) LVIS profiles; (b) P-band; (c) L-band, with same vertical resolution as P-band; (d) L-band, full-track set. White line: estimated ground location.

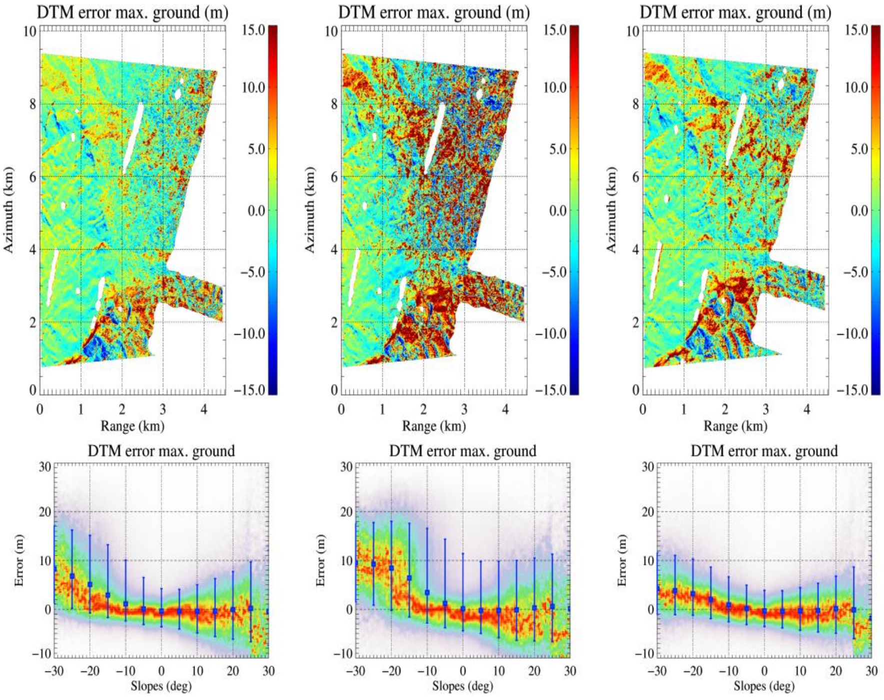

(a) (b) (c)

Fig. 9. Lopé: Ground estimation error vs LVIS ground at P- and L-band and for different vertical geometric resolutions. Columns from left to right: (a) P-band; (b) L-band, with same vertical resolution as P-band; (c) L-band, full-track set. Top panel: maps in the range-azimuth plane; bottom panel: distribution of the height estimation error as a function of terrain slopes. For the selected values of slopes, the blue square symbols indicate the mean values, while the vertical bars delimit the error interval where 75% of the estimates are found.

Fig. 8 shows representative TomoSAR Capon profiles for $\mu_{\max}$ in the range - height plane for a fixed azimuth coordinate at L- and P-band, and the corresponding LVIS waveforms projected into the slanted radar geometry. The selected area includes a transition from a flat to a hilly area with slopes changing from positive to negative. The estimated ground location is overplotted. A non-negligible volume backscattering is present in the $\mu_{\max}$ channel at both frequencies, although P-band presents the most powerful ground scattering [Fig. 8(b)], which is attenuated at L-band [Fig. 8(c)-(d)]. Consistently with the results in Fig. 6, the backscattered power of the ground relative to the volume

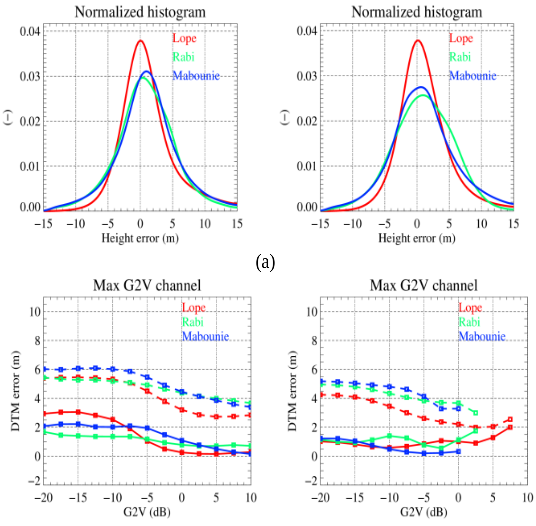

(a)

(b)

Fig. 10. TomoSAR ground estimation error across test sites with respect to the LVIS DTM in flat areas, (a) histograms; (b) mean value (continuous lines) and standard deviation (dashed lines) as a function of $\mu_{\max}$. For both (a) and (b), P-band is plotted on the left-hand side and L-band (full-track set) on the right-hand side.

TABLE II
GROUND ESTIMATION PERFORMANCE IN FLAT AREAS

Test site		Near range		Global	
		L-band	P-band	L-band	P-band
Lopè	Bias, m	0.03	0.01	0.16	0.23
	Std, m	2.87	3.09	3.86	4.18
Mabounie	Bias, m	-0.04	-0.20	0.07	0.21
	Std, m	3.57	4.35	4.63	4.77
Rabi	Bias, m	0.06	-0.13	0.08	-0.02
	Std, m	3.63	4.3	4.8	4.57

power is higher for the flat area. The estimated TomoSAR ground location at both frequencies is in good agreement with the LVIS one. The presence of slopes (especially negative ones) reduces the “visibility” of the ground. Due to the slanted geometry, the forest extension from the ground to the canopy top appears narrower in correspondence of negative slopes. The reduced $\mu_{\max}$ levels combined with the limited vertical TomoSAR resolution reduces the agreement between the ground locations estimated from the LVIS and the TomoSAR profiles. An increase of vertical resolution at L-band by using the full-track set apparently provides less biased estimates [Fig. 8(d)].

A quantitative interpretation of the profiles shown in Fig. 8 is given in Fig. 9 and Fig. 10. Fig. 9(a) and (b) show the ground height estimation error maps and their distribution as a function of the terrain slopes at L- and P-band for the Lopé test site. In order to ensure the same vertical resolution, first the reduced L-band data set (i.e. using only the first seven tracks with horizontal distances up to 40 m) has been processed. It is apparent that for non-negative slopes at P-band an accurate and unbiased ground estimate can be obtained with a standard deviation lower than 4 m in flat areas that increases in positive sloped terrain. This is partly due to the decrease of $\mu_{\max}$ (see Fig. 6), but also due to an increase of the geometric decorrelation. However, for negative slopes the ground height estimates are positive biased (even up to 10 m) and have a larger standard deviation. As already commented for Fig. 8, this loss in estimation performance is induced by the vertical shrinking of the volume scattering due to the slanted geometry and the limited vertical TomoSAR resolution. The same effect is observed moving from near to far range (see also Section II.B). At L-band, the ground estimation performance is in general confirmed to be worse than at P-band as a consequence of the lower $\mu_{\max}$ [see Fig. 9(b)]. The significant number of negative errors, i.e. cases where the TomoSAR estimated ground height is lower than the LVIS DTM, is caused by the misinterpretation of sidelobes. The error standard deviation is in general larger than 5 m.

As expected, the improvement in vertical resolution obtained by processing the L-band full-track set turns into an improved ground estimation performance, as shown in Fig. 9(c). The obtained estimation error and its behavior as a function of the terrain slope become now comparable to the P-band ones despite the large difference in $\mu_{\max}$. Moreover, the estimation bias at the negative slopes is reduced with respect to P-band due to the more favorable vertical resolution. The remaining bias is now around 5 m for slopes steeper than -15°.

Similar results have been obtained in the other test sites. In absence of significant slopes in Rabi and Mabounie, the assessment focuses only on flat areas where an LVIS DTM is available for comparison. The performance results are shown in Fig. 10(a) and the mean values and standard deviations are

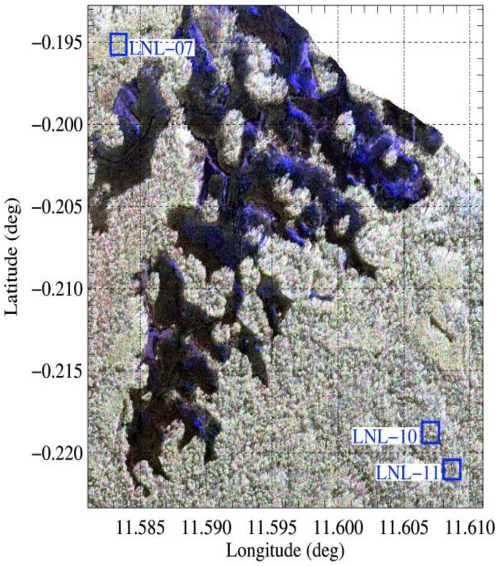

Fig. 11 Lopé: Location of the ground inventory plots (blue rectangles) used in the comparison of Fig. 11, overlaid on the L-band Pauli RGB composite image.

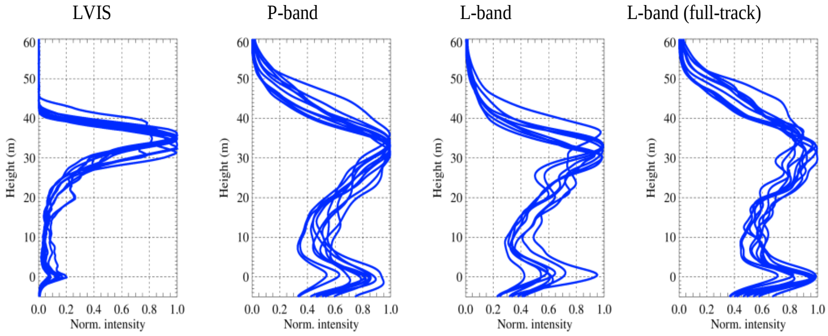

(a) Plot no. 1 (LNL-07)

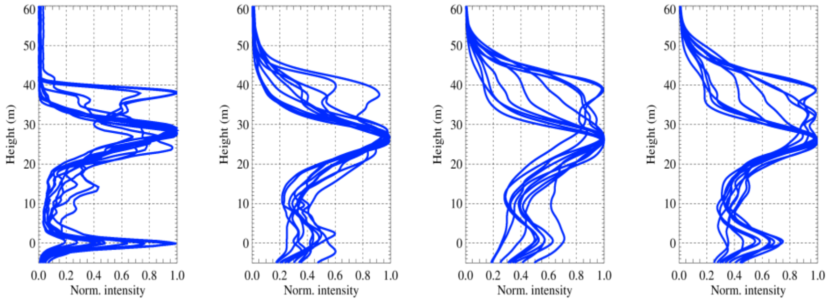

(b) Plot no. 2 (LNL-11)

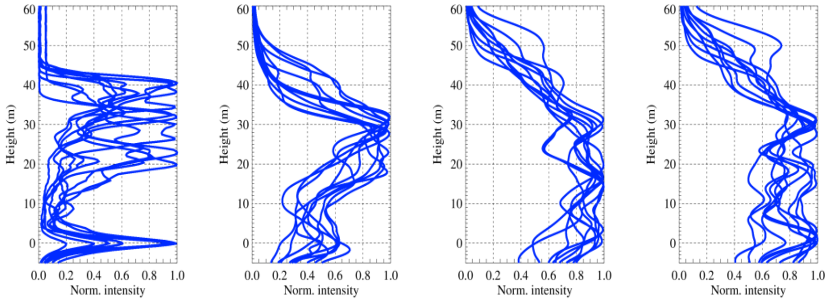

(c) Plot no.3 (LNL-10)

Fig. 12. Lopé: each row shows vertical profiles along the central longitude transect in three inventory plots. Columns from left to right: (1) LVIS profiles; (2) P-band TomoSAR profiles, (3) L-band profiles with same vertical resolution as P-band, and (4) L-band profiles with the full-track set. The ground height is at 0 m.

reported in Tab. II explicitly for all sites. The performance obtained at P- and L-band is in general comparable, with negligible estimation biases at both frequencies and an overall estimation accuracy of 3 to 5 m. The achieved standard deviation is slightly better in Lopé due to the shorter forest volumes in the other sites. At near range the ground estimation performance improves sensitively in agreement with the improved vertical TomoSAR resolution and the higher ground scattering level leading to a standard deviation between 3 and 4 m. Finally, in connection to the analysis in Section IV.A, the dependency of the ground estimation performance on $\mu_{\max}$ is investigated [see Fig. 10(b)]. Clearly, both the mean value and the standard deviation of the estimation error decrease with increasing $\mu_{\max}$. At L-band, however, they increase again especially in Lopé and for high $\mu_{\max}$ levels. This might be due to the low number of L-band cells with high $\mu_{\max}$, that may make the error statistics less reliable. In general, at high $\mu_{\max}$ levels the standard deviation reduces down to 2.5 m. For all test sites, an estimation bias lower than 1 m is obtained at P-band for $\mu_{\max} > 0$ dB. At L-band, the high vertical TomoSAR resolution of the full-track data set provides an estimation bias lower than 1 m for the whole $\mu_{\max}$ range (at least where the estimation performance can be evaluated reliably).

V. COMPARISON OF PROFILE-DERIVED FOREST 3-D STRUCTURE PARAMETERS

In this Section, TomoSAR profiles and LVIS waveforms are compared in terms of ability to distinguish 3-D forest structure variations within the same and across the different AfriSAR sites.

The TomoSAR Capon profiles are estimated from the separated volume-only coherence matrix $\boldsymbol{\Gamma}_V$ (see Section III). While at P-band the Capon profiles are estimated by using the full set of tracks, at L-band the full and the reduced 7-track set

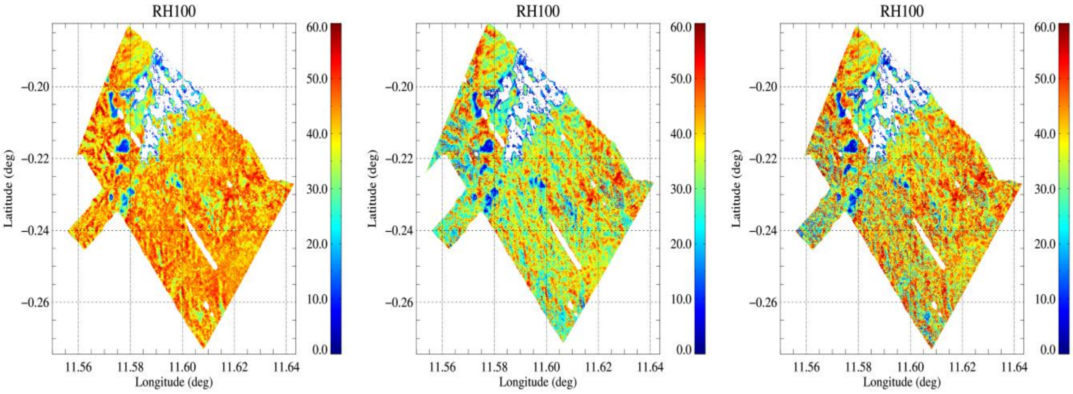

(a) (b) (c)

Fig. 13. Lopé: maps of RH100 in the longitude-latitude plane for (a) LVIS, (b) P-band, and (c) L-band (full-track set).

have been used in order to ensure a comparison between frequencies at the same vertical resolution.

It is worth remarking the significant geometric difference between a lidar waveform and the TomoSAR profiles. While the former is acquired in off-nadir geometry, the latter is estimated along the normal-to-slant-range direction and then projected onto the vertical height axis. For a better comparison, the TomoSAR profiles have been 3-D geocoded, i.e. for each vertical height the range-azimuth coordinates have been transformed into the same latitude and longitude grid as the LVIS profiles with a spacing of 10 m. The transformation is performed by means of pre-calculated look-up tables as described in [17].

In order to get a first impression of the sensitivity to different forest structure types, a total of 8 LVIS and TomoSAR profiles have been extracted every 10 m along a transect at mid latitude crossing three inventory plots in Lopé. The location of the plots is shown in Fig. 11, and the corresponding profiles are plotted in Fig. 12.

Plot no. 1 seems very homogeneous. The LVIS profiles have only a distinct maximum close to the top canopy height (40 m), probably due to the high attenuation. The TomoSAR profiles look similar with the strongest peak located slightly lower than in the LVIS profile. Furthermore, the lower attenuation at L- and P-band makes visible scattering contributions close to the ground (0 m).

On plot no. 2 the majority of the LVIS profiles have a pronounced maximum around 30 m. In addition, contributions (peaks) at lower and higher heights appear. The TomoSAR profiles behave similarly. However, the contributions closer to the tree tops are less pronounced and with gentler variations at P- than at L-band.

Finally, plot no. 3 appears highly heterogeneous. The LVIS profiles essentially change from one footprint to the next. The strongest contributions are located between 20 and 40 m. In the P-band profiles, instead, the peaks are distributed within a narrower height range. Contributions above this range are mostly very small. At L-band these contributions are more pronounced than at P-band. In addition, the L-band profiles reveal stronger contributions closer to the ground which are "invisible" at P-band. These peaks at 50 m visible in the L-band profiles are actually artifacts coming from the reduced sidelobe rejection capability of the Capon spectral estimator in presence of both irregular tracks and large volume decorrelation.

In summary, this first comparison indicated an increased sensitivity of the L- and P-band TomoSAR profiles to vegetation elements located below the main canopy and closer to the ground. Their contributions are weaker or even not given in the LVIS waveforms. L-band appears more sensitive to elements that are closer to the canopy top than P-band, but less sensitive to their spatial variation than the LVIS waveforms. These characteristics appear to be widely independent of the vertical TomoSAR resolution.

A. Comparison of relative height metrics

As already anticipated in Section II, the use of LVIS relative height measurements (RH) is quite common, and such metrics have been successfully used to relate to biomass and forest structure [2]. This is particularly true for the so-called HOME (Height Of Median Energy), i.e. the RH50 [1].

For comparison, we calculated the RH metrics for the (volume-only) TomoSAR profiles. It is important to note here that in the TomoSAR case the effective noise floor is not so much due to the noise level in the SAR data (that is given by the Noise Equivalent Sigma Zero NESZ level), but much more to the sidelobes of the tomographic impulse response. In turn, the sidelobe level in a profile depends on the track distribution, the tomographic imaging algorithm used and the volume coherences. Accordingly, for the TomoSAR profiles the following ad-hoc procedure has been implemented for the estimation of the RH heights. For each profile, the tallest peak with amplitude greater than 10% of the maximum peak has been identified. Then, the height above the highest peak at which the amplitude decreases by 3 dB is defined as RH100. Finally, the amplitudes between the ground height and the so-defined RH100 have been cumulated, and the other RH metrics have been calculated accordingly. In order to avoid any additional degree of uncertainty, the resulting heights have been referred to the LVIS DTM.

The obtained LVIS and L- and P-band TomoSAR RH100 maps for the Lopé site are plotted in Fig. 13. A certain agreement between them is apparent. However the radar RH100 values are lower as a consequence of the reduced

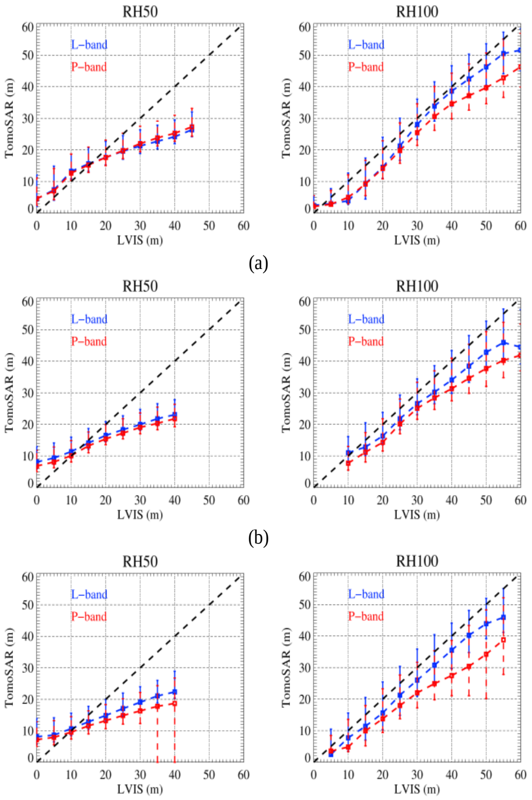

(a)

(b)

(c)

Fig. 14. Comparison of RH50 and RH100 at L- (full-track set) and P-band against the same LVIS metrics in (a) Lopé, (b) Mabounie, (c) Rabi. The square symbols indicate mean values, while the vertical bars delimit the height interval where 75% of the RH estimates are found.

sensitivity to the top canopy elements. The differences have been quantified statistically in Fig. 14. Depending on the site, the L-band RH100 is about 5 to 10 m lower than the LVIS one, while the P-band RH100 can be even 10 m lower than at L-band.

Fig. 14 compares also the TomoSAR and the LVIS HOME. For all sites, the TomoSAR HOME is noticeably lower (up to 20 m) than the LVIS HOME. More interestingly, the L- and P-band HOME share the same mean values: differences are in the order of few meters. A situation of this kind is depicted in some of the profiles of Fig. 12. This might be a consequence of an increased sensitivity at L-band to smaller vegetation elements in the understory. However, residual ground scattering contributions may also appear in the L-band profiles, as the ground scattering could be less polarized at L- than at P-band. These two effects are however difficult (if not impossible) to be separated by using the profiles only. Note that the TomoSAR RH metric closer to a fixed LVIS HOME may vary. For instance, fixed LVIS HOME equal to 20 m, the L-band RH metrics in the interval [RH45, RH65] provide the best fitting in around 50% of cases. For LVIS HOME equal to 30 m, the best-fitting TomoSAR RH interval moves to [RH60, RH80]. The TomoSAR RH100 can be the one closest to the LVIS HOME for a non-negligible number of cases. These trends are essentially the same across test sites. In contrast, a certain dependency on the frequency has been observed.

Before concluding this analysis, three remarks are in order. Firstly, the L-band results in Figs. 13 and 14 have been derived from the full set of tracks. However, this improvement in vertical resolution (with respect to the reduced set of tracks) has only a minor impact on the analysis and does not change the main conclusions. Secondly, the radiometric accuracy of the Capon beamformer is not optimized for volumes. Therefore, we also calculated the RH metrics by applying the procedure outlined above to the Fourier-based beamforming profiles [29], [30], that allows a more accurate radiometric reconstruction at the cost of a reduced vertical resolution compared to the Capon reconstruction. Interestingly, the RH metrics (which express a cumulated, thus low resolution, radiometry) show no relevant changes. Finally, the LVIS RH metrics include the ground return, while the ground has been compensated as much as possible in the TomoSAR profiles. It is expected that a ground cancellation in the LVIS waveforms will increase the height of the RH metrics derived and thus the difference to the TomoSAR ones. However, this will not change the conclusions of the comparison substantially.

B. Comparison of 3-D vertical structure descriptors

The objective of this Section is to compare the different 3-D reconstructions with respect to their ability to describe physical vertical forest structure. In addition to a rather qualitative assessment across the different sites, the main emphasis will be on the Rabi test site where the 25 ha inventory plot allows the validation of the vertical forest structure descriptors against field data.

Physically, forest structure is linked to the 3-D size, location and arrangement of trees, trunks and branches in a forest [33], [34]. However, appropriate descriptors for vertical forest structure reflecting tree size variability in an unambiguous way are still missing today in ecology and forestry. Indices as the Shannon Index or the standard deviation of tree heights [35] have been used to express vertical forest structure both based on tree height that is usually not measured in situ, but estimated from the measured tree dbh. In order to reduce the additional and often large uncertainties introduced by the estimation of tree height from dbh, the standard deviation of tree dbh which reflects as well tree size variability [36] can be used instead, and the vertical structure index becomes:

$$VS_{field} := \mathrm{std}\left(\left\{\mathrm{dbh}\right\}\right), \qquad (7)$$

where $\left\{\mathrm{dbh}\right\}$ is the ensemble of diameter at breast height of all the trees included in the structure window and $\mathrm{std}(\cdot)$ is the standard deviation operator. The so-defined vertical structure index VS_{field} appears to be more sensitive to successional stages than the indices relying on height diversity only [34].

Aiming to establish a vertical structure index VS derived from the reconstructed TomoSAR or LVIS profiles consistent with the definition of VS_{field}, an approach based on the distribution of the peaks of the reconstructed profiles has recently been proposed [15], [37]. After the extraction of the peaks of all the profiles within a chosen structure window,

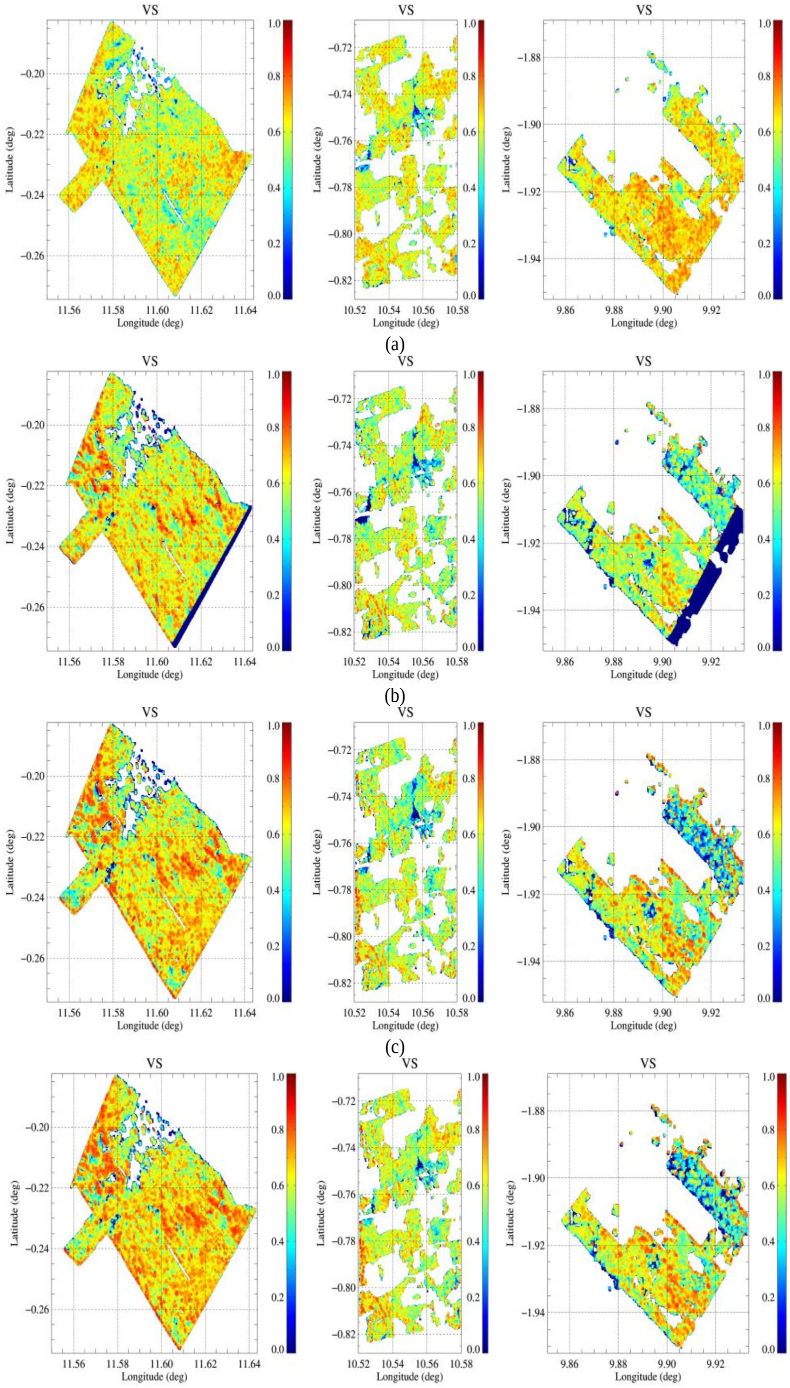

(a)

(b)

(c)

(d)

Fig. 15. Maps of vertical forest structure at 100 × 100 m scale for (a) LVIS profiles, (b) P-band profiles, (c) L-band profiles, (d) L-band profiles with full-track set. From left to right: (1) Lopé, (2) Mabounie, (3) Rabi.

denoting with $Z_P = \{z_{p_1}, z_{p_2}, \dots, z_{p_M}\}$ the set of M unique heights at which these peaks appear, VS is defined as:

$$VS := M \operatorname{var}(Z_P), \tag{8}$$

where $\operatorname{var}(\cdot)$ denotes the variance of a set of values. Note that in case two or more peaks appear at the same height the number of heights in Z_P is smaller than the number of peaks. The vertical structure index of equation (7), similar to most physical forest structure descriptors in forestry and ecology, rely on individual tree parameters: single tree measurements (in the case of (7) single tree dbh measurements) are used to

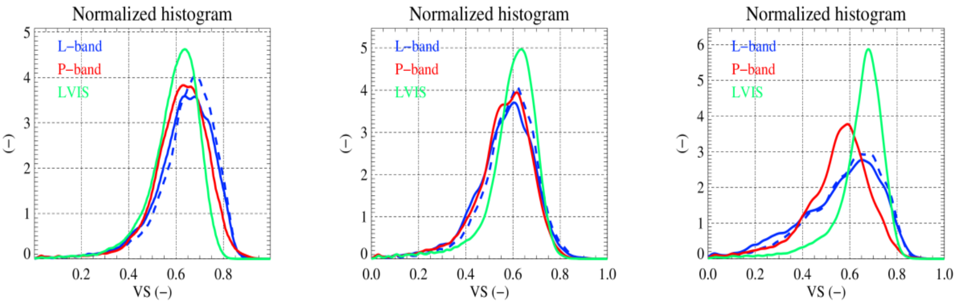

(a) (b) (c)

Fig. 16. Histograms of vertical forest structure indices estimated in (a) Lope, (b) Mabounie and (c) Rabi. Dashed lines refer to the L-band data set with full-track set.

estimate plot level parameters as basal area, species composition and / or stand density on plot level and use these to derive the different structure indices. Equation (8) aims to reflect the same structure information as in (7), but accounts for the fact that conventional SAR configurations are not able - in terms of spatial resolution - to distinguish single trees, making a direct correspondence to (7) not possible. Equation (8) assumes the physical significance of reflectivity peaks, implying that the 3D distribution of reflectivity peaks reflects the variability in the distribution of trees within the stand. This assumption is not per se valid at all frequencies and / or spatial scales, but is supported by a number of models and experiments in the literature [9], [38]. Indices similar to VS have been employed in past works for lidar full waveforms [39] as well.

The vertical structure descriptor VS in (8) has been calculated by considering the profile peaks within a 100 × 100 m (sliding) structure window. Since profiles are spaced 10 m apart, each structure window contains 100 profiles. However, remembering that the actual profile horizontal resolution is 20 m, VS is calculated by aggregating information from 25 statistically independent cells. A smaller window would reduce the statistical validity of the number of independent cells, while a larger window could provide biased values of VS and VS_{field} as different structure types would be mixed together, and therefore lose ecological significance. Without loss of generality, the estimated VS are normalized to the overall common maximum across the three sites and the different sensors. Thus, VS is 0 for a vertically homogeneous stand, while it is 1 for a heterogeneous stand. The maps of VS derived from the LVIS and the TomoSAR profiles for the three sites are shown in Fig. 15. The histograms of the vertical structure indices for each of the sites are shown in Fig. 16. The fact that each of the sites itself is not uniform in terms of vertical structure, but consists of a diversity of forest stands, reduces the significance of a direct comparison. However, it can be observed that higher vertical structure descriptors are obtained, as expected, from the TomoSAR profiles in Lope and Rabi than in Mabounie, at least at for LVIS and at L-band. It can also be observed that the sensitivity to vertical structures is higher at L-band than at P-band.

Focusing now on the ground measurement plot area in Rabi, Fig. 17 shows the distribution of peaks along a transect crossing the plot. For the LVIS profiles, most of the peaks appear within 20 to 45 m, while peaks below 20 m are rather seldom. On the other hand, the TomoSAR peaks at L- as well as at P-band are distributed across the whole canopy extent down to the ground. The peaks from the P-band TomoSAR profiles are particularly numerous closer to the ground level. Occasionally, gaps in the canopy layer become visible at P-band which are not noticeable at L-band or in the LVIS profiles.

The VS maps derived by means of (8) from the profile peaks within a 100 × 100 m (sliding) window and the VS_{field} map derived from the field data by means of (7) are shown in Fig. 18. It can be seen that all maps highlight an area of high vertical structure at the south eastern part of the site, which is the mean feature in the plot. Note that slight shifts in the position of this area in the maps result from the different viewing geometry of the configurations employed. More to the North, another high structure area is indicated in the map derived from the field data. This feature is also visible in the LVIS map and in the L-band map with the high(er) vertical resolution, while it becomes hardly visible at the P-band and in the L-band map with lower vertical resolution. This is also reflected on the histograms of the five vertical forest structure indices for the plot area shown also in Fig. 18. The index derived from the L-band TomoSAR data shows the widest range of structure values compared to the P-band and the LVIS derived maps. Finally, only the map derived from the L-band data set with the high(er) vertical resolution seems appropriate to reconstruct the full range and distribution of structure indices obtained from the field data. The reduced range of the LVIS vertical structure descriptor is due to the lower penetration of LVIS into the vegetation layer. Due to the increased vertical resolution, LVIS profiles are more sensitive than TomoSAR reflectivity profiles to variations mostly concentrated in the highest part of the canopy. However, radar systems are more sensitive to variations of vertical structure when these are driven by the presence of sub-canopy elements.

VI. CONCLUSIONS

In this paper, an assessment of the information content of L- and P-band TomoSAR data in terms of forest structure for three tropical forest sites located in Gabon was attempted. The

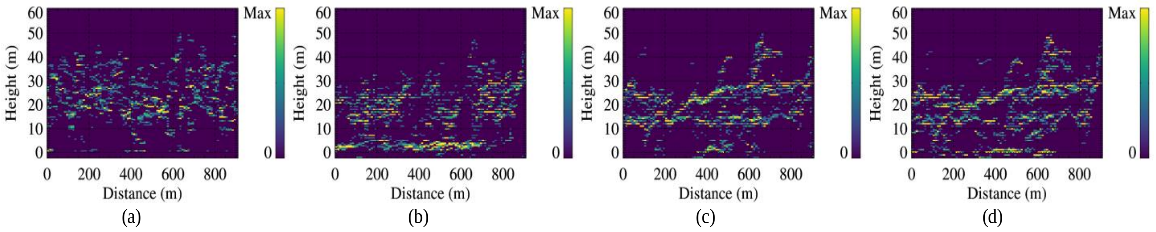

Fig. 17. Peaks of the profiles in a transect across the 25 ha plot in Rabi for (a) LVIS and TomoSAR reflectivity profiles at (b) P-band, (c) L-band (reduced track set), and (d) L-band with full-track set.

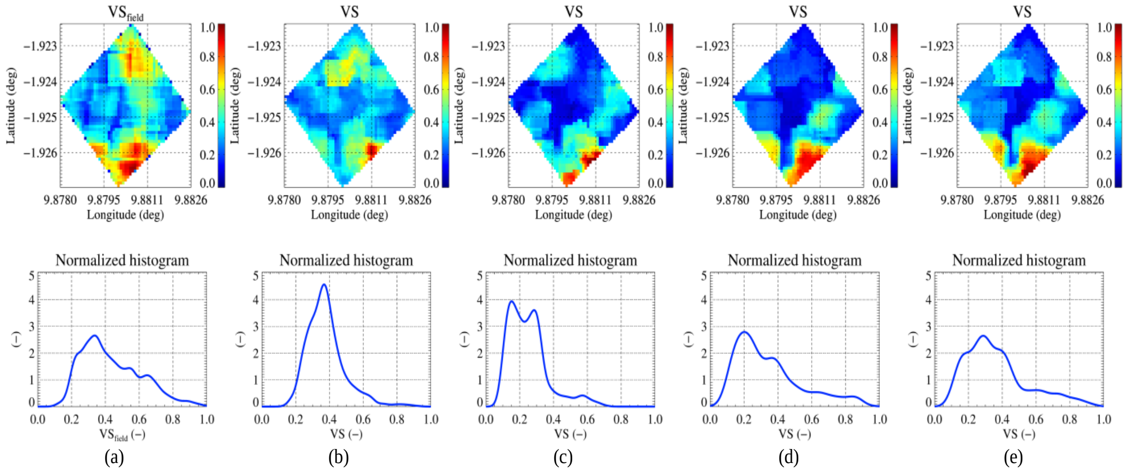

Fig. 18. Maps of vertical structure at 100m × 100m scale (top row) and related histograms (bottom row) at the test site in Rabi from (a) field data, (b) LVIS and TomoSAR reflectivity profiles at (c) P-band, (d) L-band (reduced track set), and (e) L-band with full-track set.

L- and P-band TomoSAR data were also compared to lidar waveform data. All data have been acquired during the AfriSAR campaign in 2016.

The penetration through the canopy at L- and P-band has been assessed by investigating the visibility of the ground. This has been performed by characterizing the behavior of the ground-to-volume ratio as a function of terrain slope and off-nadir angle as well as across the different polarization channels, and by evaluating the estimation accuracy of the underlying ground location.

It has been seen that the variation with polarization of the ground-to-volume ratio at L-band is much lower than at P-band due to the higher attenuation of the vegetation volume, yet providing a valuable polarimetric optimization space. The variation of the maximum ground-to-volume ratio as a function of the range terrain slopes appears to be dominated by changes of the ground scattering power. A still significant ground scattering component is present at L-band despite the much higher attenuation of the vegetation than at P-band. This is in agreement with results obtained in similar forest conditions [5].

The performance in the estimation of the location of the ground using the Capon TomoSAR profiles with respect to the LVIS DTM has been evaluated. As expected, for a fixed number of looks, the ground estimation performance increases with increasing ground-to-volume ratio and with improving vertical TomoSAR resolution. Accordingly, P-band benefits from the higher ground-to-volume ratio levels while L-band needs a higher vertical resolution to reach a similar performance. The ground could be localized in the Capon profiles with a standard deviation of 2 to 5 m consistently across all three sites. A strong performance dependency on the terrain slope and the off-nadir angle has been demonstrated with negative slopes to be particularly critical due to the low(er) ground-to-volume ratio levels as well as the unfavorable geometry. It is worth remarking that an accurate estimate of the ground (sub-canopy) topography is also important to compensate for topographic variations that can bias the evaluation of forest structure parameters at a given (larger) scale. In this regard, better performing algorithms can be developed to estimate the ground height and relax the need of large(r) baselines.

The ability and complementarity of TomoSAR L- and P-band profiles and LVIS waveforms to distinguish among different tropical forest structure types has been addressed. The analysis of the TomoSAR RH100 indicated that L-band is definitely more sensitive than P-band to the top vegetation layer, although it does not reach the LVIS sensitivity. Furthermore, the performance to derive physical forest structure descriptors has been evaluated over a 1 ha scale. For this, vertical structure indices derived from the volume-only 3-D radar reflectivity at L- and P-band and from the LVIS profiles have been compared against each other. Although a direct comparison across test sites was made difficult by the high diversity of forest structure, the results indicate that at L-band the sensitivity to vertical structure is in general higher than at P-band. For the ForestGEO plot within the Rabi site, the vertical structure descriptor could also be derived from the ground inventory measurements and compared to the lidar- and radar-derived descriptors. The reduced penetration of LVIS reduces also the range of distinguishable vertical structures to the ones that exhibit profile variations mostly close to the top of the canopy. In contrast, the L-band TomoSAR profiles show the widest range of structure values. This is not only an effect of the increased penetration, but also a matter of sensitivity to significant structure elements. At P-band the reconstructed structure range is narrower. Finally, at L-band an increased vertical resolution seems crucial for mapping the full range and distribution of structure indices obtained from the field data.

ACKNOWLEDGEMENT

Laser Vegetation and Ice Sensor (LVIS) data sets were provided by the team in the Laser Remote Sensing Branch at NASA Goddard Space Flight Center with support from the University of Maryland, College Park. The authors would like to thank the F-SAR team for its invaluable effort during the campaign operation and the data processing.

REFERENCES

[1] J. B. Drake, R. O. Dubayah, D. B. Clark, R. G. Knox, J. B. Blair, M. A. Hofton, R. L. Chazdon, J. F. Weishampel, S. D. Prince, “Estimation of tropical forest structure characteristics using large-footprint lidar,” *Remote Sensing of the Environment*, vol. 79, no. 2-3, pp. 305-319, Feb. 2002.

[2] R. O. Dubayah, S. L. Sheldon, D. B. Clark, M. A. Hofton, J. B. Blair, G. C. Hurtt, R. L. Chazdon, “Estimation of tropical forest height and biomass dynamics using lidar remote sensing at La Selva, Costa Rica,” *Journal of Geophysical Research*, vol. 115, 2010.

[3] K. Papathanassiou, S. Cloude, “Single-baseline polarimetric SAR interferometry,” *IEEE Trans. Geosci. Remote Sens.*, vol. 39, no. 11, pp. 2352-2363, Nov. 2001.

[4] A. Reigber, A. Moreira, “First demonstration of airborne SAR tomography using multibaseline L-band data,” *IEEE Trans. Geosci. Remote Sens.*, vol. 38, no. 5, pp. 2142-2152, Sept. 2000.

[5] I. Hajnsek, F. Kugler, S. K. Lee, K. Papathanassiou, “Tropical-forest-parameter estimation by means of Pol-InSAR: The INDREX-II Campaign,” *IEEE Trans. Geosci. Remote Sens.*, vol. 47, no. 2, pp. 481-493, Feb. 2009.

[6] S. K. Lee, F. Kugler, K. Papathanassiou, I. Hajnsek, “Quantification of temporal decorrelation effects at L-band for polarimetric SAR interferometry applications,” *IEEE Journal Sel. Topics Applied Earth Obs. Remote Sens.*, vol. 6, no. 3, pp. 1351-1367, Mar. 2013.

[7] F. Kugler, S. K. Lee, I. Hajnsek, K. Papathanassiou, “Forest height estimation by means of Pol-InSAR data inversion: The role of the vertical wavenumber,” *IEEE Trans. Geosci. Remote Sens.*, vol. 53, no. 10, pp. 5294-5311, Oct. 2015.

[8] F. Kugler, D. Schulze, I. Hajnsek, H. Pretzsch, K. Papathanassiou, “TanDEM-X Pol-InSAR performance for forest height estimation,” *IEEE Trans. Geosci. Remote Sens.*, vol. 52, no. 10, pp. 6404-6422, Oct. 2014.

[9] O. Frey, E. Meyer, “Analyzing tomographic SAR data of a forest with respect to frequency, polarization, and focusing techniques,” *IEEE Trans. Geosci. Remote Sens.*, vol. 49, no. 10, pp. 3648-3659, Oct. 2009.

[10] S. Tebaldini, F. Rocca, “Multibaseline polarimetric SAR tomography of a boreal forest at P- and L-bands,” *IEEE Trans. Geosci. Remote Sens.*, vol. 50, no. 1, pp. 232-246, Jan. 2012.

[11] M. Mariotti d’Alessandro, S. Tebaldini, F. Rocca, “Phenomenology of ground scattering in a tropical forest through polarimetric synthetic aperture radar tomography,” *IEEE Trans. Geosci. Remote Sens.*, vol. 51, no. 8, pp. 4430-4437, Aug. 2012.

[12] D. Ho Tong Minh, T. Le Toan, F. Rocca, S. Tebaldini, M. Mariotti d’Alessandro, L. Villard, “Relating P-band synthetic aperture radar tomography to tropical forest biomass,” *IEEE Trans. Geosci. Remote Sens.*, vol. 52, no. 2, pp. 967-979, Feb. 2014.

[13] M. Pardini, A. Cantini, F. Lombardini, K. Papathanassiou, “3-D structure of forests: First analysis of tomogram changes due to weather and seasonal effects at L-band,” *Proc. 10th European Conf. Synthetic Aperture Radar*, Berlin, Germany, pp. 48-51, Jun. 2014.

[14] M. Tello Alonso, V. Cazcarra Bes, K. Papathanassiou, “Assessment of forest structure estimation by means of SAR tomography: Potential and limitations,” *Proc. of 2016 IEEE Int. Geosci. Remote Sens. Symp.*, IGARSS 2016, Beijing, China, pp. 32-35, Jul. 2016.

[15] V. Cazcarra Bes, M. Tello Alonso, R. Fischer, M. Heym, K. Papathanassiou, “Forest structure dynamics by means of L-band SAR tomography,” *Remote Sensing*, 9(12), 1229, Nov. 2017.

[16] P. C. Dubois-Fernandez, T. Le Toan, S. Daniel, H. Oriot, J. Chave, L. Blanc, L. Villard, M. W. J. Davidson, M. Petit, “The TropiSAR airborne campaign in French Guiana: Objectives, description, and observed temporal behavior of the backscatter signal,” *IEEE Trans. Geosci. Remote Sens.*, vol. 50, no. 8, pp. 3228-3241, Aug. 2012.

[17] I. Hajnsek, M. Pardini, M. Jäger, R. Horn, J. S. Kim, H. Jörg, K. Papathanassiou, P. Dubois-Fernandez, X. Dupuis, V. Wasik, S. Lewis, N. Labriere, L. Villard, T. Koleck, *Technical assistance for the development of airborne SAR and geophysical measurements during the AfriSAR campaign*, Final technical report, ESA contract no. 4000114293/15/NL/CT. Available at: https://earth.esa.int/documents/10174/134665/AfriSAR-Final-Report.

[18] M. Hofton, J. Blair, D. Rabibe, C. Brookes, H. Cornejo, “Canopy height and structure measurements of Gabon from medium footprint waveform lidar,” *Proc. of 2017 IEEE Int. Geosci. Remote Sens. Symp.*, IGARSS 2017, Fort Worth, TX, U.S.A., pp. 4294-4295, Jul. 2017.

[19] T. Le Toan, S. Quegan, M. J. W. Davidson, H. Baltzer, P. Paillou, K. Papathanassiou, S. Plummer, F. Rocca, S. Saatchi, H. Shugart, L. Ulander, “The BIOMASS mission: Mapping global forest biomass to better understand the terrestrial carbon cycle,” *Remote Sensing of Environment*, vol. 115, issue 11, pp. 2850-2860, 2011.

[20] P. Rosen, Y. Kim, R Kumar, T. Misra, R. Bhan, V. Raju Sagi, “Global persistent SAR sampling with the NASA-ISRO SAR (NISAR) mission,” *Proc. of 2017 IEEE Radar Conf.*, RadarConf 2017, Seattle, WA, USA, May 2017.

[21] A. Moreira, G. Krieger, I. Hajnsek, K. Papathanassiou, M. Younis, P. Lopez Dekker, S. Huber, M. Villano, M. Pardini, M. Eineder, F. De Zan, A. Parizzi, “Tandem-L: A highly innovative bistatic SAR mission for global observation of dynamic processes on the Earth’s surface,” *IEEE Geosci. Remote Sens. Magazine*, vol. 3, Issue 2, pp. 8-23, Jun. 2015.

[22] R. Dubayah, “The Global Ecosystem Dynamics Investigation (GEDI) lidar,” *Proc. of 1st BIOMASS Science Workshop*, Frascati, Italy, Jan. 2015.

[23] M. Pardini, K. Papathanassiou, “Spaceborne SAR tomography over forests: Performance and trade-offs for repeated single pass polinsar acquisitions,” *Proc. of 2015 IEEE Int. Geosci. Remote Sens. Symp.*, IGARSS 2015, Milan, Italy, pp. 1551-1554, Jul. 2015.

[24] S. Tebaldini, F. Rocca, M. Mariotti D’Alessandro, L. Ferro-Famil, “Phase calibration of airborne tomographic SAR data via phase center double localization,” *IEEE Trans. Geosci. Remote Sens.*, vol. 54, no. 3, pp. 1775-1792, Mar. 2016.

[25] S. Tebaldini, “Algebraic synthesis of forest scenarios from multibaseline PolInSAR data,” *IEEE Trans. Geosci. Remote Sens.*, vol. 47, no. 12, pp. 4132-4142, Dec. 2009.

[26] B. Göransson, B. Ottersten, “Direction estimation in partially unknown noise fields,” *IEEE Trans. Sig. Proc.*, vol. 47, no. 9, pp. 2375-2385, Sept. 1999.

[27] M. Pardini, K. Papathanassiou, “On the estimation of ground and volume polarimetric covariances in forest scenarios with SAR tomography,” *IEEE Geosci. Remote Sens. Lett.*, vol. 14, no. 10, pp. 1860-1864, Oct. 2017.

[28] S. Cloude, K. Papathanassiou, “Three-stage inversion process for polarimetric SAR interferometry,” *IEE Proc. – Radar Sonar Navig.*, vol. 150, no. 3, 125- 134, Jun. 2003.

[29] F. Lombardini, A. Reigber, “Adaptive spectral estimation for multibaseline SAR tomography with airborne L-band data,” *Proc. of 2003 IEEE Int. Geosci. Remote Sens. Symp.*, IGARSS 2003, Toulouse, France, pp. 2014-2016, Jul. 2003.

[30] P. Stoica, J. Li, X. Tan, “On spatial power spectrum and signal estimation using the Pisarenko framework,” *IEEE Trans. Signal Proc.*, vol. 56, no. 10, pp. 5109-5119, Oct. 2008.

[31] P. Stoica, R. Moses, *Spectral Analysis of Signals*, Prentice Hall, 2005.

[32] M. A. Hofton, J. B. Minster, J. B. Blair, "Decomposition of laser altimeter waveforms," *IEEE Trans. Geosci. Remote Sens.*, vol. 38, no. 4, pp. 1989-1996, Jul. 2000.

[33] M. Snyder, "What is forest stand structure and how is it measured?," *Northern Woodlands*, issue no. 64, p. 15, Mar. 2010.

[34] T. A. Spies, "Forest Structure: A Key to the Ecosystem," *Northw. Scien.*, vol. 72, special issue no. 2, pp. 34-36, Feb. 1998.

[35] I. Barbeito, F. Montes, I. Canellas, "Evaluating the behavior of vertical structure indices in Scots pine forests," *Annals of For. Science*, vol. 66, no. 710, pp. 1-10, 2009.

[36] C. McElhinny, P. Gibbons, C. Brack, J. Bauhus, "Forest and woodland stand structural complexity: Its definition and measurement," *Forest Ecology and Manag.*, vol. 218, issues 1-3, pp.1-24, 2005.

[37] M. Tello, V. Cazcarra-Bes, K. Papathanassiou, "Forest structure characterization from SAR tomography at L-band," *submitted to IEEE Journal Sel. Topics Applied Earth Obs. Remote Sens.*, Nov. 2017.

[38] M. Brolly, I. H. Woodhouse, "Vertical backscatter profile of forests predicted by a macroecological plant model," *Int. Journal Remote Sens,*, vol. 34, no. 4, pp. 1026-1040, 2013.

[39] A.S. Whitehurst, A. Swatantran, J. B. Blair, M. A. Hofton, R. Dubayah, "Characterization of canopy layering in forested ecosystems using full waveform lidar," *Remote Sensing, 5*(4), 2014-2036, Apr. 2013.

Curriculum Vitae

Personal Information

Name: Víctor Cazcarra Bes
Date of birth: 18th June 1985
Place of birth: Barcelona, Spain
Institution: German Aerospace Center (DLR)
Microwaves and Radar Institute (HR)
Address: Münchener Str. 20, 82234 Weßling, Germany
Email: victor.cazcarrabes@dlr.de; victor.cazcarra@gmail.com

Education

2014 - 2019	Doctor Degree ETH, Institute of Environmental Engineering, Zürich (Switzerland) Thesis: *Forest Structure Characterization from SAR Tomography*
2007 - 2010	Master of Science in Telecommunication engineering University Miguel Hernández of Elche, Elche (Spain) Thesis: *Extension of an electromagnetic model of rice crops in remote sensing application in polarimetric SAR systems* DOI:10.13140/RG.2.2.35690.72644
2003 - 2007	Bachelor of Science in Telecommunication Technical Engineer University of Alicante, Alicante (Spain) Thesis: *Amplitude calibration of SAR images from ERS and Envisat satellites* DOI:10.13140/RG.2.2.22268.95363

Work experience

10/2009 - 11/2010	Scholarship University of Alicante, Alicante, Spain. Development of an electromagnetic model of rice crops.
05/2011 - 07/2011	IT consultant Newshore, Barcelona, Spain. Software development in PHP & SQL for web applications.
07/2011 - 07/2012	Junior engineer Indra, Barcelona, Spain. Software development in C/C++ for ticket transport validation.
11/2012 - 02 /2014	Research engineer Starlab, Barcelona, Spain. Development of an end-to-end satellite mission simulator.
Since 07/2014	PhD candidate and Research scientist German Aerospace Center (DLR), Oberpfaffenhofen, Germany. Forest applications with SAR tomography.

Courses

- International Summer School on Radar/SAR - Fraunhofer FHR,July 2013, Bonn, Germany.
- SAR Principles and Application - Carl-Cranz-Gesellschaft e.V. (CCG), October 2014, Oberpfaffenhofen, Germany.
- Advanced Course on Radar Polarimetry, ESA ESRIN, January 2015, Frascati, Italy.
- Spatial Diversity Imaging Systems, tutorial on the European Conference on Synthetic Aperture Radar conference, June 2016, Hamburg, Germany.
- Machine Learning in Remote Sensing, tutorial on the European Conference on Synthetic Aperture Radar conference, June 2018, Aachen, Germany.
- Earth Observation Big Data Intelligence: theory and practice of deep learning and big data mining, Tutorial on the International Geoscience and Remote Sensing Symposium, July 2018, Valencia, Spain

Peer-reviewed publications

First author

1. V. Cazcarra-Bes, M. Tello-Alonso, R. Fischer, M. Heym, K. Papathanassiou, "Monitoring of forest structure dynamics by means of L-band SAR tomography," *Remote Sensing*, vol. 9, no. 12, p. 1229, 2017. DOI:10.3390/rs9121229
2. V. Cazcarra-Bes, M. Pardini, M. Tello-Alonso, K. Papathanassiou, "Comparison of Tomographic SAR Reflectivity Reconstruction Algorithms for Forest Applications at L-band," *IEEE Transactions on Geoscience and Remote Sensing*, vol. 58, no. 1, pp. 147-164, Jan. 2020. DOI: 10.1109/TGRS.2019.2934347
3. V. Cazcarra-Bes, M. Pardini, K. Papathanassiou, "Optimization of Tomographic SAR Configurations for Forest Structure Applications at L-band," *IEEE Geoscience and Remote Sensing Letters*. Submitted in October 2019.

Co-author

1. M. Tello, V. Cazcarra-Bes, M. Pardini, K. Papathanassiou, "Forest Structure Characterization From SAR Tomography at L-Band," *IEEE Journal of Selected Topics in Applied Earth Observations and Remote Sensing*, vol. 11, no. 10, pp. 3402-3414, Oct. 2018. DOI: 10.1109/JSTARS.2018.2859050
2. M. Pardini, M. Tello, V. Cazcarra-Bes, K. P. Papathanassiou, I. Hajnsek, "L-and P-Band 3-D SAR Reflectivity Profiles Versus Lidar Waveforms: The AfriSAR Case," *IEEE Journal of Selected Topics in Applied Earth Observations and Remote Sensing*,vol. 11, no. 10, pp. 3386-3401, Oct. 2018. DOI 10.1109/JSTARS.2018.2847033
3. M. Pardini, J. Armston, W. Qi, S. Lee, M. Tello, V. Cazcarra-Bes, C. Choi, K. Papathanassiou, R. Dubayah, T. Fatoyinbo, "Early Lessons on Combining Lidar and Multi-baseline SAR Measurements for Forest Structure Characterization," *Surveys in Geophysics*, Jul. 2019, DOI: 10.1007/s10712-019-09553-9
4. N. Knapp. R, Fischer, V. Cazcarra-Bes, A. Huth, "Structure metrics to generalize biomass estimation from lidar across forest types from different continents,". *Remote Sensing of Environment*, vol. 237, pp. 111597, Feb. 2020. DOI: 10.1016/j.rse.2019.111597

Conferences and Workshops

First author

1. V. Cazcarra-Bes, M. Tello Alonso, K. Papathanassiou, "The role of polarimetry on the estimation of forest structure from SAR tomography," *POLinSAR 2019; International Workshop on Science and Applications of SAR Polarimetry and Polarimetric Interferometry*, Frascati, Italy, January 2019
2. V. Cazcarra-Bes, M. Pardini, K. Papathanassiou, "Towards a Physical Interpretation of SAR Tomography for Forest Structure Estimation", *International Workshop on Retrieval of Bio- & Geophysical Parameters from SAR data for Land Applications*, Oberpfaffenhofen, Germany, November 2018
3. V. Cazcarra-Bes, M. Tello-Alonso, M. Pardini, K. Papathanassiou, "On the Effect of Number and Distribution of Acquisitions in L-Band SAR Tomography for Forest Structure Estimation," *IGARSS 2018 - 2018 IEEE International Geoscience and Remote Sensing Symposium*, Valencia, Spain, 2018, pp. 4055-4058. DOI:10.1109/IGARSS.2018.8519342
4. V. Cazcarra-Bes, M. Tello-Alonso, M. Pardini, K. P. Papathanassiou, "Assessment of Tomographic SAR Processing Techniques for Forest Structure Estimation," *EUSAR 2018; 12th European Conference on Synthetic Aperture Radar*, Aachen, Germany, 2018, pp. 1-6. ISBN:9783800746361
5. V. Cazcarra-Bes, M. Tello Alonso, K. Papathanassiou, M. Pardini, "Evaluation of Tomographic SAR Inversion Algorithms for Forest Applications," *POLinSAR 2017; International Workshop on Science and Applications of SAR Polarimetry and Polarimetric Interferometry*, Frascati, Italy, January 2017.
6. V. Cazcarra-Bes, M. Tello-Alonso, K. Papathanassiou, "Estimation of forest structure using synthetic aperture radar tomography," *IEEE YP GRSS Conference*, Munich, October 2016.
7. V. Cazcarra-Bes, M. Tello-Alonso, K. Papathanassiou, "Estimation of Forest Structure using TomoSAR Techniques," *16th ONERA-DLR Aerospace Symposium (ODAS)*,Munich, June 2016.
8. V. Cazcarra-Bes, M. Tello-Alonso, K. Papathanassiou, M. Heym, P. Biber, "Monitoring Forest Structure Dynamics by means of TomoSAR Techniques at L-band," *Proceedings of EUSAR 2016: 11th European Conference on Synthetic Aperture Radar*, Hamburg, Germany, 2016, pp. 1-6. ISBN: 9783800742288
9. V. Cazcarra-Bes, M. Tello Alonso, K. Papathanassiou, "3D forest structure estimation from sar tomography by means of a full rank polarimetric inversion based on compressive sensing," *POLinSAR 2015; International Workshop on Science and Applications of SAR Polarimetry and Polarimetric Interferometry*, Frascati, Italy, January 2015. ISBN: 9789292212933

Co-author

1. M. Pardini, V. Cazcarra-Bes, C. Choi, K. Papathanassiou, "Characterization of Forest Structure by Means of Multi-Frequency Multi-Baseline SAR Measurements: Status and Challenges," *ESA Living Planet Symposium*, Milan, Italy, May 2019
2. M. Pardini, V. Cazcarra-Bes, K. Papathanassiou, "An evaluation of Pol-InSAR complementarities between L- and S-band in forest structure observation," *POLinSAR 2019; International Workshop on Science and Applications of SAR Polarimetry and Polarimetric Interferometry*, Frascati, Italy, January 2019
3. M. Pardini,V. Cazcarra-Bes, K. Papathanassiou, "An assessment of the contribution of multiple frequencies to the observation of 3-D forest structure by means of multi-baseline SAR data",*International Workshop on Retrieval of Bio- & Geophysical Parameters from SAR data for L-band Applications*, Oberpfaffenhofen, Germany, November 2018
4. M. Pardini, J. Armston, W. Qi, S.K. Lee, C. choi, V. Cazcarra-Bes, M. Tello, K. Papathanassiou, R. Dubayah, L. Fatoyinbo ,"Understanding the link between Lidar and SAR measurements towards enhanced forest structure products: The model-based and the structure-based frameworks",*International Workshop on Retrieval of Bio- & Geophysical Parameters from SAR data for L-band Applications*, Oberpfaffenhofen, Germany, November 2018
5. K. Papathanassiou, V. Cazcarra Bes, M. Pardini, "Monitoring 3D Structure of Forest Volumes by Means of Multibaseline L-Band SAR Remote Sensing - Potentials, Challenges and Synergies," *The Forest Spatial Analysis Technologies conference*, Meryland, USA, October 2018

6. K. Papathanassiou,M. Tello-Alonso, V. Cazcarra Bes, M. Pardini, K. Su Kim, "Forest structure monitoring by means of multi-baseline SAR configurations," *The Forest Spatial Analysis Technologies conference*, Meryland, USA, October 2018

7. K. Papathanassiou, M. Pardini, J. Kim, M. Tello-Alonso, V. Cazcarra-Bes, "Forest Structure Parameter Estimation by Means of Multi-Baseline Pol-Insar Techniques: Status and Challenges," *IGARSS 2018 - 2018 IEEE International Geoscience and Remote Sensing Symposium*, Valencia, Spain, 2018, pp. 8090-8091. DOI:10.1109/IGARSS.2018.8519150

8. M. Tello, V. Cazcarra-Bes, R. Fischer, K. Papathanassiou, "Multiscale Forest Structure Estimation from SAR Tomography," *EUSAR 2018; 12th European Conference on Synthetic Aperture Radar*, Aachen, Germany, 2018, pp. 1-4. ISBN:9783800746361

9. M. Pardini, M. Tello Alonso, V. Cazcarra-Bes, K. Papathanassiou, "Describing 3-D structure of tropical forests from radar acquisitions: potentials, challenges, and links to ground and lidar measurements," *European Conference of Tropical Ecology*, Paris, France, March 2018.

10. A. Pulella, P. C. Bispo, M. Pardini, F. Kugler, V. Cazcarra-Bes, M. Tello, K. Papathanassiou, H. Balzter, I. Rizaev, M. N. Santos, J. R. dos Santos, L. S. Araujo, K. Tansey, "Tropical forest structure observation with TanDEM-X data," *2017 IEEE International Geoscience and Remote Sensing Symposium (IGARSS)*, Fort Worth, TX, 2017, pp. 918-921. DOI:10.1109/IGARSS.2017.8127102

11. M. Tello Alonso, V. Cazcarra-Bes, M. Pardini, K. Papathanassiou, "SAR Tomography for Forest Structure Characterization: Comparison of Temperate and Tropical Forests at L band," *POLinSAR 2017; International Workshop on Science and Applications of SAR Polarimetry and Polarimetric Interferometry*, Frascati, Italy, January 2017.

12. M. Tello, V. Cazcarra-Bes, M. Pardini, K. Papathanassiou, "Assessment of forest structure estimation by means of SAR Tomography: Potential and limitations," *2016 IEEE International Geoscience and Remote Sensing Symposium (IGARSS)*, Beijing, 2016, pp. 32-35. DOI:10.1109/IGARSS.2016.7728999

13. M. Tello, V. Cazcarra-Bes, J. sun Kim, M. Bertoluzza, A. Torano-Caicoya, M Pardini, K. Papathanassiou, "SAR Tomography for Forest Structure Classification and Monitoring: Actual Status and Perspectives", *International Workshop on Retrieval of Bio- & Geophysical Parameters from SAR data for Land Applications*, Harwell, UK, November 2015.

14. M. Tello, V. Cazcarra-Bes, M. Pardini, K. Papathanassiou, "Structural classification of forest by means of L-band tomographic SAR," *2015 IEEE International Geoscience and Remote Sensing Symposium (IGARSS)*, Milan, 2015, pp. 5288-5291. DOI:10.1109/IGARSS.2015.7327028

15. M. Pardini, M. Tello-Alonso, F. Kugler, A. Torano-Caicoya, V. Cazcarra-Bes, I. Hajnsek, K. Papathanassiou, "Monitoring Forest Change By Means Of Multibaseline L-Band SAR Remote Ssensing: The Traunstein Test Case," *2015 NASA Carbon Cycle & Ecosystem Joint Science Workshop*, Meryland, USA, April 2015.

16. M. Tello-Alonso, V. Cazcarra-Bes, M. Pardini, A. Torano-Caicoya, K. Papathanassiou, "3D Monitoring of forest structure by means of Synthetic Aperture Radar Tomography", *Der Gepixelte Wald conference*, Freising, Germany, March 2015.

17. A. Reppucci, J. Marquez, V. Cazcarra-Bes, G. Ruffini, "Advanced SAR simulator with multi-beam interferometric capabilities", *Proceedings Volume 9243, SAR Image Analysis, Modeling, and Techniques XIV*, Amsterdam, Netherlands, 2014. DOI:10.1117/12.2067201

18. A. Reppucci, J. Marquez, V. Cazcarra-Bes, G. Ruffini, C. Buck, "A Dual-Beam Interferometric Simulator for Wavemill Instrument Assessment," *EUSAR 2014; 10th European Conference on Synthetic Aperture Radar*, Berlin, Germany, 2014, pp. 1-4. ISBN:9783800736072

19. J. M. Lopez-Sanchez, J. D. Ballester-Berman, S. Paya, V. Cazcarra-Bes, V. D. Navarro, "An advanced electromagnetic model for rice fields at X-band: Development and interpretation of dual-pol TerraSAR-X images," *8th European Conference on Synthetic Aperture Radar*, Aachen, Germany, 2010, pp. 1-4. ISBN:9783800732722